UNIVERSITÀ DEGLI STUDI DI PADOVA

Sede Amministrativa : Università degli Studi di Padova

Dipartimento di Ingegneria Meccanica – Settore Materiali

SCUOLA DI DOTTORATO DI RICERCA IN
SCIENZA ED INGEGNERIA DEI MATERIALI
CICLO XXIII

Tesi di Dottorato

NOBLE METAL / METAL OXIDE NANOCOMPOSITE THIN FILMS FOR OPTICAL GAS SENSORS

Direttore della Scuola: Ch.mo Prof. Gaetano Granozzi

_____

Supervisore: Ch.mo Prof. Alessandro Martucci

_____

Dottorando: Enrico Della Gaspera

_____

DATA CONSEGNA TESI

31 gennaio 2011

This is to certify that:

(i) the work presented in this thesis has been developed only by myself during this PhD project, except where indicated;

(ii) all other materials used have been correctly acknowledged.

Enrico Della Gaspera

_____

Abstract *(English)*

In the last decades, the research field known as nanotechnology has been deeply investigated since it helps to understand the properties of the materials, and provides a useful tool to design materials with tailored properties, that can be exploited for many applications across the whole field of science. Nanomaterials exhibit distinctive size-dependent properties, and a high surface to volume ratio, extremely useful in applications like sensing and catalysis.

In this doctoral project, different combinations of noble metals and transition metal oxides have been used to prepare inorganic thin films to be used as reducing gases sensors through an optical interface: while the semiconductive metal oxide is usually responsible for the detection mechanism, metal nanoparticles play the role of optical probes, enhancing the optical response, and/or catalysts, improving the sensor performances. The main work presented here was focused on the synthesis of these nanocomposite materials through different strategies, according to the desired quality of the final material, the easiness of the procedure, the control on key aspects like size and shape of the particles, their size distribution, the crystallinity of the different components, the porosity.

In the first part, noble metal (Au, Ag, Pt) ions have been embedded inside oxide matrixes by means of sol-gel or impregnation processes, and reduced to metal nanoparticles through high temperature annealing, which is necessary also to promote the oxides crystallization: remarkable gas sensing properties have been observed for $NiTiO_3$-TiO_2-Au films for hydrogen sulfide detection, with extremely good sensitivity and selectivity towards interfering gases like CO and H_2. The experimental results suggest a catalytic oxidation of H_2S to sulfur oxides promoted by $NiTiO_3$ crystals, while Au nanoparticles are not involved directly in the reaction mechanism, but act as probes providing an easily detectable optical signal. Quite good sensing properties for CO and hydrogen detection have been presented for other nanocrystalline thin films like SiO_2-NiO-Ag prepared

combining sol-gel and impregnation processes, sol-gel ZnO-NiO-Au nanocomposites, and microstructured WO_3-Au-Pt films synthesized with the sputtering technique and a subsequent impregnation process.

The second part is based on the colloidal synthesis of metal (Au, Pt, Au@Pt core@shell) and oxide (TiO_2, ZnO pure and doped with transition metal ions) nanoparticles with desired size and distribution: purification and concentration protocols have been developed and the final colloidal solutions have been directly used for films deposition, obtaining nanocrystalline coatings at low temperatures. TiO_2-based films show good sensitivity for CO and H_2, with a detection threshold of about 2 ppm, quite remarkable considering that films are only 40-60 nm thick. These materials were also able to detect ethanol vapors at room temperature. Moreover samples containing both Au and Pt NPs are able to reversibly detect hydrogen at room temperature, thanks to the synergetic effect occurring between the optical properties of Au and the catalytic properties of Pt. ZnO-based samples have been tested as CO sensors with a detection limit down to 1-2 ppm, and a relationship between type of dopant (Ni, Co, Mn) and response intensity has been presented.

The third part is focused on the deposition of Au nanoparticles layers on properly functionalized substrates, and their subsequent coating with sol-gel films: when Au nanoparticles are in close contact with each other, a coupling of the plasmon frequencies is found to occur, and this effect can be used to enhance sensing, SERS and catalytic performances. Au nanoparticles layers covered with NiO or TiO_2 films showed promising gas sensing properties for CO and hydrogen detection at high temperatures, and for ethanol sensing at low temperatures. More complex structures composed of an Au nanoparticles layer sandwiched between two different oxide layers (NiO, TiO_2, ZnO) are also prepared, trying to enhance the selectivity towards interfering gases by providing two different noble metal / metal oxide interfaces.

Abstract *(Italiano)*

Negli ultimi decenni, il campo delle nanotecnologie è stato largamente studiato, poiché tramite esso si è in grado di comprendere le proprietà dei materiali, ed esso stesso fornisce un mezzo per progettare materiali aventi le proprietà desiderate, che possono essere utilizzati in diverse applicazioni nell'intero campo della scienza. I nanomateriali presentano interessanti proprietà dipendenti dalla dimensione delle particelle, e inoltre il rapporto superficie-volume in questi materiali è estremamente alto, il che li rende utili per applicazioni in sensoristica e catalisi.

In questo progetto di dottorato, diverse combinazioni di metalli nobili e ossidi di metalli di transizione sono state sfruttate per preparare film sottili inorganici, utilizzati come sensori ottici di gas riducenti: solitamente l'ossido semiconduttivo è responsabile per il meccanismo di rilevazione, mentre le nanoparticelle metalliche agiscono da sonde ottiche, aumentando la sensibilità, e/o da catalizzatori, migliorando le prestazioni del sensore. Il principale lavoro presentato in questa tesi è stato focalizzato sulla sintesi di questi materiali attraverso diverse strategie, a seconda della qualità desiderata per il materiale finale, della semplicità operativa, del controllo su parametri chiave come forma e dimensione delle particelle, la loro distribuzione dimensionale, la cristallinità dei diversi costituenti, la porosità.

Nella prima parte, ioni di metalli nobili (Ag, Au, Pt) sono stati inseriti all'interno di matrici di ossidi attraverso sintesi sol-gel o processi di impregnazione, e successivamente ridotti a particelle metalliche attraverso trattamenti termici ad alta temperatura, che sono necessari anche per la cristallizzazione degli ossidi: i sistemi $NiTiO_3$-TiO_2-Au hanno dimostrato notevoli proprietà sensoristiche nella rilevazione di acido solfidrico, con elevata sensibilità e selettività nei confronti di gas interferenti quali H_2 e CO. I risultati sperimentali suggeriscono un effetto dei cristalli di $NiTiO_3$ nel promuovere l'ossidazione catalitica dell'H_2S a ossidi di zolfo, mentre le nanoparticelle di oro non sono coinvolte

direttamente nella reazione, ma agiscono come sonde ottiche, producendo un segnale ottico facilmente rilevabile.

Discreti risultati per la rilevazione di CO e idrogeno sono stati presentati per altri film sottili nanocristallini, come SiO_2-NiO-Ag, preparati combinando la tecnica sol-gel e il processo di impregnazione, film sol-gel a base di una matrice di ZnO e NiO contenenti nanoparticelle di Au, e film microstrutturati di WO_3 contenenti nanoparticelle di Au e Pt sintetizzati combinando sputtering e impregnazione.

La seconda parte di questa tesi è basata sulla sintesi colloidale di nanoparticelle di metalli (Au, Pt, Au@Pt core@shell) e di ossidi (TiO_2, ZnO puro e drogato con ioni di metalli di transizione), aventi la desiderata dimensione e distribuzione dimensionale: protocolli di purificazione e concentrazione sono stati sviluppati, e le soluzioni ottenute sono state direttamente utilizzate per la deposizione di film sottili, ottenendo così rivestimenti nanocristallini a bassa temperatura. I film a base di TiO_2 hanno mostrato buona sensibilità per idrogeno e CO, con un limite di rilevazione di circa 2 ppm, notevole se considerato che i film sono spessi solo 40-60 nm. Inoltre questi materiali si sono dimostrati capaci di rilevare vapori di etanolo a temperatura ambiente. Infine, campioni contenenti nanoparticelle di oro e platino sono in grado di rilevare idrogeno a temperatura ambiente, grazie all'effetto sinergico che avviene tra le proprietà ottiche dell'oro e quelle catalitiche del platino. I film a base di ZnO sono stati testati come sensori di CO, dimostrando una soglia di rilevazione di circa 1-2 ppm, e una relazione fra il tipo di dopante utilizzato (Ni, Co, Mn) e l'intensità della risposta è stata presentata.

La terza parte è focalizzata sulla deposizione di strati di nanoparticelle di oro su substrati opportunamente funzionalizzati, e il loro successivo ricoprimento con film sol-gel: quando le particelle di oro sono molto vicine le une alle altre, le risonanze plasmoniche si accoppiano, e questo effetto può essere sfruttato per migliorare le prestazioni in ambiti quali sensoristica, SERS e catalisi. Strati di particelle di Au ricoperti da film di NiO o TiO_2 hanno mostrato promettenti proprietà per la rilevazione di CO e idrogeno ad alte temperature, e di vapori di etanolo a basse temperature. Inoltre, strutture più complesse a base di uno strato di particelle di oro immobilizzato fra due film di ossidi diversi (NiO, TiO_2, ZnO) sono state preparate, con lo scopo di migliorare la selettività verso gas interferenti, fornendo due diverse interfacce metallo/ossido.

To all the people that somehow helped me,
were close to me, cared about me,
and fortunately still do.
This is for You.

Preface

This doctoral project has generated some results that have been published or presented at international conferences. Presentations and publications (also papers in preparation) are listed in the following. Moreover part of the work described in this thesis has been carried out at overseas facilities, and specialization classes or schools have been attended: they are listed in the following as well.

Refereed Journal Publications

E. Della Gaspera, D. Buso, M. Guglielmi, A. Martucci, V. Bello, G. Mattei, M. Post, C. Cantalini, S. Agnoli, G. Granozzi, A. Sadek, K. Kalantar-zadeh, W. Wlodarski, "Comparison study of conductometric, optical and SAW gas sensors based on porous sol-gel silica films doped with NiO and Au nanocrystals", *Sens. Actuators B*, **2010**, *143*, 567-573.

E. Della Gaspera, M. Guglielmi, S. Agnoli, G. Granozzi, M. L. Post, V. Bello, G. Mattei, A. Martucci, "Au nanoparticles in nanocrystalline TiO_2-NiO films for SPR-based, selective H_2S gas sensing", *Chem. Mater.*, **2010**, *22*, 3407-3417.

E. Della Gaspera, D. Buso, M.L. Post, A. Martucci, "TiO_2 sol-gel thin films containing Au and Pt nanoparticles with controlled morphology: optical study and gas sensing properties", *Proc. SPIE*, **2010**, *7726*, 7726OI, doi: 10.1117/12.854544.

A.J. Morfa, G. Beane, B. Mashford, B. Singh, E. Della Gaspera, A. Martucci, P. Mulvaney, "Fabrication of ZnO thin films from nanocrystal inks", *J. Phys. Chem. C*, **2010**, *114*, 19815-19821.

E. Della Gaspera, A. Martucci, M.L. Post, "ZnO-NiO thin films containing Au nanoparticles for CO optical sensing", *Sens. Lett.*, in press.

E. Della Gaspera, A. Martucci, M. Yaacob, J. Ou, K. Kalantar-Zadeh, W. Wlodarski, "WO_3-Au-Pt nanocrystalline thin films as optical gas sensors", *Sens. Lett.*, in press.

E. Della Gaspera, M. Guglielmi, A. Martucci, G. Giallongo, S. Agnoli, G. Granozzi, F. Quaglio, "Role of Au nanoparticles and $NiTiO_3$ matrix in H_2S sensing and its catalytic oxidation to SO_x", *Sens. Lett.*, in press.

E. Della Gaspera, A. Antonello, M. Guglielmi, M.L. Post, V. Bello, G. Mattei, F. Romanato, A. Martucci, "Colloidal approach to Au-loaded TiO_2 thin films with optimized optical sensing properties", *J. Mater. Chem.*, in press.

E. Della Gaspera, M. Pujatti, M. Guglielmi, M.L. Post, A. Martucci, "Structural evolution and hydrogen sulfide sensing properties of $NiTiO_3$-TiO_2 sol-gel thin films containing Au nanoparticles", *Mater. Sci. Eng. B*, submitted.

E. Della Gaspera, V. Bello, G. Mattei, A. Martucci, "Synthesis and gas sensing properties of SiO_2 mesoporous thin films containing Ag and NiO nanoparticles", *J. Mater. Sci.*, submitted.

C. Yogi, K. Kojima, T. Hashishin, N. Wada, Y. Inada, E. Della Gaspera, M. Bersani, A. Martucci, L. Liu, T.K. Sham "Size Effect of Au Nanoparticles on TiO_2 Crystalline Phase of Nanocomposite Thin Films and Their Photocatalytic Properties", *J. Phys. Chem. C*, submitted.

E. Della Gaspera, S. Schutzmann, M. Guglielmi, A. Martucci, "Spectroscopic ellipsometry analyses of thin films in different environments: new "reverse side" approach allowing multiangle measurements", in preparation.

E. Della Gaspera, A. Martucci, G. Perotto, S. Agnoli, G. Granozzi, M.L. Post, "Effect of doping ZnO colloids with transition metal ions on the CO sensing properties of nanocrystalline ZnO-Au thin films", in preparation.

E. Della Gaspera, M. Karg, T.L. Nguyen, M. Bersani, G. Mattei, P. Mulvaney, A. Martucci, "Low temperature synthesis of nanocrystalline TiO_2 films containing Au and Pt nanoparticles with enhanced hydrogen optical sensing properties", in preparation.

A. Martucci, E. Della Gaspera, M. Karg, E. Menin, G. Maggioni, P. Mulvaney, "Au nanoparticles monolayers covered with sol-gel oxide thin films as optical gas sensors", in preparation.

Presentations during National and International Conferences

The Royal Australian Chemical Institute's National Convention (RACI) 2010, Melbourne (VIC), Australia, 4^{th} – 8^{th} July 2010, "Au nanoparticles dispersed inside porous metal oxide thin films: high performance optical gas sensors through localized surface plasmon resonance monitoring" (oral presentation).

13^{th} International Meeting on Chemical Sensors (IMCS), Perth (WA), Australia, 11^{th} – 14^{th} July 2010, "TiO_2-NiO nanocomposite thin films with Au nanoparticles for optical H_2S detection" (oral presentation).

13^{th} International Meeting on Chemical Sensors (IMCS), Perth (WA), Australia, 11^{th} – 14^{th} July 2010, "WO_3-Au-Pt nanocrystalline thin films as optical gas sensors" (poster presentation).

Visits overseas

Part of the work done during this doctoral project has been developed during visits at overseas facilities, listed below.

2nd June 2009 – 29th September 2009: Visiting researcher at the *Institute for Chemical Process and Environmental Technology (ICPET)* of the National Research Council of Canada (NRC), Ottawa (ON), Canada. Host: Dr. Mike Post.

31st May 2010 – 16th September 2010: Visiting researcher at the *School of Chemistry and Bio21 Institute* of the University of Melbourne, Melbourne (VIC) Australia; Host: Prof. Paul Mulvaney.

Specialization schools and classes

International Sol-Gel Society (ISGS) Summer School "Sol-Gel in small dimension: Nanoparticles and Thin Films", Alghero, Italy, August 2008.

J.A. Woollam Ellipsometry School "Application oriented Woollam WVASE Training Course", Darmstadt, Germany, October 2008.

Acknowledgements

The first person I'd like to acknowledge and deeply thank is my supervisor, Prof. Alessandro Martucci, without whom my research activity wouldn't have been so satisfactory and rewarding. Thank you for always being keen on answering all my questions, thank you for your patience, your understanding, and for encouraging me to do everything at my best.

Prof. Massimo Guglielmi is gratefully acknowledged for the productive discussions and for being a professional inspiration.

A lot of fruitful collaborations have been carried out during this doctoral project, and I am sincerely grateful to all the people listed below for their help in the characterization of the materials and in the discussions of the experimental results.

Dr. Mike Post is deeply acknowledged for performing most of the optical gas sensing tests, and for hosting me during my visit at the facilities of the National Research Council of Canada.

A grateful acknowledgement goes to Prof. Paul Mulvaney, for giving me the opportunity to spend a period at the Melbourne University, and for the useful discussions and precious suggestions. A great thanks goes also to all the students and researchers from the NanoScience Lab (Anthony, Matthias, Steve, Julia, Tich-Lam, Christian, Brandon, Gary, Nick, Sarah, Chris, Joe, Anneke) for helping me with SEM, TEM, impedance spectroscopy measurements, and for letting me have the best possible stay in Australia.

Prof. Giovanni Mattei and Dr. Valentina Bello are deeply acknowledged for the precious TEM cross sectional measurements.

Prof. Gaetano Granozzi, Dr. Stefano Agnoli and Mr. Giuseppe Giallongo are gratefully acknowledged for XPS analyses.

Dr. Stefano Schutzmann is acknowledged for the precious suggestions and help in fitting the ellipsometric data.

Dr. Gianluigi Maggioni is acknowledged for the VOCs sensing tests and for RBS measurements at the INFN laboratories.
Prof. Carlo Cantalini (University of L'Aquila), Prof. Woytech Wlodarski and Prof. Kourosh Kalantar-Zadeh (Royal Melbourne Institute of Technology, RMIT) are acknowledged for the ongoing collaborations in the electrical and optical gas sensing field, and for the fruitful discussions.
Mr. Franco Quaglio and Mr. Claudio Cocheo are acknowledged for the reaction products analyses performed at Fondazione Salvatore Maugeri.
I wish to thank all the people I worked with during these three years at the Department of Mechanical Engineering – Materials of the University of Padova: Marco, Giovanni, Alessandro, Giulio, Cekdar, Marta, Anna, Gioia, Jlenia, Laura, Giovanni, Dario, Filippo, and also Mauro, Sirio and Roberta.

The most important acknowledgement goes to my parents for the unconditioned support throughout all my life. Many thanks to my brother, to the new born Alessandro, and to all my relatives. A great "thank you" to all my friends: it doesn't matter where you are and how often we see each other, as long as we can count on each other. I'm honored to be part of your life, and to have shared with you all so many experiences. Simply, thank you.

Contents

List of Figures

List of Tables

Chapter 1

Overview on optical gas sensors

Contents

1.1 Introduction

Dangerous gases detection has become in the last years a challenging task for several applications, first of all in the safety of working and living environments: in fact, toxic gases like CO or volatile organic compounds like formaldehyde are commonly found in these locations, the former coming for example from insufficient oxygen content in the combustion of coal or gases for heating devices, the latter coming from indoor furniture, because it is commonly used in combination with urea, melamine or phenol to obtain thermosetting resins which are used in coatings, adhesives and foams. Another key topic associated to sensors is related to the so called comfort applications, for example in air monitoring inside buildings or cars, where the target gas may not be highly hazardous or toxic, but its detection and elimination from the environment can improve the air quality. Other applications can be found in chemical plants, inside reactors, pipes, furnaces, where the reacting atmosphere has to be checked in order to keep the overall process inside

standard parameters, or where the exhaust gases have to be purified from dangerous compounds before being discharged in the environment.

It is easy to understand that highly sensitive and possibly selective devices are mandatory for these applications; moreover an ideal sensor should also be as much miniaturized as possible, stable in a wide range of temperatures and environments, cheap, user-friendly, long-lasting and it should also allow *in situ* measurements with the operator being at safety distance from the hazardous source. Of course a sensor with all these requirement does not exist nowadays, and maybe it never will: so a compromise depending on the application is required. For example to check the exhaust gases of a nuclear plant the cost of the sensor and its working life are obviously less important compared to its accuracy in determining one particular gas, and its absolute concentration; moreover the response has to be as fast as possible.

A sensor can be defined as a device able to convert a target chemical or physical variation to be monitored into an easily processable signal; the sensing element has to fulfill essentially two different tasks: first, it has to interact with the target gas through various mechanisms like surface adsorption, charge transfer, ionic exchange (*receptor* task); then this interaction has to be transformed into an easily processable signal, like for example a change in electrical conductivity or in optical transmission (*transducer* task). There is a variety of sensing devices that rely on different chemical or physical phenomena: in fact the analyte presence can be detected through changes in electrical properties (conductivity [1], impedance [2], capacitance [3]), optical properties (absorption [4], reflection [5], luminescence [6], refractive index [7]) or other physical properties (mass [8], thermal conductivity, acoustic waves propagation [9]), measuring the reaction heat, analyzing specific electrochemical or biochemical recognition, and so on.

The first and at the moment more established sensors are based on a conductometric interface: historically the birth of electrical sensor is dated 1962, when SnO_2 has been assessed as good material for gas detection [10] and Taguchi patented the first commercial semiconductor gas sensor [11]: the sensing material resistivity change with the surrounding atmosphere is monitored and related to the target gas concentration. The main problem of the electrical devices is the intrinsic lack of selectivity: in fact all the gases with similar chemical-physical behavior will produce similar electrical variation (increase or decrease of resistance). To overcome this limitation, many electrical sensors with different sensing materials were combined in arrays in order to allow multiple gases simultaneous detection, limiting the extent of interference between different compounds:

the idea behind this approach was to simulate the human odor reception, so these sensor arrays have been named electronic noses [12,13].

More recently, a combination of different type of sensors has been achieved, connecting together different materials but also different type of transducing signals (electrical, thermal, optical, acoustic etc.): for example Baltes *et al.* reported a microsystem composed of three different sensors - capacitive, mass sensitive and calorimetric - and they demonstrated that the combination of various types of recognitions allows the improvement of the device selectivity [14].

Optical sensors have attracted a lot of interest in the last decades since they allow to widen the range of operative parameters compared to electrical sensors: in fact variation in intensity, frequency, polarization and phase of the transmitted/reflected light can be analyzed, and this can in principle improve the device performances by lowering the cross sensitivity between different gases. Moreover optical sensors have high temperature, corrosion and fire resistance, they are electromagnetic noise independent, they don't require contact measurements; eventually they can be implemented in optical fiber devices allowing fast and easy signal transport and *in situ* measurements with a compact, flexible and environmental robust setup [15,16].

A detailed description of all the optical devices is not the purpose of this thesis, and so only a brief overview on the most common optical sensors will be presented; extensive reviews on optical sensors have been published by Sberveglieri *et al*. [17], Comini et al. [18], Baldini *et al*. [19], together with a high number of papers and patents that will be used in this brief overview as references.

Optical sensors can be roughly divided into three main groups: *absorbance-based*, *luminescence-based* and SPR-based, according to the different principles of gas detection.

The absorbance-based sensors employ variation in optical absorption, transmission or reflection after the interaction of the light with the active materials in the presence of a target molecule; these sensors will be discussed in section 1.2.

In the luminescence-based sensors, the photo-luminescence or chemo-luminescence properties of the sensing material are monitored and related to the target gas concentration: the setup is the basically the same of absorbance-based sensors, with the exception of the photoluminescence based devices, that require the presence of an excitation source to promote the luminescence properties of the material; these sensors will be presented in section 1.3.

The SPR-based sensors utilize the variation of the oscillation frequency of the surface electrons of a thin metal layer (usually Ag or Au) when the gas interact with the active material deposited over this metal layer; these type of sensors will be presented in section 1.4.

1.2 Absorbance-based sensors

As stated before, under the name absorbance-based sensors a variety of different optical devices can be listed, with many different configurations: the two main groups they can divided into are *transmission* and *reflection* mode. The physics of the gas reaction with the sensing material is the same, a change in the absorption properties caused by the target molecules, but the detector is placed differently: behind the sample in transmission mode, or in front of the sample (at a fixed angle) in reflection mode. So the light that reaches the detector is the transmitted light in the first case, or the reflected light, in the second case.

In details, in the transmission mode the light emitted by a source (lamp, LED, etc.) passes through the active material and it is collected behind the sample by a detector (for example a photodiode). When the material is exposed to the target gas, changes in the absorption properties are monitored by the detector as light intensity changes as a function of wavelength, allowing to establish a relationship between the sensitivity of the device and the analysis wavelength, that of course is not possible for standard conductometric devices.

In the reflection mode, the active material is deposited on a reflective substrate: so the incoming electromagnetic wave passes through the sample, reflects on the substrate and the reflected light at a fixed angle is collected by the detector. Again, during target gas exposure, the reflection intensity as a function of wavelength is monitored.

Such simple experimental setups can be easily implemented on an optical fiber-based platform, where the fibers direct the emitted light from the source to the active material and collect the light after the interaction with it. As discussed earlier, the fiber optics technology present many advantages, the most important being the possibility to bring and collect the light from the same fiber, and the possibility to position the source and the detector far from the detection site, while the active material can be conveniently positioned in it.

One of the first publication related with optical sensing devices using optical fibers is dated back to 1984 when Ito and coworkers patented an hydrogen sensor based on the Pd-catalyzed H_2 reaction over amorphous WO_3 deposited on a polymer fiber tip [20], as shown in Figure 1.1. The partial reduction of W^{6+} to W^{5+} ions caused by hydrogen, introduces a strong optical absorption band in the visible-near infrared region (in fact tungsten trioxide is widely used in electrochromic devices) and this increase in absorption causes a decrease in the reflection intensity that is monitored and related to hydrogen concentration.

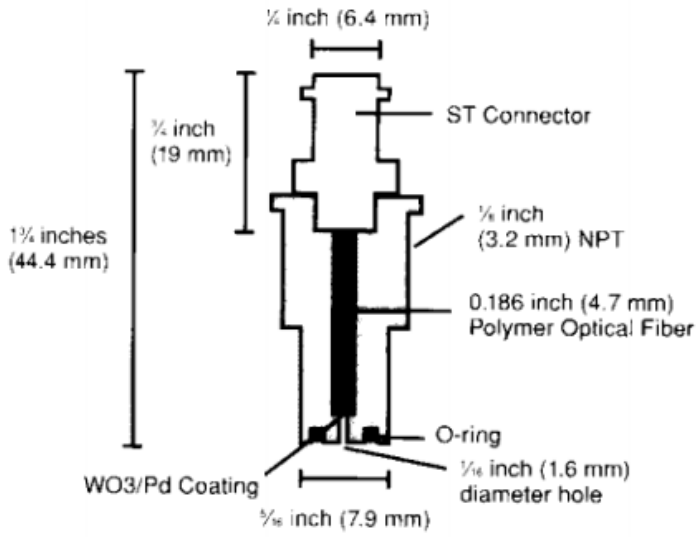

Figure 1.1. Scheme of an optical fiber-based hydrogen sensor adapted from the work proposed by Ito and colleagues [20].

Few years later, Saaski *et al*. [21] patented a setup for transmission and reflection gas sensing and pH tests using optical fibers: the two setups are shown in Figure 1.2. In the transmission mode, an optical fiber coming from the light source is connected to a transparent cell provided with inlet and outlet for the gas stream; the active film deposited on a transparent substrate is mounted orthogonal to the light direction and the sample holder is provided with a heater to perform high temperature tests. On the other side of the transparent cell, the output optical fiber is placed and the light is then transferred to a detector.

The setup for the reflection mode is similar, but only one fiber is used to bring the light to the sample and collect the reflected light after the interaction with the sample. For this reason, a reflecting mirror has to be placed behind the active film.

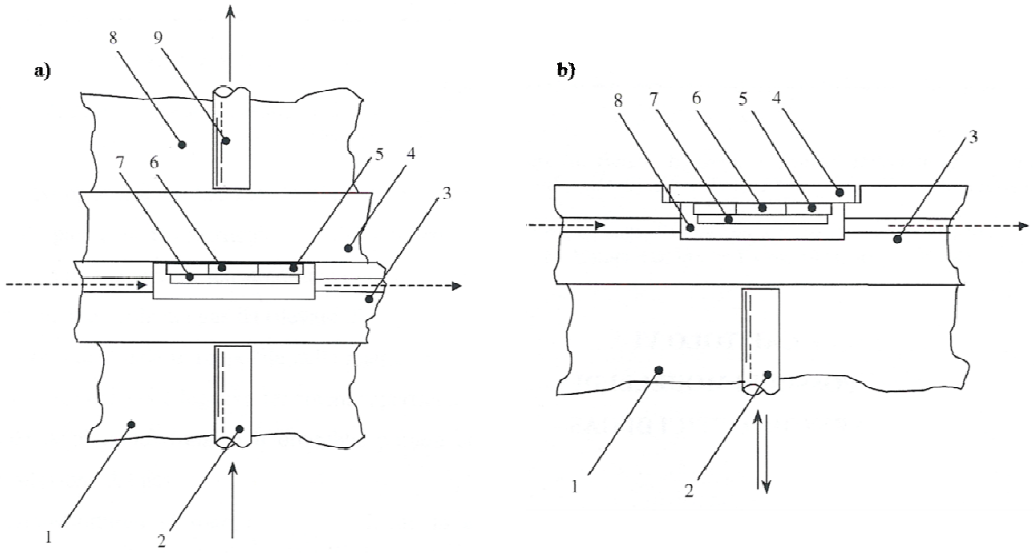

Figure 1.2. a) Scheme of the transmission-based setup as described by Saaski and coworkers: 1) scaffold; 2) input optical fiber; 3, 4) transparent scaffolds; 5) heating device; 6) window; 7) active material; 8) scaffold; 9) output optical fiber. b) Scheme of the reflection-based setup as described by Saaski and coworkers: 1) scaffold; 2) input optical fiber; 3) transparent scaffold; 4) reflecting mirror; 5) heating device; 6) window; 7) active material; 8) test cell. In both schemes the dashed lines represent the gas flow, while the straight lines represent the light direction. Both images adapted from [21].

There are several key points that have to be addressed carefully with these setups, in order to avoid low detected intensity and low signal to noise ratio. First of all, the couplings between fibers and scaffolds have to be checked and optimized, in order to avoid scattering and unwanted reflection at the interfaces. Moreover the heating device has to be calibrated, preventing in this way undesired localized heating that can affect negatively the measurement and can also cause corrosion problems. In the end, for the reflection mode setup, great care has to be put in the selection of the reflecting mirror, according to the operational wavelengths and temperatures.

A different configuration for the reflection measurements has been presented again by Ito and colleagues [22]: in this particular setup, both the active layer and the reflecting mirror are deposited at the end of the fiber tip. Figure 1.3 shows the conventional setup for reflection-based sensors, where the reflected light is collected with another optical fiber and where the mirror is placed outside the fibers inside a test cell (dashed box in figure 1.3a), compared with the innovative setup where everything (active layer, mirror) is implemented at the end of one single fiber (Figure 1.3b), allowing smaller and more

flexible devices and limiting all the problems related with coupling and alignment of the fibers.

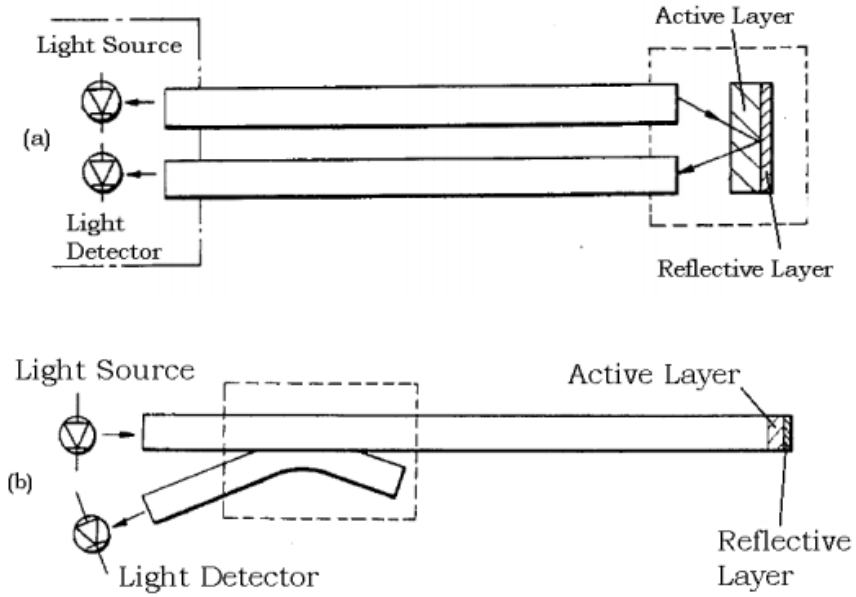

Figure 1.3. Scheme of the reflection-based setup as described by Ito and coworkers: a) general two fibers setup; b) single fiber setup (taken from [22]).

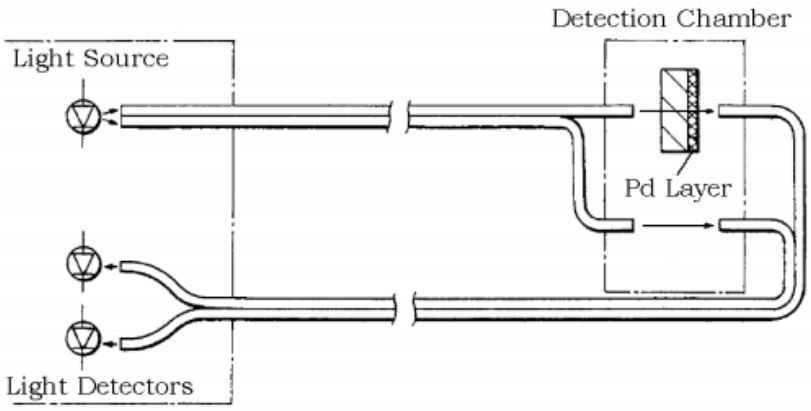

Figure 1.4. Scheme of the transmission-based setup with one fiber used as reference, as described by Garcia and Mandelis [23,24].

Many scientists took inspiration from these pioneering works, and from the beginning of the nineties a lot of patents and papers describing gas sensing setups based on optical fibers started to appear. For example Butler presented a thin film of Pd as reflecting mirror to be put at the end of the optical fiber in the single fiber reflection setup [25]. More recently, an improvement of the transmission mode system has been presented by

Garcia [23] and Mandelis [24]: the light coming from a diode laser was separated into two beams using a beamsplitter and directed into two different fibers: one fiber was attached to the sample and the light coming out from the back of the sample was collected by a third fiber and brought to the detector, while the other fiber was used as a reference, as shown in Figure 1.4. In this way a more careful and accurate evaluation of the gas concentration was possible.

A subsequent step in the optimization of the optical fiber-based devices is the integration of the sensing layer on the optical fiber itself: this is possible removing the jacketing material in a portion of the fiber and substituting it with a layer of an active material [22]. This active layer can be made of a metal oxide material of proper refractive index so as to maintain the total internal reflection condition of the optical fiber, as described by Robillard [16], or can be a thin metal layer, providing the conditions for a SPR (Surface Plasmon Resonance) device (see section 1.4)

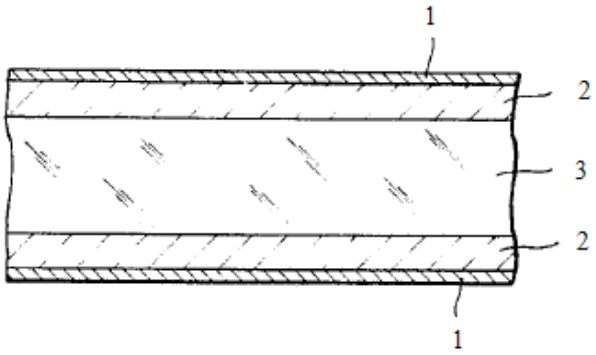

Figure 1.5. Scheme of the section of an optical fiber portion used as hydrogen sensing described by Ito and coworkers: 1) thin Pd layer; 2) oxide layer; 3) fiber core (taken from [22]).

With this setup the optical fibers are not only responsible for carrying the light beam to and from the active layer, but they are part of the sensing system itself, being the active layer deposited on the fiber. In this way the response intensity can be substantially increased compared to the standard transmission or reflection setups, thanks to the multiple reflections occurring at the fiber/active material interface.

Many authors have used over the years this idea to create sensing devices for gases, vapors and even liquids (as a matter of fact, the patent presented by Saaski *et al*. [21] describes also a pH sensor, so a sensing device for H^+ ions in liquids). For example, Bevenot and colleagues [26] used a thin Pd layer deposited on a part of an optical fiber where the jacketing and cladding materials were removed as hydrogen sensor: the authors

exploited the Pd layer for its known selectivity towards hydrogen detection and to create the conditions for the surface plasmon resonance reflection. Mechery and Singh [27] published a paper describing the NO_2 sensing performance of a sensing material dispersed inside a porous inert SiO_2 matrix in three different measurement setups: in the first one, the sensing material is deposited over a reflecting mirror and a single fiber is used to bring the light to the sample and collect the light reflected from the sample, as described earlier; in the second setup, the geometry is similar to the previous example, but the reflecting layer is absent and the active film is tilted at the Brewster angle, so providing maximum reflection itself; in the third setup, the optical fiber core is substituted for a certain portion with the SiO_2-based active material itself: in this way an extremely high sensitivity is achieved, because almost all the guided modes in the fiber core interact with the sensing material, hence improving the light interaction length and the final sensing response.

Another experimental setup has been presented by Tao *et al*. [28] for a highly sensitive ammonia and humidity sensor: the jacketing and the cladding materials of a portion of the fiber carrying the light beam were removed and the bare core was coated with a porous silica-based active layer.

A slightly different approach has been used by Lin and coworkers [29]: the active materials in this particular case is composed of an assembly of Au nanoparticles (NPs) deposited on an unclad portion of an optical fiber: in this case the optical properties of Au NPs (localized surface plasmon resonance, LSPR, in the visible range) are exploited to increase the sensitivity of the optical device.

Another possible setup is based on Bragg reflectors, as published by Bailey and Hupp [30] and Jalkanen *et al*. [31]: in the first case a micropatterned vapochromic film deposited on a transparent substrate was used as active material, while in the second case a porous silicon Bragg reflector is used as organic vapors sensor, analyzing the shift of the resonant peak.

Besides all these examples, there are also more "conventional" optical sensors that remind the traditional conductometric devices: the sensing element is coupled directly with the electronic support, and for this reason these devices are called *solid body* optical sensors. One of these configurations is reported in Figure 1.6: the light source is usually a cheap and low power consumption LED, and the sensitive layer is deposited either directly on top of the detector or on a surface immediately above it. The internal surface of the embodiment is totally reflective and usually there is also a reference detector

uncovered with the sensing layer: in this way the light intensity that reaches the detector in one case is filtered through the active material, and so the sensing response is given comparing the signals arriving at the two detectors.

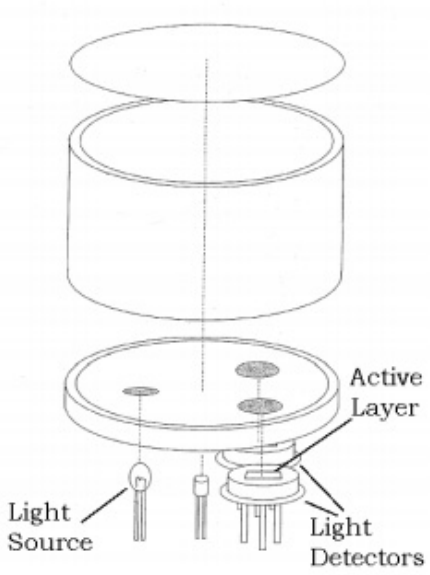

Figure 1.6. Scheme of a possible configuration for a solid body optical sensor.

As briefly discussed, there is a variety of possible configurations for an optical sensing device based on absorbance change of the active material. The nanostructured films prepared during this doctoral project have been tested mainly in transmission using test cells inside commercial spectrophotometers, but also in reflection mode, as described in the Appendix section. These are easy and convenient ways to test the sensing properties of the material itself: once its ability to detect gaseous species has been proved, a subsequent step that lies outside this project is to deposit the active material in an actual sensing device using for example one of the previously presented configurations and check its sensing performances in a real environment.

1.3 Luminescence-based sensors

Fluorescence-based sensors have been widely investigated in the latest years as a consequence of some advantages they present with respect to other different chemical sensors: first of all, fluorescence measurements are extremely sensitive, down to the single molecule detection; moreover the experimental setup is quite easy and versatile, and for certain conditions, also cheap [32-34]. As anticipated before there are mainly two

types of luminescence-based sensors, that exploit the photoluminescence or chemoluminescence properties of the active material: in the case of photoluminescence a light source is used to excite electrons of the active compound that returning to the standard, low energy state, emit light at higher wavelengths, while in the case of chemoluminescence, the chemical reaction itself triggers the light emission. Another classification can be based on the type of the sensing material: nanoparticles (usually semiconducting quantum dots, QDs) or organic dyes or organic complexes of transition metal ions; an interesting review dealing with these two types of active materials and their possible interaction has been presented by Prodi [35]. There are several ways in which the analyte can interact with the active material: for example quenching the luminescence of quantum dots, or shifting the emission peak, or again promoting new emissions. In any case the field of luminescence-based sensors is extremely wide, so only few example of some interesting and promising applications will be presented in the following.

One of the first thorough study on luminescent active materials used as sensors has been published by Carraway *et al*. [36]: the authors presented a study on transition metals organic complexes as oxygen sensors, based on oxygen capability to quench the emission intensity of these compounds.

Benner and Stedman [37] presented a sensor for sulfur-containing compounds based on a different approach: the analytes are drawn inside a hydrogen flame and the resulting compounds are let react with ozone: this reaction produces excited sulfur dioxide that has an emission peak at about 350 nm. So, by monitoring this wavelength, the authors related the emission intensity to the target gas concentration, with a detection limit below 1 ppb, and almost no cross sensitivity with other sulfur-free compounds. In this setup the analyte is the active material itself, because after the reaction with ozone, it is responsible for the light emission. These luminescent properties of excited SO_2 species have been exploited also by Zhang *et al*. [38] in the design of a hydrogen sulfide sensor: H_2S was catalytically oxidized over transition metal oxides (Fe_2O_3 for example) and the emission of the excited SO_2 state was monitored and related to the gas concentration, with a linear relationship in the 8-2000 ppm. Of course there are others excited gaseous species that can be monitored: for example Zhou *et al*. [39] presented a formaldehyde sensor based on the cataluminescence properties of an intermediate compound formed from the reaction of formaldehyde and oxygen on the surface of proper catalysts.

A lot of published material discussing the quenching of the luminescence of both organic and inorganic emitting materials is available: for example Dasgupta and coworkers [40]

used an alkaline fluorescein mercuric acetate as optical probe again for hydrogen sulfide detection, due to the well-known capability of H_2S to reduce the emission intensity of that particular compound [41].

Mauro *et al*. [42] presented quantum dots-proteins assemblies for biomolecules sensing, using the highly specific bonding between the analyte and a proper protein, and monitoring the QDs luminescence quenching due to the fluorescence resonance energy transfer (FRET) occurring between the two biological compounds. Few years later, some of the authors used the same idea to create a 2,4,6 trinitrotoluene (TNT) sensor in aqueous environments [43].

Recently, Su and colleagues [44] reported a CdTe-polyelectrolyte composite film as gaseous formaldehyde sensor based on the quenching of the QDs luminescence, with excellent sensitivity (down to 1 ppb) and also good selectivity; the main problem with these types of sensors is the reversibility of the reaction: once the analyte has been removed from the environment, often the initial luminescence is not recovered, because the sensing material has been modified permanently.

Without going far beyond the purpose of this section, in conclusion some interesting reviews can be cited: Parker [45] presented a detailed collection of lanthanide-based sensors for pH, oxygen and some anions that monitor the luminescence change due to interaction of these analytes with the lanthanide complexes. In the same year, Prodi *et al*. [34] described a variety of organic complexes for the detection of traces of transition metal ions in biological environments.

More recently, Callan and colleagues [46] presented an extensive review discussing several organic dyes as metal cations and anions sensors, focusing on different reaction mechanisms and on the selectivity between different ions competing for the same reaction site.

As briefly discussed, the luminescence-based sensor field is widely studied and extremely promising, especially for specific molecules recognition.

1.4 Surface Plasmon Resonance-based sensors

The concept behind the Surface Plasmon Resonance (SPR) sensors lies in the excitation and propagation of surface plasmons at the interface between a metal (usually Ag or Au) and a dielectric: a surface plasmon resonance is an oscillation of the charge density that

may exist at the interface of two media with dielectric constants of opposite signs, precisely, a metal and a dielectric. The charge density wave is associated with an electromagnetic wave, the field vectors of which reach their maxima at the interface and decay evanescently into both media [47]. If the metal is constituted by a thin film (with thickness of few tens of nm), these waves are also on the boundary of the metal and the external medium: their amplitude is therefore very sensitive to any change of this boundary, such as the adsorption of molecules to the metal surface [18].

Since these coherent oscillations of metal surface electrons are extremely sensitive to change in the dielectric properties (for example the refractive index) of the interfacing material, this property can be exploited to create a sensor with high sensitivity. The theoretical basis of the phenomenon was laid by Wood [48] at the beginning of the twentieth century, analyzing the anomalous light diffraction on diffraction gratings, but a real progress was made when Ritchie [49] theoretically demonstrated the existence of surface plasma excitations at a metal surface and Otto [50] and Kretschmann [51] described the attenuated total reflection (ATR) prism coupling scheme to make practical the excitation of the surface electromagnetic waves by a light beam.

The SPR angle mainly depends on the properties of the metal film, the wavelength of the incident light and the refractive index of the media on both side of the film. The propagation constant β of the surface plasma wave propagating at the interface between a semi-infinite dielectric and metal is given by the following expression:

$$\beta = k\sqrt{\frac{\varepsilon_m n_s^2}{\varepsilon_m + n_s^2}} \tag{1.1}$$

where k denotes the free space wave number, ε_m the dielectric constant of the metal, and n_s the refractive index of the dielectric. As may be concluded from equation (1), the surface plasmon wave may be supported by the structure providing that $\varepsilon_{1m} < -n_s^2$. Metals that satisfy this requirement are for example silver, gold, copper, aluminium, sodium, and indium [52]. Among them, gold and silver are preferable, since indium is quite expensive, sodium too reactive, copper and aluminium too broad in their SPR response; gold is the most used thanks to its high resistance to oxidation compared to silver, even if a silver film may yield a more distinct SPR spectrum with respect to gold.

In most common practical applications, the metal film is deposited onto the base of a glass prism (the Kretschmann configuration, see below); from a certain angle of incidence, the incoming light is totally reflected, and an evanescent wave penetrates

through the metal film: This electromagnetic field is called evanescent wave because the amplitude of the wave decreases exponentially with increasing distance from the interface surface, decaying over a distance of about one light wavelength [53]. As a result of this evanescent wave formation, a decrease of intensity of the reflected light is observed.

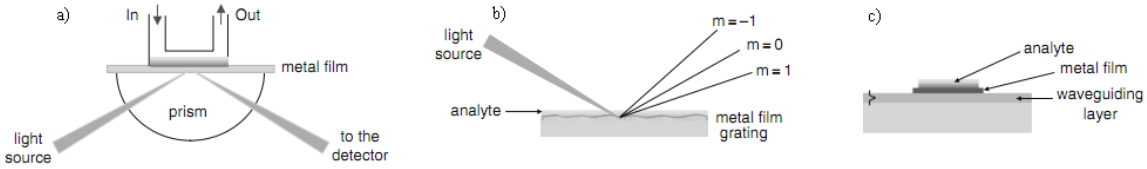

Figure 1.7. Different possible configurations for a SPR device: a) prism coupling; b) grating coupling; c) waveguide coupling (taken from [18]).

A SPR device can exist in several configurations: prism coupled systems, grating coupled systems, and optical waveguide systems (Figure 1.7). Moreover, the prism can be coupled to the metal layer in different ways: in the Otto configuration [50] a low refractive index medium is placed in between the metal and the total internal reflection (TIR) surface (Figure 1.8a.). This configuration is commonly used for SPR in solid-phase media. This distance in the Otto configuration limits the SPR efficiency: so when analyzing liquid solutions or gases it is preferable to use the Kretschmann configuration [51], where the metal layer is directly on top of the TIR surface (Fig. 1.8b), enabling a more efficient plasmon generation. A third configuration (Figure 1.8c) is similar to the Otto arrangement but uses a special layer to enhance TIR and a resonant mirror to couple the TIR light to plasmons.

The glass prism can also be replaced by a diffraction grating covered with the metal: for a proper combination of the period of the grating, the angle and wavelength of the incident wave, a surface plasmon is generated (Figure 1.9a).

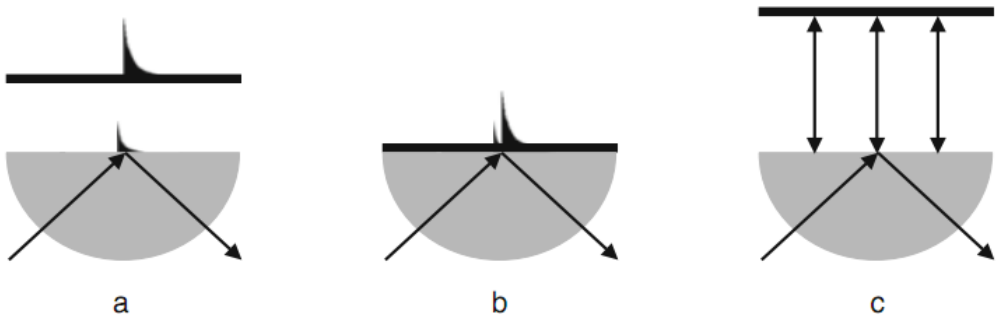

Figure 1.8. Different possible configurations for a prism-coupled SPR device: a) Otto configuration; b) Kretschmann configuration; c) modified Otto configuration (taken from [18]).

Eventually, also an optical waveguide can constitute a SPR device: in fact in a waveguide the radiation is confined inside a layer as in optical fibers, with the difference that usually optical waveguides are planar and not with axial symmetry. By depositing a thin metal layer on the surface of an optical waveguide, and using proper wavelength/guided modes combinations, it is possible to excite surface plasmons on the metal layer. An example of the use of planar waveguides as hydrogen sensors is reported in Figure 1.9b.

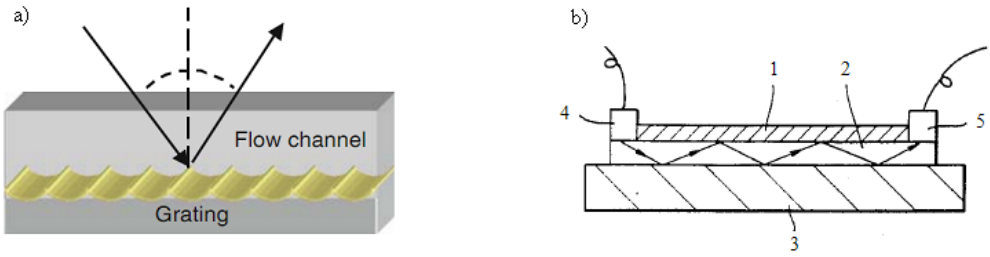

Figure 1.9. Possible setup for a) a grating-coupled SPR sensor; b) a planar waveguide SPR hydrogen sensor: 1) metal thin film; 2) high refractive index layer; 3) low refractive index substrate; 4) light source; 5) detector (taken from [22]).

It is immediately clear that such a system can be easily coupled with optical fibers technology (refer to Figure 1.5), exploiting all the advantages of the optical fibers: multiple reflections, low-cost setup, *in situ* measurements, etc.

The SPR sensors are intrinsically non-selective, because every analyte that can cause a variation in the electric-dielectric properties at the interface with the metal layer are in principle capable to alter the plasmon propagation: the specificity of SPR sensors is

usually achieved by modifying the metal surface with a functional layer to allow specific binding between the ligand molecules and the analyte (Figure 1.10).

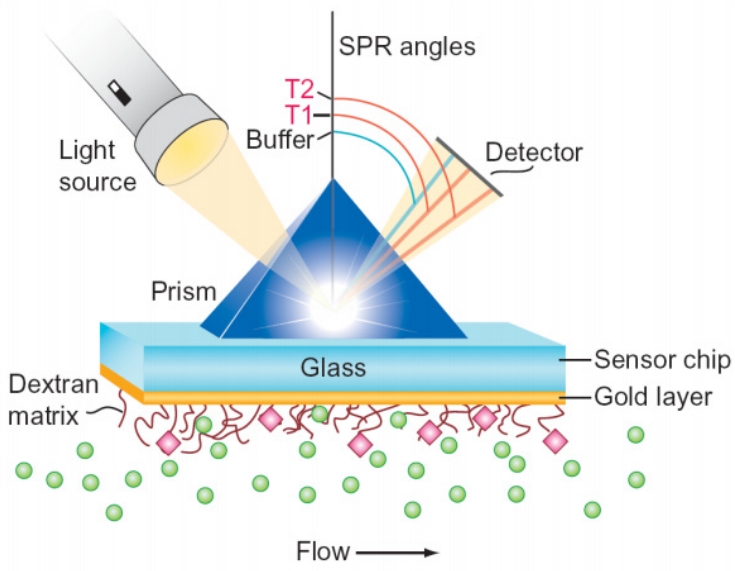

Figure 1.10. Prism coupled SPR sensor with a modified gold layer capable to anchor specific analyte molecules (taken from [54]).

A distinctive characteristic of optical sensor is the possibility to monitor different parameters: in SPR devices the interaction of the target gas with the metal layer can be appreciated looking at the intensity of the reflected light [55], variation of the resonant angle of incidence of the light [56], and variation of the resonant wavelength of the incident light [57].

In conclusion of this brief overview, the works published by Homola *et al*. [47] and by Ince *et al*. [58] is worth to be cited, since both are detailed reviews on SPR sensors materials and devices.

Bibliography

[1] G. Heiland, *Sens. Actuators*, **1981-1982**, *2*, 343-361.

[2] N. Miura, M. Nakatou, S. Zhuiykov, *Sens. Actuators B*, **2003**, *93*, 221–228.

[3] T. Ishihara, S. Matsubara, *J. Electroceram.*, **1998**, *2*, 215-228.

[4] M. Ando, T. Kobayashi, S. Iijima, M. Haruta, *J. Mater. Chem.*, **1997**, *7*, 1779-1783.

[5] D. Richter, D.G. Lancaster, F.K. Tittel, *Appl. Optics*, **2000**, *39(24)*, 4444-4450.

[6] C.C. You, O.R. Miranda, B. Gider, P.S. Ghosh, I.B. Kim, B. Erdogan, S.A. Krovi, U.H.F. Bunz, V.M. Rotello, *Nature Nanotechnology*, **2007**, *2*, 318-323.

[7] R. Bjorklund, J. Hedlund, J. Sterte, H. Arwin, *J. Phys. Chem. B.*, **1998**, *102*, 2245-2250.

[8] V. Lazarova, L. Spassov, V. Gueorguiev, S. Andreev, E. Manolov, L. Popova, *Vacuum*, **1996**, *47*, 1423-1425.

[9] A.J. Ricco, S.J. Martin, T.E. Zipperian, *Sens. Actuators*, **1985**, *8*, 319-333.

[10] K. Ihokura, J. Watson, *The Stannic Oxide Sensor, principles and applications*, CRC Press, **1994**.

[11] N. Taguchi, *Japan Patent 45-38200*, **1962**.

[12] M.S. Freund, N.S. Lewis, *Proceeding of the National Academy of Science*, **1995**, *92*, 2652-2656.

[13] K.J. Albert, N.S. Lewis, C.L. Schauer, G.A. Sotzing, S.E. Stitzel, T.P. Vaid, D.R. Walt, *Chem. Rev.*, **2000**, *100*, 2595−2626.

[14] C. Hagleitner, A. Hierlemann, D. Lange, A. Kummer, N. Kerness, O. Brand, H. Baltes, *Nature*, **2001**, *414*, 293-296.

[15] K. Educhi, *Optical gas sensors*, in *Gas Sensors*, Edited by G. Sberveglieri, Kluwer Academics Publishers, Dordrecht, **1992**, 307-328.

[16] J.J. Robillard, U*.S. Patent 5436167*, **1995**.

[17] G. Sberveglieri, *Gas Sensors*, Kluwer Academics Publishers, Dordrecht, **1992**.

[18] E. Comini, G. Faglia, G. Sberveglieri, *Solid State Gas Sensing*, Springer, Dordrecht, **2008**.

[19] F. Baldini, A.N. Chester, J. Homola, S. Martellucci, *Optical chemical sensors*, Springer, Dordrecht, **2006**.

[20] K. Ito, T. Kubo, *Proceedings of the 4th Sensor Symposium*, Tsukuba, Japan, **1984**, 153-156.

[21] E.W. Saaski *et al*., *U.S. Patent 5039492*, **1989**.

[22] K. Ito, T. kubo, Y. Yamauchi, *U.S. Patent 4661320*, **1987**.

[23] J.A. Garcia, A. Mandelis, *Review of Scientific Instruments*, **1996**, *67(11)*, 3981

[24] A. Mandelis, J.A. Garcia, *Sens. Actuators B*, **1998**, *49*, 258.

[25] M.A. Butler, *Journal of the Electrochemical Society*, **1991**, *138*, L46.

[26] X. Bevenot, A. Trouillet, C. Veillas, H. Gagnaire, M. Clement, *Meas. Sci. Technol.*, **2002**, *13*, 118-124.

[27] S.J. Mechery, J.P. Singh, *Anal. Chim. Acta*, **2006**, *557*, 123-129.

[28] S. Tao, J.C. Fanguy, L. Xu, *Mater. Res. Soc. Symp. Proc.*, **2005**, *828*, A1.9.1-A1.9.8

[29] L.K. Chau, Y.F. Lin, S.F. Cheng, T.J. Lin, *Sens. Actuators B*, **2006**, *113*, 100-105.

[30] R.C. Bailey, J.T. Hupp, *J. Am. Chem. Soc.*, **2002**, *124*, 6767-6774.

[31] T. Jalkanen, V. Torres-Costa, J. Salonen, M. Bjorkqvist, E. Makila, J.M. Martinez-Duart, V.P. Lehto, *Optics Express*, **2009**, *17*, 5446-5456.

[32] J.P. Desvergne, A.W. Czarnik, *Fluorescent Chemosensors of Ion and Molecule Recognition*, Kluwer Academic Publishers, Dordrecht, **1996**.

[33] A.P. de Silva, H.Q.N. Gunaratne, T. Gunnlaugsson, A.J.M. Huxley, C.P. McCoy, J.T. Rademacher, T.E. Rice, *Chem. Rev.*, **1997**, *97*, 1515.

[34] L. Prodi, F. Bolletta, M. Montalti, N. Zaccheroni, *Coord. Chem. Rev.*, **2000**, *205*, 59.

[35] L. Prodi, *New J. Chem.*, **2005**, *29*, 20-31.

[36] E.R. Carraway, J.N. Demas, B.A. DeGraff, J.R. Bacon, *Anal. Chem.*, **1991**, *63*, 337-342.

[37] R.L. Benner, D.H. Stedman, *Anal. Chem.*, **1989**, *61*, 1268-1271.

[38] Z. Zhang, H. Jiang, Z. Xing, X. Zhang, *Sens. Actuators B*, **2004**, *102*, 155-161.

[39] K. Zhou, X. Ji, N. Zhang, X. Zhang, *Sens. Actuators B*, **2006**, *119*, 392-397.

[40] A.A. Cardoso, H. Liu, P.K. Dasgupta, *Talanta*, **1997**, *44*, 1099-1106.

[41] D.H. Axelrod, J.H. Cary, J.E. Bonelli, J.P. Lodge Jr., *Anal. Chem.*, **1969**, *41*, 1856.

[42] I.L. Medintz, A.R. Clapp, H. Mattoussi, E.R. Goldman, B. Fisher, J.M. Mauro, *Nature Materials*, **2003**, *2*, 630-638.

[43] E.R Goldman, I.L. Medintz, J.L. Whitley, A. Hayhurst, A.R. Clapp, H. T. Uyeda, J.R. Deschamps, M.E. Lassman, H. Mattoussi, *J. Am. Chem. Soc.*, **2005**, *127*, 6744-6751.

[44] Q. Ma, H. Cui, X. Su, *Biosens. Bioelectron.*, **2009**, *25*, 839-844.

[45] D. Parker*, Coord. Chem. Rev.*, **2000**, *205*, 109-130.

[46] J.F. Callan, A. Prasanna de Silva, D.C. Magri, *Tetrahedron*, **2005**, *61*, 8551-8588.

[47] J. Homola, S.S. Yee, G. Gauglitz, *Sens. Actuators B*, **1999**, *54*, 3-15.

[48] R.W. Wood, *Philosophical Magazine*, **1902**, *4*, 396402.

[49] R.H. Ritchie, *Phys. Rev.*, **1957**;*106*, 874–881.

[50] A. Otto, *Zeitschrift Physik*, **1968**, *216*, 398-410.

[51] E. Kretschmann, H. Raether, *Zeitschrift fur Naturforschung*, **1968**, *23A*, 2135-2136.

[52] M.A. Ordal, L.L. Long, R.J. Bell, S.E. Bell, R.R. Bell, R.W. Alexander, J. Ward, C.A. Ward, *Appl. Opt.*, **1983**, *11*, 1099–1119.

[53] K. Nagata, H. Handa, *Real-Time Analysis of Biomolecular Interactions: Application of Biacore*, Springer-Verlag, **2000**.

[54] W.D. Wilson, *Science*, **2002**, *295*, 2103-2105.

[55] C. Nylander, B. Liedberg, T. Lind, *Sens. Actuators*, **1982**, *3*, 7988.

[56] K. Matsubara, S. Kawata, S. Minami, *Appl. Optics*, **1988**, *27*, 1160-1163.

[57] L.M. Zhang, D. Uttamchandani, *Electron. Lett.*, **1988**, *23*, 1469-1470.

[58] R. Ince, R. Narayanaswamy, *Anal. Chim. Acta*, **2006**, *569*, 1-20.

Chapter 2

Wet chemistry syntheses of thin films containing nanoparticles of metals and oxides

Contents

2.1 Introduction

Semiconductor and dielectric matrixes containing noble metal nanoparticles have been deeply investigated in the last few years, due to their unique properties and potential applications in different scientific fields, such as catalysis and photocatalysis [1-3], gas sensing [4,5], optics and optoelectronics [6-8].

Au and Ag NPs have attracted a lot of interest for their strong optical absorption in the visible range due to localized surface plasmon resonance (LSPR) and their chemical activity. In particular Au has been widely used in optical devices thanks to its great stability in a wide range of temperatures and environments; on the contrary, Ag is usually susceptible of oxidation, even if it present a more intense and sharper SPR band [9]. Pt

and Pd NPs don't present interesting optical properties in the visible and near infrared range, but they have been extensively studied due to their interesting catalytic properties, for example for the oxidation of alcohols, for hydrogen splitting reactions, and so on. As far as the semiconducting oxides are concerned, a great variety of materials has been analyzed and a list of the main oxides investigated will be absolutely incomplete and will go beyond the purpose of this section.

Different methods to create nanocomposites composed of metal NPs embedded in a semiconducting or dielectric oxide matrixes are available, such as sputtering [10,11], electrochemical reactions [12], electron beam deposition [13], spray pyrolisis [14], evaporation [15], ion implantation [16], CVD [17], sol-gel [18,19]. All these techniques have distinctive advantages and disadvantages: for example with physical deposition methods the stoichiometry of the materials can be easily controlled, but usually the synthesized films are dense, so not ideal for gas sensing or catalysis applications, where a proper porosity and a high specific surface are required. Moreover, many of the previous cited techniques require highly expensive setups. The sol-gel technique is rather simple, allows the preparation of multi-component and mixed oxide materials, and a discrete control on porosity is achievable, but the resulting thin films usually suffer from poor control over physical and morphological properties and often size tuning and ensuring particle monodispersity is difficult to achieve.

Since this doctoral project was based on the synthesis of nanocrystalline thin films trough wet chemistry techniques, some strategies for the preparation of such materials will be presented in the following sections: in the first part, the synthesis of amorphous thin films via sol-gel method and the crystallization of both oxide and metal NPs through high temperature annealings will be discussed; then a different approach based on the preparation of colloidal solutions of the desired NPs with tailored properties coming from an accurate control on size, shape and monodispersity, and the deposition of thin films using these colloids will be presented; eventually, metal NPs monolayer possibly covered with different oxide films will be shown as a further example of materials engineering at the nanoscale. These three sections represent also the three main experimental chapter in which this thesis is divided.

2.2 High temperature crystallization of metals and oxides

A simple, convenient method to synthesize nanocomposite thin films composed of an oxide matrix containing metal nanoparticles consists on the preparation of a solution starting from suitable precursors, a film deposition with standard wet chemistry techniques, and then the oxidation of the metal oxide precursors and the reduction of noble metal precursors with high temperature annealings. With this procedure, usually high sample thickness is achievable, it is possible to mix different precursors aiming to obtain nanocrystals of different oxides or even complex mixed oxides, and high concentration of noble metal NPs is usually possible. Moreover the experimental setup is rather simple and cheap.

In the past years, noble metal NPs such as Au, Ag, Pt or Pd have been successfully embedded inside various sol-gel oxide layers like SiO_2, TiO_2, ZrO_2, ZnO, Al_2O_3. The reduction of noble metal precursors inside sol-gel matrixes with annealing temperature has been described by Sakka and Kozuka [20] for a variety of noble metals and oxide matrixes. As far as Au is concerned, usually a suitable salt as hydrogen tetrachloroaurate ($HAuCl_4 \cdot xH_2O$) is dissolved in the sol-gel based solution and the mixture is directly deposited with spinning or dipping techniques on suitable substrates. With thermal annealing, the Au precursor is progressively reduced to metallic Au: first the metal salt is de-hydrated at 100 °C, then at 160 °C Au^{3+} ions are reduced to Au^{+}, and eventually at 200 °C Au^{+} ions are completely reduced to Au^{0}, *i.e.* metallic gold [21]. For example, Kozuka and Sakka [22] presented SiO_2-Au composite thin films mixing a sol-gel silica solution with $HAuCl_4$ and then reducing the Au ions with heat treatment. Also Lee *et al*. [23] reported the synthesis of Au-doped silica sol-gel matrix, analyzing the effect of annealing time and temperature on the crystallization and growth of Au crystals, and the third-order optical non-linearity of such nanocomposite films. Mazzoldi and coworkers [24] showed the formation of AuCu alloy NPs in sol-gel SiO_2 matrix when annealing in reducing atmosphere, while if annealing in air, Au and CuO NPs are observed to form. More recently, Buso *et al*. [25] embedded inside a porous silica matrix both Au and NiO nanocrystals that for certain annealing conditions form interesting two-fold structures. Au NPs have been also dispersed in other oxide sol-gel films, as TiO_2 [26], ZnO [27], Al_2O_3 [28], ZrO_2 [29].

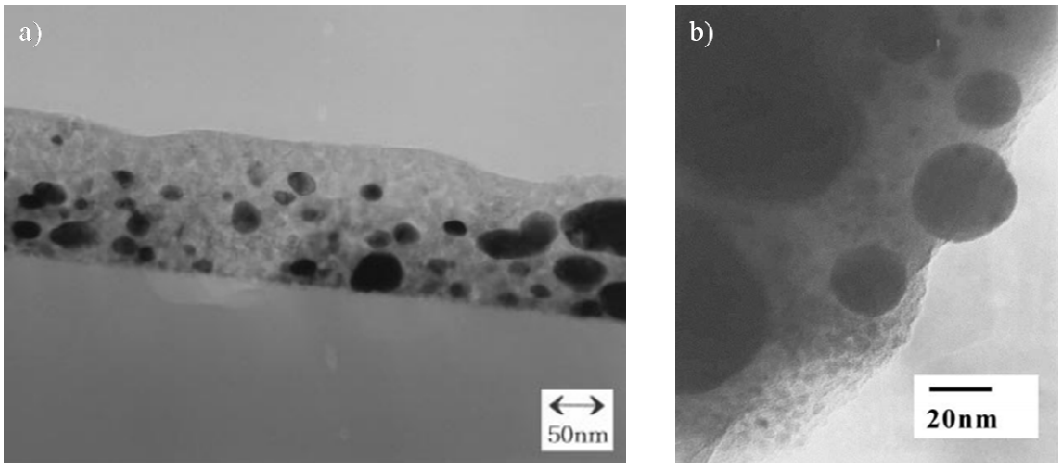

Figure 2.1. Bright Field TEM images of a) TiO_2-Au film (taken from [26]); b) SiO_2-Ag film (taken from [30]).

Silver NPs have been also widely studied recently and successfully embedded in various oxides matrixes; the most common precursor is silver nitrate ($AgNO_3$) due to its solubility in polar solvents as water and methanol. The reduction of Ag ions to metal NPs is more difficult compared to gold, because the electrochemical redox potential is much lower for Ag than for Au [31]. Anyway, it has been demonstrated that inside sol-gel films annealed at high temperature, organic compounds that decompose are able to donate electrons to Ag ions, promoting the reduction to metal NPs [20]. In several publications, the reduction of Ag precursor is achieved with annealing in reducing atmosphere or through UV irradiation, as presented in the following, even if some other techniques like γ irradiation have been adopted as well [32]. For example, De *et al*. [33] presented the synthesis of silica sol-gel films with embedded Ag NPs precipitated after high temperature annealing in air, while Kovalenko *et al*. [34] prepared Ag-doped SiO_2 sol-gel films by stabilizing first the matrix with a thermal treatment in air, and then using hydrogen-rich atmosphere to reduce embedded Ag^+ species to Ag NPs. The parameters controlling the nucleation and growth of Ag NPs inside SiO_2 sol-gel films have been discussed by Villegas and colleagues [35]. As for Au, also Ag NPs have been embedded inside different oxide materials, like TiO_2 (even if in this case a slightly different approach was followed, based on the initial synthesis of the porous TiO_2 matrix, followed by the impregnation of Ag ions and their subsequent reduction) [36], ZrO_2 [29], $BaTiO_3$ [37]. A review on Au, Ag and Cu NPs embedded inside oxide matrixes has been presented by Tondello and coworkers [38].

While Ag and Au (and with minor importance, also Cu) have been embedded inside oxide matrixes for their interesting optical properties due to the LSPR peak in the visible range, other noble metals like Pd and Pt have been dispersed into sol-gel oxide matrixes, mostly because of their catalytic properties, very useful for sensing and catalysis applications. As for the previous examples, suitable precursors are metal salts like chlorides (H_2PtCl_6 and $PdCl_2$ for example) that can be easily dissolved in alcoholic media and mixed with the sol-gel precursors of the matrix. Focusing on Pd NPs, Zhao *et al*. [39] presented a detailed study on the effect of temperature and atmosphere of annealing on the crystallization and growth of Pd NPs inside a TiO_2 matrix. Also Chan and coworkers [40] prepared titania films loaded with Pd nanocrystals with a similar procedure, and demonstrated the increase in photocatalytic activity of these films compared to pure TiO_2 samples. Pd NPs were also embedded inside a sol-gel SnO_2 matrix to enhance the sensing properties of tin oxide thin films [41].

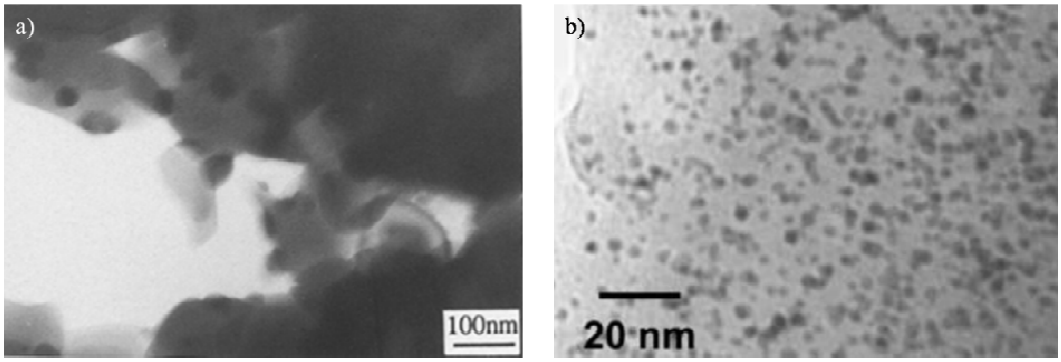

Figure 2.2. Bright Field TEM images of a) TiO_2-Pd film (taken from [39]); b) AuPt alloy NPs inside a SiO_2 film (taken from [42]).

As far as Pt NPs are concerned, De and Rao [42] presented the formation of Au, Pt and AuPt alloy NPs inside a silica sol-gel matrix as a consequence of the thermal annealing, while Morazzoni *et al*. [43] showed the embedding of Pt ions inside a SnO_2 sol-gel matrix, and the eventual formation of Pt metallic species upon thermal treatment. Zayat *et al*. [44] successfully embedded Pt NPs inside WO_3 films to be used as optical sensors due to the gasochromic properties of tungsten trioxide and the catalytic properties of Pt NPs. Eventually, Epifani and coworkers [45] presented SnO_2 based films containing different metals like Pt and Pd and their influence on the morphology of the crystalline oxide matrix.

All the examples presented have some obvious advantages, such as the intrinsic simplicity of the procedure, and the relatively fast time scale for the synthetic process; there are though quite a few disadvantages, mainly related on the poor control on the microstructural properties of the resulting composite material, especially as far as size, shape, size distribution of the different nanocrystals are concerned, as can be seen from Figures 2.1 and 2.2: in fact, metal particles shown in these pictures are quite polydisperse, of various shapes, and sometimes aggregation phenomena can be experienced. Of course these disadvantages might be of minor relevance compared to the easiness of the approach, or on the contrary they might affect negatively the properties of the resulting material: the balance between pros and cons relies on the specific application.

2.3 Colloidal syntheses of metal and oxide nanoparticles

Wet chemical synthesis of metal [46-49] , semiconductor [50-53] or oxide [54-58] colloids provides a useful tool for obtaining high quality NPs with desired size, shape and dispersion. Colloidal methods also allow the particle surface chemistry to be modified, which greatly extends the processing strategies and stability in the desired host matrix.

Materials properties at the nanoscale differ from those in the bulk, and they are strongly affected by particle size and shape. Accurate control over such parameters is important for the achievement of desired functionalities. Moreover, when dealing with nanocomposite fabrication, also the control of the overall microstructure is of paramount importance. This includes homogeneous dispersion of the particles inside the matrix, maintaining the interface between different phases and proper porosity, all these characteristics being required if the material has to interact with the surrounding environment.

The so-called *ex-situ* synthesis allows the control on these parameters, because all the constituents of the nanocomposite are synthesized with colloidal techniques with tailored morphology, structure and physical properties; moreover, being the as-synthesized materials already with the desired final properties, the nanocomposite films can be deposited without the need of a high thermal treatment, so a variety of delicate substrates can be used like polymers, soda-lime glass slides, SPR substrates, and so on. Besides all these obvious advantages, there are some limitations of this approach: for example, the compatibilization of different nanoparticles is sometimes a challenging task, because

great care has to be put in the surface chemistry of the particles, choosing appropriate ligands and complexing agent. Moreover, there are several different types of synthesis according to the type of solvent (water, alcohols, organic media etc.), the reaction conditions (pH, temperature), etc., so the compatibilization of the different components of the final nanocomposite might not be easy, and sometimes it requires several reaction steps. So the price to pay for a higher quality film is related to the technical difficulties the operator might encounter during the synthesis and deposition processes. The first attempts to synthesize high quality nanocomposites were based on the colloidal synthesis of the dopant material (metal NPs) its protection with a proper complexing agent (usually polymers) and its encapsulation inside a sol-gel oxide matrix: with this approach, the control on the morphology and structure of the metal NPs is achieved, but the film has still to be annealed at high temperature if a crystalline matrix is needed. In addition, during the deposition procedure, the solvent evaporates and the metal NPs may not be stable anymore, and this fact will lead to aggregation of the particles, and so to a film of poor quality: for this reason, the control on compatibilization and stability of the different components is of great importance. An example of metal NPs embedded inside a sol-gel matrix has been presented by Selvan *et al*. [59]: the authors described the colloidal synthesis of Au NPs, their protection with PVP and a subsequent step in which the colloidal suspension of PVP-capped Au NPs was mixed with a silica-based sol-gel solution, in order to obtain SiO_2-Au nanocomposite films. More recently, Buso *et al*. [60] showed the synthesis of monodisperse Au NPs, their protection with 11-mercaptoundecanoic acid (MUA) and their dispersion in high quality TiO_2 sol-gel films. Silver NPs have been embedded as well inside oxide sol-gel matrixes: for example Guo and Tao [61] reported the colloidal synthesis of Ag NPs capped with a mercaptosilane, and their subsequent embodiment inside a silica sol-gel solution that was deposited on an optical fiber and the resulting film was used as ammonia sensor. Hong *et al*. [62] showed the synthesis of Ag NPs and their dispersion inside a sol-gel based ZnO film, and analyzed the optical and electrical properties of the final nanocomposite. This approach has been also used to embed semiconductor quantum dots inside sol-gel matrixes: for example Bullen *et al*. reported a strategy to synthesize high quality sol-gel SiO_2 [63] and SiO_2-ZrO_2 [64] films containing luminescent quantum dots, while Bawendi and colleagues [65] used a similar approach to embed II-VI semiconductor quantum dots (QDs) inside a sol-gel based TiO_2 matrix. As can be seen from Figure 2.3, the metal and

semiconductor NPs embedded inside sol-gel films are spherical and monodisperse, thanks to the control over such parameters during the colloidal synthesis.

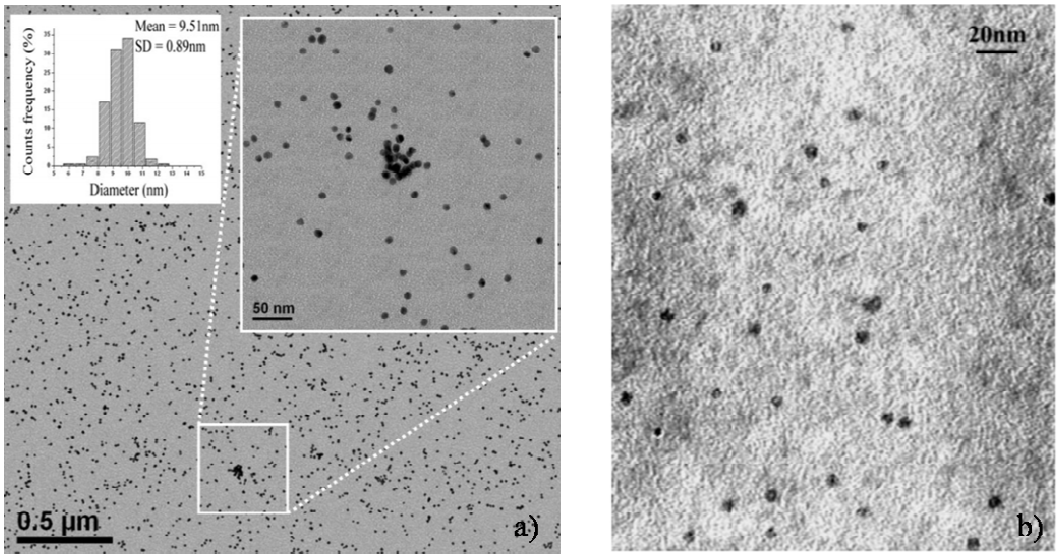

Figure 2.3. Bright Field TEM images of a) TiO_2 sol-gel film containing Au NPs (taken from [60]); b) SiO_2-ZrO_2 sol-gel films containing CdS@ZnS QDs (taken from [64]).

All the previous examples are of course an improvement of the high temperature crystallization approach, but they suffer from the limitation that the film has to be annealed if a crystalline oxide matrix is needed: so, semiconductor QDs are likely to oxidize, and also the shape of the nanoparticles can be modified by the thermal treatment (for example Au nanorods are known to reduce in length and to become spherical when heated at about 50-100 °C [66]). As a consequence, if a crystalline matrix at low temperature is needed, a different approach has to be carried out: the idea of the synthesis of both matrix and dopant materials through colloidal techniques and the deposition of thin films starting from crystalline NPs suspensions came in order to make possible to obtain low-temperature, crystalline and high quality noble metals / metal oxides nanocomposite thin films. Only few examples of this approach are reported in the literature: for example Cohen and coworkers [67] presented a layer-by-layer deposition of commercial SiO_2 and TiO_2 colloids to realize antireflecting and self-cleaning coatings at room temperature. Norberg *et al.* [68], prepared nanocrystalline ZnO films by synthesizing ZnO colloids, purifying them and using them directly for thin films deposition. Several authors reported the synthesis of TiO_2 films starting from colloidal

solutions in the anatase phase [69], brookite phase [70], and also starting from nanorods [71]. Sanchez and coworkers [72] described a colloidal approach to the synthesis of thin films composed of metal-organic frameworks (MOF). Adyl and colleagues [73] presented the synthesis of a nanocrystalline film starting from PbSe colloids as active layer coupled with a sputtered ZnO film inside a solar cell device. Konstantatos *et al*. [74] prepared colloidal PbS QDs and casted the particle suspension to create nanocrystalline thin films at room temperature as photodetectors with higher detectivity compared to the best epitaxially grown devices. In the end, it is worth to cite the perspective article published by Noone and Ginger [75], in which the authors describe the advantages of the colloidal approach and some strategies to the fabrication of semiconducting functional thin films starting from colloidal solutions.

As briefly discussed, with the colloidal approach it is possible to perform a deeper control on the physical and chemical properties of the material, obtaining high quality nanocrystalline films, without the need for high annealing temperatures; obviously, such improvement in the quality of the material is balanced with a more complicated and challenging synthetic procedure.

2.4 Metal nanoparticles layers covered with oxide films

A different approach to the synthesis of noble metal / metal oxide nanocomposite thin films that helps to produce high quality coatings without the need of mixing together different NPs is based on the initial synthesis of the desired noble metal NPs with colloidal techniques, their deposition on a properly functionalized substrate and the eventual deposition of a thin oxide film on top of the metal NPs layer. In this way, anchoring metal NPs to a suitable substrate and using it as a substrate itself for a sol-gel film deposition allows more freedom in the selection of metal oxides to couple with the metal NPs, and avoids all the problems related with the compatibilization of the different solutions (in both cases of colloidal NPs dispersed in a sol-gel matrix, or in the “all colloidal” approach). Moreover, interesting optical properties can be gained if the metal NPs exhibit a SPR peak in the visible range: in fact, if a monolayer of Ag or Au NPs with high surface coverage is deposited, the metal NPs are in close proximity and the small mutual distance between the particles leads to a coupling of the plasmon resonances [76]

that can be exploited for several applications like surface enhanced Raman scattering (SERS), or sensing.

One of the first reports on Au NPs monolayers has been presented by Brust *et al*. [77]: glass substrate functionalized with mercapto moieties were immersed in Au NPs colloidal solutions, resulting in a layer of Au NPs deposited on the substrate; the authors also demonstrated the increase in absorbance and the red shift of the Au SPR peak with increasing the number of deposited layers, as a consequence of the higher number of Au NPs deposited, and the increase in their proximity, respectively. Later, Hao e Lian [78] presented a synthetic route to produce polymer/Au NPs multilayered thin films, based on hydrogen bonding formation between amino and carboxylic groups coming from the Au NPs capping agent and the functionalized substrate. Wang and Chumanov [79] combined colloidal and sol-gel techniques for the synthesis of WO_3-Ag nanocomposite films: Ag colloids are first anchored to a glass substrate, and then covered with a tungsten oxide sol-gel solution; the resultant composite film exhibited largely improved electrochemical stability. Other examples of metal NPs layers have been presented by Astilean and colleagues [80] and by Lu and coworkers [81]: the metal NPs layer formation is similar in both work, and it consists on the activation of the glass substrate with an aminosilane, and a subsequent immersion of the functionalized substrate inside the metal NPs colloidal solution. In the first case, Au NPs layers are used as SERS substrates and LSPR sensors, while in the second case Au NPs, Ag NPs and Au nanoshells layers have been characterized and used as VOCs optical sensors.

A paper describing the layer-by-layer approach to the synthesis of films composed of Au NPs and Au@SiO_2 core@shell NPs, and their interesting optical properties has been published by Mulvaney and colleagues [82]. A lot of publications can be found describing superlattices formation of long-chain thiol and amine capped metal NPs [83-86]: with this approach the organization is driven by the slow evaporation rate of the solvent, without the need of a functionalization of the substrate; of course, the NPs are poorly bounded to it, but this approach can be easily implemented to create stable NPs layers.

Another approach has been showed by Yang *et al*. [88]: ordered arrays of Au NPs have been embedded inside a SiO_2 matrix by means of surfactant mesophase formation. Buso *et al*. [87] prepared Au NPs monolayers promoting the reaction between carboxylic moieties of MUA-capped Au NPs and amino groups coming from a functionalized substrate: then the Au NPs layers were covered with oxide sol-gel films and used as optical gas sensors. Different techniques have been also used recently to create metal NPs

monolayer, as showed by Koshizaki and coworkers [89], that used RF-magnetron sputtering to prepare Au island covered with Al_2O_3 on proper substrates and used the resulting nanocomposite as SPR biosensor.

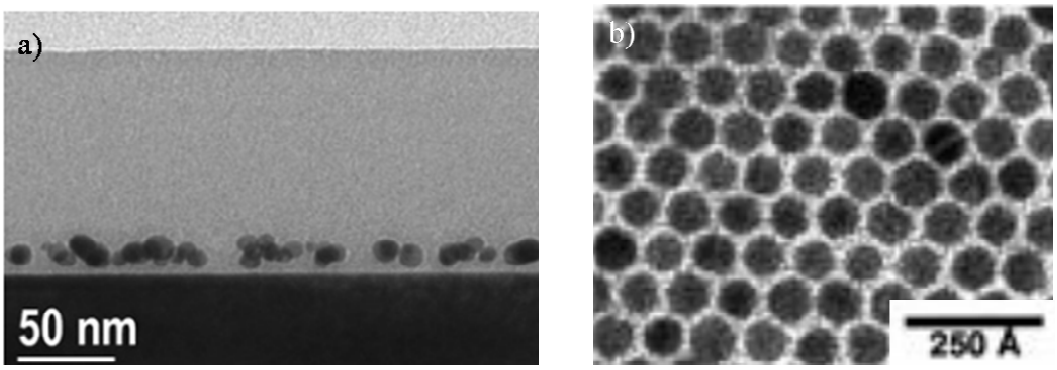

Figure 2.4. Bright Field TEM images of a) Au monolayer covered with a SiO_2 sol-gel film (taken from [87]); Ag NPs superlattice (taken from [84]).

The synthetic approach based on the deposition of a layer of active NPs covered with a thin film can be easily extended to a variety of subsequent improvements, like the multilayer synthesis of different noble metals / metal oxides coatings, so creating different interfaces that can enhance the overall device performances: for example, in the case of chemical sensors, multilayered films can provide an increase in selectivity, by tuning the sensing response according to type of analyte and type of interface between the different constituents; moreover, if the porosity of the different layers is tailored properly, the multilayered films can also act as a filter than progressively separates different analytes according to their size or their affinity with the different layers.

As briefly discussed in this chapter, several wet chemistry techniques are available for the synthesis of nanocomposite films composed of noble metals and metal oxides nanoparticles; some of them will be used for the synthesis of the thin films prepared in this doctoral project. In details, in **Chapter 3** the high temperature crystallization procedure is used to prepared sol-gel oxide films doped with Au, Ag and Pt NPs. In **Chapter 4** colloidal syntheses of metals (Au, Pt, Au@Pt) and oxides (ZnO, TiO_2) are described and films starting from colloidal suspensions are prepared. Eventually in **Chapter 5** Au NPs layers covered with films of different oxides are described. All these materials have been tested as optical sensors for reducing gases and VOCs detection.

Bibliography

[1] J. He, I. Ichinose, T. Kunitake, A. Nakao, Y. Shiraishi, N. Toshima, *J. Am. Chem. Soc.*, **2003**, *125*, 11034.

[2] A. Hagfeldt, M. Gratzel, *Acc. Chem. Res.*, **2000**, *33*, 269.

[3] M.A. Aramendía, A. Marinas, J.M. Marinas, J.M. Moreno, F.J. Urbano, *Catal. Today*, **2005**, *101*, 187.

[4] M. Ando,T. Kobayashi, M. Haruta, *Catal. Today*, **1997**, *36*, 135.

[5] A.M. Ruiz, A. Cornet, K. Shimanoe, J.R. Morante, N. Yamazoe, *Sens. Actuators B*, **2005**, *108*, 34.

[6] S. Deki, Y. Aoi, H. Yanagimoto, K. Ishii, K. Akamatsu, M. Mizuhata, A. Kajinami, *J. Mater. Chem.*, **1996**, *6*, 1879.

[7] T. Ung, L.M. Liz-Marzan, P. Mulvaney, *J. Phys. Chem. B*, **2001**, *105*, 3441.

[8] H.B. Liao, W.J. Wen, J.K.L. Wong, *J. Appl. Phys.*, **2003**, *93*, 4485.

[9] U. Kreibig, M. Vollmer, *Optical Properties of Metal Clusters*, ed. Springer, Verlag, Berlin, **1995**.

[10] M. Ando, H. Steffes, R. Chabicovsky, M. Haruta, G. Stangl, *IEEE Sens. J.*, **2004**, *4*, 232.

[11] U. Pal, C. Garcia-Serrano, G. Casarubbias-Segura, N. Koshizaki, T. Sasaki, S. Terahuchi, *Solar Energy Materials and Solar Cells*, **2004**, *81*, 339.

[12] P. Liu, S. Lee, C.E. Tracy, J.A. Turner, J.R. Pitts, S.K. Deb, *Solid State Ionics*, **2003**, *165*, 223.

[13] O. Berger, W.J. Fischer, V. Melev, *J. Mater. Sci.*, **2004**, *15*, 463.

[14] L. Madler, A. Roessler, S.E. Pratsinis, T. Sahm, A. Gurlo, N.A. Barsan, U. Weimar, *Sens. Actuators B*, **2006**, *114*, 283.

[15] C.H. Liu, L. Zhang, Y.J. He, *Thin Solid Films*, **1997**, *304*, 13.

[16] R.H. Magruder III, L. Yang, R.F. Haglund Jr., C.W. White, L. Yang, R. Dorsinville, R.R. Alfano, *Appl. Phys. Lett.*, **1993**, *62*, 1730.

[17] M. Okumura, S. Nakamura, S. Tsubota, T. Nakamura, M. Azuma, M. Haruta, *Catal. Lett.*, **1998**, *51*, 53.

[18] J. Zhuou, L. Li, Z. Gui, X. Zhang, D.J. Barber, *Nanostruct. Mater.*, **1997**, *8*, 3, 321.

[19] G. Zhao, H. Kozuka, S. Sakka, *J. Sol-Gel Sci. Technol.*, **1995**, *4*, 37.

[20] S. Sakka, H. Kozuka, *J. Sol-Gel Sci. Techn.*, **1998**, *13*, 701.

[21] B.F.G. Johnson, R. Davis, *Comprehensive Inorganic Chemistry*, Vol. 3, Pergamon, New York, **1973**, 129.

[22] H. Kozuka, S. Sakka, *Chem. Mater.*, **1993**, *5*, 222-228.

[23] M. Lee, T.S. Kim, Y.S. Choi, *J. Non-Cryst. Solids*, **1997**, *211*, 143-149.

[24] G. De, G. Mattei, P. Mazzoldi, C. Sada, G. Battaglin, A. Quaranta, *Chem. Mater.*, **2000**, *12*, 2157-2160.

[25] D. Buso, M. Guglielmi, A. Martucci, G. Mattei, P. Mazzoldi, C. Sada, M.L. Post, *Cryst. Growth Des.*, **2008**, *8*, 744-749.

[26] M. Lee, L. Chae, K.C. Lee, *Nanostruct. Mater.*, **1999**, *11*, 195-201.

[27] X.H. Wang, J Shi, S. Dai, Y. Yang, *Thin Solid Films*, **2003**, *429*, 102-107.

[28] J. Matsuoka, H. Yoshida, H. Nasu, K. Kamiya, *J. Sol-Gel Sci. Technol.*, **1997**, *9*, 145-155.

[29] M. Epifani, C. Giannini, L. Tapfer, L. Vasanelli, *J. Am. Ceram. Soc.*, **2000**, *83*, 2385-2393.

[30] M.G. Garnica-Romo, J.M. Yanez-Limon, M. Villicana, J.F. Perez-Robles, R. Zamorano-Ulloa, J. Gonzalez-Hernandez, *J. Phys. Chem. Solids*, **2004**, *65*, 1045-1052.

[31] D.R. Lide, *CRC Handbook of Chemistry and Physics*, 87th edition, Taylor and Francis, Boca Raton, FL, **2007**, 8-20.

[32] Y. Xie, Z.P. Qiao, M. Chen, Y.J. Zhu, Y.T. Qian, *Adv. Mater.*, **1999**, *11*, 1512.

[33] G. De, A. Licciulli, C. Massaro, L. Tapfer, M. Catalano, G. Battaglin, C. Meneghini, P. Mazzoldi, *J. Non-Cryst. Solids*, **1996**, *194*, 225-234.

[34] D.L. Kovalenko, D.S. Gurin, N.E. Bogdanichikova, V.B. Prokopenko, A.A. Alexeenko, I.M. Melnichenko, *J. Alloys Compd.*, **2002**, *341*, 208-210.

[35] M.A. Villegas, M.A. Garcia, S.E. Paje, J. Llopis, *Mater. Res. Bull.*, **2005**, *40*, 1210-1222.

[36] E.D. Martinez, L. Granja, M.G. Bellino, G.J.A.A. Soler-Illia, *Phys. Chem. Chem. Phys.*, **2010**, *12*, 14445-14448.

[37] J. Zhou, L. Li, Z. Gui, X. Zhang, D.J. Barber, *Nanostruct. Mater.*, **1997**, *8*, 321-328.

[38] L. Armelao, F. Barreca, G. Bottaro, A. Gasparotto, S. Gross, C. Maragno, E. Tondello, *Coord. Chem. Rev.*, **2006**, *250*, 1294-1314.

[39] G. Zhao, H. Kozuka, S. Sakka, *J. Sol-Gel Sci. Technol.*, **1995**, *4*, 37-47.

[40] C.C. Chan, C.C. Chang, W.C. Hsu, S.K. Wang, J. Lin, *Chem. Eng. J.*, **2009**, *152*, 492-497.

[41] M.I. Ivanovskaya, P.A. Bogdanov, D.R. Orlik, A.C. Gurlo, V.V. Romanovskaya, *Thin Solid Films*, **1997**, *296*, 41-43.

[42] G. De, C.N.R. Rao, *J. Mater. Chem.*, **2005**, *15*, 891-894.

[43] F. Morazzoni, C. Canevali, N. Chiodini, C. Mari, R. Ruffo, R. Scotti, L. Armelao, E. Tondello, L.E. Depero, E. Bontempi, *Chem. Mater.*, **2001**, *13*, 4355-4361.

[44] M. Zayat, R. Reisfeld, H. Minti, B. Orel, F. Svegl, *J. Sol-Gel Sci. Technol.*, **1998**, *11*, 161-168.

[45] M. Epifani, M. Alvisi, L. Mirenghi, G. Leo, P. Siciliano, L. Vasanelli, *J. Am. Ceram. Soc.*, **2001**, *84*, 48–54.

[46] Y. Sun, Y. Xia, *Science*, **2002**, *298*, 2176.

[47] Y. Sun, B. Gates, B. Mayers, Y. Xia, *Nano Lett.*, **2002**, *2*, 165.

[48] L.M. Liz-Marzàn, *Langmuir*, **2006**, *22*, 32.

[49] S.E. Habas, H. Lee, V. Radmilovic, G.A. Somorjai, P. Yang, *Nature Materials*, **2007**, *6*, 692-697.

[50] C.B. Murray, D.J. Norris, M.G. Bawendi, *J. Am. Chem. Soc.*, **1993**, *115*, 8706.

[51] J. Van Embden, J. Jasieniak, P. Mulvaney, *J. Am. Chem. Soc.*, **2009**, *131*, 14299.

[52] M.A. Hines, G.D. Scholes, *Adv. Mater.*, **2003**, *15*, 1844-1849.

[53] J.E. Murphy, M.C. Beard, A.G. Norman, S.P. Ahrenkiel, J.C. Johnson, P. Yu, O.I. Micic, R.J. Ellingson, A.J. Nozik, *J. Am. Chem. Soc.*, **2006**, *128*, 3241-3247.

[54] M. Niederberger, M.H. Bartl, G.D. Stucky, *J. Am. Chem. Soc.*, **2002**, *124*, 13642.

[55] N.R. Jana, Y. Chen, X. Peng, X. *Chem. Mater.*, **2004**, 16, 3931.

[56] N. Niederberger, N. Pinna, *Angew. Chem. Int. Ed.*, **2008**, *47*, 5292.

[57] J. Park, K. An, Y. Hwang, J.G. Park, H.J. Noh, J.Y. Kim, J.H. Park, N.M. Hwang, T. Hyeon, *Nature Materials*, **2004**, *3*, 891-895.

[58] S.G. Kwon, T. Hyeon, *Acc. Chem. Res.*, **2008**, *41*, 1696-1709.

[59] S.T. Selvan, Y. Ono, M. Nogami, *Mater. Lett.*, **1998**, *37*, 156-161.

[60] D. Buso, J. Pacifico, A. Martucci, P. Mulvaney, *Adv. Funct. Mater.*, **2007**, *17*, 347-354.

[61] H. Guo, S. Tao, *Sens. Actuators B*, **2007**, *123*, 578-582.

[62] C.S. Hong, H.H. Park, J. Moon, H.H. Park, *Thin Solid Films*, **2006**, *515*, 957-960.

[63] S.T. Selvan, C. Bullen, M. Ashokkumar, P. Mulvaney, *Adv. Mater.*, **2001**, *13*, 985-988.

[64] C. Bullen, P. Mulvaney, C. Sada, M. Ferrari, A. Chiasera, A. Martucci, *J. Mater. Chem.*, **2004**, *14*, 1112-1116.

[65] V.C. Sundar, H.J. Eisler, M.G. Bawendi, *Adv. Mater.*, **2002**, *14*, 739-743.

[66] A.S.A.M. Al-Sherbini, *Colloids Surf. A*, **2004**, *246*, 61-69.

[67] D. Lee, M.F. Rubner, R.E. Cohen, *Nano Lett.*, **2006**, *6*, 2305-2312.

[68] N.S. Norberg, K.R. Kittilstved, J.E. Amonette, R.K. Kukkadapu, D.A. Schwartz, D.R. Gamelin, *J. Am. Chem. Soc.*, **2004**, *126*, 9387-9398.

[69] A.M. Peirò, J. Peral, C. Domingo, X. Domenech, J.A. Ayllon, *Chem. Mater.*, **2001**, *13*, 2567-2573.

[70] S.J. Kim, K. Lee, J.H. Kim, N.H. Lee, S.J. Kim, *Mater. Lett.*, **2006**, *60*, 364-367.

[71] G. Caputo, C. Nobile, T. Kipp, L. Blasi, V. Grillo, E. Carlino, L. Manna, R. Cingolani, P.D. Cozzoli, A. Athanassiou, *J. Phys. Chem. C*, **2008**, *112*, 701-714.

[72] P. Horacajada, C. Serre, D. Grosso, C. Boissiere, S. Perruchas, C. Sanchez, G. Ferey, *Adv. Mater.*, **2009**, *21*, 1931-1935.

[73] K.S. Leschkies, T.J. Beatty, M.S. Kang, D.J. Norris, E.S. Adyl, *ACS Nano*, **2009**, *3*, 3638-3648.

[74] G. Konstantatos, I. Howard, A. Fischer, S. Hoogland, J. Clifford, E. Klem, L. Levina, E.H. Sargent, *Nature*, **2006**, *442*, 180-183.

[75] K.M. Noone, D.S. Ginger, *ACS Nano*, **2009**, *3*, 261-265.

[76] R.G. Freeman, K.C. Grabar, K.J. Allison, R.M. Bright, J.A. Davis, A.P. Guthrie, M.B. Hommer, M.A. Jackson, P.C. Smith, D.G. Walter M.J. Natan, *Science*, **1995**, *267*, 1629.

[77] M. Brust, D. Bethel, C.J. Kiely, D.J. Schiffrin, *Langmuir*, **1998**, *14*, 5425-5429.

[78] E. Hao, T. Lian, *Chem. Mater.*, **2000**, *12*, 3392-3396.

[79] Z. Wang, G. Chumanov, *Adv. Mater.*, **2003**, *15*, 1285-1289.

[80] F. Toderas, M. Baia, L. Baia, S. Astilean, *Nanotechnology*, **2007**, *18*, 255702.

[81] C.S. Cheng, Y.Q. Chen, C.J. Lu, *Talanta*, **2007**, *73*, 358-365.

[82] T. Ung, L.M. Liz-Marzan, P. Mulvaney, *Colloids Surf. A*, **2002**, *102*, 119-126.

[83] J.R. Heath, C.M. Knobler, D.V. Leff, *J. Phys. Chem. B*, **1997**, *101*, 189-197.

[84] B.A. Korgel, S. Fullam, S. Connolly, D. Fitzmaurice, *J. Phys. Chem. B*, **1998**, *102*, 8379-8388.

[85] S. Sun, C.B. Murray, D. Weller, L. Folks, A. Moser, *Science*, **2000**, *287*, 1989-1992.

[86] C. Shen, C. Hui, T. Yang, C. Xiao, J. Tian, L. Bao, S. Chen, H. Ding, H. Gao, *Chem. Mater.*, **2008**, *20*, 6939-6944.

[87] D. Buso, L. Palmer, V. Bello, G. Mattei, M. Post, P. Mulvaney, A. Martucci, *J. Mater. Chem.*, **2009**, *19*, 2051-2057.

[88] K. Yang, H. Fan, K.J. Malloy, C.J. Brinker, T.W. Sigmon, *Thin Solid Films*, **2005**, *491*, 38-42.

[89] S. Gao, N. Koshizaki, H. Tokuhisa, E. Koyama, T. Sasaki, J.K. Kim, J. Ryu, D.S. Kim, Y. Shimizu, *Adv. Funct. Mater.*, **2010**, *20*, 78-86.

Chapter 3

High temperature crystallization of oxide and metal nanoparticles

Contents

3.1 Introduction and background

As described in the previous chapters, the sol-gel chemistry coupled with high temperature annealing is a simple and straightforward method to obtain nanostructured materials, thanks to the crystallization of oxides and the reduction of noble metal ions to metal nanoparticles. In this chapter, nanocomposite thin films composed of different combinations of metal oxides and noble metals will be explored and their gas sensing performances will be analyzed and discussed.

In the first part of the chapter an innovative material for hydrogen sulfide (H_2S) detection will be presented: H_2S is a well-known toxic gas that can be produced or can be a by-product in several processes like oil refining, coal or natural gas manufacturing, fuel cells, food processing industries. This gas is dangerous for human health even at low

concentrations: exposure at 250 ppm can seriously injure the human body and even cause death [1], so the threshold limit for human exposure is usually set by governmental legislation (for example in the US it is 10 ppm for every 10 minutes of exposure, with the exposure level decreasing with time) [2]. In addition, H_2S can act as a poison which highly degrades the activity of catalysts and electrochemical devices [3].

Thence, great efforts have been put to develop materials for highly sensitive and selective hydrogen sulfide sensors, and to develop new efficient and low cost devices capable of real time fast detection of even very small amounts of H_2S; most of the literature in this field deals with resistive electrical sensor devices, where the active materials are powders [4-6] , thin [7,8] or thick films [9,10]. Most of the sensing materials reported in H_2S detection are CuO, SnO_2, ZnO, WO_3 or a combination of them [11-26]. Some others techniques are based on the detection of the products generated from the interaction of H_2S with the sensor materials, i.e. sulfide species analyzed by gas chromatography [27-30], high pressure liquid chromatography (HPLC) [31] or electrochemical methods [32].

As described in Chapter 2, optical sensors represent an alternative and innovative detection mode where the changes of the optical properties of the device are analyzed, and developing materials tailored to accomplish such a task is very relevant to current material science research. However, only few examples of optical H_2S sensors have been reported so far, and most of them depend on organic dyes or organic complexes of transition metals as active materials [33-35], although some articles discussing fully inorganic optical gas sensors have been published [36-38].

The two specific metal oxide components of the studied nanocomposite films, *i.e.* TiO_2 and NiO, were selected because of the known catalytic and sensing properties of these materials, and the embedding of Au NPs was performed to enhance optical sensitivity of the nanocomposites.

While most of the literature concerning TiO_2-NiO nanocomposite materials deals with catalysis [39-42] and photocatalysis [43-45], and other particular applications of these systems are electrochromism [46-48], solar cells [44,49] and supercapacitors [50], only few gas sensing studies on similar material have been reported so far [51-53]. In particular, neither the optical gas sensing properties of TiO_2-NiO films, nor studies on Au NPs dispersed inside TiO_2-NiO films have been reported yet.

In the second part, the focus will be set on materials for hydrogen (H_2) and carbon monoxide (CO) detection. These two reducing gases have been widely investigated in the

recent years, because they are very common in many industrial processes like hydrocarbons processing, polymers synthesis and fuel cells production, especially hydrogen. CO is also highly toxic for human health, and since it is a result of incomplete combustion, it can be produced not only in industrial processes, but also inside houses and lived-in buildings. As a result, cheap and highly sensitive CO and H_2 sensors are required: in the case of hydrogen, the main purpose is the control of the reaction parameters inside industrial lines or chemical plants, in order to keep the process inside some safety and/or quality standards, while carbon monoxide detection is a key topic for living environment monitoring, especially old houses and workplaces, where the heating system might have been built without strict safety regulations, and so it deteriorating with time may result in CO production.

There is a huge number of publications dealing with materials for CO and H_2 sensing, and a comprehensive review is not the purpose of this study: but just to give few examples, some of the most studied materials for reducing gases detection are tin oxide (SnO_2) [54], tungsten oxide (WO_3) [55], zinc oxide (ZnO) [56], titanium oxide (TiO_2) [57], usually doped with different ions or used in combination with some catalysts (platinum or palladium layers for example). A comprehensive review has been published by Eranna and coworkers [58], where they present the state of the art in solid state gas sensing comparing different metal oxides: the great majority of the data they show are related to conductometric sensors, and so the cross sensitivity between different gases might be very high, as discussed in the previous chapter.

The materials studied in this chapter for CO and H_2 detection are the following: first SiO_2-NiO nanocomposites with Ag NPs will be explored, since the SiO_2-NiO-Au system synthesized with the sol-gel method was already studied in the past [59-62] and showed promising sensing performances. The Ag-loaded SiO_2-NiO films have been realized with a different approach, based on a initial synthesis of a mesoporous oxide film, followed by a pore functionalization and then a subsequent impregnation of the pores with silver ions, that are eventually reduced to Ag nanoparticles. Silver was chosen because it presents a higher extinction coefficient at the SPR frequency compared to Au [63,64] and it is cheaper than Au, but sometimes its high chemical reactivity and instability inside sol-gel matrixes prevent its use [65], so the impregnation protocol has been developed. Recently, a paper has been published [66] describing the enhancement in glucose sensitivity of a sensors based on NiO-Ag nanofibers compared to NiO nanofibers or Ag electrodes, showing promising performances of the NiO-Ag interface as sensing material.

Another interesting material for sensing applications is ZnO: it has been studied for long time due to its interesting optical and electronical properties [67,68] that attracted a lot of attention especially for possible application in the fields of sensing, catalysis, optoelectronic devices, solar cells, transistors and so on: ZnO-based thin films containing Au and NiO nanoparticles synthesized with a simple sol-gel method will be presented as CO sensors, discussing the contribution of NiO and Au in the sensing performances.
Eventually, Tungsten trioxide (WO_3) based nanocomposites will be investigated: WO_3 is a well known n-type semiconductive material for gas sensing applications, especially for reducing gases [69-71], because of tungsten multiple oxidation states: in fact W^{6+} ions can be reduced to W^{5+} during exposure to gases like CO and H_2 resulting in a change of both electrical and optical properties; nevertheless, it has also been used in the detection of oxidizing gases like NO_2 [72]. An improvement of sensor sensitivity can be achieved when the semiconductor is coupled with noble metal nanoparticles (NPs), thanks to their catalytic [54,73] and optical properties [74]. Microstructured WO_3 thin films containing Au and Pt nanoparticles prepared with a different approach in collaboration with the *Royal Melbourne Institute of Technology* (Melbourne, Victoria, Australia) will be characterized as reducing gases sensors.

3.2 Au nanoparticles inside thin films of Ti and Ni oxides

3.2.1 Synthesis

The nanocomposite films were obtained by the sol-gel method: different solutions were prepared according to the desired final composition of the sample. Figure 3.1 summarizes the overall synthetic procedure adopted to obtain the final nanocomposite films. The precursor TiO_2 solution involved the controlled hydrolysis of titanium(IV) butoxide (TiBu) in a mixture of ethanol and water, in the presence of 2,4-pentanedione (or acetylacetone, AcAc). Acetylacetone coordinates the titanium precursor molecules through a slightly exothermic reaction, while ethanol decreases the overall viscosity of the solution. TiBu, AcAc and ethanol were first mixed at 1:1.6:5 molar ratios and allowed to react with stirring for 20 min in a closed vessel, in order to create the Acac-TiBu complex. Then water was added according to a $Ti:H_2O$=1:4 molar ratio, and the solution was left to stir additional 10 minutes. The precursor NiO solution was prepared separately by dissolving $NiCl_2 \cdot 6H_2O$ (nickel chloride hexahydrate) in ethanol, and adding

it to the TiO_2 solution with constant stirring, according to the desired Ti:Ni molar ratio, and letting it stir 20 minutes before deposition (hereafter called TiO_2–NiO solution). TiO_2-NiO films containing Au NPs were prepared by adding, 10 minutes before deposition, a solution of $HAuCl_4 \cdot 3H_2O$ (Hydrogen tetrachloroaurate trihydrate) in ethanol to the TiO_2–NiO solution, leading to a Au:(Ti+Ni)=0.05 molar ratio. Au-free samples were prepared by diluting the TiO_2–NiO solution with ethanol in order to obtain the same precursor concentration of the Au containing solution, kept constant at 50 g/l based on nominal TiO_2+NiO weight. Pure TiO_2 and Au-TiO_2 samples were also prepared for comparison purposes, according to the same procedure, replacing the NiO solution with ethanol. In a typical synthesis for a 50% molar TiO_2 – 50% molar NiO sample, 0.55 mL of Titanium Butoxide are added to 0.47mL of EtOH under stirring; 0.266 mL Acac are subsequently added and the solution is stirred for 20 minutes; then 0.117 mL of water are slowly added under vigorous stirring. In two separate vessels, 0.384g of $NiCl_2 \cdot 6H_2O$ are dissolved in 2.95 mL EtOH and 51mg $HAuCl_4 \cdot 3H_2O$ are dissolved in 0.647 mL EtOH. The TiO_2 and NiO solutions are mixed under stirring, and the Au solution, or 0.647 mL EtOH are eventually added, leading to Au-containing, or Au-free solutions, respectively. All the solutions were prepared in 10mL glass vials.

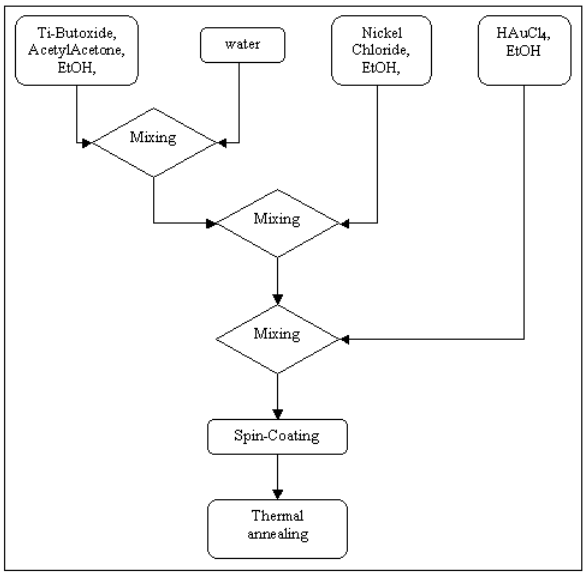

Figure 3.1. Scheme of the overall synthetic process developed to prepare TiO_2–NiO nanocomposite films.

The final solution was then deposited on either SiO_2 glass or on Si substrates. The spin-coating technique was chosen for film deposition, with rotating speed ranging from 2500 to 4000 rpm at room temperature (20 °C) and under constant nitrogen flux in order to

keep humidity under 5%, to prevent uncontrolled condensation of the TiO_2 matrix. Samples were annealed directly at 500 °C in air for 1 hour in a preheated oven. When desired, subsequent treatment at 600 °C for 30 minutes was performed. To indicate the samples with different nominal composition in X mol%, in the following the XT(100-X)N classification will be adopted, with T and N referring to TiO_2 and NiO respectively.

3.2.2 XRD characterization

A study to understand crystallization and growth processes of the different phases of the oxide matrix has been carried out preparing samples with different compositions and then analyzing the X-ray diffraction patterns. An initial test was carried out on 50T50N films without Au annealed at different temperatures ranging from 400 °C to 900 °C. Two annealing procedures were followed, a direct treatment for 30 minutes at the desired temperature, and a step-like treatment from 400 °C to the desired temperature, with 30 minutes of treatment every 100 °C. There were no significant differences between the two treatments, in fact in both cases the samples remained amorphous up to 600 °C, while at 700 °C the $NiTiO_3$ crystalline phase (JCPDS No. 76-0335) was detected; the higher the annealing temperature, the higher the intensity and the smaller the full width at half maximum (FWHM) of the diffraction peaks, indication of a higher amount of crystalline phases and bigger crystallites size, according to Scherrer formula.

Then a second set of samples composed of 50T50N, 70T30N and 30T70N films without Au was subjected to isothermal annealing at 500 °C or 600 °C up to 10 hours to understand the kinetic of crystals formation and growth: even after 10 hours of thermal treatment at 500 °C, all the films are found to be amorphous, while for the isothermal annealing at 600 °C diffraction peaks have been detected if the sample underwent the thermal treatment for a sufficient time. Similar sol-gel thin films obtained from different precursors showed crystalline peaks even at 400 °C [75], at variance with the results presented here. In details, 70T30N sample just after 30 minutes of treatment at 600 °C showed both TiO_2-rutile (JCPDS No. 87-0920) and $NiTiO_3$ peaks, 50T50N sample showed only nickel titanate pattern after 2 hours at 600°C, while in 30T70N film, NiO (JCPDS No. 47-1049) peaks were detected after 30 minutes of annealing, while $NiTiO_3$ peaks started to appear after 4 hours of treatment. No TiO_2-anatase (JCPDS No. 84-1286) peaks have been detected. As a first result from this initial set of experiments, when the molar ratio between Ti and Ni is equal to 1, only the stochiometric compound Nickel Titanate is formed, while if increasing one of the two component, also the respective

oxide (Nickel oxide or Titanium oxide in the rutile phase) is detected. Moreover, at least 600 °C are mandatory to obtain a crystalline matrix, and sometimes high annealing times are needed.

Then samples with the same composition but containing Au NPs were prepared and annealed at 500° C for 30 minutes and eventually at 600 °C for 30 minutes, and they were compared to Au-free samples subjected to the same thermal treatment. Results are reported in Figure 3.2. All the samples containing Au (Figure 2b) show gold diffraction peaks (JCPDS No. 04-0714) both at 500 °C and 600 °C, indicating, as discussed also in the previous chapter, that reduction of gold ions inside a sol-gel oxide matrix during the annealing of the film occurs at quite low temperature, usually below 200 °C [76]. It is also evident that the presence of Au NPs promotes the overall crystallization of the matrix: in fact at 500 °C NiO nanocrystals are already present in the 30T70N sample. This can be due to the very small lattice mismatch between the two cubic structures, which allows NiO to crystallize over gold nuclei (in a previous work by Buso *et al*. [61] it has been demonstrated the epitaxial growth of NiO over Au crystals inside a SiO_2 sol-gel matrix). All samples annealed at 600 °C show $NiTiO_3$ peaks, while Ti-rich and Ni-rich samples show also TiO_2-rutile and NiO peaks, respectively. It is worth underlining that diffraction peaks of the samples containing Au NPs are slightly more intense and sharper if compared to the samples without gold, indicating a larger amount of crystalline phase, and larger crystallite size. As shown in Table 3.1, a clear increase in crystals size is observed in Au-TiO_2-NiO samples for all the crystalline phases.

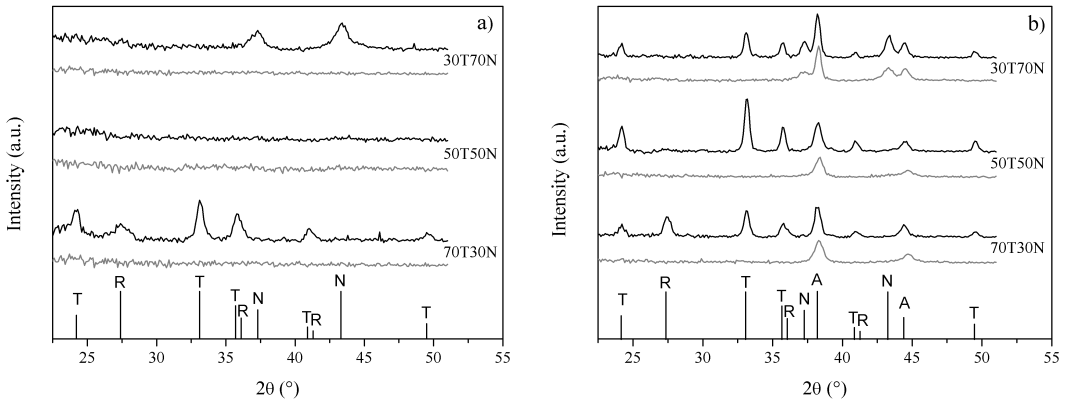

Figure 3.2. XRD patterns of (a) TiO_2–NiO and (b) Au-TiO_2–NiO nanocomposite films, annealed at 500 °C (grey line) and 600 °C (black line). Theoretical diffraction lines for TiO_2-Rutile (R), NiO (N), $NiTiO_3$ (T) and Au (A) are shown at the bottom.

Table 3.1. Mean crystallite diameter calculated according to the Scherrer equation for the diffraction peaks of 70T30N and 30T70N films annealed at 600 °C with and without gold (50T50N film is not considered in this table because without gold it is still amorphous).

	Diameter (nm)			
	70T30N	70T30N-Au	30T70N	30T70N-Au
TiO_2	10	15	-	-
$NiTiO_3$	12	17	-	-
NiO	-	-	6	15

Due to better gas sensing results, as will be described in detail later on in Section 3.2.6, a deeper and more focused study has been performed on samples containing Au and with Ni amount ranging from 0% to 50%, as shown in Table 3.2.

Table 3.2. List of samples series prepared and their nominal composition

Sample	Ti/(Ti+Ni) molar	Ni/(Ti+Ni) molar	Au/(Ti+Ni) molar
50T50N	0.5	0.5	0.05
60T40N	0.6	0.4	0.05
70T30N	0.7	0.3	0.05
80T20N	0.8	0.2	0.05
90T10N	0.9	0.1	0.05
100T0N	1	0	0.05

Initially, samples were annealed isothermally at 500 °C and 600 °C up to 10 hours as for Au-free samples. Table 3.3 reports the results for the six samples and the 3 crystalline oxides detected: TiO_2 in the rutile phase, TiO_2 in the anatase phase and $NiTiO_3$. As expected there was no NiO phase present, due to the Ni precursor amount never being predominant in the solutions, and in the sample with the highest Ni amount (50T50N) it is stoichiometric with Ti, thus leading only to nickel titanate formation. Au diffraction peaks are evident in all samples for all thermal treatments, so they were not taken into consideration for these analyses. The presence of Au NPs promotes the overall crystallization of the matrix: thus diffraction peaks can be detected even at 500 °C if the annealing time is long enough, while all Au-free samples were almost amorphous even after 10 hours of annealing, with the exception of low Ni content samples (0% and 10%), which show TiO_2 anatase peaks. At 600 °C after 30 minute treatments, the crystalline

phases are easily detectable in all Au-containing samples, while without the noble metal, annealing times of 1-2 hours are usually needed to produce any evidence of crystalline oxides. Also, when the annealing time is increased, diffraction peaks become more intense and sharper, as a consequence of the expected crystal growth and the increase of the crystalline fraction.

Table 3.3. Crystalline phases detected for the 6 samples annealed isothermally at 500 °C and 600 °C from 30 min up to 10 hours. Au NCs are detectable in all samples for all the annealing parameters studied, so they were not presented in this table. ($^{\#}$) decreasing intensity with time.

Sample	Temperature (°C)	TiO_2-rutile	TiO_2-anatase	$NiTiO_3$
50T50N	500	Absent	Absent	Absent
	600	Absent	Absent	After 30 min
60T40N	500	Absent	Absent	After 10h
	600	After 30 min	Absent	After 30 min
70T30N	500	After 10 h	Absent	After 10h
	600	After 30 min	After 1h$^{\#}$	After 30 min
80T20N	500	After 10 h	After 4 h	After 10 h
	600	After 30 min	After 30 min$^{\#}$	After 30min
90T10N	500	Absent	After 30 min	Absent
	600	After 1 h	After 30 min	After 30 min
100T0N	500	Absent	After 30 min	Absent
	600	Absent	After 30 min	Absent

In addition to the isothermal annealings, also a progressive treatment from 500 °C to 800 °C has been analyzed, with 4 steps (increasing by 100 °C each step) and with 30 minutes isothermal at every step. Figure 3.3 summarizes all the results evaluated from the diffraction patterns of the 6 samples. On the horizontal axis annealing temperature is reported, while the vertical axis presents the relative intensity of the main XRD peak of the crystalline phases detected, calculated as the ratio between the peak of interest and the most intense peak for every dataset. As reported before, being nickel content always below 50% molar, no NiO crystals were detected, so the diffraction peaks taken into consideration are the (101) reflection at 25.3°, the (110) reflection at 27.4° and the (104) reflection at 33.1° for TiO_2-anatase, TiO_2-rutile and $NiTiO_3$, respectively. The stoichiometric 50T50N sample shows only nickel titanate peaks, with intensity increasing with annealing temperature, even if a very small amount of TiO_2-rutile is formed at high

temperature, possibly due to an unwanted excess of Ti precursor used to prepare the starting solution. Increasing Ti content up to 90% results in a progressive intensification of rutile peaks, while titanate peaks become less intense; nevertheless, for both these two phases, for higher annealing temperature the intensity of the peaks increases, suggesting a higher degree of crystallization. As far as anatase is concerned, for the pure TiO_2 matrix it is the only crystalline phase detected, even for 800 °C treatment; for 90T10N and 80T20N samples (and with a barely detectable signal also for 70T30N) anatase start to form at lower temperatures, but when the annealing temperature is increased, the TiO_2 matrix evolves into the rutile phase. At 800 °C anatase is no longer detectable in any of the Ni-containing films.

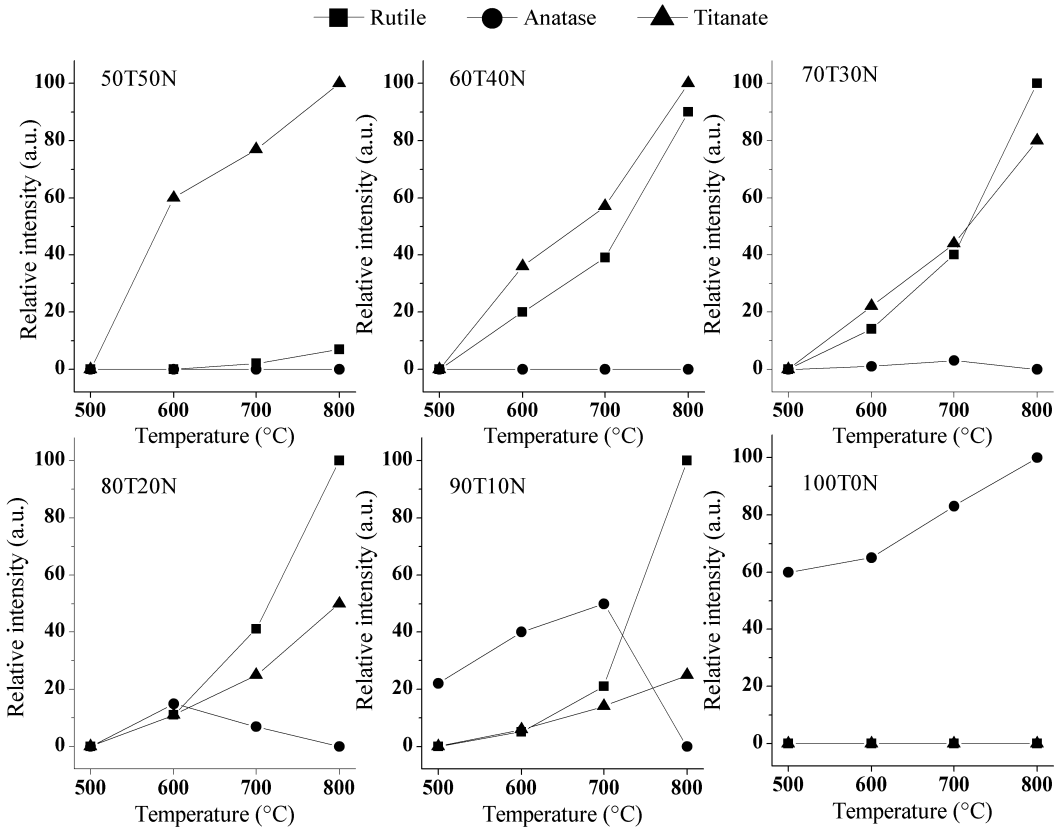

Figure 3.3. Comparison between the relative intensity of the main diffraction peaks for TiO_2-rutile (■), TiO_2-anatase (●) and Nickel Titanate (▲), for the six Au-containing samples as a function of the annealing temperature. The Au diffraction peak intensity was not reported because it was almost insensitive to annealing temperature.

So the presence of nickel promotes the crystallization of titanium oxide in the rutile phase even for a low amount of Ni, but when the titanium content is over 70%, a transition

process from anatase to rutile is observed. In fact, as reported in the literature [77], rutile is stable when the crystalline size is larger than 35 nm, while for a lower crystal size, anatase and brookite are thermodynamically favored: in the present samples, the presence of nickel is found to be a trigger to rutile crystallization, also for small TiO_2 crystals. Again, Au diffraction peaks do not undergo any significant change during thermal annealing, at least in the analyzed temperature range, so Au NPs are stable inside the oxide matrix and therefore the Au main diffraction peak was not taken into account for the plots reported in Figure 3.3.

For all the samples and all the crystalline phases (with the exception of anatase in 8T2N and 9T1N samples, where crystals undergo structural changes with temperature) an increase of annealing temperature causes a sharpening of diffraction peaks, indicating the growth of the crystals with thermal treatment.

3.2.3 Electron Microscopy characterization

Scanning Electron Microscope (SEM) was used to evaluate the surface morphology of the nanocomposites: low resolution images taken on 70T30N, 50T50N and 30T70N samples with Au NPs are reported in Figure 3.4. It can be seen that an increase in the amount of NiO leads to a more irregular and crystalline film, also confirmed by XRD data. The difference in morphology can be easily related to the different amount of Nickel ions in the sol-gel solution: in fact thin films prepared from Titanium alkoxide precursors are usually homogeneous and with small surface roughness [78,79] , while solutions of Nickel salts only dissolved in a solvent usually lead to less homogeneous and rougher films [80]. EDX results in terms of average atomic percentage are reported in Table 3.4, together with the experimental and theoretical Ti/Ni ratios: the samples composition is here confirmed, taking into account that the error for the EDX measurement is around 5%.

High resolution SEM images for 70T30N sample stabilized at 500 °C and then progressively annealed at 600 °C and 700 °C are reported in Figure 3.5 together with respective XRD diffraction patterns; crystallite sizes evaluated with the Scherrer relationship for the three crystalline phases detected (TiO_2-rutile, $NiTiO_3$ and Au, using respectively 27.4°, 33.1° and 38.2° diffraction peaks) are also reported in Table 3.5. As can be noticed, the morphology of the sample changes with the annealing temperature, being the surface smoother at lower temperature, and becoming a little bit rougher and structured at higher temperatures. As explained in the previous section and also shown in

the XRD patterns of Figure 3.5b, the oxide matrix is amorphous at 500 °C annealing and becomes crystalline with higher thermal treatments, while Au particles are already formed at 500 °C.

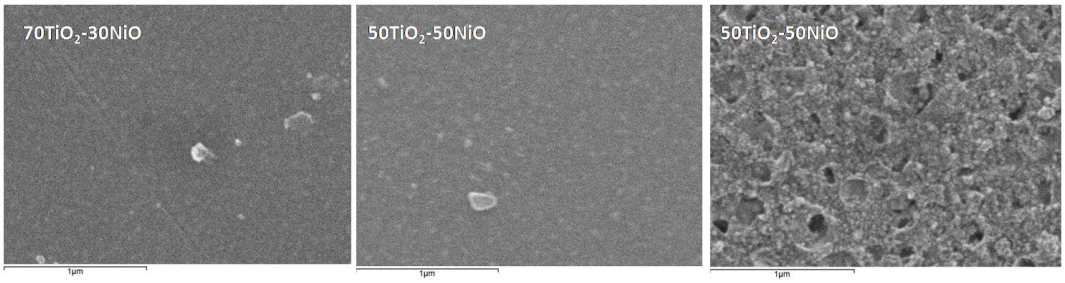

Figure 3.4. Bright field SEM images of the surface of different films containing Au NPs annealed at 500 °C. The scale bar is 1μm.

Table 3.4. Chemical composition (atomic) of the Au containing nanocomposite films annealed at 500 °C evaluated with SEM-EDX by positioning the electron beam on 5 different regions of each sample; because all the films were deposited on silica glass, only Ti and Ni amount refers to film composition, while oxygen and silicon content are due also to the substrate. Au is not reported as it was used as conductive coating.

Sample	% C	% O	% Si	% Ti	% Ni	Ti/Ni (experimental)	Ti/Ni (nominal)
70T30N	19.4	54.3	25.2	0.82	0.37	2.2	2.3
50T50N	18.3	55.3	24.8	0.79	0.73	1.1	1.0
30T70N	17.9	57.9	23	0.31	0.85	0.4	0.4

Considering that the magnification is the same for all the three SEM images, a clear grain growth can be appreciated with higher annealing temperatures, as also confirmed from the narrowing of the diffraction peaks. Nevertheless, a considerable amount of residual porosity is detectable even after 700 °C, a fundamental requirement for samples to be used in gas sensing devices. Due to the high magnification imaging, also gold NPs as bright spots can be observed: they are statistically dispersed through the sample and no aggregation phenomena appear to occur.

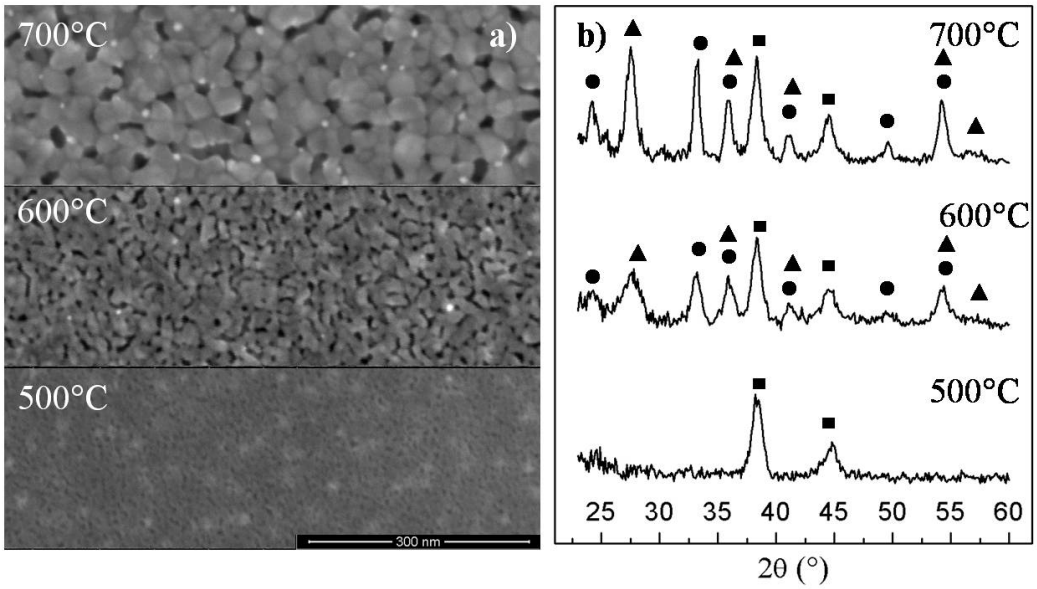

Figure 3.5. a) SEM micrographs of the 70T30N sample annealed at different temperatures. b) Respective XRD diffraction patterns with highlighted Au (■), TiO_2-rutile (▲), $NiTiO_3$ (●) peaks.

Table 3.5. Mean crystallite diameter calculated according to the Scherrer equation for the diffraction peaks of 70T30N film annealed at 500 °C, 600 °C and 700 °C.

Temperature	Diameter (nm)		
(°C)	TiO_2-rutile	$NiTiO_3$	Au
500	/	/	11.5
600	6.5	11.7	11.2
700	11.2	18.5	12

Transmission Electron Microscopy (TEM) analysis on scratched fragments of the film deposited on a carbon copper grid (Figure 3.6) revealed the presence of polydispersed Au NPs (σ=4.2nm) with an average diameter of about 13 nm. The visual contrast of the image in bright field TEM is related to two factors: mass-thickness contrast and scattering (diffraction) contrast. Elements with high atomic numbers (in this case, Au) maximize both components, with respect to the lighter oxide matrix components: so Au NPs appear in bright field TEM images as darker spots. Only for the Ni-rich sample another crystalline phase (NiO) can be detected inside the amorphous matrix, as confirmed also by the XRD data. Polydispersion of Au NPs comes from the poor control on the reduction process of Au^{3+} ions inside the film: immediately after the deposition there is no evidence of metallic gold inside the matrix, because the reduction occurs during the annealing

process due to the thermal decomposition of gold chloride species (first a reduction from $AuCl_3$ to AuCl around 160 °C, and then a second reduction to metallic gold at about 200 °C) and oxidation of the organic compounds that can act as reducing agents, donating electrons to gold ions, so leading to Au NPs nucleation [81,82].

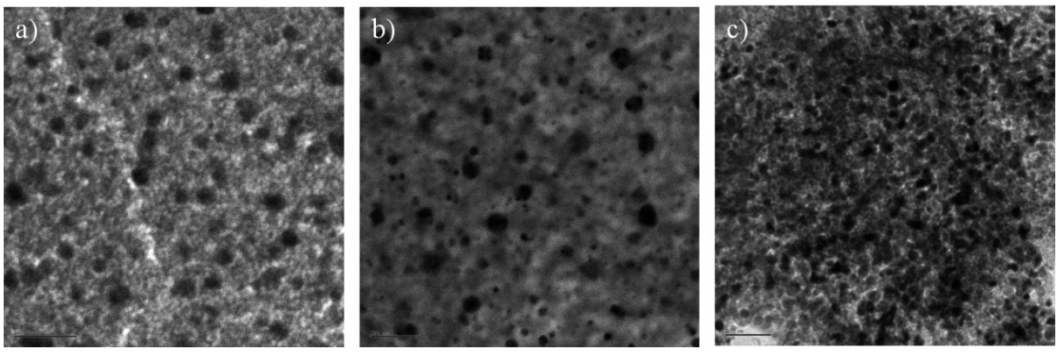

Figure 3.6. Bright field TEM images of 70T30N (a) 50T50N (b) and 30T70N (c) nanocomposite films with Au NPs annealed at 500 °C. Au NPs are clearly detectable as darker spots. The scale bar is 100 nm.

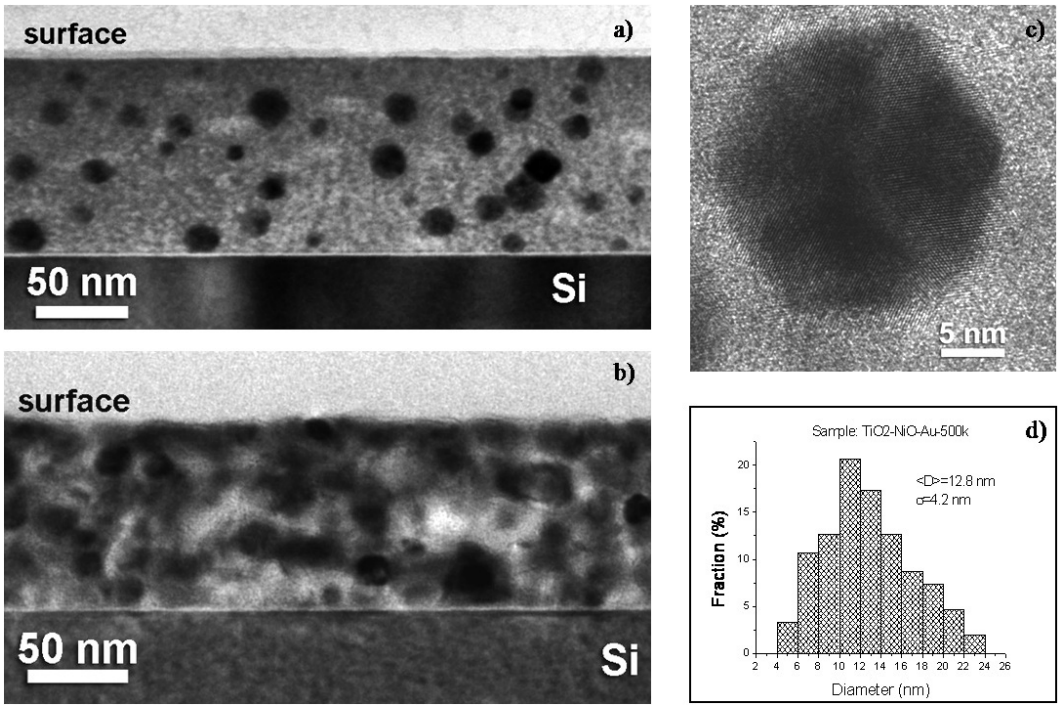

Figure 3.7. Bright field cross-sectional TEM images of the Au-70T30N nanocomposite film deposited on Si substrate and annealed at 500 °C (a) and 600 °C (b). c) High magnification image of an Au NP; d) size distribution of Au NPs.

Figure 3.7 shows cross-sectional TEM images of 70T30N sample annealed at 500 °C and at 600 °C: Au NPs homogeneously dispersed through the film thickness are clearly visible as darker spots in the 500 °C sample, while after 600°C annealing, also the crystalline phases of the matrix appear with a higher contrast. Fast Fourier Transform (FFT) analysis on high resolution TEM images of the sample annealed at 600°C (Figure 3.8) has been performed in order to measure lattice distances, and a comparison with theoretical data for different phases has been made. The measured lattice parameters are compatible with Au, TiO_2-Rutile and $NiTiO_3$ phases, although some TiO_2-anatase lattice planes are also present. This can be due to the partial crystallization of anatase that rapidly evolved into the rutile phase, also confirmed by the XRD measurements discussed previously.

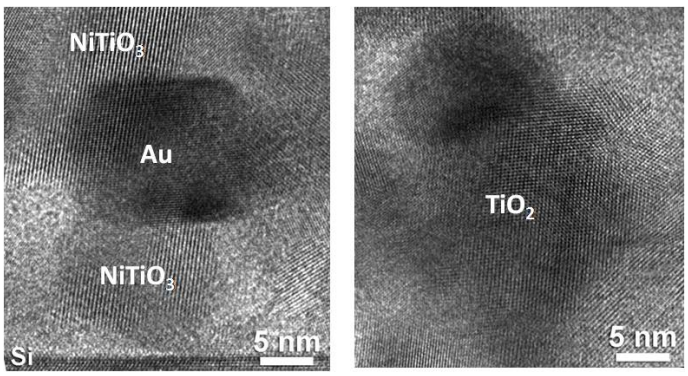

Figure 3.8. Bright field HR-TEM images of Au-70T30N nanocomposite film annealed at 600 °C highlighting the formation of TiO_2, $NiTiO_3$ and Au nanocrystalline phases.

From the cross sectional HR-TEM images reported in Figure 3.7 the porosity of the film can be also recognized: the sample annealed at 500 °C shows higher porosity as compared to the sample treated at 600 °C, but even after 600 °C annealing the film is still porous. In addition, both samples appear to be slightly more dense near the surface.

3.2.4 XPS characterization

In order to achieve a surface characterization of the studied films, we have measured the core level photoemission data obtained by using the XPS of the whole set of samples deposited on a Si wafer: however, differences are irrelevant in the XPS data of the samples with different TiO_2–NiO composition and for this reason in Figure 3.9 we only report the investigated XPS regions (i.e. Ni 2p, Ti 2p and Au 4f) for the Au-70T30N

nanocomposite sample (*i.e.* the most significant composition of the films in relation to gas sensing performance, see section 3.2.6) after annealing at 500 °C and 600 °C. The Ni 2p spectra are indicative of stoichiometric NiO, as evidenced by the position of the binding energy (BE) of the Ni $2p_{3/2}$ component (855.8 eV), as well as by the intensity and energy spacing of the higher BE satellites lines. In the case of the Ti 2p photoemission spectra, the Ti $2p_{3/2}$ peak is centered at 459 eV and it is characterized by a full width at half maximum (FWHM) compatible with just one component indicating the presence of fully stoichiometric TiO_2. It can be also seen that core level XPS data do not undergo to any significant change as a consequence of thermal annealing from 500 °C to 600 °C: there is no modification either on the energy position or in the FWHM of both Ti and Ni photoemission lines. Even so, the fingerprint of the $NiTiO_3$ species would be quite difficult to resolve between NiO and TiO_2, since the oxidation state of Ni^{2+} and Ti^{4+} is unaltered, so the presence of $NiTiO_3$ cannot be excluded [83]. However, from the surface stoichiometries obtained by XPS after annealing at 500 °C and 600 °C (see Table 3.6 and compare with the corresponding data of bulk composition reported in Table 3.4), a surface segregation of the NiO component with respect to TiO_2 can be clearly observed. In addition, it can be seen that the surface stoichiometry of the samples treated at at the two different annealing temperatures (500 °C or 600 °C) remain essentially the same, excluding therefore any annealing-induced surface segregation phenomenon in the explored temperature range.

The Au $4f_{7/2}$ photoemission line is centered for all samples at 83.8 eV which is in good agreement with the value reported for bulk metal Au (84.0 eV). The very small shift to lower BE can be attributed to the presence of very small particles with an extended Au-O interface. Again, in the case of Au no BE change is observable for the sample treated at higher temperature. The contribution to surface stoichiometry from the Au NPs (Table 3.6) is below to the nominal bulk values (Table 3.4), indicating that they are predominantly located into the film bulk, in agreement with the cross-sectional HR-TEM images reported in Figure 3.7. A somewhat better signal/noise ratio observed in the higher temperature sample is connected to the almost triple value evidenced in Table 3.6, which is possibly related to some temperature-induced surfacing of Au NPs in the higher temperature sample, as it can be seen in Figure 3.7.

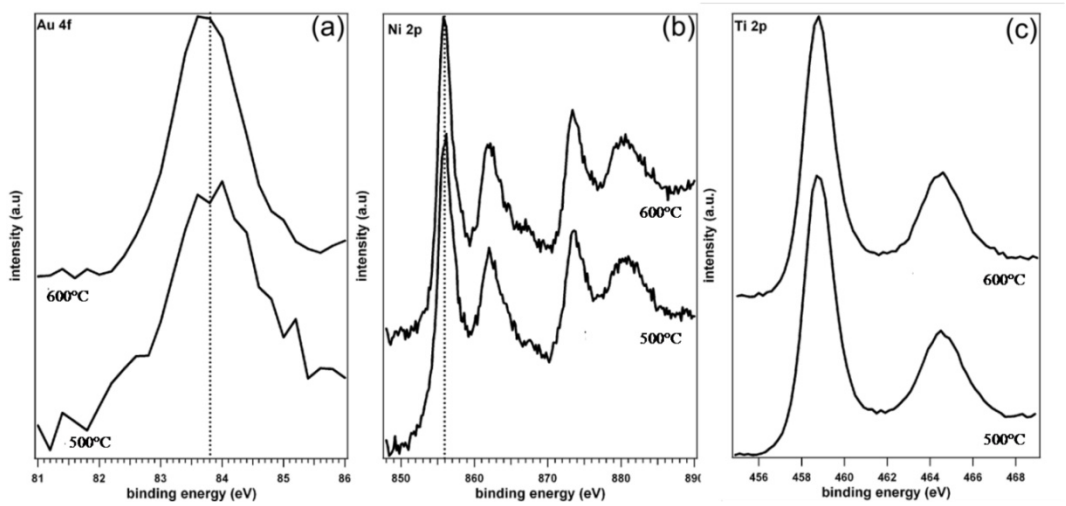

Figure 3.9. Al-K_α excited XPS core level regions for 70T30N nanocomposite film containing Au NPs annealed at 500 °C and 600 °C.

Table 3.6. Surface stoichiometry derived from XPS data of the investigated 70T30N film with Au NPs.

Atomic per cent (%)	500°C	600°C
Ni	12%	12%
Ti	16%	16%
O	55%	53%
Au	0.1%	0.3%
C	17%	18.7%

To explore the possible presence of interfacial states among the TiO_2 and NiO nanocomposite components, we have also measured the valence-band (VB) region of the TiO_2–NiO films of different composition using UPS. Figure 3.10 shows the VB region obtained by He II radiation (40.8 eV) of the different films (without Au) annealed at 500 °C. The UPS data for the different films are rather dissimilar: the spectrum of the Ti-rich sample 70T30N is very much reminiscent of the UPS data of a pure titania powder sample, whereas the one of the 30T70N sample shows the unusual structure (four distinct peaks) of NiO [84,85]. However, the spectrum of the 50T50N sample is effectively the sum of the spectra of the two different oxides. With the degree of accuracy obtainable with a standard UPS experiment, we can say that there is no clear evidence of the appearance of distinct features to be associated with specific TiO_2–NiO interfacial states. In contrast, no distinct feature is observed in the UPS data of the TiO_2–NiO films containing Au NPs, due to the low concentration of Au.

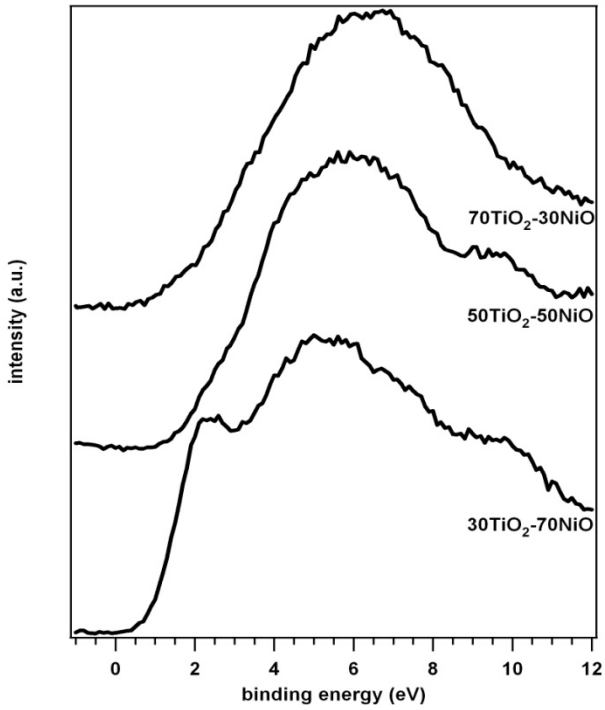

Figure 3.10. He I excited UPS VB spectra of different TiO_2–NiO films annealed at 500 °C.

According to this set of data, it can be said that the films are a simple mechanical blend of the parent oxides and that possible interfacial states due to the previously observed Au/NiO epitaxial growth [61] are hardly visible adopting such standard UPS technique.

3.2.5 Optical characterization

Together with morphological and structural characterization, Au-containing samples were also characterized with optical absorption and spectroscopic ellipsometry in the UV-Vis-NIR region. Figure 3.11 shows the optical absorption spectra of the six samples listed in Table 3.2 annealed at 500 °C: Au NPs localized surface plasmon resonance peak is clearly visible in all samples, and it appears red shifted with increasing Ti amount. This can be ascribed to the different refractive index of the films according to sample composition, because of the higher value of rutile and anatase (2.51 and 2.7 at 590 nm, respectively [86]) compared to NiO (2.33 at 620 nm [87]) and $NiTiO_3$ (2.42 at 630 nm [88]).

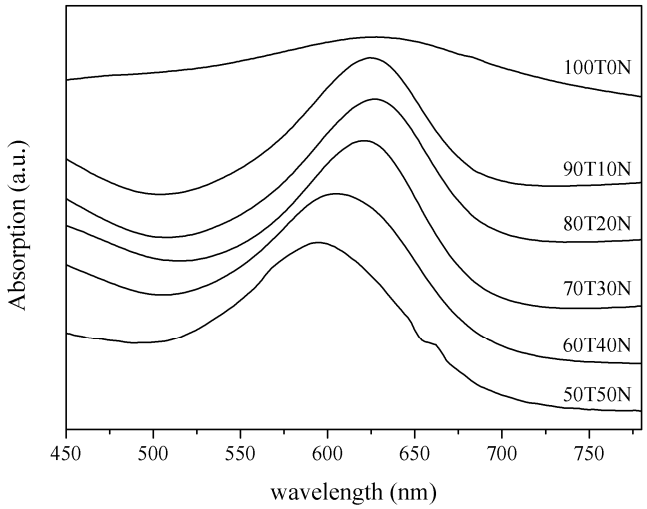

Figure 3.11. Optical absorption spectra for the samples with Ni amount ranging from 0% to 50% annealed at 500 °C.

Moreover a slight broadening of SPR peak can be experienced when increasing Ti amount, especially for 90T10N and 100T0N samples. This fact can be ascribed to two factors: the first is a real physical mechanism, and it is related to the interaction between Au NPs and anatase crystals, that causes a scattering of the surface free electrons at the Au/TiO_2 interface, spreading the range of plasmon frequencies as described by Hoffmann [89] and Lee [90]. The second cause is related to the higher refractive index of the Ti-rich samples, that can cause interference phenomena that make the SPR peak appear broadened. Since the optical spectra are collected in absorbance mode, so it's not possible to distinguish between absorption and reflection; this is evident in the 100T0N sample, in which the plasmon peak lays over a broad interference fringe.

Refractive index dispersion curves versus wavelength for the six samples listed in Table 3.2 annealed at 500 °C are reported in Figure 3.12a: a clear increase in refractive index together with Ti amount is observed, as prefigured before. The dispersion curves are affected by the Au localized SPR band, that causes the perturbation between 600 nm and 800 nm as predicted by Kramers-Kroning relationship. For this reason, a comparison between refractive indexes has been done considering the values at 1100 nm, far enough from the Au-SPR region to be modeled with a Cauchy dispersion: results are reported in Figure 3.12b, together with the SPR band position determined from the absorption spectra. As expected, an increase in refractive index causes a red shift of the plasmon band, although for some samples this effect seems more pronounced. Such behavior can be explained taking into account that the refractive index measured with ellipsometry is

an average value, while the Au SPR band is affected from the matrix properties in the proximity of the particle surface. So it is likely that for some samples, the matrix has a slightly different composition, amount of crystallization, or porosity in close proximity to the gold particles compared to the average value, influencing the Au plasmon peak position.

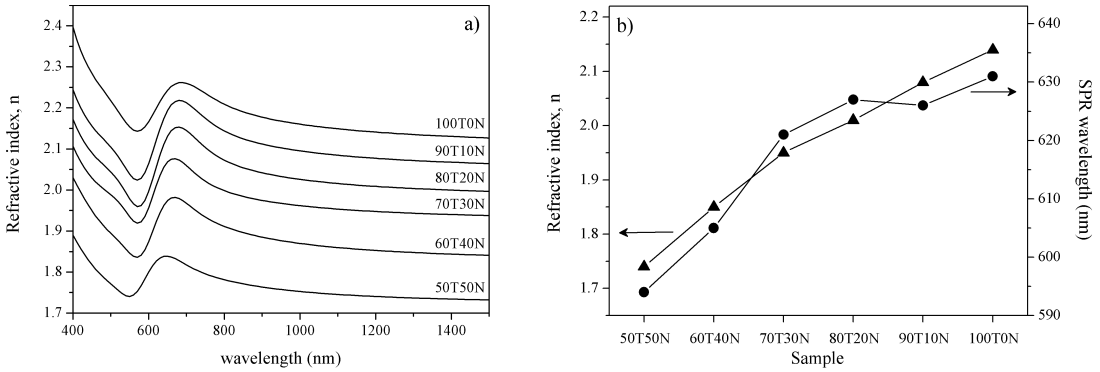

Figure 3.12. a) Refractive index dispersion curves for the six samples listed in table 3.2 annealed at 500 °C: a clear increase in n is observed when the amount of the Ti component of the film is increased from 50% to 100%. b) Comparison between refractive index values measured at 1100 nm and the Au NPs SPR wavelength for the same samples.

Considering the tabulated refractive index values for the different oxides detected, and comparing them with the data measured with ellipsometry, it is evident that the experimental values for all the six samples are substantially lower than the expected values for a fully dense material of the same chemical composition. This difference is due to the residual porosity of the films that can be seen as an effective medium composed of dense materials and pores. Porosity was estimated by means of the Bruggerman relationship [91], using the formula reported below (where n is the experimental refractive index and n_{TiO2} is the refractive index for fully dense anatase), and considering as bulk material the film annealed at 1000 °C, even if a residual porosity also at that temperature cannot be totally excluded, and so the porosity determination is on the conservative side.

$$Porosity = \frac{\left(\frac{n_{TiO_2}^2 - n^2}{n_{TiO_2}^2 + 2n^2}\right)}{\left(\frac{n_{TiO_2}^2 - n^2}{n_{TiO_2}^2 + 2n^2}\right) - \left(\frac{1 - n^2}{1 + 2n^2}\right)} 100\% \qquad (3.1)$$

The 70T30N sample was annealed from 500 °C to 1000 °C with 30 minutes steps every 100 °C, and ellipsometric measurements have been performed at each step in order to calculate the refractive index evolution with annealing temperature. It is noteworthy saying that XRD measurements performed after each thermal treatment up to 1000 °C exclude the formation of different crystalline phases (for example due to the reaction between the film and the SiO_2 substrate), while an annealing at 1050-1100 °C is likely to cause the formation of a silicate compound as observed in the past [92], possibly as a consequence of the diffusion of Si atoms due to the proximity of SiO_2 substrate temperature of glass transition. The obtained refractive index dispersion curves are reported in Figure 3.13a, where a clear increase in refractive index with temperature can be noticed, as a consequence of the decrease in porosity. Again, porosity determination was made by considering refractive index values at 1100 nm, far enough from Au SPR peak not to be affected by its absorption. Refractive index values at the different temperatures and porosity are reported in Figure 3.13b.

Porosity of the nanocomposite films is in the range 16%-23% up to an annealing temperature of 800°C, then it decreases to 7% at 900 °C. As anticipated, this estimation is conservative because the film annealed at 1000 °C was chosen to represent a full dense material, even if its refractive index is lower than the theoretical value for a material composed of TiO_2-rutile and $NiTiO_3$, so a small amount of residual porosity is likely to be present in the sample annealed at 1000 °C.

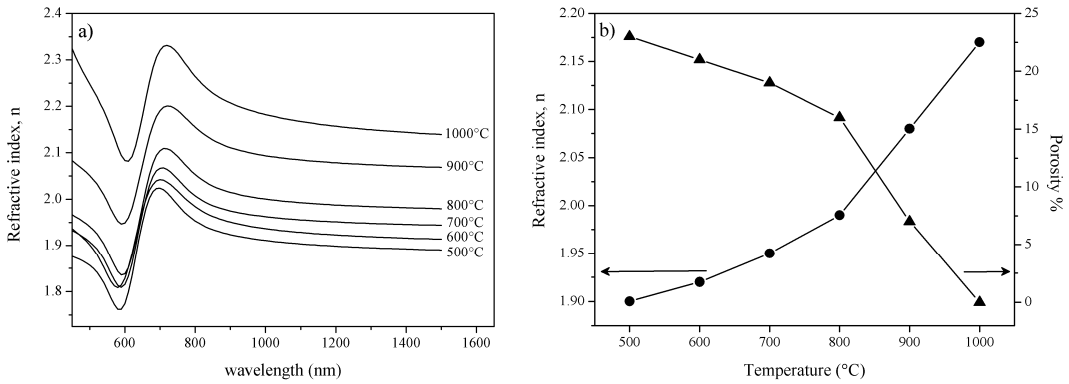

Figure 3.13. a) Refractive index dispersion curves for the 70T30N sample annealed from 500 °C to 1000 °C. b) Evolution of refractive index and estimated porosity with temperature for the same sample.

Another experiment has been performed to have a more accurate indication on the porosity of these samples: ellipsometric analyses have been carried out under nitrogen

and ethanol vapors atmospheres thanks to a custom-built cell provided with a sample holder so the pores are filled with nitrogen in the first case, with ethanol the second one. Knowing the refractive index values of the two media, it is possible to isolate the pore volume fraction *P* as a function of the measured refractive index (see Appendix section for details).

Figure 3.14 shows the refractive index dispersion curves measured in nitrogen and ethanol vapors for a 50T50N sample containing Au NPs annealed at 500 °C; at 1100 nm the difference in refractive index is 0.098, leading to a porosity volumetric fraction of about 27%. Similar values of porosity fraction have been evaluated also for other samples with different compositions. It is noteworthy that also this method underestimates the porosity, because it takes into account only open porosity and it is hard to specifically determine if ethanol enters all the open pores: so this evaluation is on the conservative side, and it is reasonable to assume that the porosity is at least 27%, reasonably close to the value obtained with the previous method.

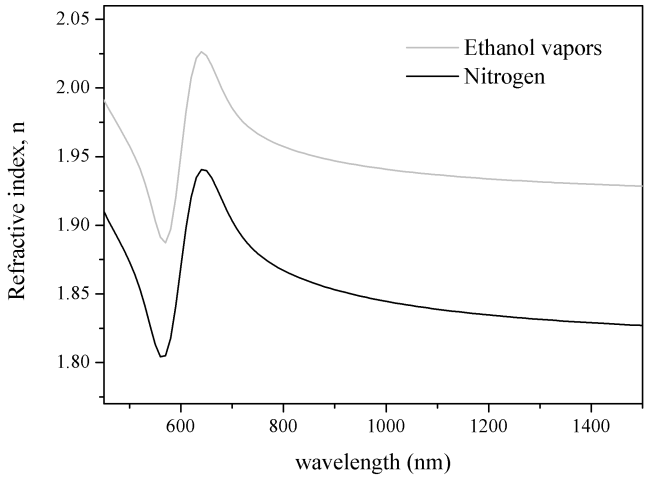

Figure 3.14. Refractive index dispersion curves of 50T50N film with Au NPs annealed at 500 °C, measured at room temperature under nitrogen (black line) and ethanol vapors (light grey line) atmospheres.

Spectroscopic ellipsometry analysis is also helpful to measure sample thicknesses: keeping the precursor concentration and deposition parameters (spinning rate and time) constant, the thickness of 500 °C annealed samples decreases almost linearly from about 200 nm to 100 nm when the Ni content is reduced from 50% to 0%, suggesting a role of Ni^{2+} ions in increasing solution viscosity by creating a complex with acetylacetone or promoting hydrolysis and condensation processes of titanium butoxide.

3.2.6 Gas sensing tests

3.2.6.1 Samples annealed at 500 °C

The nanocomposite films have been subjected to gas sensing tests at temperatures between room temperature and 350 °C and they were exposed to the following gases: H_2 (1% v/v), CO (1% v/v), Propane (0.3% v/v) and H_2S (different concentration ranging from 2 ppm to 100ppm). First 70T30N, 50T50N and 30T70N samples were tested in order to explore the role of the different phases (NiO, TiO_2, $NiTiO_3$) in the gas sensing performances. Samples without Au did not give any appreciable optical response towards any of the tested gases, while thin films containing Au NPs gave a good response only to H_2S, so all results reported from now on refer to the Au-containing samples. Exposure to CO, H_2 or propane gave almost no variation in the absorption spectra. Figure 3.15 shows the optical absorption spectra of the three samples annealed at 500 °C and collected at the operative temperature (OT) of 350 °C in air and after H_2S exposure. Tests at lower temperatures have also been performed, giving low or null response up to 200 °C. Tests at OT=300 °C had quite good response but longer recovery times, and the baseline sometimes was not fully recovered, so each test reported here, if not specified, has been performed at OT= 350 °C.

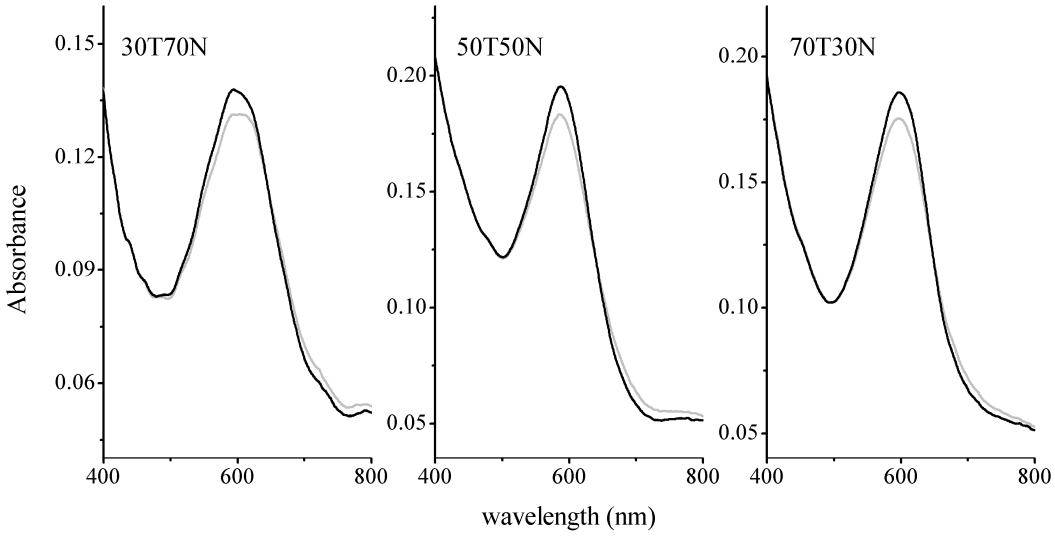

Figure 3.15. Absorption spectra of the three films with Au NPs annealed at 500 °C measured in air (black line) and during exposure to 0.01% v/v H_2S (light grey line) at the operative temperature OT= 350 °C.

Au Surface Plasmon Resonance (SPR) peak centered around 600 nm is clearly visible in all the optical absorption spectra; the peak wavelength position is substantially smaller than the expected value for Au NPs of the same size in a TiO_2-NiO matrix, considering the tabulated refractive indexes for the two oxides: this is due to the residual porosity of the film, as described before, that lowers the average refractive index, causing a blue-shift of the Au SPR peak. During H_2S exposure, the form of Au plasmon peak undergoes distinctive changes, *i.e.* a decrease of maximum intensity and a broadening especially at high wavelengths, while no shifts in the frequency of the peak have been observed.
This behavior suggests an interaction between H_2S and the surface of Au NPs, that leads to a reduction in the number of surface oscillating free electrons, due to a charge transfer between Au and S, with a depletion in Au d-electrons, that provides a decay path for excited s-electrons, spreading the surface plasma resonance in a wider range of wavelengths, damping and broadening the plasmon peak. The same behavior has been observed also on thin films composed of Au NPs dispersed inside a SiO_2 matrix, where no interaction is established between the target gas and the inert oxide matrix, so the variation in the optical properties is due to the interaction of hydrogen sulfide with Au particles, as can be seen in Figure 3.16

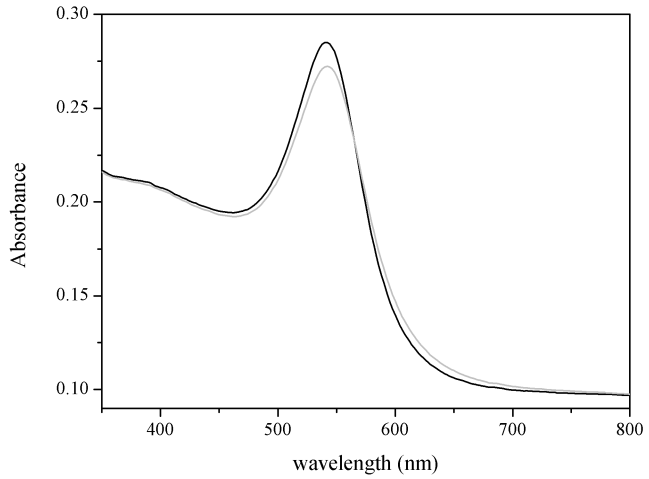

Figure 3.16. Absorption spectra of a SiO_2 film with Au NPs annealed at 500 °C measured in air (black line) and during exposure to 0.01% v/v H_2S (light grey line) at the operative temperature OT= 350 °C.

At low temperatures the reaction between the sample and hydrogen sulfide was found to be irreversible as will be described later, so using this setup it is possible to expose the sample to the target gas at high temperature, and then to cool it down to room temperature

with hydrogen sulfide flowing in the test cell. By this method, the sample remains "frozen" when taken back to air at room temperature. This is confirmed by the optical absorption spectra that show the irreversible modification of the Au NPs plasmon peak, and so the cause of the Au SPR modification remains inside the sample. The "frozen" status is maintained for several days, so it is possible to perform characterizations like XRD, XPS, ellipsometry and UV-Vis spectroscopy on the sample modified by H_2S.

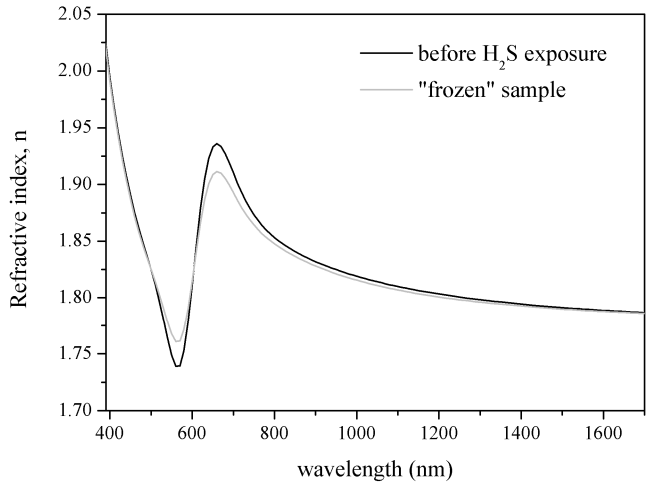

Figure 3.17. Refractive index dispersion curves of 70T30N film with Au NPs annealed at 500 °C before H_2S exposure (black line) and after the "freezing" process (light grey line).

Ellipsometric analyses performed on "frozen" samples revealed a difference in the dielectric properties compared to pristine unexposed films only in the Au SPR wavelength range, while almost no variations in refractive index are observed in the non absorbing region (Figure 3.17). Au-free samples did not present any relevant change in either refractive index or absorption coefficient, suggesting again a key role played by Au NPs in the interaction with the target gas.

Significant sensitivity changes are observed in the films with different compositions, as can be seen from Figure 3.18: the absorbance variation calculated as the difference between absorbance in air and absorbance during target gas flowing, named Optical Absorbance Change, OAC, is lower for the NiO-rich nanocomposite film, while 50T50N and 70T30N films showed very similar behavior. Due to the strong SPR of Au NPs in the visible region, the optical response of the sensor can be tuned by choosing an appropriate wavelength of analysis, as reported in literature for thin films composed of a matrix of metal oxides with embedded Au NPs [93]. From the shape of the OAC curves in Figure

3.18a, a negative minimum and a positive maximum can be determined. Exposure to H_2S leads to a decrease of the optical absorption of the sample if the testing wavelength is near the minimum of the OAC curve, while operating near the maximum of the OAC curve leads to an increase of optical absorption, as reported in Figure 3.19. It is also possible to recognize some wavelengths in which the sensor response is null: this behavior allows the operator to tune the sensitivity of the optical sensor by selecting the analysis wavelength. Moreover, different gases usually promote different optical variations so in principal it is possible to selectively detect one particular gas inside a complex gas mixture by using wavelength modulation [62,94].

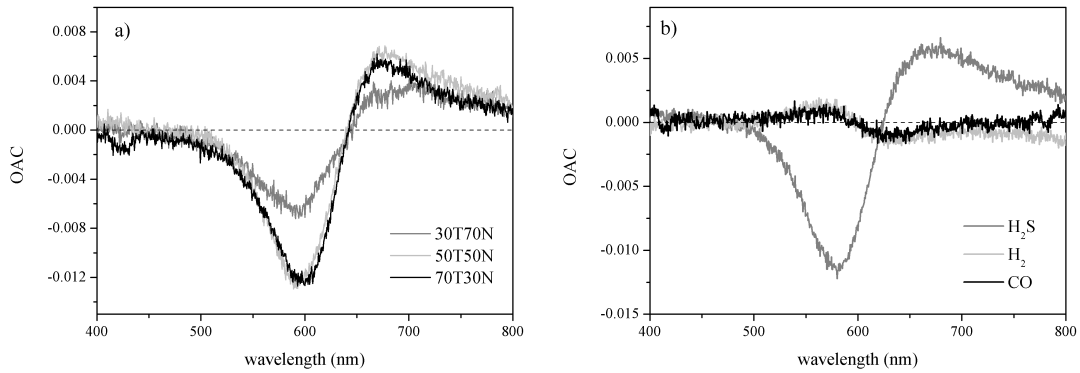

Figure 3.18. a) OAC plots of 70T30N (black line), 50T50N (light grey line) and 30T70N (dark grey line) films containing Au NPs annealed at 500 °C after exposure to 0.01% v/v H_2S at OT=350 °C. The zero response value is highlighted with a dotted line. b) OAC values of 50T50N sample containing Au NPs annealed at 500 °C after exposure to 0.01% v/v H_2S (dark grey line), 1% v/v H_2 (light grey line) and 1% v/v CO (black line) at OT=350 °C.

Interestingly, the 30T70N film shows the worse behavior, with a small signal to noise ratio and a poor dynamic performance, while 50T70N and 70T30N samples show a good dynamic behavior, with fast response after initial hydrogen sulfide exposure, stable signal during the gas flow phase, and good recovery of the baseline level, as can be seen from Figure 3.19. It is also observed that the Ti-rich sample shows a slightly more stable signal and a faster recovery compared to 50T50N film. As expected from the OAC curves reported in Figure 3.18b, the samples show almost no variation during hydrogen exposure, while the Au-TiO_2 reference sample gives response to H_2S but also to both CO and H_2, as already known from a previous work [95].

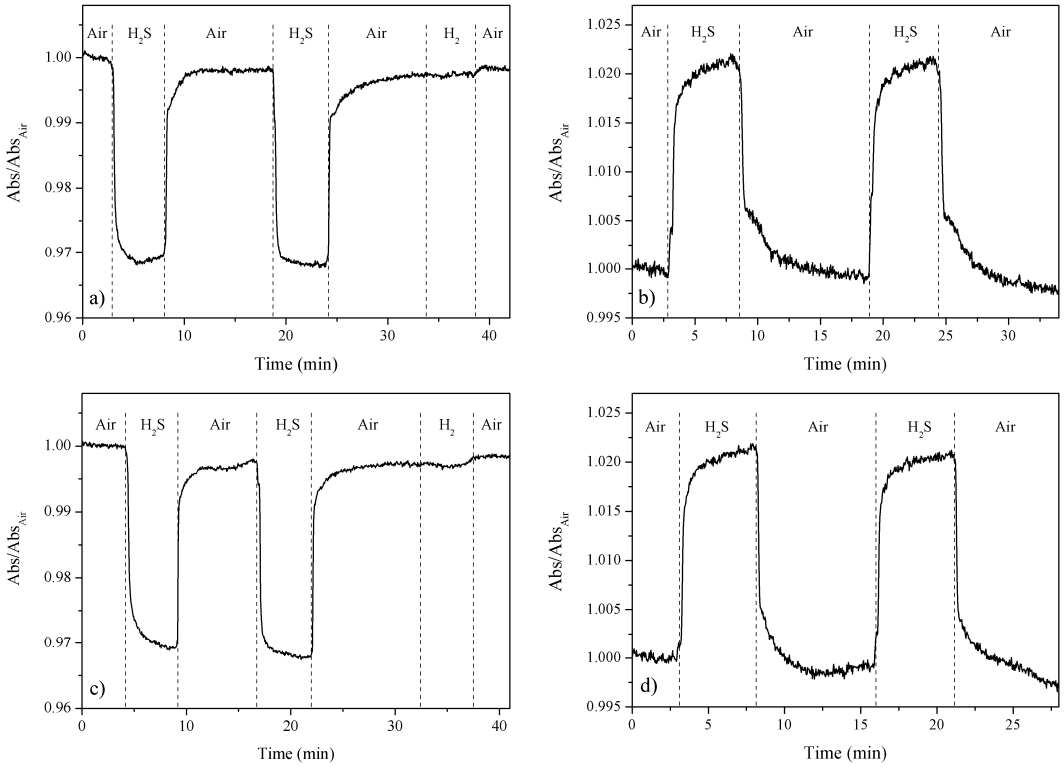

Figure 3.19. Dynamic response of 70T30N film annealed at 500 °C at 605 nm (a) and 690 nm (b) towards 0.01% H_2S and 1% H_2 at the operative temperature OT=350 °C. Dynamic response of 50T50N nanocomposite film annealed at 500 °C at at 600 nm (c) and 690 nm (d) towards 0.01% H_2S and 1% H_2 at the operative temperature OT=350 °C.

As anticipated at the beginning of this section, at operative temperatures lower then 350 °C the sensor performances become worse: in particular down to 300 °C OT the material response remains acceptable, being response times quite fast and the intensity of the response comparable with the measurements performed at 350 °C OT, while the recovery becomes very slow and sometimes incomplete. An additional decrease in operative temperature starts to affect also the sensor response, that becomes less intense and slower, and the material modifications, *i.e.* the damping and broadening of the Au SPR peak, turn out to be irreversible. This fact has been exploited to perform the "freezing" process as described before, so as to be able to characterize the samples modified by H_2S with standard *ex-situ* techniques like XRD, ellipsometry, XPS, etc. Figure 3.20 shows two dynamic tests performed on the 70T30N sample at 300 °C and 200 °C OT, highlighting the worsening of the sensing behavior when lowering the operative temperature.

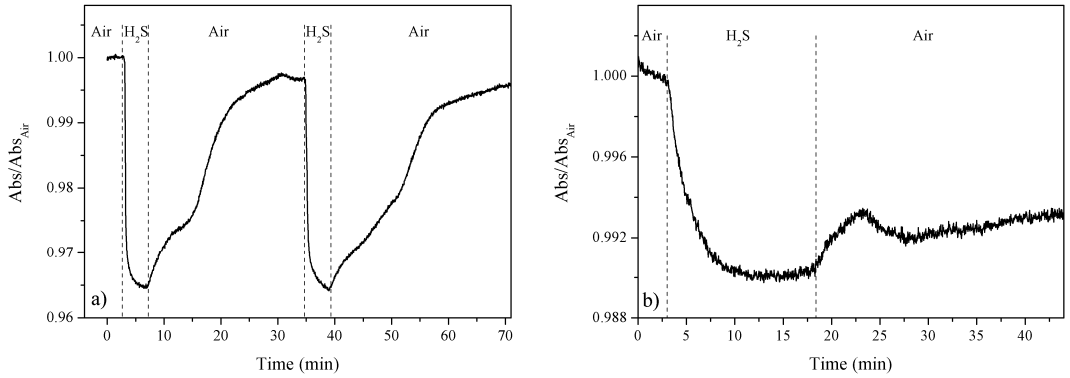

Figure 3.20. Dynamic response of 70T30N nanocomposite film annealed at 500 °C at 605 nm at 300 °C OT (a) and at 200 °C OT (b) towards 0.01% H_2S.

3.2.6.2 Samples annealed at 600 °C

After the 600 °C thermal treatment, the sensing performances of the films are improved: in fact, as can be seen from Figure 3.21a, optical sensitivity of the nanocomposite film annealed at 500°C is lower with respect to the same sample annealed at 600 °C. Also the dynamic behavior (Figure 3.21b) is improved by the thermal treatment, and response time is very fast (about 20 seconds to reach 90% of the total variation). There is a stable signal during hydrogen sulfide exposure, and the recovery of the baseline is almost perfect and rapid. This improvement of sensor performance can be directly related to the microstructure of the nanocomposite film: the annealing process induces further crystallization without compromising the porosity of the matrix, as confirmed by TEM, SEM and the ellipsometry measurements previously reported.

To check cross sensitivity to another gas species, during H_2S (0.01%) exposure, H_2 (1%) was introduced inside the test cell, keeping total flow rate constant. As can be seen from Figure 11b, there is almost no response to hydrogen: this result confirms that the Au-70T30N sample can selectively detect hydrogen sulfide in a H_2:H_2S = 100:1 mixture in air.

Further experiments on 600 °C treated samples were performed with lower H_2S concentrations, and the results are reported in Figure 3.22: looking at the spectrum in Figure 3.22a, the absorption value during 10 ppm and 100 ppm H_2S exposure is almost the same, but the dynamic performance is slightly different. This behavior suggests a saturation of reactive sites of the sample, even with 10 ppm, and so an equilibrium between absorption and desorption of H_2S over the active surface occurs. Moreover, from the gas-to-air transient, a slower recovery of the baseline is observed after 100 ppm exposure, indicating a slower desorption of hydrogen sulfide and reaction products from

the reactive sites. This can be related to the longer time needed to complete the evacuation of the test chamber after 100 ppm H_2S exposure, compared to 10 ppm exposure, the flow rate being constant during the different tests.

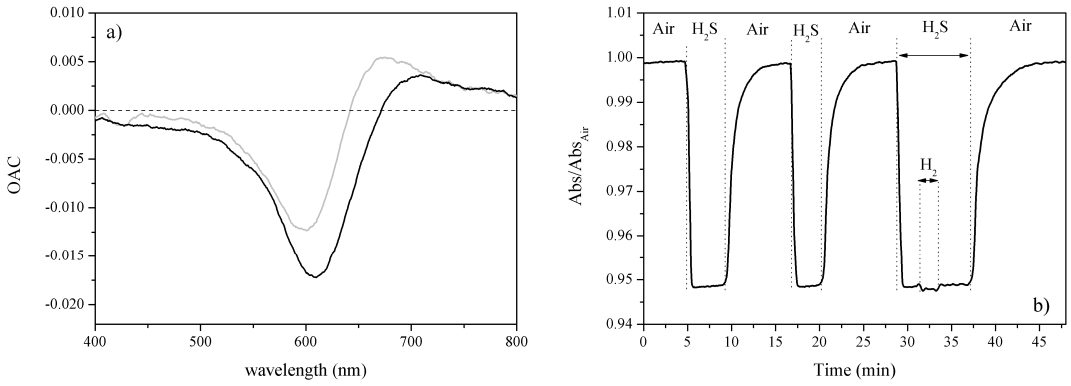

Figure 3.21. a) OAC of 70T30N nanocomposite film annealed at 500 °C (grey line) and 600°C (black line) after exposure to 0.01% v/v H_2S at the operative temperature OT=350°C; b) Dynamic response at 605 nm of 70T30N film annealed at 600 °C towards 0.01% H_2S and 1% H_2 at the operative temperature OT=350 °C.

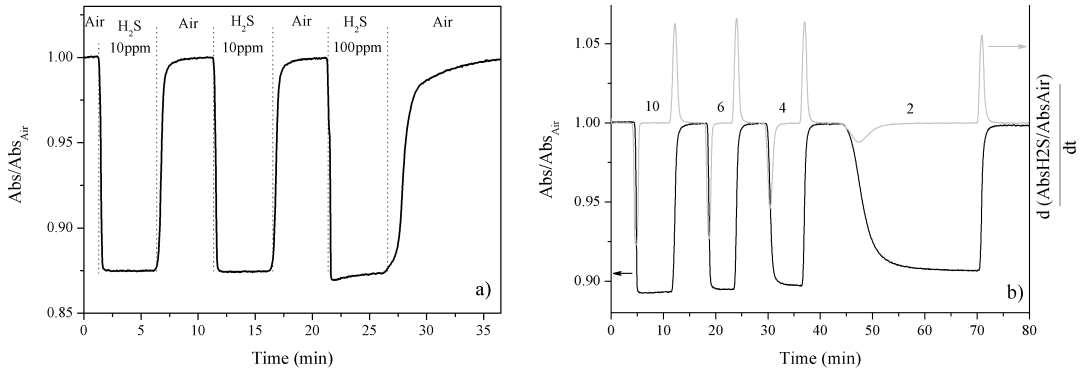

Figure 3.22: a) Dynamic response at 605 nm of Au-70T30N nanocomposite film annealed at 600 °C towards 10 ppm and 100 ppm H_2S at the operative temperature OT=350 °C. b) Dynamic response at 590 nm of Au-50T50N nanocomposite film annealed at 600 °C under exposure to different H_2S concentrations (10, 6, 4 and 2 ppm) at 350 °C OT (black line) and derivative of this spectrum (grey line).

Figure 3.22b reports a dynamic test with H_2S concentrations ranging from 2 to 10 ppm, and the derivative of this spectrum: the saturation is still reached with 6 ppm H_2S, while the absorption change during 4ppm and especially during 2 ppm exposure is slightly lower, indicating that around 5 ppm H_2S there is the threshold for saturation of reactive sites. In addition, a decrease in target gas concentration produces longer response times,

while – for quite low concentrations, *i.e.* up to 10 ppm – recovery times are not affected by hydrogen sulfide concentration. This effect can be clearly seen in the derivative spectrum, where the negative peaks represent the air-to-gas transient, and the positive peaks represent the gas-to-air transient. Comparing these peaks, we can see that the desorption behavior is very similar for the different concentrations (positive peaks are comparable in intensity and broadening), whereas absorption behavior changes significantly. Higher concentrations lead to very sharp and intense peaks (very fast response), while low concentrations result in broad and less intense peaks, indicating longer response times.

So the material is sensitive also to very low concentration of H_2S, with response and recovery times strongly related to gas concentration: for high concentrations (100 ppm) the recovery behavior is worse compared to lower concentrations, indicating a desorption equilibrium, while for very low concentrations (few ppm) the response time increases, and eventually results in a saturation of reaction sites for H_2S concentrations above about 5 ppm.

Since the best sensing results were obtained with 50T50N and 70T30N samples (so with Ni amount less than 50%) annealed at 600 °C, the six samples listed in Table 3.2 were compared after the 600 °C thermal treatment, that was found to be a good compromise between porosity and crystallinity.

By comparing these samples, the behavior during hydrogen sulfide exposure is substantially the same, but the intensity of the response is different, being slightly smaller in the samples with lower amount of nickel. This can be noticed in Figure 3.23 and can be related to the decrease in sensor film thickness observed with lowering the nickel amount in the starting solution, as discussed above; another explanation of the decrease in intensity of OAC curves can be ascribed to the fact that in high Ti amount samples, a broadening of Au SPR peak has been experienced, as explained before, and so the interaction of hydrogen sulfide with the sample, that causes itself a damping and broadening of the plasmon peak, might be less effective.

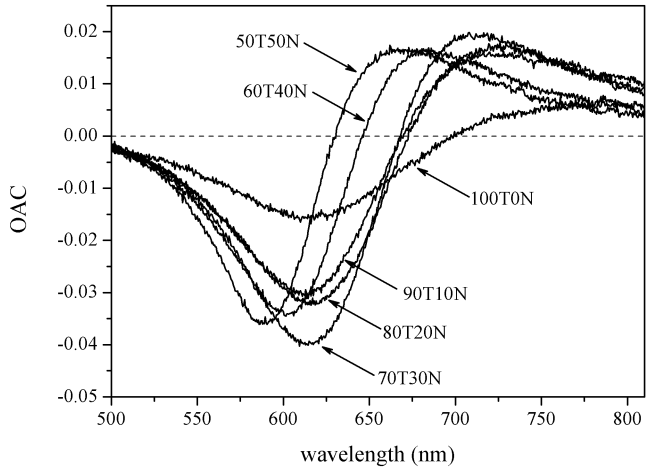

Figure 3.23. Comparison of OAC curves for the sample with Ni amount from 0% to 50% annealed at 600 °C, collected after exposure to 0.001% v/v H_2S at the operative temperature OT=350 °C

However, when the samples are exposed to 1% CO and 1% H_2, almost no response is observed, especially for Nickel-rich samples, while a small response starts to appear for samples containing more than 70% Ti. This effect can be related to the presence of the anatase phase in samples with a lower amount of Ni, these being anatase-gold nanocomposites which is an already studied system for reducing gas detection [95]. Hence, nickel titanate and rutile are shown to be rather insensitive to carbon monoxide and hydrogen presence, even at high concentrations (1%, *i.e.* 10000 ppm). To prove that the two polymorphic structures of TiO_2 have different sensitivity towards CO and H_2, both Au-doped rutile and Au-doped anatase thin films of the same thickness and with the same Au amount have been prepared and tested at 350 °C OT with 1% CO and 1% H_2, and the results are presented in Figure 3.24a. As would be expected, the rutile response to the two gases is lower compared to anatase, confirming the higher activity of the anatase phase for CO and hydrogen detection.

This difference in sensitivity between the two TiO_2 phases is demonstrated also in the nanocomposites containing $NiTiO_3$, as stated previously. The progressive increase in sensitivity to hydrogen and CO when the Ti content is increased in the nanocomposite can be clearly seen in Figure 3.24b. This data for the two gases is obtained by measuring the sensors response at the respective maxima of OAC curves, and the data has been normalized to the H_2S response value at the same wavelength. It is evident that the presence of anatase, due to the lower amount of nickel in the film, enables the nanocomposite to be sensitive also to the other two gases.

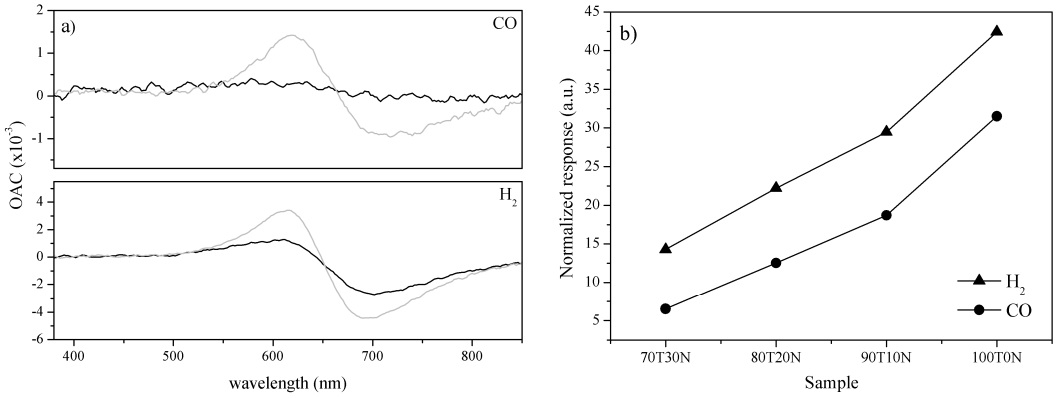

Figure 3.24. a) OAC curves for rutile-Au (black lines) and anatase-Au (grey lines) thin films when exposed to 1% CO or 1% H_2 in air. b) Normalized response towards H_2 (▲) and CO (●) for the Ti-rich samples; data collected at the wavelength corresponding to the maximum of OAC curves for the two gases.

Analyzing the dynamic response behavior of the films subjected to repeated air - hydrogen sulfide - air exposure cycles, response times are in the range of few tens of seconds for all samples, as are the recovery times. A more rapid sensor response performance is evident in samples with Ni content ranging between 50% and 30%. For lower nickel concentrations, the response and recovery times are still acceptable, but sometimes an incomplete return to the baseline and a slightly unstable signal during gas flow appears. The observed differences can be again related to the microstructure and the crystalline phases of the nanocomposite films. Thus, nickel titanate and rutile, the only crystalline phases present when the Ni content is around 30%, are more capable to promote decomposition of the sulfide species on Au NPs, leading to shorter transient times and more stable signals during steady-state gas flow. In an opposite way, anatase appears to be less efficient in decomposing H_2S, resulting in slightly longer response and recovery times, and in a drift of the optical absorption level when hydrogen sulfide is flowed for a prolonged period. So samples with lower Ni content are more sensitive to carbon monoxide and hydrogen but they have a slower dynamic response towards hydrogen sulfide detection.

These two assumptions – slightly worse H_2S dynamic behavior and higher cross sensitivity with H_2 and CO of the Ti-rich samples – are well summarized in Figure 3.25, where the dynamic behavior of 60T40N sample (composed of $NiTiO_3$ and TiO_2-rutile) and 100T0N (composed of TiO_2-anatase) with 10 ppm hydrogen sulfide, 1% CO and 1%

hydrogen are compared. To have a more effective comparison, dynamic plots have been calculated as before, but then normalized to the H_2S response, in order to take into account the differences in thickness of the two samples.

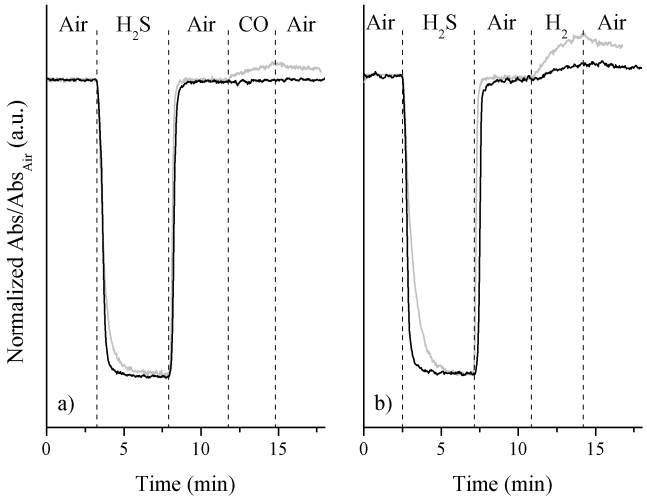

Figure 3.25. Dynamic response of 60T40N at 600 nm (black line) and 100T0N at 615 nm (grey line) nanocomposite films annealed at 600 °C towards 10 ppm H_2S, 1% CO (a) and 1% H_2 (b) at the operative temperature OT=350 °C.

As can be seen, the response and recovery to hydrogen sulfide are almost ideal in the 60T40N sample, while in the TiO_2-Au sample the response time is higher; moreover, the nanocomposite containing Ni is absolutely insensitive to CO and the response to hydrogen is only scarcely detectable, while the anatase-based film shows a small but definitely detectable response to both gases.

As claimed before for samples annealed at 500 °C, also for the nanocomposites annealed at 600 °C the dynamic behavior is highly dependent from the operative temperature: Figure 3.26 shows one air-10 ppm H_2S-air cycle for the $NTiO_3$-Au sample at 6 different OTs from 300 °C to 350 °C. The intensity of the response is nearly the same for the 6 measures, because the small differences can be assigned to discrepancies in the baseline subtraction: in fact the higher the operative temperature, the higher the emissivity of the heating coil attached to the sample holder, (as can be seen in the Appendix section), and so the spectrophotometer detector can receive a different light intensity according to the temperature of the heater. Also the response time is almost identical, confirming that lowering the operative temperature down to 300 °C does not affect the sensor response after the introduction of the target gas. What the figure points out is the great influence of the operative temperature on the recovery time, suggesting that the desorption of H_2S and

of the reaction products from the surface of the nanocomposite films is a kinetic-limited process, because the recovery of the baseline, even if slower, is complete also at 300 °C OT.

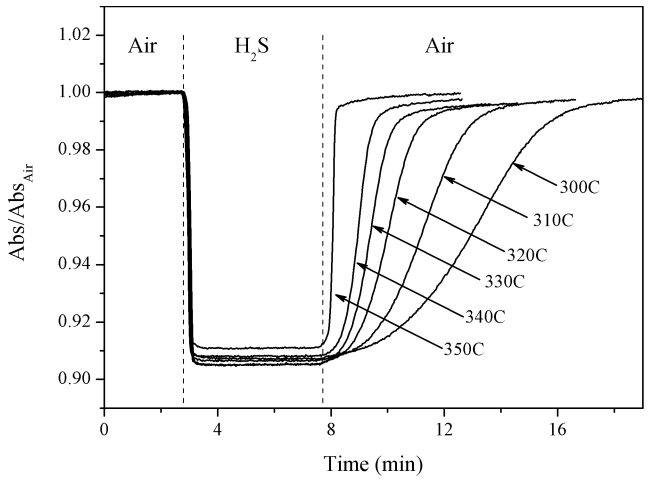

Figure 3.26. Dynamic response at 590 nm of the 50T05N nanocomposite film annealed at 600 °C under exposure to air-0.001%H_2S-air cycle at operative temperatures ranging from 300 °C to 350 °C.

Another interesting characteristic of the $NiTiO_3$-based nanocomposites is the relationship occurring between the intensity of the response and the flowrate of the target gas. In all previous experiments, the flowrate has been set constant at 0.4 L/min, in order to keep the experimental setup parameters fixed as much as possible. The results in changing the gas stream flowrate are shown in Figure 3.27: the effect of H_2S on the sample is the same, *i.e.* a reduction in intensity and a broadening of the Au SPR peak, but the amount of this modification is dependent on the flowrate. By reducing the flowrate of the 100 ppm H_2S stream from 0.4 L/min to 0.1 L/min, a decrease of about 4 times in the sensor response is experienced, as clearly shown in the inset of Figure 3.27b, where the OAC negative maximum is found to decrease from $2.9 \cdot 10^{-2}$ to $7.8 \cdot 10^{-3}$. This effect can be ascribed to the fact that with low flowrates, the sample kinetics in adsorbing H_2S molecules, converting them into reaction products, and desorbing these products from the sample surface are faster than the speed of the hydrogen sulfide molecules that approach the sample, leading to an apparent smaller response intensity, that is due to a small ratio between adsorbed and desorbed molecules. When the flowrate is increased, the adsorption speed of H_2S molecules on the surface is increased, together with the ratio between adsorbed and desorbed species, producing a higher optical variation on the SPR band of Au NPs.

Eventually the adsorption and desorption speed will become equal, and at that point a further increase in the flowrate will not affect the optical variation: this theoretical model is supported from the fact that at high flowrates the change in response is very small, as can be noticed in the inset of figure 3.27b, where the plot seems to reach a plateau.

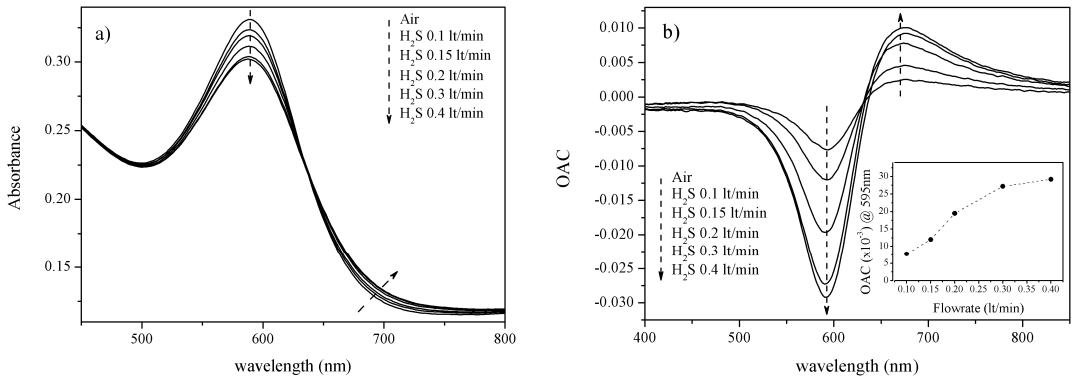

Figure 3.27. a) Absorption spectra of a 50T50N film with Au NPs annealed at 500 °C measured in air and during exposure to 0.01% v/v H_2S at different flowrates and at the operative temperature OT= 350 °C. b) OAC curves calculated from the previous spectra. The inset shows the increase of the negative maximum of OAC curve measured at 595 nm with increasing the flowrate.

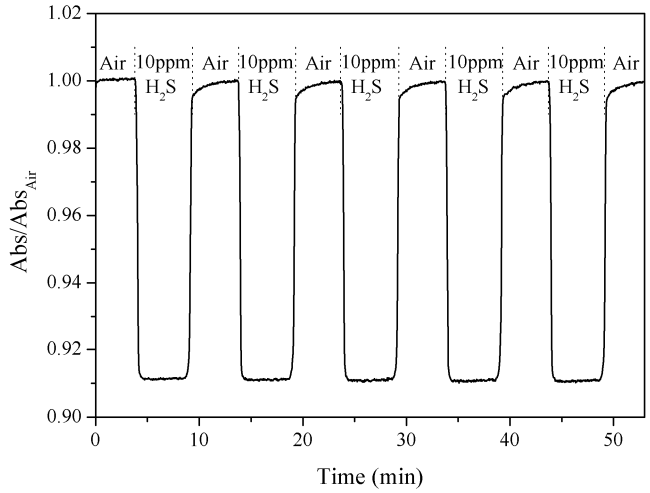

Figure 3.28. Dynamic response at 590 nm of the 50T50N nanocomposite film annealed at 600 °C under exposure to five air-0.001%H_2S-air cycles at 350 °C OT.

The samples have been also tested to multiple cycles air-H_2S-air, showing great signal stability and reproducibility: Figure 3.28 shows the dynamic response of the 50T50N sample collected at 590 nm (negative maximum of OAC curve) when exposed to five cycles air-H_2S-air: the behavior is almost ideal, with a square-like signal characterized by

a great stability during gas flow, an extremely good reversibility and very fast transient times, with response and recovery times being 15 and 30 seconds, respectively.

3.2.6.3 Reaction mechanism

The possible interaction mechanisms between H_2S and the sensor have also been analyzed. It is well known that one of the most common way to remove hydrogen sulfide from waste gases generated in industrial processes and to produce sulfur is the Claus method, a two-step reaction in which hydrogen sulfide is first thermally oxidized to sulfur dioxide (SO_2) and water at high temperature (usually around 1000 °C) and then a catalytic reaction between SO_2 and H_2S takes place at lower temperature (around 300 °C), over some particular catalysts, leading to the formation of water and elemental sulfur [96-98]. The main reason for the development of this two-step process is that the direct oxidation of H_2S to elemental sulfur, although being thermodynamically favored at low temperatures, has very low rate and yield of conversion, while the complete oxidation of H_2S to SO_2 is achievable only at high temperature, due to thermodynamic reasons [99].

It has also been reported that exposing metal oxides (like CuO, SnO_2, WO_3, Cr_2O_3) to H_2S at quite low temperatures (below 400 °C) usually leads to the formation of metal sulfides, that can be then oxidized by treatment in oxygen or air, resulting in the formation of the initial oxide and of gaseous SO_2 [100-102]. The sensing properties of this kind of materials are related to the different electric conductivity of sulfide species compared to the initial oxide: a variation in resistivity is thus generated, which can be easily detected and related to H_2S content. However, it has been demonstrated by a focused surface science study [103] that H_2S absorbed on TiO_2 reacts at temperatures above 300 °C with surface oxygen, and forms SO_2 which easily desorbs from TiO_2. It is noteworthy that a similar temperature range is required for the gas sensing activity of the presently studied nanocomposites. Thence, according to the whole body of these data, it is reasonable to propose that SO_2 is the product of the interaction of H_2S with the present nanocomposite sensor.

A preliminary gas phase reaction product analysis to demonstrate the presence of SO_2 in the exhaust gases of the sensor films in working conditions was performed using Radiello® diffusion samplers [104] positioned inside a sealed chamber provided with gas inlets and outlets, at the exit of the sensing cell containing the sample; for this particular experiment, a 70T30N film containing Au NPs annealed at 500 °C was used, and the operating temperature was 350°C. Sulfur dioxide was clearly detected as a reaction

product, in an amount which increased with exposure time, confirming that the reaction of H_2S with the sensor consumes the target gas.

The formation of SO_2 can be related to two different processes: either catalytic oxidation of H_2S over the Au-TiO_2-NiO nanocomposite, or the rapid formation and decomposition of metal sulfides due to reactions of the oxide matrix with H_2S and O_2, respectively.

Some evidence for the actual mechanism operating in our sensors comes from XPS analysis performed on the 70T30N "frozen" sample, containing Au NPs and annealed at 500 °C. In this data, the S 2p photoemission peak (see Figure 3.29) is centered at 169.5 eV, indicating the presence of highly oxidized SO_x species i.e. SO_2 [105], while no evidence of sulfides has been found. In addition, no changes can be seen prior and after the H_2S dosing from the analysis of the XPS spectra of Au 4f, Ti 2p and Ni 2p, and no modifications in XRD diffraction peaks can be envisaged either. This evidence supports a direct catalytic oxidation of H_2S rather than a metal sulfide mediated transformation. However, concerning the role of Au in such a process, there is no direct evidence for that, except indirectly from the ellipsometric analyses performed on the "frozen" samples which suggests that the optical response is due to a interaction of the gas with the Au NPs. Most probably, XPS does not provide sufficient sensitivity to directly monitor the interaction of H_2S with the few and mostly embedded Au NPs. So the evidences so far suggest that the probable mechanism for the overall process is a first interaction of H_2S with the surface of Au NPs, as can be easily monitored from the modification of the Au SPR peak shape, and then a second step involving the catalytic oxidation of H_2S to SO_x occurs, as confirmed by Radiello® samplers analysis combined to XPS and XRD measurements that show no formation of metal sulfides.

The formation of a shell of Au sulfide around metallic Au NPs has been also excluded because, as known from Mie theory (and its extensions) and also reported in literature [106,107], a shell of a material with high refractive index on Au NPs will produce a red-shift of the Au SPR band, also with a very thin shell, while in our sample no shift can be seen after H_2S interaction. A set of simulations has been performed considering a core-shell structure in which an Au core of radius 10 nm is surrounded by a shell of increasing thickness of Au_2S, inside a host matrix with refractive index of 1.95: due to the lack of experimental data on the dielectric function of Au_2S a nonabsorbing scheme with constant $n = 2.33$ has been assumed as it was done also in the literature [108].

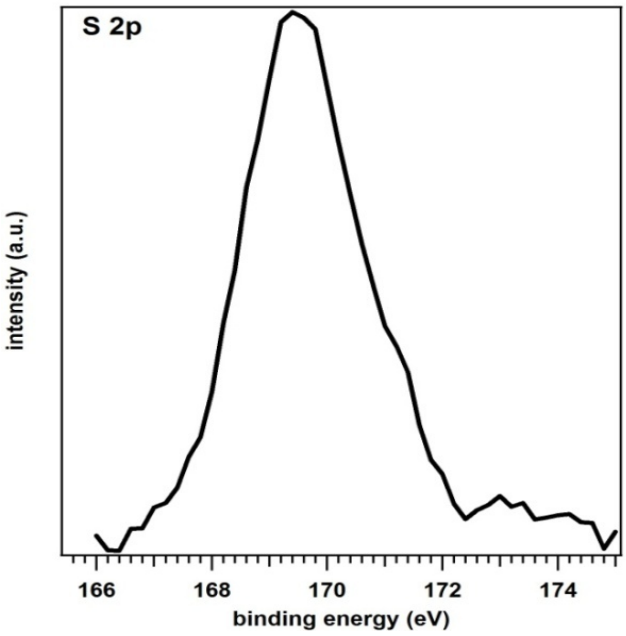

Figure 3.29. XPS S 2p region of the Au doped 70T30N film annealed at 500 °C after the exposure to H_2S.

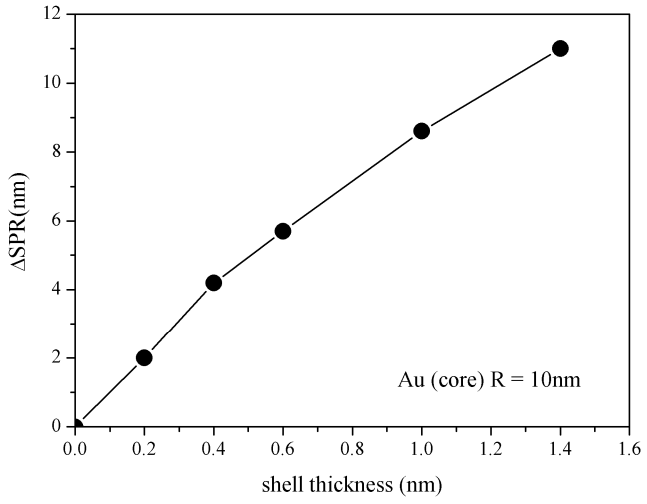

Figure 3.30. Simulation of the Au SPR wavelength shift when spherical Au NPs of 10 nm radius are covered with an Au_2S shell of increasing thickness.

A shift of 2 nm in the SPR position is already detectable with a shell of 0.2 nm, as can be seen from Figure 3.30. Since no such shift has been measured in our samples, we exclude the formation of a shell of sulfide, because in that case we should experience a shift of the SPR peak. Moreover in all the different samples prepared (that have Au SPR at different wavelengths, coming from different refractive indexes of the matrix) there is no shift of the SPR band when exposed to H_2S, as discussed in the previous section, so even in the

very particular case that Au sulfide shell matches exactly the refractive index of the surrounding matrix, this could happen only in one of the samples, so it can be assumed that no change in refractive index around the gold NPs is happening.

Besides, it has also been demonstrated [109] that Au-S bond decomposes in air in the 490-525 K range (217-252 °C): since our experiments have been carried out at 350 °C, no Au sulfide species can exist at that temperature.

The supposed reaction mechanism is an interaction between sulfur atoms and the surface of Au NPs, being the nature of this bond intermediate between a covalent bond and a coordination bond [110] leading to a surface passivation of the metal, depleting Au d-electrons and so reducing the intensity of Au SPR peak.

After these results, a more thorough study to understand the reaction mechanism has been carried out coupling Radiello, XPS and XRD analyses to detect simultaneously the reaction products and possible modification on the material. Samples prepared for this study are summarized in Table 3.7. The composition of the samples was chosen in order to isolate the contribution of Au, $NiTiO_3$ and TiO_2 (both in rutile and anatase phase) in the detection mechanism and in the oxidation of H_2S. To obtain with the same synthetic procedure reported before nanocrystalline rutile thin films, avoiding a very high annealing temperature, a little amount of Nickel precursor (ratio Ni:Ti=9:1) is required: in this way, a small amount of $NiTiO_3$ is supposed to crystallize, but its effect is negligible for the study reported here.

Table 3.7. List of samples prepared for the reaction product analysis study and their nominal composition.

Name	Nominal composition	Au amount (%)	Ni:Ti ratio
S1	$NiTiO_3$	0	1
S2	$NiTiO_3$-Au	5	1
S3	TiO_2-anatase-Au	5	0
S4	TiO_2-rutile-Au	5	0.1

Figure 3.31 shows optical absorption spectra for the samples during air (black lines) and 100ppm H_2S (grey lines) exposure: as can be noticed, Au-free sample (S1) did not give any detectable response, while all samples containing Au show a modified absorption spectrum during H_2S exposure, with the already discussed decrease in Au SPR intensity and broadening of the peak.

According to the previously presented explanation, Au NPs seem to have only a role as optical probes in the detection mechanism, that is they are useful to acquire an optical signal of the presence of H_2S, but they are not directly involved in its decomposition. In fact the same material ($NiTiO_3$) by itself does not show an optical response to H_2S (sample S1), while with Au NPs the signal is easily detectable.

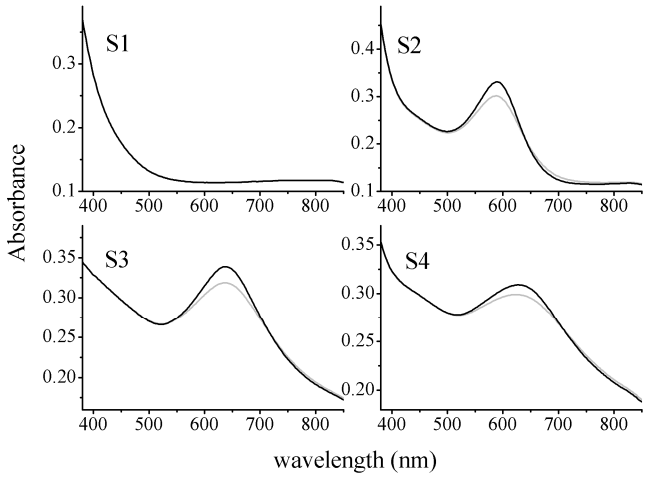

Figure 3.31. Optical absorption spectra for the samples (see Table 3.7) exposed to air (black lines) and to 100 ppm H_2S (grey lines) at 350 °C OT.

Using Radiello® diffusion samplers, the amount of SO_x evolved by the reaction of H_2S with the sensing material was monitored. A set of experiments has been done, exposing the samples to H_2S for different times (1, 2 and 4 hours) at the same flow rate: SO_x were clearly detected as reaction products (see Figure 3.32a), with amount increasing almost linearly with time of exposure (correlation coefficient R^2>0.98 in all cases), indicating a constant H_2S conversion with time.

Once the data have been normalized to each other subtracting the environmental (test cell, tubes, quartz substrate) contribution in SO_x formation, it was found that $NiTiO_3$ is more efficient than TiO_2 in decomposing H_2S, as can be noticed in Figure 3.32b: a similar behavior can be observed in samples S1 and S2, while S3 and S4 provide a much lower amount of H_2S conversion, that can be supposed near zero, since it is comparable to the contribution detected for the SiO_2 substrate used as reference. On the other hand, comparing the data of samples S1 and S2, only a minor role (if any) of Au NPs on the decomposition mechanism is evidenced, since the amount of SO_x is within the error bar in the two cases.

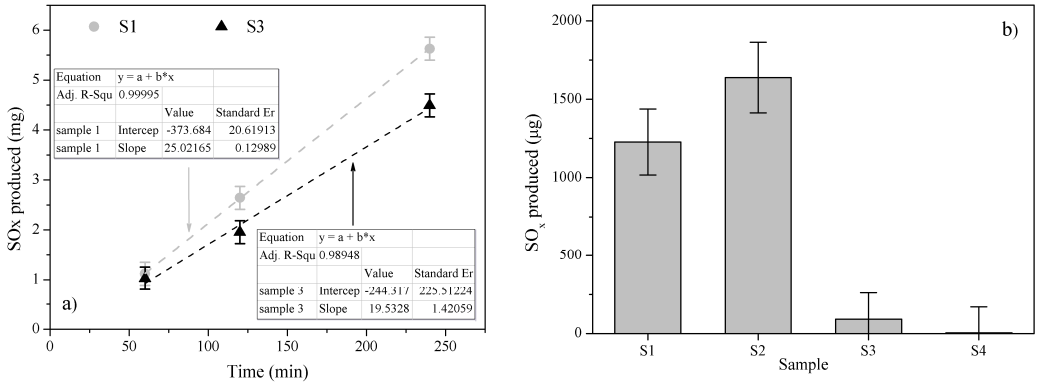

Figure 3.32. a) Absolute amount of SO_x produced by samples S1 and S3 as a function of time. b) Normalized amount of SO_x produced from the samples (see Table 3.7) tested after 4 hours of exposure. Error bars are calculated taking into account the experimental error in the gas flow rate determination.

On the other hand, the XPS data can give indications on the relative quantity of SO_x which remains trapped into the film. The XPS data reported in Figure 3.33 confirm the trend seen in Figure 3.32: the S 2p peak, whose BE is compatible with SO_x species, is more intense in S1 and S2 samples compared with S3 and S4, confirming that a larger concentration of SO_x is left on the surface of the $NiTiO_3$ samples.

Considering the O 1s peak, it can be noticed that all samples show a shoulder at higher BE (at a BE of ca 532-533 eV, to be ascribed to S-O bonds) with respect to the main peak (at ca 530 eV, associated to the oxygen atoms bound to the transition metals). The actual position of the higher BE shoulder depends on the oxide (a shift toward higher BE is observed in the titania samples with respect to the titanate one) and the relative intensity changes are well in tune with the corresponding intensities of the related S 2p peaks.

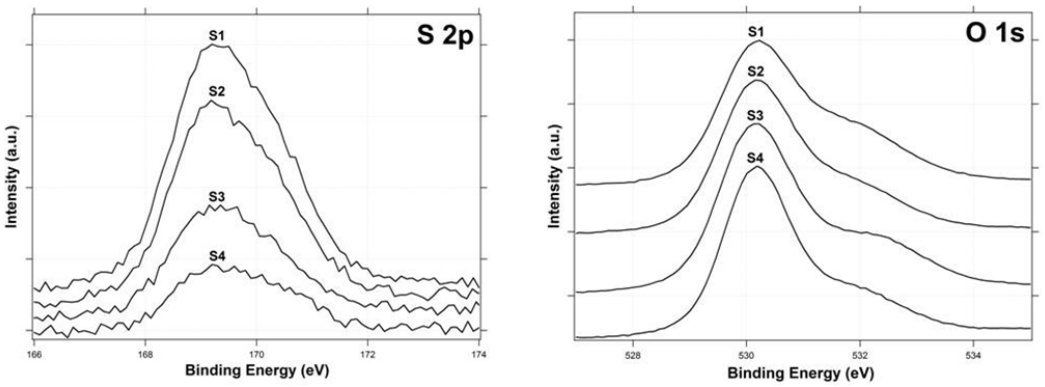

Figure 3.33. S 2p and O 1s XPS data of the samples (see Table 3.7) after 4 hours of exposure.

Comparing the S 2p and O 1s data of samples S1 and S2, it seems that the amount of SO_x trapped into the film surface is slightly higher when the Au NPs are not present. Moreover, looking at the Ti 2p and Ni 2p peaks (not reported herein) of all the examined samples, no relevant change is observed before and after the H_2S reaction, indicating again that no metal sulfide species is formed during the interaction with H_2S, in agreement with the XPS data of the S 2p region; this fact has been also confirmed by XRD patterns collected on "frozen" samples, and the resulting spectra show no difference in peaks intensity or broadening compared to spectra collected before exposing the samples to H_2S, as shown in Figure 3.34. From XRD measurements the nominal composition of the samples has been also verified: in fact according to sample composition, diffraction patterns for $NiTiO_3$, TiO_2-anatase, TiO_2-rutile and Au can be identified. As discussed previously, a small diffraction peak at about 33.2°, corresponding to the most intense $NiTiO_3$ reflection, can be recognized also in S4 sample. From the comparison between pristine and "frozen" samples, no significant changes in diffraction peaks can be envisaged, nor new peaks are detected, consequently excluding samples modification after the reaction with hydrogen sulfide.

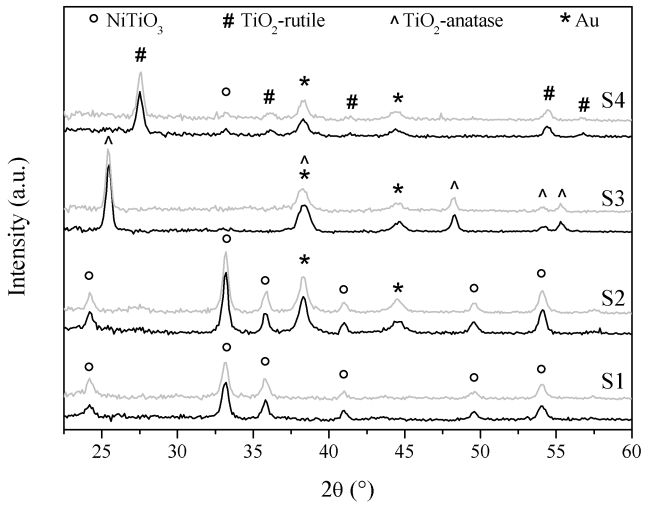

Figure 3.34. XRD patterns of the samples listed in Table 3.7 before (black lines) and after (grey lines) the "freezing" process. Diffraction peaks assigned to all the crystalline phases are also outlined.

An interesting and unexpected behavior of some samples is related to an oscillating response found to occur during the flowing of H_2S, as shown in Figure 3.35. Such a phenomenon occurred without prediction when testing a sample slightly different

compared to the ones presented in this study, a double layer 50T50N sample containing colloidal Au NPs of 10 nm in diameter and annealed at 500 °C, that was prepared in the past. No oscillating response was observed for none of the 500 °C annealed samples synthesized in this study. As can be seen from the dynamic test performed on this sample, there is the usual decrease of absorbance due to hydrogen sulfide effect on Au SPR peak, but after a short induction period a quite regular oscillating response with a well defined period of about 15 seconds takes place, and stops only when air is let flow again inside the test cell. From the dynamic spectrum taken with higher time resolution, the actual shape of these oscillations can be seen: quite sharp positive peaks (corresponding to an increase in absorbance, *i.e.* an increase in intensity of the SPR peak towards the value it shows in air) are separated by an induction time, while no "negative" peaks are seen, the word negative meaning with absorbance value lower than the usual value under H_2S flow. So this behavior resembles more a series of impulse functions, rather than a sinusoidal curve.

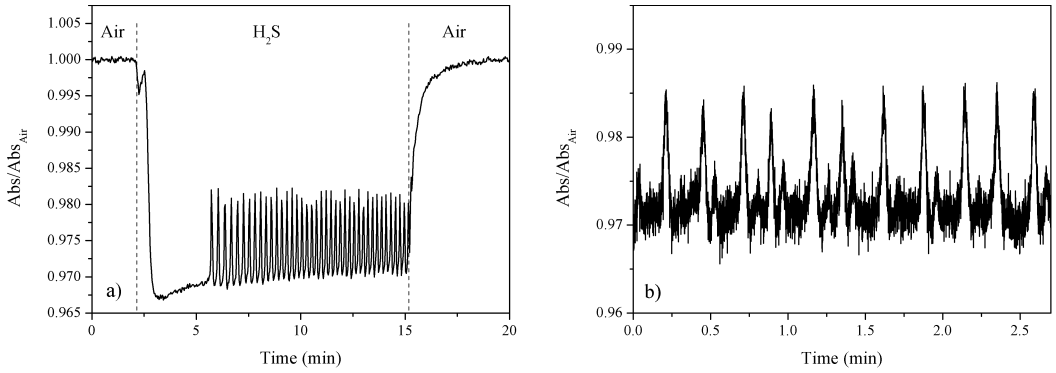

Figure 3.35. a) Dynamic response at 580 nm of a 50T50N nanocomposite film with Au colloidal NPs annealed at 500 °C under exposure to 0.01%H_2S at 350 °C OT, showing the oscillating response. b) Higher time resolution of the oscillating response.

Since this particular samples was prepared in the past, so it remained under ambient conditions for about 2 years, and it was synthesized with different Au NPs and with a double layer, we ascribed the oscillating behavior to one or a combination of these factors. An external effect (like variations in the heating power for example due to lack of communication between the thermocouple and the heater, problems with the detector of the spectrophotometer, an oscillating flux of hydrogen sulfide) is to be excluded because the possible causes of this behavior related to the instrumentation setup have been

carefully checked. Moreover, subsequent attempts to replicate this behavior synthesizing again similar samples starting with Au colloids were unsuccessful.

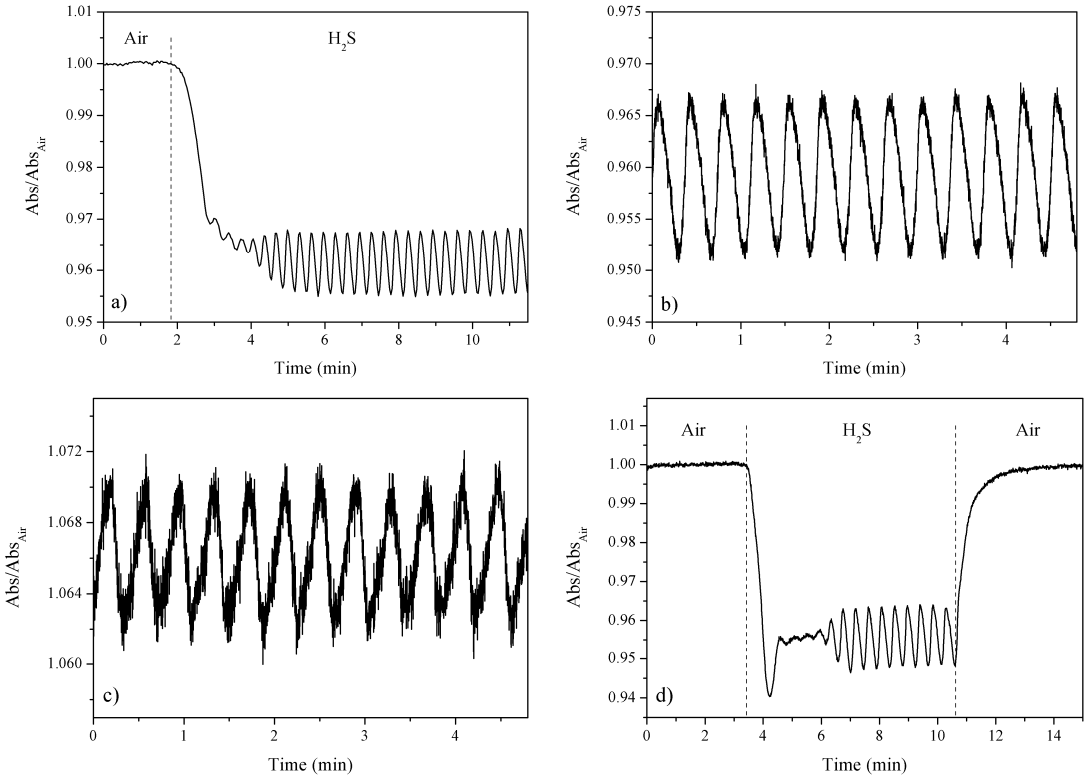

Figure 3.36. a) Dynamic response at 605 nm of a 70T30N nanocomposite film with Au NPs annealed at 600 °C under exposure to 0.001%H_2S at 350 °C OT, showing the oscillating response. b) Higher time resolution of the oscillating response at 605 nm. c) Higher time resolution of the oscillating response at 705 nm. d) Dynamic response of the same sample at 605 nm showing the start and the end of the oscillations.

Unexpectedly, also one of the samples prepared in this study, specifically 70T30N film annealed at 600 °C showed a similar oscillating behavior, as a matter of fact only when tested few months after the preparation, while the same sample tested only few weeks from preparation did not show any anomalous response. It is noteworthy saying that again none of the other samples annealed at 600 °C did show an unusual response neither if tested after several months from preparation. Some examples of the oscillations in response of this sample are shown in Figure 3.36: this time there does not seem to be an induction time, since the oscillations start immediately after the H_2S is let flow inside the test cell; moreover the shape of these oscillations is rather dissimilar to the previous ones: in fact in this sample the behavior resembles a sinusoidal curve, with bottoms and tops alternating over an average “zero” value. From the dynamic spectra taken with higher

time resolution, the great uniformity of the oscillations can be seen: in fact they show an extremely regular oscillation period of 23 seconds, and also the intensity of the tops and bottoms of the fluctuating curve are of the same intensity throughout the whole measure. The oscillations have been found to occur also at different wavelength: indeed, when operating at the wavelength corresponding to OAC negative maximum (for this sample 605 nm, Figure 3.36b), the oscillations are summed to the "usual" H_2S effect, so the overall absorbance is lower than the value in air; on the contrary, when operating at the wavelength corresponding to OAC positive maximum (for this sample 705 nm, Figure 3.36c), the oscillations are still present, but this time the absorbance variation is positive. As in the previous sample the oscillations can be immediately stopped by introducing again air inside the cell (Figure 3.36d).

The fact that the oscillations are summed to the normal hydrogen sulfide effect on Au SPR peak (increase or decrease in absorption according to the wavelength) can be useful to try to explain such a strange behavior: the Au SPR band is found to modify completely after the H_2S introduction, and at a certain point starts to "vibrate", as if the surface of Au NPs is feeling a concentration of H_2S that varies quickly and periodically with time. So it can be that for certain combinations of film thickness, film composition, Au amount, H_2S concentration, when the gas reaches the surface of the sample causes the damping and broadening of the Au SPR peak, but it is rapidly decomposed, leaving a lower concentration of sulfide species at the surface of the sample, causing the increase of absorption experienced when working at OAC negative maximum, and the decrease of absorption when working at OAC positive maximum. But at this point a non-equilibrium situation is created, because the concentration of H_2S at the surface of the sample is lower than the average value inside the cell, so sulfide molecules are drawn towards the sample, causing again the complete modification of the optical properties of the sample, and so on. This push-pull behavior has also been observed in the past for different combinations of gases and catalysts: for example Nakata *et al*. [111] explained the oscillations observed in the conductivity of a SnO_2 sensor when exposed to carbon monoxide analyzing the temperature effect of CO absorption and oxidation on the surface of tin oxide, showing a relationship between the sample temperature and the increase or decrease of conductivity, ascribing these changes to the exothermic oxidation of CO to CO_2 and to the decrease in temperature due to CO absorption on the sample, respectively.

In a different study, Kovalenko *et al*. [112] discovered a relationship between the oscillation in SO_2 concentration produced from the catalytic oxidation of H_2S over a V-

Al-Ti oxide catalyst, and the absorption of sulfur and polysulfides on the surface of the catalyst.

The main problem with the oscillating behavior experienced in the Au-loaded Ti-Ni oxide thin films described in this chapter is their reproducibility: unfortunately the parameters responsible for this unusual response are still to be isolated, and so a sample prepared on purpose presenting the oscillating response has not been successfully prepared yet.

3.3 Ag and NiO nanoparticles inside SiO_2 mesoporous thin films

3.3.1 Synthesis

3.3.1.1 SiO_2-NiO matrix

SiO_2-NiO thin films having molar composition 70%SiO_2-30%NiO and 60%SiO_2-40%NiO have been synthesized with the sol gel method: first, Tetraethoxy Silane (TEOS) was let hydrolyze in a mixture of Ethanol (EtOH), hydrochloric acid (HCl) and water (molar ratios TEOS:H_2O:EtOH:HCl = 1:4:4:0.003) for 1 hour at 25°C; then a solution of Pluronic F127 in a mixture of EtOH, H_2O and HCl (molar ratios EtOH:H_2O:HCl = 8:1:0.003) was slowly added to the prehydrolized TEOS solution under stirring and let stir an additional hour at room temperature. The molar ratio F127:TEOS was set equal to 0.01 or 0.005, giving samples with higher or lower porosity after heat treatment, respectively. The total solution was then refluxed at 70 °C for 2 hours to complete the hydrolysis process of TEOS, and then cooled down to room temperature. In a separate vessel, a proper amount of nickel chloride hexahydrate ($NiCl_2 \cdot 6H_2O$) was dissolved in ethanol, and subsequently a complexing agent (N[3(trimethoxysilyl)propyl]-ethylenediammine, DAEPTMS) was added, keeping the molar ratio Ni/DAEPTMS = 1 for 70%SiO_2-30%NiO samples, or 0.7 for 60%SiO_2-40%NiO samples; the Ni content was calculated in order to achieve Si:Ni=7:3 or 6:4 molar ratios, taking into account also the Si coming from DAEPTMS. The Ni solution was then added to the silica solution giving a SiO_2+NiO content of 75g/l based on nominal silicon oxide and nickel oxide molar weights, and the final solution was let stir for additional 60 minutes before deposition.

In a typical synthesis for 70%SiO_2-30%NiO sample with high content of Pluronic, 1.57 mL EtOH, 1.5 mL TEOS, 0.485 mL H_2O, 0.02mL HCl 1N are mixed in this order under stirring. Separately, 847 mg F127 are dissolved in 3.13 mL EtOH, 0.12 mL H_2O and 0.02 mL HCl 1N, and added dropwise to the previously prepared solution. The Nickel solution

was prepared dissolving 1.19 g $NiCl_2 \cdot 6H_2O$ in 6.52 mL EtOH, and subsequently adding 1.09 mL DAEPTMS under stirring. The two solutions were then mixed and the resulting solution was used to deposit the films.

Thin films were deposited by spin coating on either Si and SiO_2 substrates at 2500 rpm for 40 seconds under a controlled atmosphere (RH<25%) in order to prevent rapid condensation of the sol-gel matrix; the films were dried at 70 °C for 5 minutes on a hot plate and then fired at 500 °C for 30 minutes. Progressive treatments up to 800 °C with 30 minutes annealing every 100 °C step were performed to study crystallization and densification processes. Thicknesses after the 800 °C annealing are all in the 500-700 nm range, as measured with spectroscopic ellipsometry.

The ratios between SiO_2 and NiO and between Pluronic and TEOS, together with the name used to label the different samples analyzed in this study, are summarized in Table 3.8.

Table 3.8. List of the different sample series prepared.

Sample series	SiO_2/NiO ratio	F127/TEOS ratio
73L	70/30	Low (=0.005)
73H	70/30	High (=0.01)
64L	60/40	Low (=0.005)
64H	60/40	High (=0.01)

3.3.1.2 Ag impregnation

After the 800 °C annealing step, samples pores were functionalized with two different molecules capable to anchor Ag ions: aminopropyltrimethoxysilane (APS) or mercaptopropyltrimethoxysilane (MPS). Before functionalization, the surface of the pores has been hydroxylated by dipping the mesoporous film for few seconds in a hot (60 °C) basic piranha solution (H_2O_2:NH_3:H_2O = 3:1:5); X-ray diffraction (XRD) and contact angle measurements before and after this treatment confirmed the higher wettability of the treated samples, and the absence of structural modification due to the basic etching. Functionalization of the activated samples was performed preparing hot (60 °C) toluene solutions of APS and MPS (5%) and dipping the samples for 5 minutes: after the functionalization process, samples were washed with fresh toluene and dried in a nitrogen stream.

Ag ions impregnation was performed preparing an aqueous solution of silver nitrate (0.1M) and dipping the functionalized samples for 4 hours in dark; the samples were then washed with acetone to remove surface unbonded ions and dried in air. Impregnated samples were annealed at 700°C in air to precipitate metallic Ag nanoparticles.

3.3.2 Characterization

3.3.2.1 SiO_2-NiO matrix

A high temperature annealing treatment is necessary to burn the organic, stabilize the silica matrix and promote the crystallization of NiO: up to 700 °C samples remain amorphous, while after 800 °C treatment all samples present cubic NiO diffraction peaks at about 37.2° and 43.3° (JCPDS No. 71–0652), as reported in Figure 3.37.

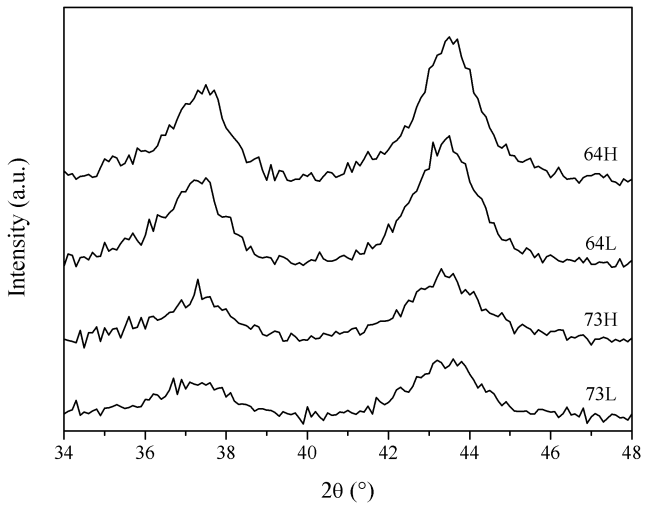

Figure 3.37. XRD patterns of the four SiO_2-NiO samples annealed at 800 °C showing cubic NiO peaks.

As expected, samples containing 40% NiO show peaks with higher intensity compared to samples containing 30% NiO, and also crystals size calculated with the Scherrer's equation is slightly smaller in 70%SiO_2-30%NiO samples (between 5 and 6 nm) compared to 60%SiO_2-40%NiO samples (between 6 and 7 nm).

Optical characterization performed with UV-Vis and FTIR spectroscopy, coupled to ellipsometric measurements provides a useful tool to investigate the oxide matrix evolution according to the annealing temperature. In Figure 3.38a the optical absorption spectra of the 64L sample at different annealing temperature is reported: a slight increase in UV absorption onset can be detected increasing heat treatment from 500 °C to 700 °C,

related to amorphous NiO absorption, while in the visible range the sample remains substantially transparent. At 800 °C a sharper and more intense absorption edge around 350 nm appear, due to the crystallization of NiO [113,114], that causes also a tail of absorption in the visible range: as a matter of fact samples annealed at 800 °C present a light grey-yellow color, while samples treated at lower temperature are optically transparent. Similar behavior are observed for all the 4 compositions studied.

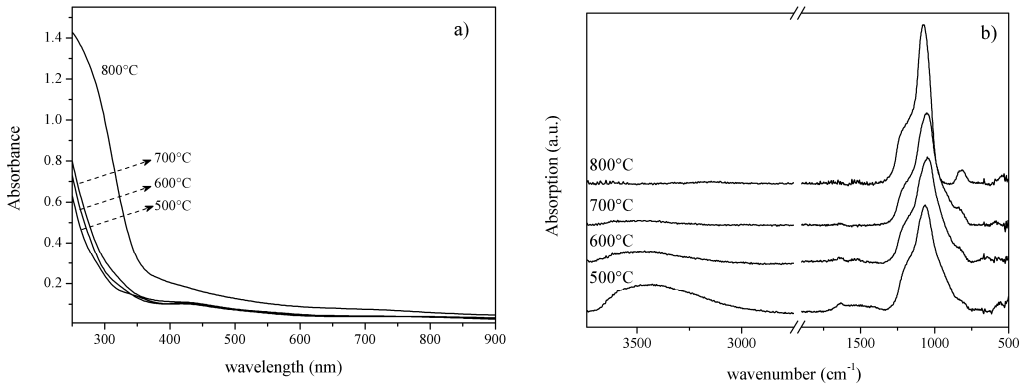

Figure 3.38. a) UV-Vis absorption spectra of 64L sample annealed at different temperatures. b) FTIR spectra of 64L sample, showing the decrease of water and silanol presence and the increase of Si-O-Si bonds with annealing temperature.

Figure 3.38b presents IR spectra collected for the same sample at the 4 annealing temperatures. The broad band between 3800 and 2800 cm^{-1} is related to the overlap of O-H vibrational modes with the organic modes from PEO and PPO groups of Pluronic F-127 molecules. The part at higher wavenumbers is due to OH groups and the shape is strongly dependent on the characteristics of the film and on its thermal treatment: it is composed of several overlapped bands assigned to different types of hydroxyl vibrations. In particular, three overlapped vibrational modes at ~3743, ~3676, and ~3635 cm^{-1} are discerned as explained by Chen and co-workers [115]. On the basis of the literature, the bands are assigned respectively to: free single silanol groups; pairs of silanols mutually hydrogen-bonded in linear configuration where only oxygen atoms form H-bonds with a hydrogen atom of an adjacent silanol; pairs of silanols mutually hydrogen-bonded in a linear configuration, where hydrogen atoms form H-bonds with an oxygen atom of an adjacent silanol. A component of that band at ~3250 cm^{-1}, as well as the single peak at 1640 cm^{-1}, are due to adsorbed water. The part at lower wavenumber at ~2950 cm^{-1} is related to C-H modes (from terminal methyl and chain methylene groups that exhibit

symmetrical and antisymmetrical stretching modes [116-118]. All these bands are not detectable after the thermal calcinations at 800 °C, indicating that the surfactant is completely burned during the thermal treatment.

The band at ~1078 cm^{-1} is related to the TO_3 mode of Si-O-Si chain: its position is strongly dependent on the polycondensation of silica and moves to high wavenumbers for higher thermal treatment [119]. The band at ~810 cm^{-1} is related to the TO_2 mode of Si-O-Si chain [120] and it becomes more resolved and intense for higher annealing temperature. The broad shoulder around 1200 cm^{-1}, is attributed in the literature to a broadened signature of the longitudinal optical (LO) component of the transverse optical (TO) antisymmetric stretching, or to a mixed LO-TO mode with a dominant LO character of the Si-O-Si chain [120]. The vibrational mode at 950 cm^{-1} is assigned to Si-OH stretching: this band decreases in intensity with the increase of the firing temperatures.

Similar IR spectra are obtained for all the prepared compositions, suggesting that the different amounts of Ni and Pluronic do not change significantly the thermal evolution of the silica structure.

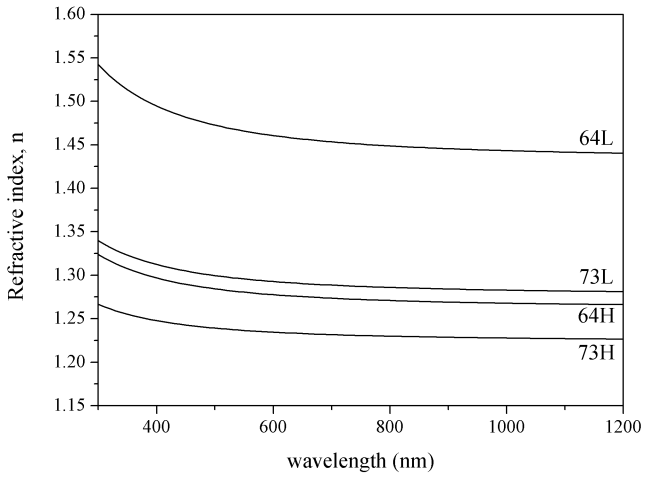

Figure 3.39. Refractive index dispersion curves for the samples annealed at 800 °C.

Figure 3.39 shows the refractive index (n) dispersion curves evaluated from experimental Ψ and Δ data using a non absorbing 3-parameter Cauchy dispersion in the 500-1200 nm region and an absorption model in the 300-500nm region, to better fit the UV edge of NiO nanocrystals. As can be seen from Figure 3a, all the n values are well below the theoretical values expected from a dense sample of the same composition. In fact, using a simple linear combination and considering n=1.46 for SiO_2 [121] and n=2.3 for NiO [87] in the visible range, the theoretical refractive index n for 70%SiO_2-30%NiO and

60%SiO_2-40%NiO (that correspond to 85%SiO_2-15%NiO and 78%SiO_2-22%NiO by volume, respectively) should be around 1.59 and 1.65, respectively.
Moreover, samples obtained from solutions with high F127 content show a lower refractive index compared to samples with the same composition but with lower amount of organic template, confirming the role of Pluronic as porogen agent.

3.3.2.2 Ag impregnation

The strategy of first synthesizing the oxide matrix and then performing the impregnation process was chosen to overcome some limitations of the sol-gel technique, like the need of mixing all the different precursors solutions, controlling the stability of the total solution, its pH, the compatibilization of all the chemicals used (metal salts, solvents, complexing agents). The impregnation of Ag ions was performed as described in section 3.3.1.2: the samples annealed at 800 °C were first immersed for few seconds in hot basic piranha solution to create dangling –OH groups on the surface and inside the pores of the films, permitting the anchorage of silanol groups coming from APS and MPS. A droplet of water was deposited on the sample before and after the basic treatment, and an evident decrease in contact angle has been observed, confirming the formation of polar groups on the surface. The functionalization process was carried out in toluene because, being not soluble with water, it prevents uncontrolled reaction of silanol groups with each other, and let APS and MPS siloxanic groups react with –OH groups coming from the surface of the film, exposing amino or mercapto groups to the surrounding environment, respectively. APS and MPS concentrations ranging from 1 to 10% wt in toluene were used, and the optimum concentration for both molecules was found to be 5%, high enough to create a lot of functional groups on the film surface, but not so high to generate undesired side reactions like condensation between each other. Again, a droplet of water deposited on the functionalized samples shows a bigger contact angle comparing to the piranha-treated sample, confirming the functionalization process.
All sample compositions were functionalized with APS or MPS and then they were immersed in aqueous silver nitrate solutions (0.05 to 0.2M) for 1 to 24 hours in dark: the optimal parameters were found to be 0.1M and 4 hours. Longer impregnation time and/or higher silver ions concentration did not lead to an appreciable increase in the concentration of the embedded Ag NPs, while performing the impregnation procedure with more diluted solutions or for shorter times causes a lower amount of Ag ions dispersed inside the oxide matrix.

Although it is known from the literature that amines can create complexes with silver ions [122], we experienced a poor Ag bonding in APS functionalized films, maybe due to high idrophobic properties of the amino-functionalized surfaces. On the contrary samples containing MPS, although showing idrophobic properties too, had a great capability to anchor silver ions, maybe due to the high strength and stability of silver thiolate bond [110, 122], or to the fact that APS may not organize properly on the oxide film surface, due to the well-known capability of amines to complex also nickel ions [123]: the APS amino groups may react preferentially with the Nickel atoms, exposing silanol and not amine terminations to the upcoming silver ions.

Impregnated silver ions were reduced to metallic NPs by high temperature annealing in air: impregnated samples were put in a preheated muffle furnace at 700 °C for 1 hour, and in a time scale of seconds they become dark-yellow colored, confirming the formation of Ag NPs. The reductions of noble metal ions like Ag and Au inside sol-gel oxide films due to thermal annealing has been widely investigated [124-127]: organic compounds present inside the sol-gel film (in our case, APS and MPS) are oxidized by the thermal annealing process and so they are able to donate electrons to metal ions dispersed inside the matrix, promoting metallic NPs formation [128].

From this study, the optimal parameters for the impregnation process have been isolated and they are summarized in Table 3.9; the results reported from now on refer to samples impregnated with that set of experimental parameters.

Table 3.9. Optimized parameters for the overall impregnation process.

	Basic Piranha	Functionalization	Impregnation
Composition	H_2O_2:NH_3:H_2O = 3:1:5	5% MPS in toluene	0.1M $AgNO_3$ in water
Temperature	60 °C	60 °C	25 °C
Time	5 seconds	5 minutes	4 hours

In Figure 3.40 XRD patterns for the 4 impregnated samples are reported: all samples show Ag diffraction peaks (JCPDS No. 04-0783) in addition to the previously observed NiO peaks, confirming the formation of metallic silver particles. The average Ag NPs dimension has been evaluated from XRD data by the Scherrer equation fitting the two most intense diffraction peaks, giving a mean diameter of about 30 nm for all samples, as shown in Table 3.10.

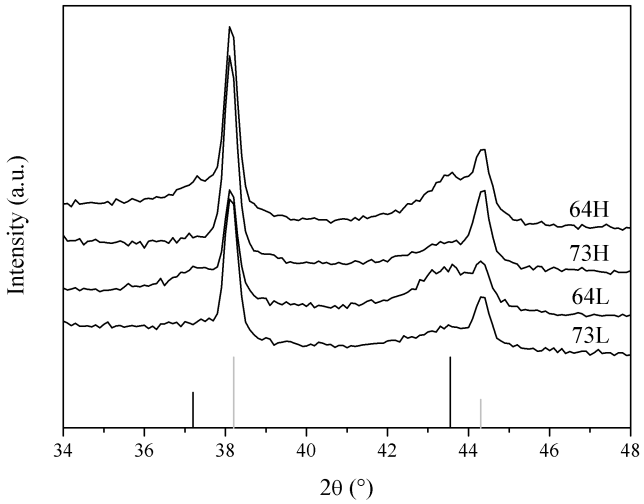

Figure 3.40. XRD patterns of the 4 impregnated samples. Theoretical peaks position for NiO (black lines) and Ag (grey lines) are reported at the bottom.

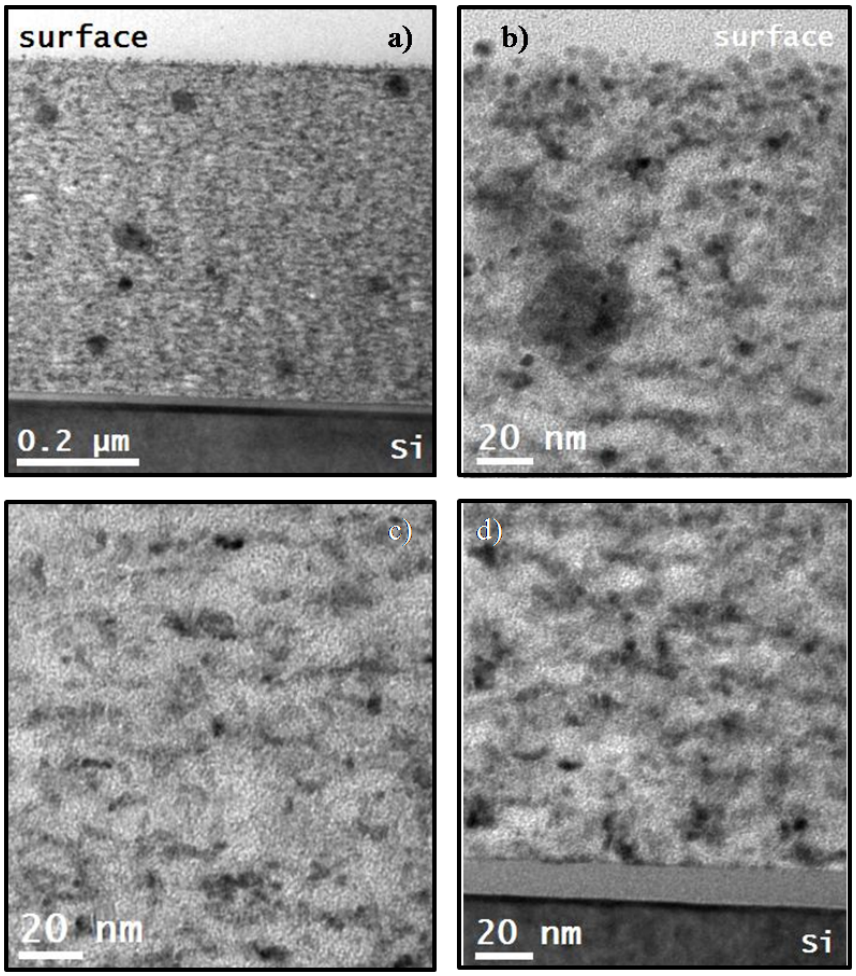

Figure 3.41. Cross sectional HR-TEM image of 73H film after the impregnation process at low magnification (a) and at high magnification near the surface (b), in the middle of the film (c) and near the bottom (d).

Comparing the intensity of Ag diffraction peaks, especially the most intense one at 38.1°, it can be noticed that in samples with lower amount of organic template (73L and 64L) the peaks are less intense, suggesting a lower amount of crystallized silver: considering that the amount of porosity is related to Pluronic presence, it is reasonable to suppose that samples with lower porosity underwent a lower degree of impregnation, while samples with higher porosity were able to anchor a higher amount of silver ions.

Table 3.10. Average crystallites size evaluated from XRD peaks through the Scherrer equation.

Sample	Diameter (nm)	
	NiO	Ag
73L	5.5	33
73H	6	32.2
64L	6.3	31.6
64H	6.8	31.7

Cross sectional HR-TEM analysis on 73H sample was performed to get a better understanding on the structure of the matrix and on the dispersion of Ag NPs, and the results are reported in Figure 3.41 and Figure 3.42. As can be seen the film thickness is around 550 nm, in good agreement with the thickness evaluated by ellipsometry. Quite polydisperse spherical or slightly elongated Ag NPs are clearly identified as darker spots: their polydispersity comes from the poor control over nucleation and growth, since silver is introduced inside the matrix as ions and it is reduced through high temperature annealing. Nevertheless, Ag NPs are homogeneously and statistically dispersed inside the oxide matrix, even if a higher amount of small Ag particles can be detected on the very surface of the sample, maybe due to the high density of thiol groups on the surface of the films than can anchor a lot of Ag ions. The great majority of Ag NPs has a size ranging between 5 and 10 nm, but much bigger particles around 40-50 nm are also detected. Porosity can as well be evaluated from TEM images, analyzing low contrast areas: a great amount of residual porosity (lighter regions) is detected, as also obtained from ellipsometry measurements, with pores sizes estimated between 2 nm and 10 nm, so in the mesoporous range. This estimation is in good agreement with the size of the majority of Ag NPs, that growing inside the matrix pores, acquire their size. The presence of bigger Ag NPs can be ascribed both to areas with bigger pores and to the sintering of

small particles nuclei that diffuse through the pores of the oxide matrix and force it to adapt around the forming metal particle: to assess them, it must be considered that the thermal treatment needed for the reduction of Ag ions is carried out at 700 °C, so the SiO_2-NiO matrix might be softened at that temperature.

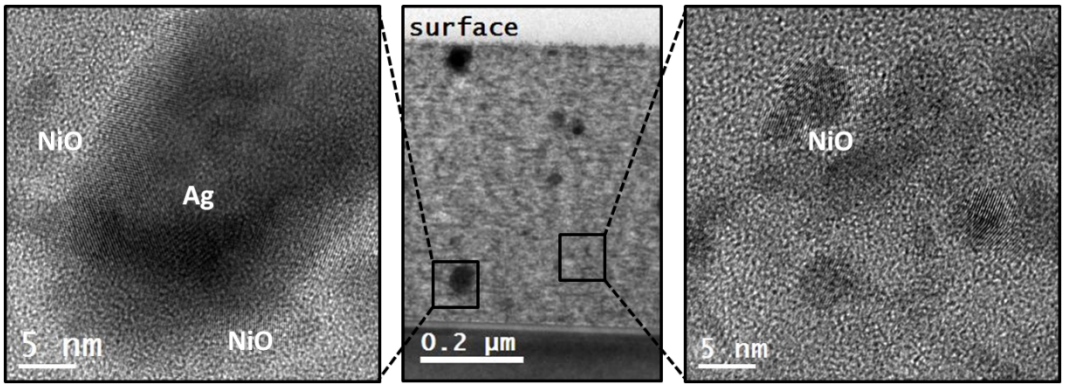

Figure 3.42. Cross sectional HR-TEM image of 73H film after the impregnation process. Different parts of the film corresponding to Ag and NiO crystals are highlighted at the bottom.

Table 3.11. Chemical composition (atomic) of the 73H sample after the impregnation process calculated according to nominal composition and evaluated with TEM-EDX.

Element	Atomic %	
	Nominal	Experimental
O	63	60
Si	26	29
Ni	11	11

Moreover, FFT analysis on selected areas confirms the crystallinity of both Ag and NiO NPs, as highlighted in Figure 3.42; in the end EDX spectroscopy analysis has verified the sample composition, as shown in Table 3.11, and also has given an atomic ratio Ag/Ni=0.1.

Another confirmation of silver NPs formation comes from optical absorption spectra of impregnated samples, reported in Figure 3.43. Ag localized SPR peak is evident in all the samples. Films prepared from solutions with higher content of Pluronic (right side of the Figure) show a more intense SPR peak that can be ascribed to the higher content of Ag due to both the higher thickness and the increased porosity after organic template removal. The peak is quite broad and it is centered around 430 nm, slightly red-shifted

compared to the estimated value for silver NPs of the same size in SiO_2 (around 410 nm [125]). Nevertheless, considering the high amount of NiO inside the films and its refractive index, a higher shift should be experienced: an explanation of that comes from the higher amount of porosity that lowers the overall refractive index, balancing the index increase due to NiO presence. So Ag NPs are faced to NiO particles but also to a highly porous silica matrix, and the sum of these two contributions generates a peak only few nanometer shifted compared to theoretical value for Ag in SiO_2.

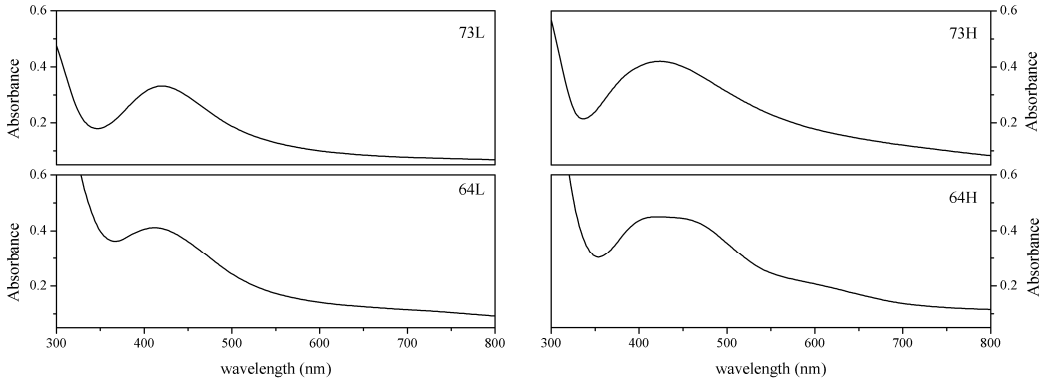

Figure 3.43. UV-Vis absorption spectra for the four impregnated samples showing the difference between low and high Pluronic content in the starting solution.

3.3.3 Gas sensing tests

Gas sensing tests are here presented as one of the possible applications of these nanocomposites since previous studies on Au-doped SiO_2-NiO films show good properties of this material as optical CO and H_2 sensor[59,129]. Films were exposed to H_2 and CO (both 0.1 and 1% v/v in dry air) at 300 °C operative temperature (OT): Figure 3.44a shows absorption spectra of 73H sample exposed to air (black line), to 1% CO (light grey line) and 1% H_2 (dark grey line). There is a strong variation in absorbance during exposure to hydrogen, while it is smaller during CO exposure, as can be seen from the OAC curves for the two gases reported Figure 3.44b. The response is wavelength dependent for both gases, about five times higher for H_2 with respect to CO at 400 nm. The optical variation is more intense in the Ag SPR wavelength range (350-500 nm), while for higher wavelength the response is quite small. This behavior has been observed in the past for Au-doped transition metal oxides [62, 130].

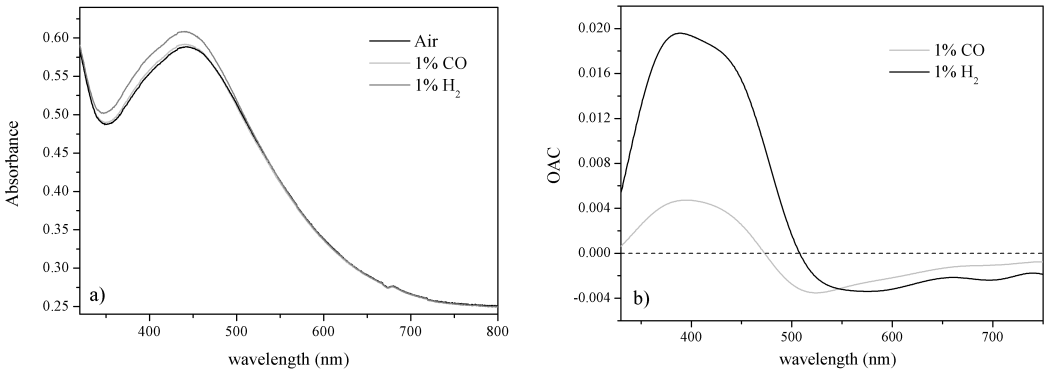

Figure 3.44. a) Absorption spectra of 73H sample measured during exposure to air (black line), to 1% CO (light grey line) and 1% H_2 (dark grey line) at 300 °C OT. b) OAC curves for 1% CO (grey line) and 1% H_2 (black line) exposure at 300 °C OT.

Both gases cause a blue-shift of the Ag plasmon resonance peak, consistent with injection of electrons inside the metal NPs as described by the Mie theory [64], and also generate an increase in the intensity of the peak: this can be ascribed to some partially oxidized silver species present inside the oxide film, as observed in the past for Ag-doped SiO_2 sol-gel films [131,132], that can be easily reduced completely to neutral metallic atoms, so enhancing the surface plasmon resonance absorption peak. Moreover, as anticipated before, hydrogen exposure causes a higher optical variation for both the previously described effects: this can be attributed to the higher reducing strength of H_2 [133] compared to CO [134]. Outside the Ag SPR region the absorbance of the films decreases when exposed to the target gas, as expected from the interaction between reducing gases and p-type semiconductors like NiO [92,135].

A comparison with previously reported results on Au-doped SiO_2-NiO thin films prepared by our group has been done. A 70%SiO_2-30%NiO film containing Au NPs of about 250 nm thickness (but deposited via the dip coating technique on both sides of the SiO_2 substrate, and so with a total thickness of the active material of about 500 nm, comparable with the 73H sample) and annealed at 700 °C showed maximum OAC values of 0.011 and 0.076 for 1% CO and 1% H_2, respectively [129], while the maximum OAC values for the 73H sample prepared in this study are 0.0045 and 0.0198 for 1% CO and 1% H_2, respectively (see Figure 3.44b). The response values of the Au-doped sample is higher but in that particular sample Au concentration was 2%, so double the Ag concentration of the 73H sample: considering that the optical response is directly related to the intensity of the surface plasmon resonance of the metal NPs [62], it can be stated

that the sensitivity of the two systems is of the same order of magnitude, so Ag NPs can be a valuable substitute of Au NPs inside porous SiO_2-NiO matrixes.

Time resolved spectra collected at 400 nm of the same sample are reported in Figure 3.45a, showing as expected a higher response for hydrogen compared to CO and an acceptable dynamic behavior, with a quite fast response time (around 40 seconds) even if the recovery is little longer, as it happens within few minutes.

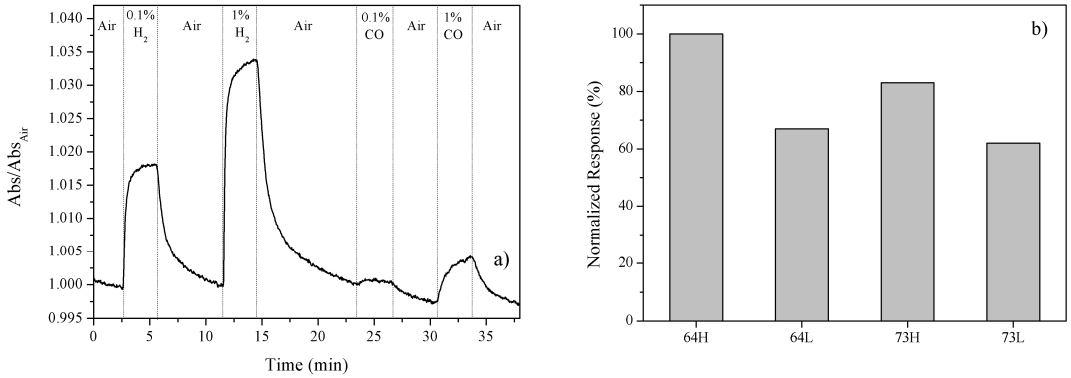

Figure 3.45. a) Dynamic absorption change of 73H sample exposed to different concentration of CO and H_2. Test performed at 400 nm and 300 °C OT. b) Normalized response intensity plot for 1% H_2 detection for the four samples: the response intensity has been evaluated considering the absolute integral of OAC curve for each sample at 300 °C OT, normalized to the thickness of the film.

As reported recently for an amperometric glucose sensor [66], when Ag and NiO nanocrystals are coupled in the sensing electrode, a synergistic effect seems to occur, with the sensitivity and selectivity strongly enhanced compared to NiO or Ag electrodes. In this view, it is interesting to compare the sensitivity of the different samples, to analyze the influence of NiO and Ag presence: since the reducing gases effect on sample absorbance is different and since NiO and Ag play a different role in changing the optical absorption during gas interaction – as explained before, outside Ag SPR wavelength range the absorbance is decreased due to p-type NiO, while inside the Ag SPR range the absorbance is increased – the parameter chosen to compare the response intensity of different sample is the absolute integral of the OAC curves. Figure 3.45b shows the response intensity for hydrogen exposure for the 4 impregnated samples, normalized to the respective thickness; the highest response value has then been set to 100%. It is evident that samples prepared from solutions with high Pluronic amount (samples with higher porosity and then higher Ag amount) show a greater response to H_2; besides, also a

role of NiO can be identified, since keeping Pluronic amount constant, the higher the NiO amount, the higher the response.

3.4 Au nanoparticles inside ZnO-NiO sol-gel thin films

3.4.1 Synthesis

ZnO and ZnO-NiO thin films doped with Au NPs have been prepared by standard sol-gel technique. First, two 0.5M ethanolic solutions of Zinc Acetate dihydrate and Nickel Chloride hexahydrate were prepared; then monoethanolamine was added dropwise under fast stirring to both solutions, keeping the ratio between the metal ion and the amine equal to 1. After 45 minutes stirring, the two solutions were mixed together according to the desired Zn:Ni molar ratio (7:3, 8:2, 9:1 or 1:0) and letting it stir a further 10 minutes. Eventually, a 0.2M tetrachloroauric ethanolic solution was added, keeping the ratio Au:(Zn+Ni)=0.05; for comparison purposes, Au-free samples were also prepared, by substituting the gold precursor solution with the same amount of ethanol. After an additional 5 minutes stirring, the solutions were deposited by spin-coating at 2500rpm for 30 seconds on SiO_2 substrates. Thin films were thermally stabilized in air at 400 °C for 10 minutes and then the spinning/stabilization procedure was repeated another 4 times. A final annealing at 500 °C for 1 hour in air was performed.

3.4.2 Characterization

When dissolving Zinc Acetate in the presence of water, it is partially hydrolyzed and the rest is ionized. The extent of hydrolysis depends upon the water available. The hydrolysis of zinc acetate results in the formation of the basic zinc acetate $Zn(OH)(CH_3COO)$, as shown in the following:

$$\begin{gathered} 2Zn(CH_3COO)_2 + H_2O \rightarrow \\ Zn(OH)(CH_3COO) + CH_3COOH + Zn^{2+} + 2CH_3COO^- \end{gathered} \tag{3.2}$$

Zinc acetate is not easily soluble in alcoholic solvents, so ethanolamine was added to help the dissolution process. The amine can react directly with basic zinc acetate species promoting the hydrolysis according to [136]:

$$Zn(OH)(CH_3COO) + HOCH_2CH_2NH_2 \rightarrow Zn(OH)OCH_2CH_2NH + CH_3COOH \quad (3.3)$$

or the amine can be initially ionized in the presence of water and then the effect of hydrolysis of zinc acetate or basic zinc acetate becomes more pronounced [137] as illustrated below:

$$HOCH_2CH_2NH_2 + H_2O \rightarrow HOCH_2CH_2NH_2^+ + OH^- \quad (3.4)$$

$$Zn(CH_3COO)_2 + OH^- \rightarrow Zn(OH)(CH_3COO) + CH_3COO^- \quad (3.5)$$

$$Zn(OH)(CH_3COO) + OH^- \rightarrow Zn(OH)_2 + CH_3COO^- \quad (3.6)$$

So, three nucleophilic species (ethanolamine, hydroxyl ions OH^- and acetate ions CH_3COO^-) compete for the Zn^{2+} Lewis acid center: attack of an OH^- group leads to the formation of zinc–oxo-acetate oligomers, which are expected to be formed from gradual forced hydrolysis of Zn–amine or Zn–acetate soluble complexes during aging [138].
Eventually the formation of Zinc oxide occur through progressive polycondensation processes of these oligomers, leading to the formation of water or acetic acid, according to the following reactions:

$$HO\text{-}Zn\text{-}OH + HO\text{-}Zn\text{-}OH \rightarrow HO\text{-}Zn\text{-}O\text{-}Zn\text{-}OH + H_2O \quad (3.7)$$

$$Zn(OH)(CH_3COO) + HO\text{-}Zn\text{-}OH \rightarrow HO\text{-}Zn\text{-}O\text{-}Zn\text{-}OH + CH_3COOH \quad (3.8)$$

Zinc oxide films obtained from alcoholic solutions of zinc acetate with ethanolamine as a complexing agent are known to crystallize with orientated grains along the *c*-axis. Various explanations of the orientation mechanism have been presented: Bao *et al.* explained the *c*-axis orientation as the result of the minimization of the internal stresses and the surface energy [139], while Almiraghi and coworkers presented a model in which the orientation is related to the highest atomic density along the (002) plane that facilitate the grain growth along that direction [140]; Oral *et al.* suggested that an heterogeneous nucleation (from amorphous to crystalline) occurring at the film-substrate interface might induce orientation along the *c*-axis direction [141]: it is actually widely accepted that interaction with the substrate plays an important role in nucleation and in the first growth stage [142], even if for amorphous glass substrates, no epitaxial growth is expected [143]. On the other hand, it is well known that in the growth of thick films, the stronger

interaction occurs between the growing particles and not between particles and substrate; in these conditions the growth processes, rather than nucleation ones, can control the orientation [144]. This has been clearly demonstrated in sputtered ZnO, where random nucleation is followed by ordered growth of dense films [145]. According to all these different explanations, a clear understanding of the orientation process has not been achieved yet.

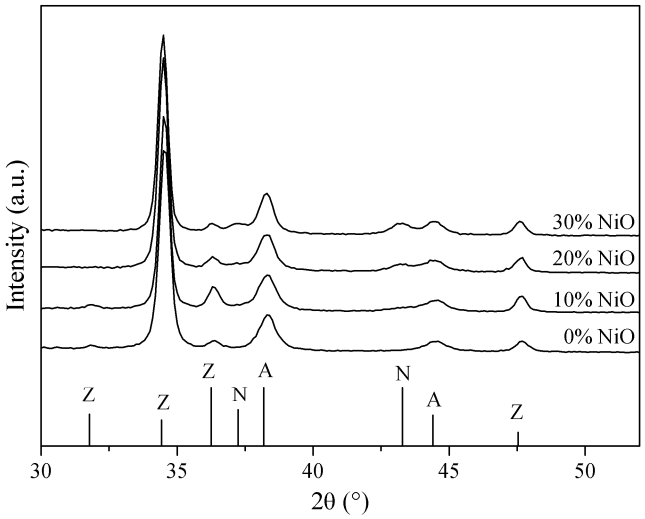

Figure 3.46. XRD patterns of ZnO-NiO-Au films with the NiO amount increasing from 0% to 30%, annealed at 500 °C. Theoretical diffraction lines for ZnO (Z), NiO (N) and Au (A) are reported at the bottom.

Figure 3.46 shows the XRD patterns of the samples containing 5% molar Au with different NiO amounts after the final annealing at 500 °C: theoretical diffraction peaks for ZnO (JCPDS No. 36-1451), NiO (JCPDS No. 47-1049) and Au (JCPDS No. 04-0784) are reported at the bottom. All samples show crystalline phases, indicating that 500 °C is high enough to pyrolise the organics inside the film, promote the reduction of Au ions dispersed inside the oxide films, and also to crystallize both Ni and Zn oxides. Analyzing the ZnO reflections, it is clear that the (002) diffraction peak is much more intense than the tabulated value, while all the other ZnO peaks are absent or very weak, indicating an extensive orientation along the *c*-axis. It can be also noticed that NiO peaks are progressively increasing in intensity as the Ni content in the starting solution increases, clearly indicating a higher amount of Nickel oxide in the films, as expected.

Diffraction peaks for the same phase are very similar in intensity and broadening in all samples, apart from the above mentioned increase in intensity of NiO peaks, confirming a

similar crystalline structure of the different nanocomposites, at least as far as Au and ZnO are concerned. In fact, performing a Lorentzian fit on the XRD peaks and measuring the full width at half maximum (FWHM), the crystallite size can be estimated by means of the Scherrer's relationship: ZnO, NiO and Au crystals sizes are respectively between 24-29 nm 11-16 nm and 14-18 nm in all the samples.

Optical absorption measurements in the UV-Vis range show in all samples the sharp absorption edge of ZnO around 370 nm. Au-containing samples show also the Au NPs SPR peak between 570 nm and 600 nm. Figure 3.47 shows the optical absorption spectra for the samples containing Au: plots for Au-free samples are not reported since they don't bring any additional information, because the only difference is that the samples are optically transparent in the visible range. The ZnO absorption edge is almost the same in all samples, and the energy associated with the band gap (around 3.3 eV) is very close to values reported in the literature for similar sol-gel films [146] and also for bulk ZnO [147], indicating that the structure of zinc oxide is not influenced by the NiO. However, the Au SPR peak undergoes some changes, being red shifted and broadened with increasing NiO content. The red shift can be explained considering the different refractive indexes of the two oxides: for ZnO it is 2.01 [148], while for NiO it is 2.33 [87], so if the amount of nickel inside the film is increased, an increase of the average refractive index of the nanocomposite results, and this causes the observed red shift of the Au SPR peak.

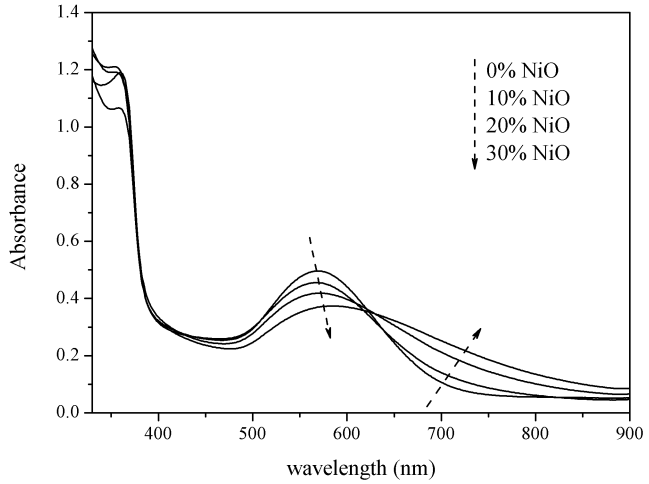

Figure 3.47. Optical absorption spectra of the 4 samples with NiO amount increasing from 0% to 30%

The broadening of the Au SPR band could be ascribed to the interaction of the noble metal NPs with the active NiO surface: in fact it has been shown [61] that Au and NiO,

having the same cubic crystalline structure with very small lattice mismatch, can form particular two-fold structures in which gold and nickel oxide crystals are coupled along the Au (111) and NiO (200) planes. This fact leads to a broadening and a strong red shift of the SPR peak, due to the high extent of interaction between the two materials. So the broadening is again due to the higher refractive index of NiO, but while the red shift is associated with an average increase in refractive index of the films, the broadening is related to a specific local interaction between NiO and Au crystals due to their low lattice mismatch.

Figure 3.48 shows bright field TEM images of ZnO-Au films without NiO (Figure 3.48a) and with 30% NiO (Figure 3.48b). Polydispersed Au NPs can be recognized as darker spots because of their higher mass-thickness contrast and scattering (diffraction) contrast, compared to the lighter oxide matrix components. It is difficult to distinguish between ZnO and NiO nanocrystals, because TEM images have not been taken at sufficiently high resolution and EDX analysis scans an area larger than the crystallite size. Nevertheless, EDX data showed the presence of Zn, Au, O, and also Ni with the exception, of course, of the sample with 0%NiO, confirming the composition of the oxide matrix (ZnO and NiO), as previously discussed.

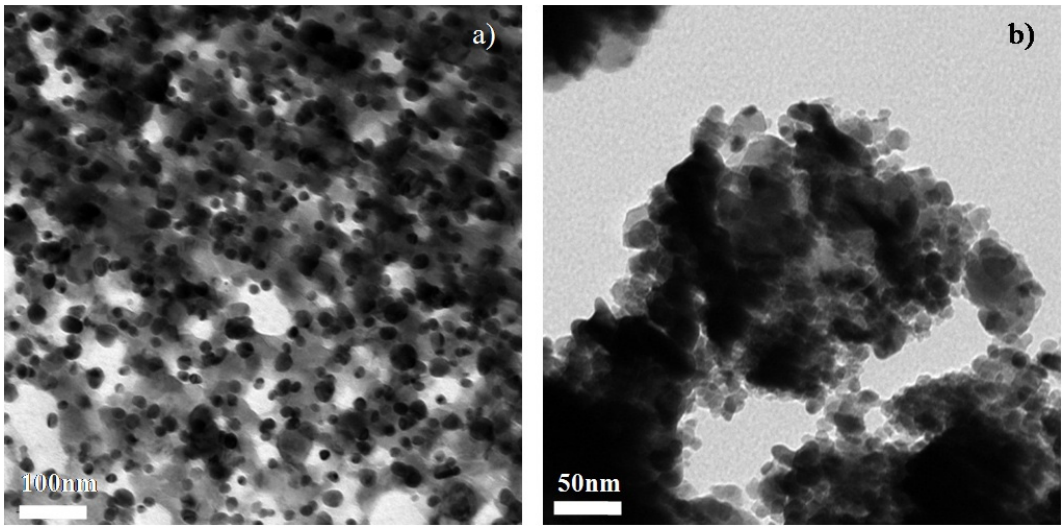

Figure 3.48. Transmission Electron Microscopy images of a) ZnO-Au and b) ZnO-30%NiO-Au scratched fragments from the thin films annealed at 500°C.

SEM micrographs of the nanocomposite film surface are reported in Figure 3.49. Zinc oxide crystalline grains are easily detectable, as well as the presence of a residual porosity. The observed morphology is desirable for gas sensor thin films, in order to

obtain a sensing material with high specific surface area and to have an easy path for the gaseous species entering and exiting the nanocomposite.

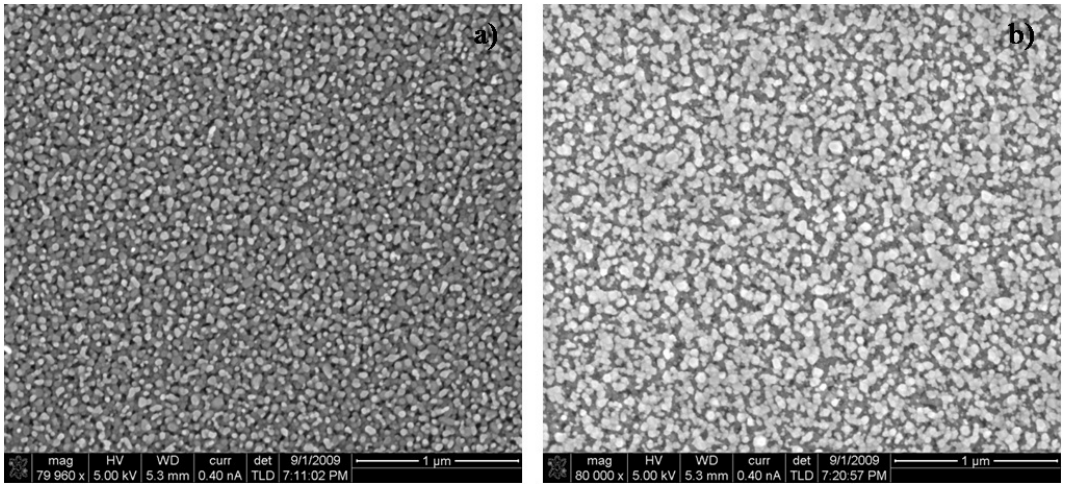

Figure 3.49. Scanning Electron Microscopy of a) ZnO and b) ZnO-Au films annealed at 500 °C.

3.4.3 Gas sensing tests

Gas sensing tests have been performed at different operative temperatures (OT): below 200 °C sensors response was very small and the dynamics of absorption/desorption were quite long. For higher temperatures the response was acceptable, so it was determined to perform all sensing tests at 300 °C OT. Figure 3.50 reports the OAC parameter versus wavelength for Au-free samples (Figure 3.50a) and Au-doped samples (Figure 3.50b). It can be noticed that pure ZnO films do not show any detectable OAC optical signal, while with increasing NiO content, the sensitivity of Au-free films increases, confirming the optical response of nickel oxide towards reducing gases [149]. The absorbance of the films decreases when exposed to the target gas, as expected from the interaction between reducing gases like CO and p-type semiconductors like NiO [135,150]. Samples containing Au NPs show the typical wavelength dependence of sensing response [130], especially in the SPR range (500-700 nm).

ZnO-Au response is symmetric, with positive and negative maxima of about the same intensity. With increasing NiO content, this behavior is added to the NiO response, so the total optical variation is no longer symmetric. The resultant effect of Au NPs is to reduce the response at lower wavelengths and to increase it at higher wavelengths. Interestingly, the highest response is observed with 10% NiO, while for larger NiO content the response is lower. This can be explained by analyzing the shape of the plasmon peak,

which becomes broader as the Ni content is increased, and so its modification caused by the reducing gas happens to be damped. Nevertheless, outside the Au SPR region, a higher NiO amount produces a higher response of the nanocomposite film, as expected considering the behavior of Au-free samples.

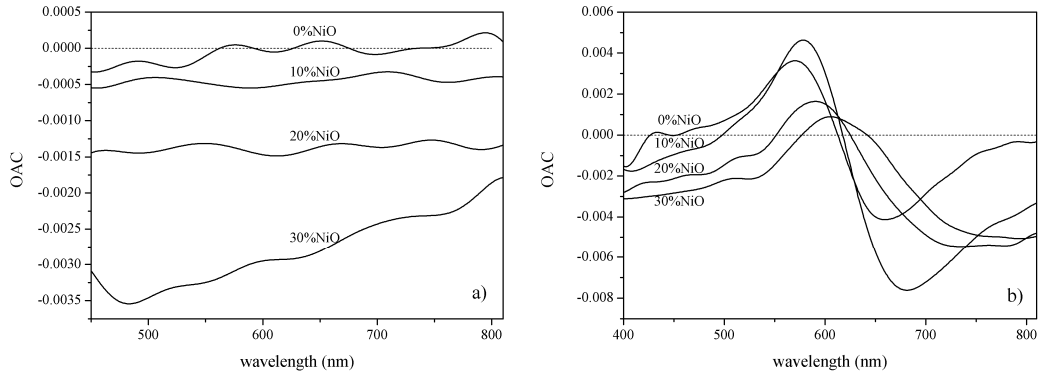

Figure 3.50. OAC curves for a) ZnO-NiO and b) ZnO-NiO-Au films, collected at 300 °C OT. Zero value for OAC is highlighted with a dotted line.

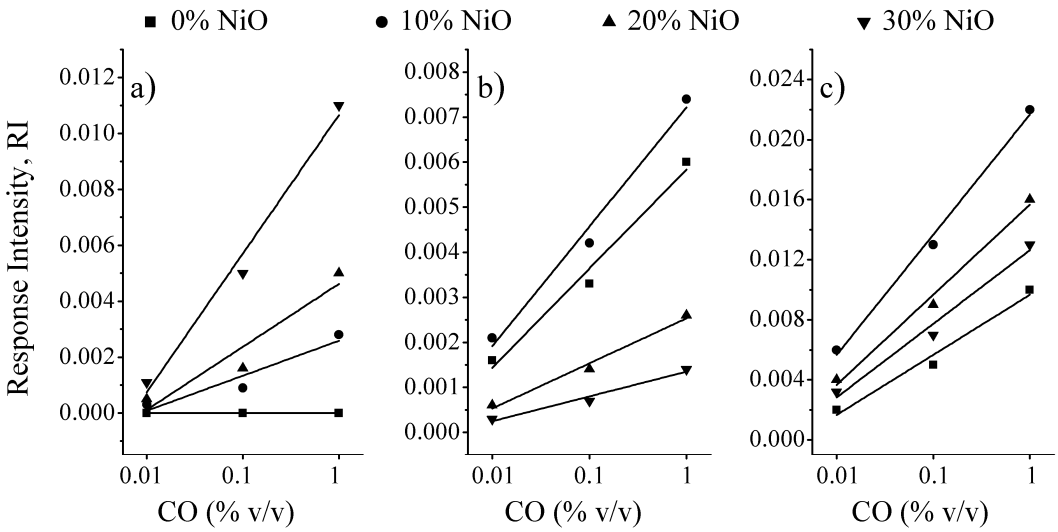

Figure 3.51. Response intensity plots at three different CO concentrations for ZnO-NiO-Au films: a) at 450 nm. b) at the wavelength corresponding to the negative maximum of OAC curve. c) at the wavelength corresponding to the positive maximum of OAC curve.

In Figure 3.51 the Response intensity parameter (RI, see Appendix section for details) at three different wavelengths (at 450 nm and at the two wavelengths corresponding to positive and negative maximum of OAC curves reported in Figure 3.50b) has been plotted versus the CO concentration. The response intensity for all the samples increases

linearly with order of magnitude of target gas concentrations, highlighting good sensitivity for low concentrations. A linear fit has been performed on data plotted in a linear-logarithmic scale, obtaining a good fit of experimental values: so the intensity of the response of all films at each wavelength can be described as linear with respect to the logarithm of the target gas concentration, giving the opportunity to easily create calibration curves for the sensitivity at different wavelengths.

As expected, outside the Au NPs plasmon range (Figure 3.51a) increasing the NiO content causes an increase in the response, while the introduction of Au NPs with their absorption peak in the visible range causes a decrease in the response when operating at a wavelength near the OAC positive maximum (Figure 3.51b) and an increase when operating near the OAC negative maximum (Figure 3.51c). The response decrease experienced for a particular range of wavelength suggests the possibility to test these materials in multiple gas detection configurations. Nevertheless, for samples with a low amount of Ni (0%, 10%) this decrease is not evident, since the intensity of the response due to NiO was absent or very small; thus the presence of Au NPs causes an improvement in the sensor performance also in the range of wavelength near the OAC positive maximum.

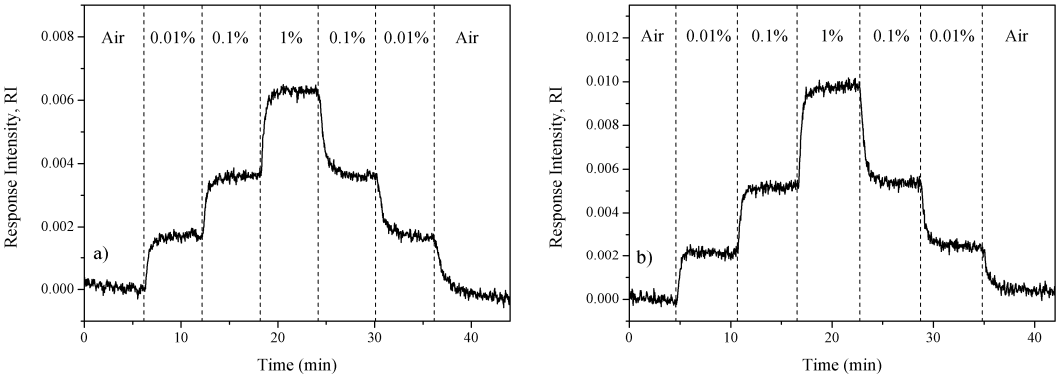

Figure 3.52. Dynamic response of ZnO-Au sample at 570 nm (a) and 670 nm (b) at 300 °C OT.

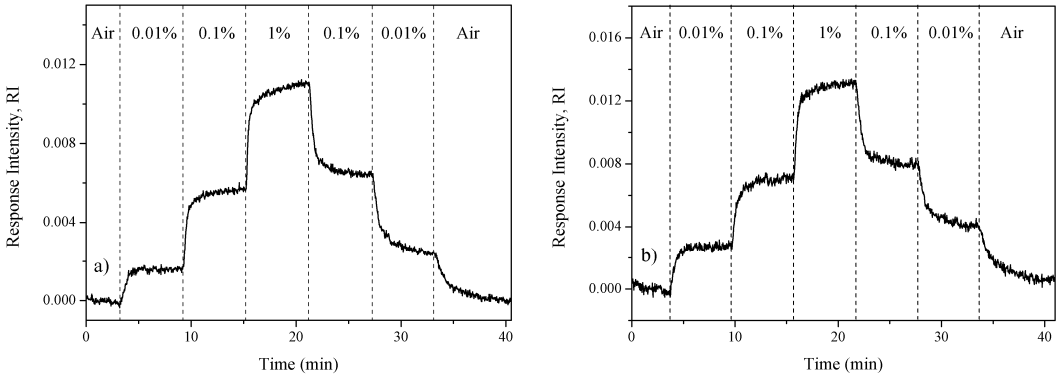

Figure 3.53. Dynamic response of 70%ZnO-30%NiO sample at 480 nm and 300 °C OT (a) and 70%ZnO-30%NiO-Au sample at 750 nm (b) and 300 °C OT.

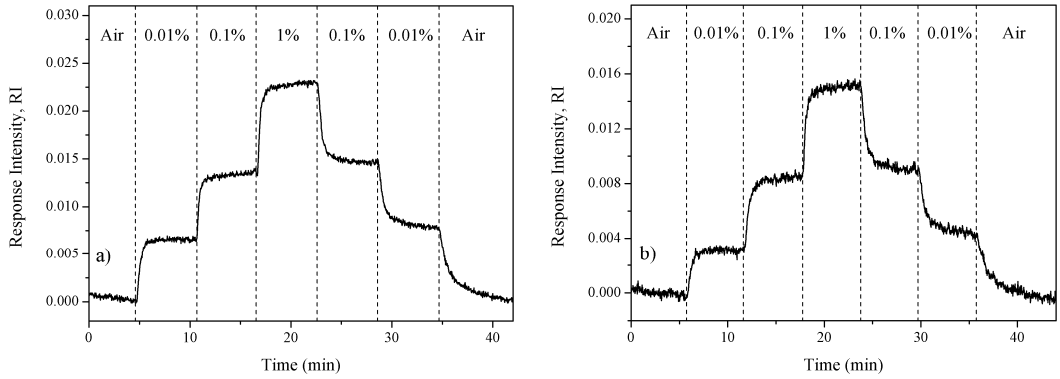

Figure 3.54. Dynamic response of 90%ZnO-10%NiO-Au sample at 680 nm and 300 °C OT (a) and 80%ZnO-20%NiO-Au sample at 740 nm (b) and 300 °C OT.

The dynamics of absorption and desorption of the target gas are fast, as can be seen in Figures 3.52, 3.53 and 3.54: the response and recovery times have found to be between 30 seconds and 1 minute for all samples. Figure 3.52 shows the dynamic behavior of ZnO-Au sample without NiO tested at two different wavelength corresponding to OAC positive maximum (Figure 3.52a) and negative maximum (Figure 3.52b): as can be seen the Response Intensity is similar in both plots, with a maximum value between 0.007 and 0.01, as already shown in Figure 3.51. The difference between the two plots is that at 570 nm the CO presence causes an increase in absorbance, while at 670 nm it causes a decrease in absorbance, as already discussed previously.

Figure 3.53 shows the comparison between the samples containing 30% NiO, with and without Au NPs, tested at the wavelengths corresponding to the maximum sensitivity (*i.e.* 480 nm for the sample without Au, and 750 nm for the sample with Au). In both cases there is a decrease in absorbance and as can be seen, the RI value is similar, confirming that also ZnO-NiO without Au is capable of detecting CO species with good sensitivity.

Finally, in Figure 3.54, sample with 10% NiO and 20% NiO both with Au NPs are compared: the tests have been performed at the wavelength corresponding to the negative maximum of OAC curve for both samples and it is clear that the sample with 10% NiO has the maximum Response Intensity value, about 0.023, and also the signal to noise value is improved (the noise is the same in all sample, because it is related to the experimental setup and the operative temperature: so the higher the sensor response, the higher the signal to noise ratio).

In conclusion, in all previous tests good CO sensing performances have been presented, with a log-linear relationship between the target gas concentration and the optical response; moreover the sensors dynamics are almost step-like, with perfect recovery of the baseline: no drifts or incomplete recoveries have been detected, validating these ZnO-NiO-Au nanocomposites as valuable materials for CO optical sensing.

3.5 Au and Pt nanoparticles inside WO_3 microstructured thin films

3.5.1 Synthesis

The WO_3 films synthesis is based on an initial synthesis of W films, and a subsequent treatment of oxidation, followed by a high temperature thermal treatment to stabilize completely the film and crystallize the WO_3 phase.

The W films were sputtered for 2 min from a pure 99.95% W target onto quartz substrates in the presence of pure argon (Ar) gas, at 300 °C and working pressure of 20 mTorr with an RF power of 100W. The film thickness is 50 nm measured with Ambios XP thickness profilometer.

Based on the tungsten oxide synthesis developed by Widenkvist *et al*. [151], the sputtered W films were boiled for 3 hrs in 100 ml 1.5M nitric acid (HNO_3) in a flask. The flask was merged in the water heated up to 50 °C in a bath. A condenser with slow water flow was connected to the flask to keep the HNO_3 concentration constant during the experiment. After the acid treatment, the films underwent a subsequent process of impregnation, in order to dope the oxide matrix with noble metal NPs: one film was impregnated with an ethanolic solution containing Au^{3+} ions, while other two films were impregnated first with Au^{3+} and then with Pt^{4+} ions, with Au/Pt molar ratio equal to 1 and 5, respectively. After drying, the samples were annealed at 500 °C for 60 min, in order to reduce noble metal ions, burn the organic compounds and transform the tungstite ($WO_3 \cdot H_2O$) crystals

into the WO_3 crystalline matrix. For comparison purposes, also an undoped sample was prepared, simply skipping the impregnation process and annealing directly the tungstite film. The samples prepared for this study are summarized in Table 3.12.

Table 3.12. List of names and compositions of the samples prepared.

Sample name	Composition	Au/Pt ratio
WO	WO_3	/
WA	WO_3-Au	/
WAP1	WO_3-Au-Pt	5
WAP2	WO_3-Au-Pt	1

3.5.2 Characterization

Figure 3.55 shows SEM images of (a) the as-sputtered W film, (b) its transformation to tungstite after the acid boiling treatment, and (c) the final transformation into the Au-doped tungsten oxide film after the impregnation and annealing processes. The sputtered W film consists of dense and uniform W grains (Figure 3.55a); during the acid treatment, the W grains with sizes of 100-500 nm were transformed into tungstite plates of 100-500 nm sizes and 10-30 nm thick (Figure 3.55b). The tungstite films were found to be approximately 150 nm thick. After impregnation and annealing, WO_3 crystallizes and the distinctive lamellar shape is maintained, even if a certain degree of degradation in the plates shape and a slight reduction in size can be detected from Figure 3.55c; in this picture, also Au NPs as brighter spots can be recognized.

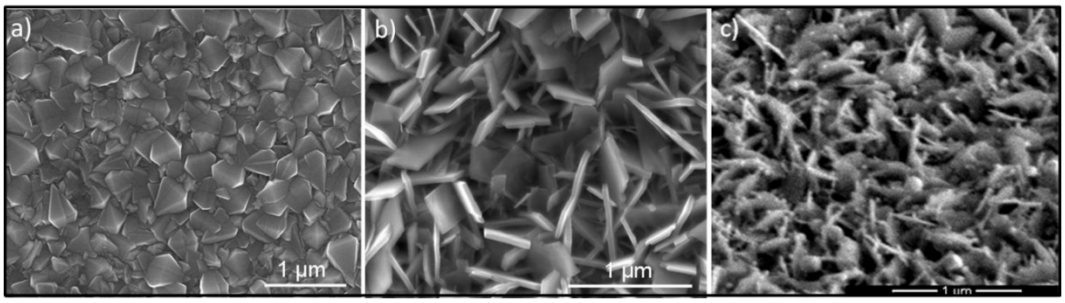

Figure 3.55. SEM images of a) sputtered W film; b) $WO_3 \cdot H_2O$ thin film before the annealing; c) WO_3-Au film after the annealing.

After the 500 °C annealing, the Au-impregnated sample shows a blue-violet color due to Au NPs SPR peak; when both Au and Pt are present inside the films, the color ranges from light to dark brown according to Pt amount. Figure 3.56a shows the absorption

spectra in the 350-900 nm range for the 3 impregnated samples: in the Au doped sample, the peak due to SPR of Au NPs is evident at about 600 nm, while increasing Pt amount results in a damping of this peak; in fact WAP1 sample shows only a little shoulder around 600 nm, while in WAP2 sample there is no evidence of Au SPR band.

This behavior has been previously observed by other authors and can be due to the alloying of the two metals during thermal annealing, or to formation of a platinum shell around gold NPs [152,153]. It is likely that Pt NPs partially nucleate over Au NPs, giving Au-Pt alloy NPs and separate Pt NPs. Nevertheless, we cannot exclude the presence of a shell of Pt around the Au-Pt alloy, as previously reported [154].

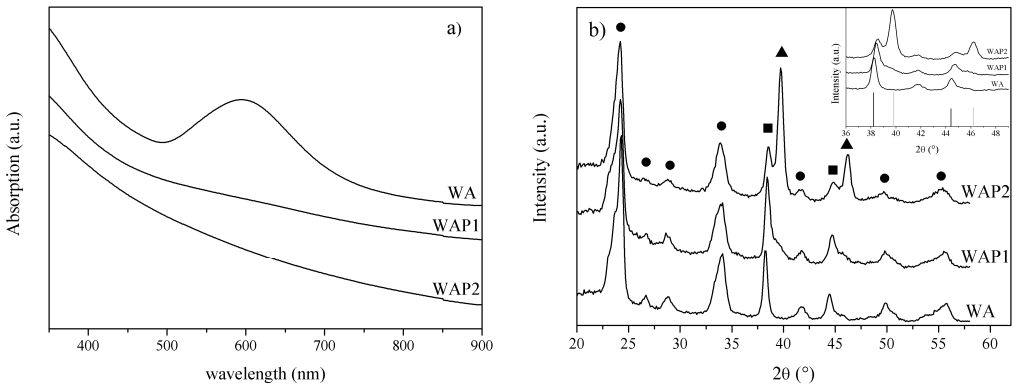

Figure 3.56. a) Absorption spectra of WO_3-Au and WO_3-Au-Pt samples. b) XRD pattern of WO_3-Au and WO_3-Au-Pt samples. Theoretical diffraction peaks for WO_3 (●), Au (■) and Pt (▲) are also reported. The inset show a detail of the Au and Pt diffraction peaks where the black and grey lines are the theoretical diffraction peaks for Au and Pt respectively: a clear shift of Au diffraction peaks at higher angles with increasing Pt amount can be noticed.

The formation of Au-Pt alloy has been confirmed also by XRD spectra reported in Figure 3.56b: WO_3 diffraction patterns (JCPDS No. 83-0951) are evident in all samples, as well as Au peaks (JCPDS No. 04-0784). Pt peaks (JCPDS No. 04-0802) are clearly identified in WAP2 sample, while in WAP1 sample (containing low amount of Pt), only two shoulders near Au peaks are detected.

The increase of the Pt content has the effect to shift Au diffraction peaks at higher angles, due to alloying of the two metals, as shown in the inset. This shift at higher angles (*i.e.* smaller planes distances) is consistent with the alloying of Pt atoms inside the Au lattice. The molar concentration of the two constituents of the alloy can be determined by means of the Vegard's law: Pt inside the Au lattice is found to be 14% in the WAP1 sample and

21% in the WAP2 sample. Considering that in WAP1 sample the Au/Pt ratio is equal to 5, almost all Pt is alloyed, as confirmed also from the very weak diffraction peak coming from separate Pt crystals; WAP2 sample shows pure Pt diffraction peaks with high intensity, confirming that most of platinum is not alloyed, even if the percentage amount of Pt in the alloy is higher.

3.5.3 Gas sensing tests

All samples were tested as active materials for optical detection of different reducing gases: in detail, the tested gases were H_2 (1% v/v), CO (1% v/v) and H_2S (0.01 v/v). Pure WO_3 sample did not give any detectable optical response, maybe because of the low thickness of the film and because of the absence of a catalyst, as reported in a previous work [155], while Au and Au-Pt doped samples revealed capability to detect all the gases, sometimes with an interesting wavelength dependent response, different according to the gas nature. Low temperature tests were performed at 100 °C, and the WA sample gave a weak reversible response only to H_2, while Pt containing samples show a better response to both CO and H_2. Hydrogen Sulfide sensing tests were not performed at 100 °C because H_2S is known to poison noble metal catalysts at low temperatures [156], since it reacts with Au and Pt surfaces forming highly stable sulfide bonds, causing irreversible reactions.

At high operating temperatures (350 °C) WO_3-Au nanocomposite is capable to detect all tested gases, with the typical wavelength behavior of Au-doped metal oxides [94], while samples containing Pt have much lower sensitivity, and the wavelength dependence is not so strong. This different behavior according to test temperature and type of catalyst can be better appreciated by referring to Figure 3.57, where the OAC curves for the films towards the different gases as a function of the wavelength of analysis is reported.

Considering samples response to CO and H_2, it can be noticed that WA sample (black lines in Figure 3.57a to d) shows a quite good behavior at high temperature: both gases cause a similar optical variation, even if the magnitude of the signal during hydrogen exposure is higher compared to CO; in samples without Au SPR band (grey lines in Figure 3.57a to d), the response of the material is better at lower temperature, thanks to the presence of Pt, a known catalyst to couple with WO_3 to enhance reducing gases sensing [157], while Au-doped sample's response is almost null with CO and only barely detectable with H_2.

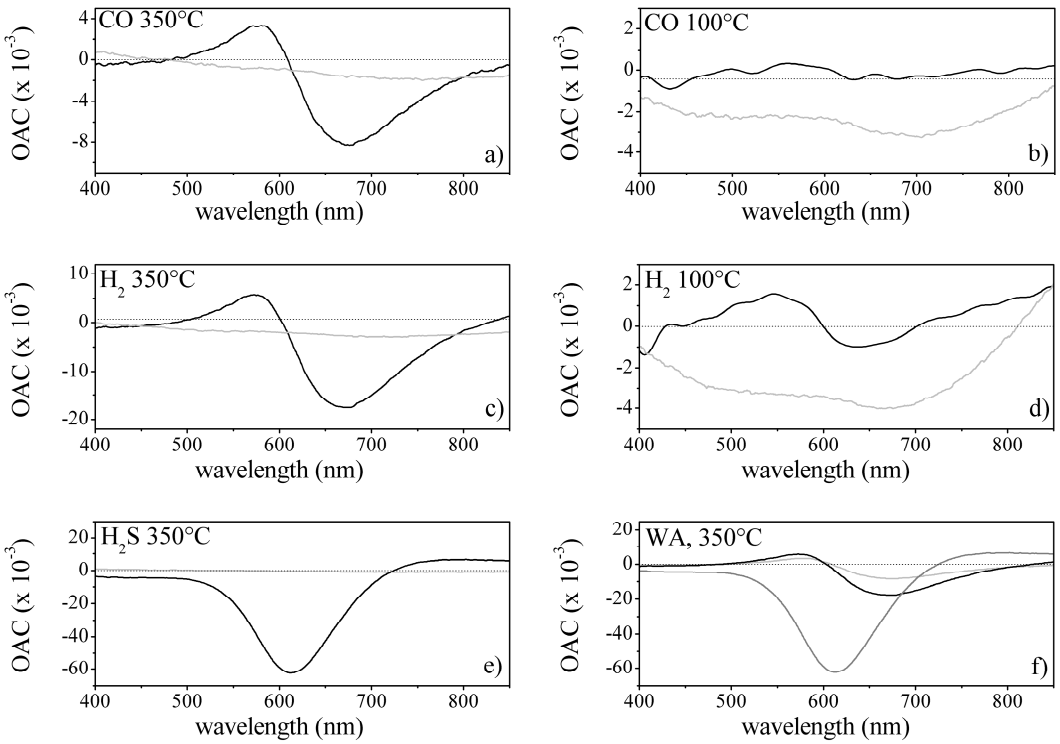

Figure 3.57. a-e) OAC curves for WA (black line) and WAP1 (grey line) in function of wavelength, for H_2, CO and H_2S at the two temperatures of analysis; f) Comparison of OAC curves for WA sample exposed to H_2 (black line), CO (light grey line) and H_2S (dark grey line); in all plots dotted lines identify the zero value.

As far as H_2S is concerned, the optical variation during hydrogen sulfide exposure is very high in WA sample, while Pt containing samples did not show an acceptable response, as can be seen in Figure 4e, where OAC plots of WA (black line) and WAP1 (grey line) sample are reported. The H_2S effect on the optical properties of Au doped samples is to damp and widen the surface plasmon band of Au NPs as already observed for the nanocomposites based on Ti and Ni oxides discussed in section 3.2.6, causing a different optical variation compared to CO and H_2, that on the contrary cause a blue-shift of the Au SPR peak, consistent with the interaction of reducing gases with n-type semiconductor matrix [95]. As can be noticed from Figure 3.57f, the optical variation during H_2S exposure is rather different compared to the other gases, so it is possible to identify some particular wavelengths that allow the tuning of the sensor's sensitivity and selectivity. At high temperature the behavior of WAP1 sample is rather poor, because of the very low sensitivity, while at low temperature it shows quite good sensitivity to H_2 and CO; on the contrary Au-doped sample is capable to detect all the gases at high temperature, with a wavelength dependent response, while at low temperature the response is negligible.

These results suggests a key role played by Au NPs optical properties in the sensing process at high temperatures, while at low temperature it is necessary the presence of Pt to catalyze the gas reaction.

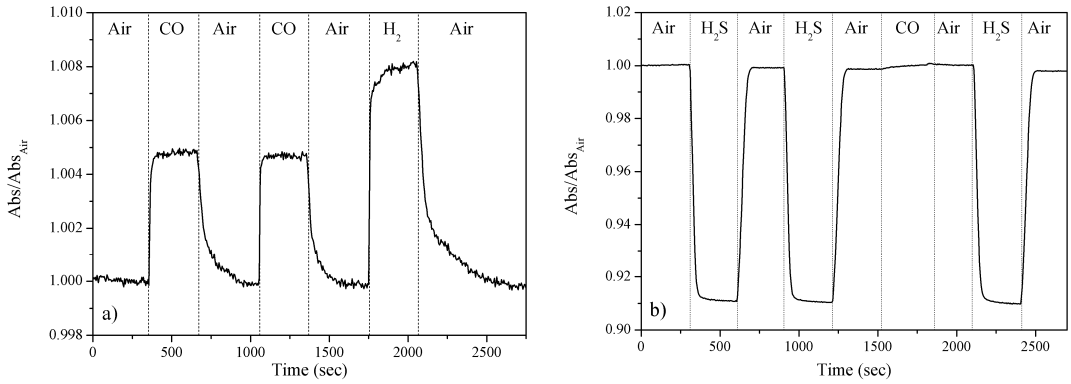

Figure 3.58. Time resolved test for WA sample at 575 nm and 350 °C (a); at 610 nm and 350 °C (b).

Time-resolved dynamic tests for WA and WAP1 samples are reported in Figure 3.58 and Figure 3.59 respectively: Au-doped sample tested at 350 °C show quite good dynamic behavior to hydrogen and CO exposure (Figure 3.58a), when operated at the wavelength corresponding to the maximum of OAC curves reported in Figure 3.57, that is 575 nm, with response times of few seconds and recovery times slightly longer, of about 30 seconds. The difference in intensity of the response between the two gases can be easily seen, being the sensitivity to hydrogen roughly twice the CO sensitivity. When WA film is tested at 610 nm (Figure 3.58b), the wavelength which corresponds to high H_2S response and almost null CO and H_2 response (as can be seen from OAC curves reported in Figure 3.57f), the sample becomes selective only for hydrogen sulfide detection. Only a very small perturbation was observed in the optical signal at this particular wavelength when 1% CO was introduced into the test cell.

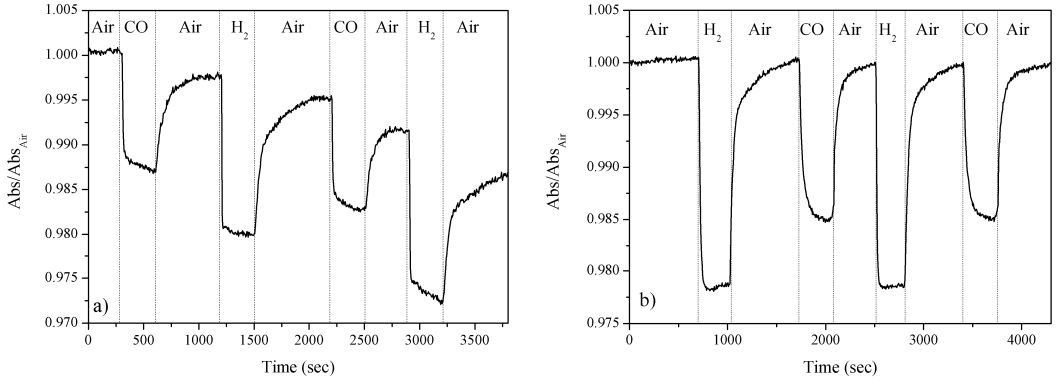

Figure 3.59. Time resolved test for WAP1 sample at 730 nm and 350 °C (a); at 700 nm and 100 °C (b).

WAP1 dynamic behavior is reported in Figure 3.59: at 350 °C (Figure 3.59a) there is a small but still detectable signal for H_2 and CO, but the baseline recovery is not complete, since a drift in the baseline has been observed also after a prolonged period of stabilization at the desired temperature. At 100 °C (Figure 3.59b) the response during H_2 exposure is again higher compared to CO response, and the dynamic behavior is better than the high temperature test; it is though slightly worse compared to WA sample tested at high temperature, because kinetic processes like gas adsorption and desorption are thermally activated, so the dynamics should in principle be improved if operating at higher temperature. Nevertheless, the behavior is still acceptable, considering that this sensor is operating near room temperature, indicating that the Pt catalyst works better at low temperatures.

3.6 Conclusions

In this chapter, different combinations of noble metals/metal oxides have been explored in order to synthesize nanocomposites thin films for gas sensing applications. The main idea behind all the syntheses presented was to deposit the film through common and easy techniques, like sol-gel, and then promote the reduction of noble metal NPs and the crystallization of the oxide matrix through a high temperature annealing (usually 500 °C or 600 °C). In this way, quite thick films composed of the desired oxide(s) material can be obtained, and the noble metal content can be very high; these advantages are though balanced with some disadvantages like poor control on size, shape and dispersity of the forming particles, and the need of substrates that can resist at high temperature, thus

excluding polymers and common soda-lime glass. Of course, depending on the particular application, the disadvantages might be too important, but if the purpose is the easy and low-cost deposition of active layers for optical detection of reducing gases, where no special control of materials microstructure is needed, the syntheses presented here might be very useful.

First, TiO_2-NiO thin films containing Au NPs were synthesized by the sol-gel technique. Structural and morphological characterizations after 500 °C and 600 °C thermal annealing demonstrate the crystallization of different phases ($NiTiO_3$, NiO, TiO_2 both in rutile and anatase phase) according to the chemical composition and to the annealing temperature of the prepared samples. The presence of nickel is found to be a promoter in the crystallization of rutile TiO_2 over the anatase phase. Optical characterization showed a tunable refractive index of the films according to the amount of Ti precursor in the starting solution, and at the same time the Au plasmon peak is observed to shift to higher wavelengths, allowing to roughly monitor the nanocomposites refractive index by simply analyzing Au SPR peak wavelength. Ellipsometry measurements performed under different environments reveal also a high amount of residual porosity of the samples, useful for thin films to be used as gas sensors.

The functionality as optical gas sensors has been analyzed after exposure to H_2, CO, H_2S and propane, confirming a highly selective response to hydrogen sulfide; the response is wavelength-dependent, allowing the tailoring of sensor selectivity towards interfering gases. The samples are sensitive also at very low concentration of H_2S (few ppm), and a correlation between target gas concentration and the sensor dynamic behavior has been presented. A saturation of response to H_2S is found at about the 5ppm to 10 ppm concentration range. The dynamic behavior is excellent with very fast response/recovery times, good baseline recuperation, high reproducibility even after extended tests and almost no interference with other reducing gases (CO, H_2), especially when the anatase phase of TiO_2 is absent.

By analyzing the reaction products and the surface chemistry of the samples after exposure to H_2S it was demonstrated that SO_2 is generated, and since no evidence of metal sulfide species formation has been found, a direct catalytic oxidation of H_2S over the Au-TiO_2-NiO nanocomposite film can be suggested. So Au NPs act as optical probes in the detection of H_2S thanks to their localized surface plasmon resonance, while on the contrary the oxide matrix itself is not capable to detect optically the target gas, but the decomposition of H_2S to SO_x seem to be rather independent from the presence of the Au

NPs, suggesting a key role of the oxide in the catalytic oxidation of H_2S; moreover the combination of Ti and Ni oxides is more efficient in this process than the pure TiO_2, both in the anatase and in the rutile phase.

Then the focus is set on materials for H_2 and CO detection: a detailed procedure to synthesize mesoporous silica film containing Ag and NiO nanoparticles through combined sol-gel and impregnation processes has been presented and discussed. First, highly porous oxide thin films have been prepared with the sol-gel method using an organic template as porogen agent, and the structural and morphological evolution of the matrix has been evaluated, resulting in small (5-6 nm) crystalline NiO NPs dispersed inside a mesoporous silica matrix after annealing at 800 °C. Then an impregnation protocol has been prepared, involving the surface functionalization of the pores and the subsequent impregnation with a silver ions solution. Ag NPs have been formed upon thermal treatment. The formation of spherical Ag NPs of about 5-50 nm has been proved with XRD, TEM and optical absorption measurements. Gas sensing tests towards CO and H_2 have been presented showing reversible response for both gases with a wavelength dependent behavior. Such a process can be easily adapted and modified in order to obtain SiO_2-based nanocomposites with desired porosity and desired metal oxide/noble metals interface.

Another combination of oxides that has been investigated is the ZnO-NiO system: a simple and reproducible sol-gel synthesis of ZnO-NiO thin films has been presented and a dispersion of Au NPs inside the porous film has also been achieved. XRD and electron microscopy characterizations confirm the crystallization of both oxides and of Au NPs, while UV-Vis spectroscopy shows the Au SPR peak red shifting and broadening with an increase in NiO content, as a consequence of the interaction between the two materials.

An increase of optical CO sensitivity with NiO content is demonstrated in the whole analyzed range of wavelengths for Au-free samples, and also outside Au SPR region in Au-doped samples. For wavelengths between 500 nm and 750 nm, the sensor response becomes wavelength dependent, giving rise to the opportunity of tuning the sensitivity by selecting the operative wavelength, and consequently making these nanocomposite films of potential use for multiple gases analysis. The dynamic behavior of these nanocomposites was very good, with response and recovery times always less than 1 minute, and a complete retrieval of the baseline even after multiple and prolonged tests.

In the end, WO_3 thin films with distinctive lamellar shape containing Au and Pt NPs have been prepared coupling sputtering, acid boiling and impregnation processes. Gas sensing tests showed a good response to reducing gases like CO, H_2 and H_2S, with the possibility to tune the sensor's response by selecting the operative wavelength. Moreover, a different sensitivity according to the test temperature and to the type of noble metal used has been detected, highlighting a key role in the gas detection played by Au and Pt at higher and lower temperature, respectively. Time resolved tests showed a quite good dynamic behavior and confirmed the selectivity towards a particular gas according to the wavelength of analysis.

Bibliography

[1] W.H. Tao, C.H. Tsai, *Sens. Actuators B*, **2002**, *81*, 237.

[2] N.S. Lawrence, J. Davis, R.G. Compton, *Talanta*, **2000**, *52*, 771.

[3] T. Xiao, L. An, W Zhang, S. Sheng, G. Xiong. *Catalysis Letters*, **1992**, *12*, 287.

[4] V.D. Kapse, S.A. Ghosh, G.N. Chaudhari, F.C. Raghuwanshi, F.C. *Talanta*, **2008**, *76*, 610.

[5] Y. Wang, Y. Wang, J. Cao, F. Kong, H. Xia, J. Zhang, B. Zhu, S. Wang, S. Wu, *Sens. Actuators B*, **2008**, *131*, 183.

[6] G.N. Chaudhari, D.R. Bambole, A.B. Bodade, P.R. Padole, *J. Mater. Sci.*, **2006**, *41*, 4860.

[7] M. Rumyantseva, M. Labeau, G. Delabouglise, L. Ryabova, I. Kutsenoka, A. Gaskov, *J. Mater. Chem.*, **1997**, *7(9)*, 1785.

[8] M. Ando, S. Suto, T. Suzuki, T. Tsuchida, C. Nakayarna, N. Miura, N. Yamazoe, *J. Mater. Chem.*, **1994**, 4, 631.

[9] G.H. Jain, L.A. Patil, M.S. Wagh, D.R. Patil, S.A. Patil, D.P. Amalnerkar, *Sens. Actuators B*, **2006**, *117*, 159.

[10] Y. Wang, S. Wang, Y. Zhao, B. Zhu, F. Kong,D. Wang, S. Wu, W. Huang, S. Zhang, *Sens. Actuators B*, **2007**, *125*, 79.

[11] G. Sberveglieri, S. Groppelli, P. Nelli, C. Perego, G. Valdre, A. Camanzi, *Sens. Actuators B*, **1998**, *55*, 86.

[12] Lin H.M. Lin, C.M. Hsu, H.Y. Yang, *Sens. Actuators B*, **1994**, *22*, 63.

[13] M.S. Wagh, L.A. Patil, T. Seth, D.P. Amalnerkar, D.P. *Mater. Chem. Phys.*, **2004**, *84*, 228.

[14] J. Tamaki, T. Maekawa, N. Miura, N. Yamazoe, N. *Sens. Actuators B*, **1992**, *9*, 197.

[15] S. Manorama, G. Sarala Devi, V.J. Rao, V.J. *Appl. Phys. Lett.*, **1994**, *64*, 3163.

[16] G. Sarala Devi, S. Manorama, V.J. Rao, *J. Electrochem. Soc.*, **1995**, *142*, 2754.

[17] J. Tamaki, K. Shimanoe, Y. Yamada, Y. Yamamoto, N. Miura, N. Yamazoe, *Sens. Actuators B*, **1998**, *49*, 125.

[18] R.B. Vasiliev, M.N. Rumyantseva, N.V. Yakovlev, A.M. Gaskov, *Sens. Actuators B*, **1998**, *50*, 186.

[19] G. Mangamma, V. Jayaraman, T. Gnanasekaran, G. Periaswami, *Sens. Actuators B*, **1998**, *53*, 133.

[20] W. Yuanda, T. Maosong, H. Xiuli, Z. Yushu, D. Guorui, *Sens. Actuators B*, **2001**, *79*, 187.

[21] C. Wang, X. Chu, M. Wu, *Sens. Actuators B*, **2006**, *113*, 320.

[22] O. Berger, T. Hoffmann, W.J. Fischer, *J. Mater. Sci.*, **2004**, *15*, 483.

[23] T. Maekawa, J. Tamaki, N. Miura N. Yamazoe, *J. Mater. Chem.*, **1994**, *4(8)*, 1259.

[24] L. Solis, S. Saukko, L.B. Kish, C.G. Granqvist, V. Lannto, *Sens. Actuators B*, **2001**, *77*, 316.

[25] G. Sarala Devi, S. Manorama, V.J. Rao, *Sens. Actuators B*, **1995**, *28*, 31.

[26] R.S. Niranjan, K.R. Patil, S.R. Sainkar, I.S. Mulla, *Mater. Chem. Phys.*, **2003**, *80*, 250.

[27] T. Ramstad, A.H. Bates, T.J. Yellig, S.J. Borchert, K.A. Mills, *Analyst*, **1995**, *120*, 2775.

[28] R. Simo, J.O. Grimalt, *J. Chromatogr. A*, **1996**, *726*, 161.

[29] J. Radford-Knoery, G.A. Cutter, *Anal. Chem.*, **1993**, *65*, 976.

[30] P.R. Berube, P.D. Parkinson, E.R. Hall, *J. Chromatogr. A*, **1999**, *830*, 485.

[31] C. Gru, P.M. Sarradin, H. Legoff, S. Narcon, J.C.Caprais, F.H. Lallier, *Analyst*, **1998**, *123*, 1289.

[32] A.V. Kroll, V.I. Smorchkov, A.Y. Nazarenko, *Sens. Actuators B*, **1994**, *21*, 97.

[33] U.M. Noor, D. Uttamchandani, *J. Sol-Gel Sci.Tech.*, **1998**, *11*, 177.

[34] M.M.F. Choi, P. Hawkins, *Sens. Actuators B*, **2003**, *90*, 211.

[35] K.J. Wallace, S.R. Cordero, C.P. Tan, V.M. Lynch, E.V. Anslyn, *Sens. Actuators B*, **2007**, *120*, 362.

[36] T.V.S. Sarma, S. Tao, *Sens. Actuators B*, **2007**, *127*, 471.

[37] Z. Zhang, H. Jiang, Z. Xing, X. Zhang, *Sens. Actuators B*, **2004**, *102*, 155.

[38] Z. Miao, Y. Wu, X. Zhang, Z. Liu, B. Han, K. Dinga, G. An, *J. Mater. Chem.*, **2007**, *17*, 1791.

[39] A.M. Rubinstein, A.A. Dulov, A.A. Slinkin, L.A. Abramova, I.S. Gershenzon, L.A. Gorskaya, V.J. Danyushevskii, M.I. Dashevskii, A.L. Klyachko-Gurvich, T.K. Lavrovskaya, L.I. Lafer, V.I. Yakerson, *J.Catal.*, **1974**, *35,1*, 80.

[40] J.R. Sohn, J.H. Han, *Appl. Catal. A*, **2006**, *298*, 168.

[41] J.R. Sohn, S.G. Lee, *Catal. Lett.*, **2008**, *120*, 116.

[42] S. Uchiyama, Y. Obayashi, T. Hayasaka, N. Kawata, *Appl. Catal.*, **1989**, *47*, 155.

[43] T. Sreethawong, Y. Suzuki, S.Yoshikawa, *Int. J. Hydrogen En.*, **2005**, *30*, 1053.

[44] H. Arakawa, K. Sayama, *Res. Chem. Interm.*, **2000**, *26, 2*, 145.

[45] T. Kamegawa, T.H. Kim, J. Morishima, M. Matsuoka, M. Anpo, *Catal. Lett.*, **2009**, *129*, 7.

[46] A. Al-Kahlout, M.A. Aegerter, *Solar En. Mater. Solar Cells*, **2007**, *91*, 213.

[47] H. Huang, S.X. Lu, W.K. Zhang, Y.P. Gan, C.T. Wang, L. Yu, X.Y. Tao, *J. Phys. Chem. Sol.*, **2009**, *70*, 745.

[48] Martini M. Martini , G.E.S. Brito, M.C.A. Fantini, A.F. Craievich, A. Gorenstein, *Electrochimica Acta*, **2001**, *46*, 2275.

[49] Y.M. Lee, C.H. Hsu, H.W. Chen, *Appl. Surf. Sci.*, **2009**, *255*, 4658.

[50] Y. Xie, C. Huang, L. Zhou, Y. Liu, H. Huang, *Comp. Sci. Tech.*, **2009**, *69*, 2108.

[51] K.I. Arshak, L.M. Cavanagh, I. Gaidan, E.G. Moore, S.A. Clifford, *IEEE Sensors Journal*, **2007**, *7(6)*, 925.

[52] C. Imawan, F. Solzbacher, H. Steffes, E. Obermeier, *Sens. Actuators B*, **2000**, *68*, 184.

[53] A. Wisitsoraat, A. Tuantranont, E. Comini, G. Sberveglieri, W. Wlodarski, *Thin Solid Films*, **2009**, *517*, 2775.

[54] D. Kohl, *Sens. Actuators*, **1989**, *18*, 71-113.

[55] H.M. Lina, C.M. Hsua, H.Y. Yanga, P.Y. Leeb and C.C. Yang, *Sens. Actuators B*, **1994**, *22*, 63.

[56] E.H. Brown, *Zinc oxide: properties and applications*, NY Pergamon Press; **1976**.

[57] H. Tanga, K. Prasada, R. Sanjinésa, F. Lévy, *Sens. Actuators B*, **1995**, *26*, 71-75.

[58] G. Eranna, B.C. Joshi, D. P. Runthala, R. P. Gupta, *Critical Reviews in Solid State and Materials Sciences*, **2004**, *29*, 111–188.

[59] G. Mattei, P. Mazzoldi, M.L. Post, D. Buso, M. Guglielmi, A. Martucci, *Adv. Mater.*, **2007**, *19*, 561-564.

[60] D. Buso, M. Guglielmi, A. Martucci, G. Mattei, P. Mazzoldi, C. Sada, M.L. Post, *Nanotechnology*, **2006**, *17*, 2429-2433.

[61] D. Buso, M. Guglielmi, A. Martucci, G. Mattei, P. Mazzoldi, C. Sada, M.Post, *Cryst. Growth Des.*, **2008**, *8,2*, 744.

[62] D. Buso, G. Busato, M. Guglielmi, A. Martucci, V. Bello, G. Mattei, P. Mazzoldi, M.L. Post, *Nanotechnology*, **2007**, *18***,** 475505.

[63] U. Kreibig, M. Vollmer, *Optical Properties of Metal Clusters*, ed. Springer, Verlag, Berlin, **1995**.

[64] C. F. Bohren, D.R. Huffman, *Absorption and Scattering of Light by Small Particles*, Wiley, New York, **1998**.

[65] M.A. Villegas, M.A. Garcia, S.E. Paje, J. Llopis, *Mater. Res. Bull*., **2005**, *40*, 1210-1222.

[66] Y. Ding, Y. Wang, L. Su, H. Zhang, Y. Lei, *J. Mater. Chem.*, **2010**, *20*, 9918.

[67] Ü. Özgür, Ya.I. Alivov, C. Liu, A. Teke, M.A. Reshchikov, S. Doğan, V. Avrutin, S.J. Cho, H. Morkoç, *J. Appl. Phys.*, **2005**, *98*, 041301.

[68] C. Klingshirn, *Chem. Phys. Chem.*, **2007**, *8*, 782–803.

[69] H.M. Lina, C.M. Hsua, H.Y. Yanga, P.Y. Leeb, C.C. Yang, *Sens. Actuators B*, **1994**, *22*, 63.

[70] G.N. Chaudhari, A.M. Bende, A.B. Bodade, S.S. Patil, V.S. Sapkal, *Sens. Actuators B*, **2006**, *115*, 297.

[71] J.L. Solis, S. Saukko, L. Kisha, C.G. Granqvist, V. Lantto, *Thin Solid Films*, **2001**, *391*, 255.

[72] C. Cantalini, M. Pelino, H.T. Sun, M. Faccio, S. Santucci, L. Lozzi, M. Passacantando, *Sens. Actuators B*, **1996**, *35-36*, 112.

[73] S. Sekimoto, H. Nakagawa, S.Okazaki, K. Fukuda, S. Asakura, T. Shigemori, S. Takahashi, *Sens. Actuators B*, **2000**, *66*, 142.

[74] Z. Wang, G. Chumanov, *Adv. Mater.*, **2003**, *15*, 1285.

[75] A. Al-Kahlout, S. Heusing, M.A. Aegerter, *J. Sol-Gel Sci. Techn.*, **2006**, *39*, 195.

[76] S. Sakka, H. Kozuka, *J. Sol-Gel Sci. Techn.*, **1998**, *13*, 701.

[77] H. Zhang, J.F. Banfield, *J. Phys. Chem. B*, **2000**, *104*, 3481.

[78] J. Yu, J.C. Yu, B. Cheng, X. Zhao, Z. Zheng, A.S.K. Li, *J. Sol-Gel Sci. Techn.*, **2002**, *24*, 229.

[79] J. Medina-Valtierra, C. Frausto-Reyes, S. Calixto, P. Bosch, V. Hugo Lara, *Materials Characterization*, **2007**, *58*, 233.

[80] P.K. Sharma, M.C.A. Fantini, A. Gorenstein, *Solid State Ionics*, **1998**, *113–115*, 457.

[81] B.F.G. Johnson, R. Davis, *Comprehensive Inorganic Chemistry*, Vol. 3 (Eds: J.C. Bailer Jr., H.J. Emeleus, R. Nyholm, A.F. Trotman-Dickenzon), Pergamon, NewYork, **1973**, 129.

[82] H. Hirai, Y. Nakao, N. Toshima, *J. Macromol. Sci. Chem.*, **1979**, *A13*, 727.

[83] V.V. Atuchin, V.G. Kesler, N.V. Pervukhina, Z. Zhang, *J. Electron Spectros. Relat. Phenom.*, **2006**, *152*, 18.

[84] V.E. Henrich, P.A. Cox, *The Surface Science of Metal Oxides*, Cambridge University Press, Cambridge, **1994**.

[85] J. M. McKay, V.E. Henry, *Phys. Rev. B*, **1984**, *53*, 2344.

[86] D.R. Lide, *Handbook of Chemistry and Physics*, CRC press, 72nd Edition, 4-108, **1991**.

[87] R.J. Powell, W.E. Spicer, *Phys. Rev. B*, **1970**, *2*, 2182.

[88] D.J. Taylor, P.F. Fleig, R.A. Page, *Thin Solid Films*, **2002**, *408*, 104.

[89] P. Alemany, R.S. Borse, J.M. Burlitch, R. Hoffmann, *J. Phys. Chem.*, **1993**, *97*, 8464.

[90] M. Lee, L. Chae, K.C. Lee, *Nanostructured Materials*, **1999**, *11*, 195.

[91] D.A.G. Bruggeman, *Ann. Phys.* (Leipzig), **1935**, *24*, 636.

[92] D. Buso, M. Guglielmi, A. Martucci, C. Cantalini, M.L. Post, A. Hachè, *J. Sol-Gel Sci. Techn.*, **2006**, *40*, 299-308.

[93] M. Ando, T. Kobayashi, S. Iijima, M. Haruta, *Sens. Actuators B*, **2003**, *96*, 589.

[94] M. Ando, T. Kobayashi, M. Haruta, *Catalysis Today*, **1997**, *36*, 135.

[95] D. Buso, M.L. Post, C. Cantalini, P. Mulvaney, A. Martucci, *Adv. Funct. Mater.*, **2008**, *18*, 3843.

[96] A. Piéplu, O. Saur, J.C. Lavalley, O. Legendre, C. Nédez, *Catal. Rev.*, **1998**, *40(4)*, 409.

[97] B.W. Gamson, R.H. Elkins, *Chem. Eng. Prog.*, **1953***, 49*, 203.

[98] P.A. Ferguson, *Hydrogen Sulfide Removal from Gases Air, and Liquids*, Noyes Data Corporation, Park Ridge New Jersey, **1975**.

[99] J.A. Baglio, T.J. Susa, D.W. Wortham, E.A. Trickett, T.J. Lewis, *Ind. Eng. Chem. Prod. Res. Dev.*, **1982**, *21*, 408.

[100] L.F. Reyes, A. Hoel, S. Saukko, P. Heszler, V. Lantto, C.G. Granqvist, *Sens. Actuators B*, **2006,** *117*, 128.

[101] G. Brauer, *Handbook of Preparative Inorganic Chemistry*, Vol. 2, Academic Press, NewYork, **1965**.

[102] T. Pagnier, M. Boulova, A. Galerie, A. Gaskov, G. Lucazeau, *Sens. Actuators B*, **2000**, *71*, 134.

[103] C. Yanxina, J. Yia, L. Wenzhaoa, J. Rongchaoa,T. Shaozhenb, H. Wenbin, *Catalysis Today*, **1999**, *50*, 39.

[104] See the website www.radiello.com and the references reported in www.radiello.com/italiano/inter_it.htm.

[105] D. I. Sayago, P. Serrano, O. Boehme, A. Goldoni, G. Paolucci, E. Román, J. A. Martín-Gago, *Phys. Rev. B*, **2001**, *64*, 205402.

[106] R.T. Tom, A. Sreekumaran Nair, N. Singh, M. Aslam, C.L. Nagendra, R. Philip, K. Vijayamohanan, T. Pradeep, *Langmuir*, **2003**, *19*, 3439.

[107] G. Oldfield, T. Ung, P. Mulvaney, *Adv. Mater.*, **2000**, *12*, 1519.

[108] R.D. Averitt, S.L. Westcott, N.J. Halas, *J. Opt. Soc. Am. B*, **1999**, *16*, 1824-1832.

[109] K. Ishikawa, T. Isonaga, S. Wakita, Y. Suzuki, *Solid State Ionics*, **1995**, *79*, 60.

[110] H. Sellers, A. Ulman, Y. Shnidman, J.E. Eilers, J.E. *J. Am. Chem. Soc.*, **1993**, *115*, 9389-9401.

[111] S. Nakata, Y. Kato, Y. Kaneda, K. Yosikawa, *Appl. Surf. Sci.*, **1996**, *103*, 369-376.

[112] O.N. Kovalenko, N.N. Kundo, V.M. Novopashina, P.N. Kalinkin, *Kinet. Catal.*, **2001**, *42*, 657-661.

[113] D. Adler, J. Feinleib, *Phys. Rev. B*, **1970**, *2*, 3112.

[114] P.S. Patil, L.D. Kadam, *Appl. Surf. Sci*., **2002**, *199*, 211-221.

[115] J. Chen, Q. Li, R. Xu, F. Xiao, *Angew. Chem. Int. Ed*., **1995**, *34*, 2694.

[116] R.N. Ward, D.C. Duffy, P.B. Davies, C.D. Bain, *J. Phys. Chem*., **1994***, 98*, 8536.

[117] Y. Su, J. Wang, H. Liu, *J. Phys. Chem. B*, **2002**, *106*, 11823.

[118] C. Guo, J. Wang, H. Liu, J. Chen, *Langmuir*, **1999**, *15*, 2703.

[119] P. Innocenzi, P. Falcaro, D. Grosso, F. Babonneau, *J. Phys. Chem. B*, **2003**, *107*, 4711-4717.

[120] R. M. Almeida, C. G. Pantano, *J. Appl. Phys*., **1990**, *68*, 4225-4232.

[121] D.R. Lide, *Handbook of Chemistry and Physics*, CRC press, 72nd Edition, **1991**, 4-95.

[122] L.D. Pettit, A. Royston, *J. Chem Soc. A*, **1969**, 1570-1573.

[123] F.A. Cotton, G. Wilkinson, *Advanced Inorganic Chemistry*, 3rd ed., Interscience Publishers, John Wiley and Sons, **1972**, 893-894.

[124] H. Kozuka, S. Sakka, *Chem. Mater*., **1993**, *5*, 222-228.

[125] M. Epifani, C. Giannini, L. Tapfer, L. Vasanelli, *J. Am. Ceram. Soc*., **2000**, *83*, 2385-2393.

[126] A. Babapour, O. Akhavan, A.Z. Moshfegh, A.A. Hosseini, *Thin Solid Films*, **2006**, *515*, 771-774.

[127] G. Mitrikas, C.C. Trapalis, G. Kordas, *J. Non-Cryst. Solids*, **2001**, *286*, 41-50.

[128] S. Sakka, H. Kozuka, *J. Sol-Gel Sci. Technol*., **1998**, *13*, 701.

[129] E. Della Gaspera, D. Buso, M. Guglielmi, A. Martucci, V. Bello, G. Mattei, M.L. Post, C. Cantalini, S. Agnoli, G. Granozzi, A.Z. Sadek, K. Kalantar-Zadeh, W. Wlodarski, *Sens. Actuators B*, **2010**, *143*, 567-573.

[130] T. Kobayashi, M. Haruta, M. Ando, *Sens. Actuators B*, **1993**, *13-14*, 545-546.

[131] H. Bi, W. Cai, C. Kan, L. Zhang, D. Martin, F. Trager, *J. Appl. Phys*., **2002**, *92*, 7491-7497.

[132] A. Babapour, O. Akhavan, R. Azimirad, A.Z. Moshfegh, *Nanotechnology*, **2006**, *17*, 763-771.

[133] D.R. Lide, in *Handbook of Chemistry and Physics*, CRC press, 87th Edition, **2007**, 8-21.

[134] H. Kita, H. Nakajima, K. Hayashi. *J. Electroanal. Chem*., **1985**, *190*, 141.

[135] F. Boccuzzi, A. Chiorino, S. Tsubota, M. Haruta, *Sens. Actuators B*, **1995**, *24–25*, 540.

[136] A. Yavuz Oral, Z. Banu Bahs and M. Hasan Aslan, *Appl. Surf. Sci.*, **2007**, *253*, 4593.

[137] H. Bahadur, A.K. Srivastava, R.K. Sharma, S. Chandra, *Nanoscale Res Lett*, **2007**, *2*, 469–475.

[138] L. Vayssieres, K. Keis, A. Hagfeldt, S.-E. Lindquist, *Chem Mater.*, **2001**, *13*, 4395.

[139] D. Bao, H. Gu, A. Kuang, *Thin Solid Films*, **1998**, *312*, 37.

[140] S. Amirhaghi, V. Craciun, D. Craciun, J. Elder, I.W. Boyd, *Microelectron. Eng.*, **1994**, *25*, 321.

[141] A. Yavuz Oral, Z. Banu Bahs, M. Hasan Aslan, *Appl. Surf. Sci.*, **2007**, *253*, 4593.

[142] F.C.M. Van de Pol, F.R. Blom, T.J.A. Popma, *Thin Solid Films*, **1991**, *204*, 349.

[143] B.M. Ataev, I.K. Kamilov, A.M. Bagamadova, V.V. Mamedov, A.K. Omaev, M.H. Rabanadov, *Mater. Sci. Eng. B*, **1999**, *68*, 56.

[144] L. Znaidi, G.J.A.A. Soler Illia, S. Benyahia, C. Sanchez , A.V. Kanaev, *Thin Solid Films*, **2003**, *428*, 257–262.

[145] I. Petrov, V. Orlinov, A. Misiuk, *Thin Solid Films*, **1984**, *120*, 55.

[146] L. Armelao, M. Fabrizio, S. Gialanella, F. Zordan, *Thin Solid Films*, **2001**, *394*, 90.

[147] J.J. Cavalieri, D.E. Skinner, D.P. Colombo, R.M. Bowman, *J. Chem. Phys.*, **1995**, *103*, 5378.

[148] D.R. *Lide, Handbook of Chemistry and Physics*, CRC press, 72nd Edition, **1991**, 4-112.

[149] A. Martucci, D. Buso, M. De Monte, M. Guglielmi, C. Cantalini,C. Sada, *J. Mater. Chem.*, **2004**, *14*, 2889.

[150] M. Ando, T. Kobayashi, S. Iijima, M. Haruta, *J. Mater. Chem.*, **1997**, 7, 1779.

[151] E. Widenkvist, R. A. Quinlan, B. C. Hollowayn, H. Grennberg, U. Jansson, *Cryst. Growth Des.*, **2008**, *8*, 3750.

[152] C. Damle, K. Biswas, M. Sastry, *Langmuir*, **2001**, *17*, 7156.

[153] L.M. Liz-Marzan, A.P. Philipse, *J. Phys. Chem.*, **1995**, *99*, 15120.

[154] G. De, C.N.R. Rao, *J. Mater. Chem.*, **2005**, *15*, 891.

[155] M.H. Yaacob, M. Breedon, K. Kalantar-Zadeh, W. Wlodarski, *Sens. Actuators B*, **2009**, *137*, 115.

[156] T. Xiao, L. An, W. Zhang, S. Sheng, G. Xiong, *Catal. Lett.*, **1992**, *12*, 287.

[157] M. Penza, C. Martucci, G. Cassano, *Sens. Actuators B*, **1998**, *50*, 52.

Chapter 4

Colloidal approach to nanocrystalline thin films deposition

Contents

4.1 Introduction and background

The idea behind the colloidal approach to the synthesis of nanocomposite thin films is to overcome some limitations presented by the sol-gel method, as discussed in Chapter 2. Briefly, with standard sol-gel method it is difficult or even impossible to control the

composite material structure in terms of size, shape and size distribution of the different phases; a sort of control can be done by selecting the temperature of the thermal treatment to promote crystallization or crystals growth, or by using templating agents to tailor porosity, but an accurate managing of the forming crystals is quite hard to accomplish.

For a gas sensing device, since the sensing process is a surface phenomenon, materials properties like surface area, size of active nanoparticles, homogeneous dispersion of the particles inside the matrix, maintaining the interface between different phases and proper porosity are of paramount importance, especially for optical sensors, because high optical quality of the nanocomposites is needed.

In the recent years, many papers dealing with size and shape control of metals [1-3] semiconductors [4,5] and oxides [6-8] nanocrystals have been published, a lot of them dealing with colloidal syntheses of nanomaterials, so there is a great interest in developing nanoparticles with tailored properties.

In this chapter the colloidal synthesis of metals and oxides will be exploited for the synthesis of metal/oxides nanocomposites. The chapter is divided in the following parts: colloidal syntheses of the different metal and oxide NPs, TiO_2-based nanocomposites and ZnO-based nanocomposites deposited from colloidal solutions.

In the first part, the colloidal syntheses of the metals (Au, Pt, core@shell Au@Pt) and the oxides (TiO_2, ZnO) nanoparticles used in this study will be described and characterized.

Then thin films will be deposited from TiO_2 and Au NPs colloidal solutions after a proper surface modification in order to obtain stable and highly concentrated solutions: these nanocomposites have been tested at low temperatures for VOCs sensing and at high temperatures for reducing gases sensing. Afterwards, TiO_2 colloids were mixed with Au, Pt, both Au and Pt and also with Au@Pt nanoparticles in order to analyze the combination of the catalytic properties of Platinum together with the optical properties of Gold in the sensing performances of reducing gases.

In the last part, colloidal solutions of Au and ZnO nanocrystals (pure and doped with transition metal ions like Mn, Ni, Co) will be mixed together after a purification and concentration protocol and used for the deposition of thin films as CO sensors. Due to preliminary sensing results, Cobalt was selected as best dopant materials, and a study on the electrical properties of thin films from ZnO (Co-doped and undoped) and Au colloids will be reported.

4.2 Colloidal Syntheses of Metals and Oxides

4.2.1 Au nanoparticles

4.2.1.1 Synthesis

Gold colloids of about 15 nm diameter were prepared according to the well-known Turkevich method [9,10] by reducing $HAuCl_4$ with trisodium citrate in water. The main reason for using this synthesis lays on the weak bond between Au NPs surface and citrate ions: in fact the absence of strong ligands allows to exchange the complexing agents with a variety of molecules like thiols, amines or polymers. But despite the operative easiness and the absence of strong capping agents, Au NPs produced with this method are of good quality, being usually monodisperse (the standard deviation is below 10%) and of spherical shape, even if some faceting has been observed.

In a standard procedure, $HAuCl_4$ was dissolved in Milli-Q water (18 MΩ) at a 0.5 mM concentration, obtaining a transparent, pale yellow-colored solution due to the presence of dissolved $AuCl_4^-$ ions. The Au solution was heated and brought to boiling point, while separately, a 1% (wt) tri-sodium citrate aqueous solution was prepared and preheated at 70 °C. The latter was added to the former under vigorous stirring in a proper amount depending on the desired Au NPs size: in a typical synthesis for about 13 nm particles, 12 mL of 1% trisodium citrate aqueous solution was added to a 200 mL boiling solution of 0.5 mM $HAuCl_4$.

The resulting solution turned immediately colorless, due to the reduction from Au^{3+} to Au^+ by citrate species; within few minutes the solution turned dark blue, purple and eventually wine red, because of Au NPs nucleation and growth. In a thorough study, Lee and coworkers [11] explained that the reasons for the different changes in color are related to the formation of wire-like clusters of small Au spheres in the early stages of the reduction process, that eventually separate and grow up to final size. In fact it is known from Mie theory that the relative proximity of metal NPs can produce a coupling of the SPR frequencies [12], causing a red shift of the SPR peak, explaining the blue color in the initial stages of Au NPs formation.

After the solution turned red-wine colored and no more color changes were detected, it was stirred at boiling point for an additional 15 minutes and then it was cooled down to room temperature. In order to remove the unreacted chemicals and obtain clean and concentrated solutions for thin films deposition, a concentration protocol has been

developed: 10.000 g/mol average molecular weight poly(N-vinylpyrrolidone) (PVP) was chosen as complexing agent because of the high solubility of PVP-protected particles in water and alcoholic solvents, and because of the capability of PVP to bind to Au NPs thanks to O and N atoms of the pyrrolidone ring [1], thus providing a steric stabilization.
PVP was dissolved in water to yield a 50 g/l concentration, and then this solution was mixed with aqueous gold colloids under constant stirring according to the ratio gPVP/molAu = 1000. After two hours, the solution was purified by means of precipitation/redispersion processes: since the starting Au colloidal solution was highly diluted, a massive amount of non-solvent was required to induce destabilization of the solution and then flocculation and precipitation of Au NPs, or without any non-solvents, an extensive centrifugation procedure (10000 rpm for 2 hours, or 14000 rpm for 30 minutes) was required. So the PVP-protected Au NPs in water were first concentrated in a rotary evaporator up to about 2mM concentration in molar gold (so the total volume of the solution was reduced about 4 times) and then they were precipitated with excess acetone (usually a ratio acetone:water=2:1 is enough to induce flocculation): as soon as the colloidal suspension changed color from wine red to violet, indicating the beginning of the precipitation process, no more acetone was added and the resulting solution was centrifuged at 4000 rpm for 5 minutes. The supernatant was discarded and the precipitate was redispersed in ethanol leading to a 30 mM concentrated stock solution. Ethanol was chosen as solvent for the Au NPs stock solution because the oxide solutions (TiO_2 and ZnO) are both in alcoholic media, and because ethanol is a good solvents for films deposition via spin coating (homogeneous depositions, good wettability of hydrophilic substrates, fast evaporation rate). The concentrated solution was stable for several months, and no changes in Au SPR peak has been observed in that period of time.
As reported in literature [13], it is quite difficult to obtain very small Au NPs (below about 8 nm) with the Turkevich method: nevertheless, a lot of different procedures to synthesize small Au NPs have been published in the last years, starting with the well-known Brust-Schiffrin method [14] that involves the reduction of Au precursor by sodium borohydride ($NaBH_4$) in a two phase (water and toluene) reaction in the presence of dodecanethiol. Then Jana and Peng [15] presented a series of syntheses in single phase to obtain Au NPs of various sizes ranging from 1 to 15 nm, and nearly monodisperse. More recently, extra small Au nanocrystals (below 2 nm in size) with luminescence properties have also been synthesized with strong reducing agents in the presence of thiols [16-18]. All these syntheses have the intrinsic problem of obtaining Au NPs with a strong ligand,

that permits the solubilization only in organic solvents. There are of course methods to replace a capping agent through multiple cycles of precipitation and redispersion, but to avoid this long process a different procedure for the synthesis of small Au NPs was followed: Au NPs of about 2.7 nm in size were prepared adapting the synthesis described by Hao and Lian [19], in which Au^{3+} ions in a methanolic solution were reduced by rapid adding a methanolic solution of sodium borohydride in the presence of polyvinvylpyridine.

In a typical synthesis, 6 mL of a 0.02M $HAuCl_4$ solution in methanol are added to a previously prepared 100 mL metahnolic solution containing 40 mg of PVP under stirring. Separately, 5.5 mL of 0.1M $NaBH_4$ methanolic solution is prepared, and after 15 minutes it is rapidly added under vigorous stirring to the Au precursor solution. After the addition of the reducing agent, the solution was let stir for 1 hour, than the solvent was removed by evaporation obtaining a dry powder that was easily dispersed in water, precipitated with acetone and eventually dispersed in ethanol in a 30 mM stock solution. If a further purification was needed, the precipitation with acetone / redispersion in water procedure can be repeated up to 3 times, with the last redispersion being in ethanol. The concentrated solution was stable for 1-2 months, after that period of time a slight modification of the Au SPR peak starts to appear, possibly caused by Ostwald ripening of the particles.

4.2.1.2 Characterization

Optical spectroscopy is the easiest and fastest way to get an insight on the synthesized nanoparticles: in fact thanks to their localized surface plasmon resonance peak and to its sensitivity to size and shape of the NPs, a first idea on the quality of the synthesis can be obtained. Figure 4.1 shows the optical absorption spectra for small Au (from now on called Au3, because the actual size evaluated with TEM is about 3 nm, see below) and big Au (from now on called Au13, because the actual size evaluated with TEM is about 13 nm, see below) NPs in ethanol, after the purification process: a sharp difference can be detected, since bigger particles show a definite peak centered at about 520 nm and a pink-red color, while smaller particles show only a shoulder at wavelengths lower than 500 nm and color of the solution is brownish, as expected from the relationship occurring from size of the Au clusters and UV-Vis absorption properties [20].

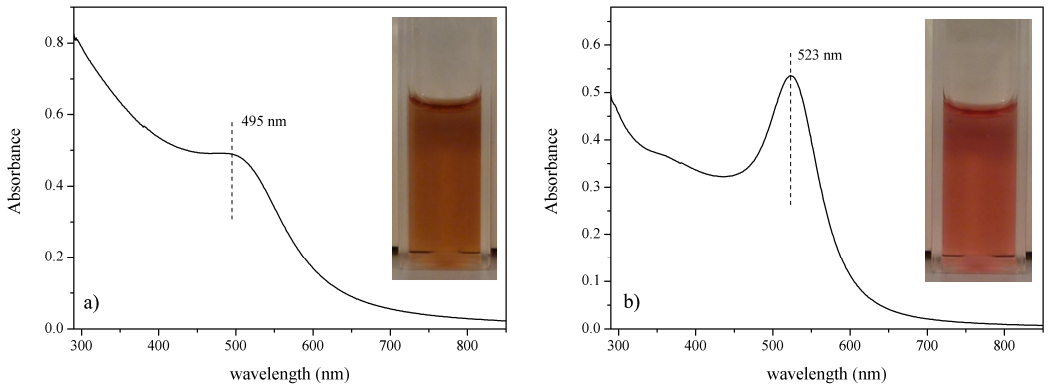

Figure 4.1. Optical absorption spectra of Au3 (a) and Au13 (b) NPs in ethanol capped with PVP. The insets show a picture of the colloidal solutions inside a standard polycarbonate cuvettes (1 cm path length).

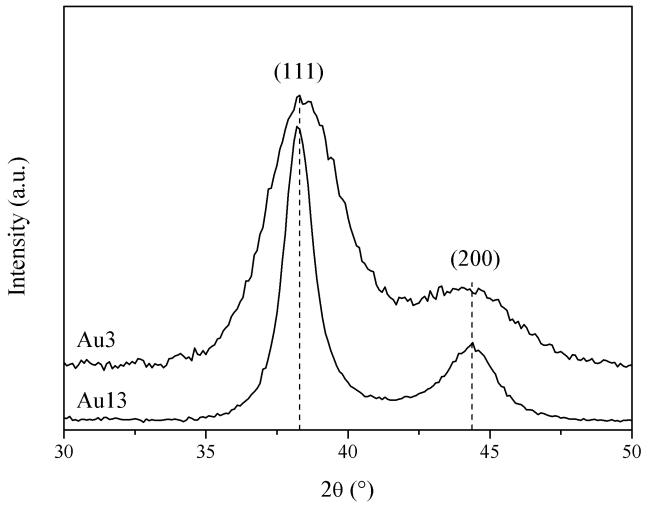

Figure 4.2. XRD patterns of Au3 and Au13 NPs showing (111) and (200) diffraction peaks.

The particles have been also characterized with XRD in order to have a confirmation of their crystallinity and to have a first idea of the particles size. Figure 4.2 shows the diffraction patterns of Au NPs synthesized with the two different syntheses: the cubic Au diffraction peaks at about 38.2° and 44.4° corresponding to (111) and (200) planes reflections (JCPDS No.04-0784) are clearly identified for the particles prepared with the Turkevich method, while for the particles reduced by $NaBH_4$ only the most intense peak is well defined, while the peak at 44.4° appears only as a shoulder. This is due to the fact that the smaller the crystals, the broader the diffraction peaks, according to the well known Debye-Scherrer formula: after fitting the experimental profiles with Lorentzian

functions, the crystallite size has been estimated to be 7.1±3.1 nm and 2.9±0.5 nm for the citrate and the sodium borohydride reduction, respectively.

The confirmation of the actual size is achieved with TEM analyses: a droplet of the diluted colloidal solutions has been deposited on a 300 mesh carbon coated copper grid and after drying the grids were directly imaged. Figure 4.3 shows the images for Au NPs synthesized with the two different syntheses and the size distribution measuring a minimum of 150 particles is also reported.

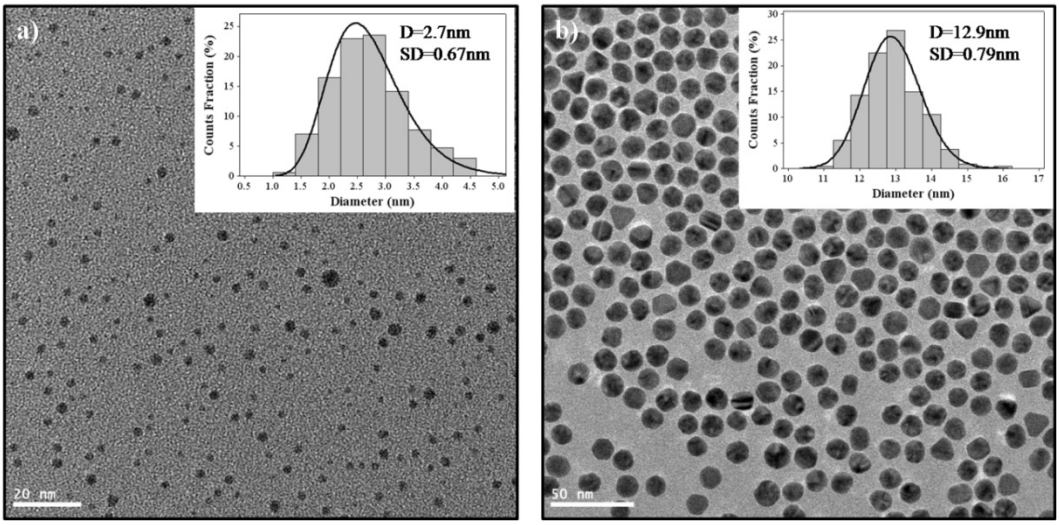

Figure 4.3. TEM micrographs of PVP-protected gold colloids of about 2.7 nm (a) and 12.9 nm (b). The particle size distribution histogram is shown in the inset.

As can be seen, Au NPs synthesized with $NaBH_4$ in methanol are quite small (2.7±0.7 nm), as expected from the shape of the optical absorption spectra, while the Turkevich synthesis leads to bigger particles (12.9±0.8 nm). Moreover, a quite big difference in the standard deviation can be experienced: in fact particles synthesized with the citrate method are rather monodisperse (the standard deviation is about 6.1%), while smaller particles are more polydisperse (standard deviation of about 24%). This because in the case of small Au NPs, the reducing agent is very strong, so the nucleation process occurs very quickly and the growth of the particles is limited by the rapid consumption of the precursor, as described by LaMer theory of nucleation and growth of nanoparticles [21], leading to small nanocrystals: moreover, being PVP a rather weak capping agent (compared for example to thiols), its presence helps reducing the size and narrowing the size distribution, but extremely small and monodisperse particles are very difficult to synthesize with the presented procedure. In fact Tsukuda *et al.* [22] reported a synthesis

similar to the one adopted here, obtaining quite small Au NPs (1.3 nm in diameter), but using almost 15 times the amount of PVP used in the presented procedure, and the standard deviation of the particles was about 23% as well.

On the contrary, in the Turkevich method the reducing agent is weak, in fact the synthesis has to be carried out at boiling point, because at room temperature the reduction does not occur, and so the nucleation and growth processes are quite long and the latter starts before the former has completed. This fact usually leads to big and polydisperse particles, but if the starting solution is diluted, the diffusion process is the rate limiting step of subsequent growth of initial nuclei and if it is let at boiling point a certain amount of time, the polydispersity is reduced by means of Ostwald ripening [23].

In the end, the particles size measured from TEM images and the crystals size evaluated from XRD patterns are in well agreement for the small particles, while they differ for the bigger ones; this is simply due to the fact that the Debye-Scherrer formula gives an estimation of the crystallites size, and not of the particles diameter: so it is likely that the small particles are monocrystalline, while the bigger particles are polycrystalline, as also confirmed by high resolution TEM images (not reported).

4.2.2 Pt nanoparticles

4.2.2.1 Synthesis

Platinum NPs of about 10 nm in diameter were synthesized with the polyol method adapting some already published recipes [24,25]. The polyol method has been widely adopted in the past for the synthesis of metals and oxides since it is easy to produce high quality nanoparticles with a range of sizes and shapes. This type of synthesis has been first developed by Fievet and coworkers for the synthesis of spherical NPs of metals and metal alloys [26]. The idea behind this process is the reduction of the metal precursor (usually a metal salt) by a polyol (usually ethylene glycol) at high temperature in the presence of a complexing agent (usually PVP). This synthesis became very popular due to its operative easiness and especially its versatility thanks to the ability for polyols to dissolve many precursor salts, their highly temperature-dependent reducing power, and their relatively high boiling points, allowing the production of many different metal and alloy nanoparticles. It is also possible to obtain NPs with a variety of shapes and with tunable size by selecting the type of capping agent and the ratio between the capping agent and the metal precursor [27]. Moreover, a detailed work has been recently published by Mavrikakis and Eichhorn [28] discussing the synthesis of Pt and Ru single,

alloys and core-shell NPs, confirming the possibility of complex structure formation with the polyol method.

In the case of Platinum, there are some studies discussing the effects of reaction parameters in the size and shape of the synthesized nanocrystals [24,25]: the operative parameters chosen for the synthesis presented here like sodium chloride (NaCl) and sodium nitrate ($NaNO_3$) concentration in order to get isotropic and almost spherical NPs of about 10 nm diameter, were based on the observations reported in these references.

In a typical synthesis, 67 mg of hexachloroplatinic acid (H_2PtCl_6) and 18.7 mg of NaCl were dissolved in 3 mL ethylene glycol, degassed and kept under inert atmosphere (nitrogen). Separately, 150 mg $NaNO_3$ and 55 mg PVP were dissolved into 13 mL ethylene glycol, degassed, and brought at 160 °C under inert atmosphere. After 20 minutes, the former solution was quickly injected into the latter: a change in color from pale orange to black was observed within few minutes. The Pt colloidal solution was kept at 160 °C under nitrogen for 30 minutes, then cooled down to room temperature, precipitated with excess acetone (about 2:1 in volume), centrifuged at 4000 rpm for 5 minutes and redispersed in ethanol leading to a 30 mM nominal concentration. The concentrated solution was stable at least 3 months, than a slight precipitation of big aggregates began.

4.2.2.2 Characterization

Optical spectroscopy is not useful to qualitatively evaluate Pt NPs since they don't present a surface plasmon resonance peak in the visible range: in fact only a tale of an absorption peak centered in the UV region is shown on the optical absorption spectrum reported in Figure 4.4a. As a matter of fact, the color of the colloidal solution was yellowish-grey or black, depending on the particles concentration, as shown in the inset, and no information, except the PT NPs formation, can be inferred from these data.

From XRD pattern reported in Figure 4.4b the peaks for cubic Pt are clearly detected (JCPDS No. 04-0802): in details, (100) and (200) reflections at about 39.8° and 46.2° are present, confirming the crystallinity of Pt NPs. Again, the Debye-Scherrer analysis was performed, and the evaluated crystals size is 9.5±0.3 nm.

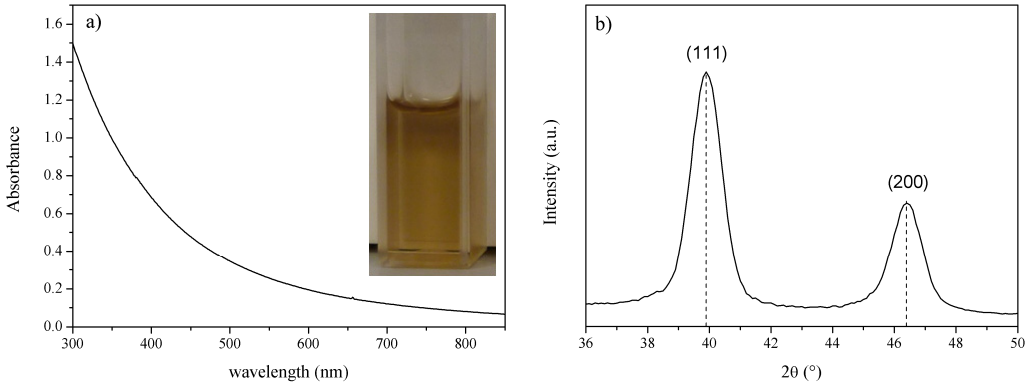

Figure 4.4. a) Optical absorption spectrum of PVP-capped Pt NPs in ethanol. The inset shows a picture of the colloidal solution inside a standard polycarbonate cuvette (1 cm path length). b) XRD patterns of the Pt NPs showing (111) and (200) diffraction peaks.

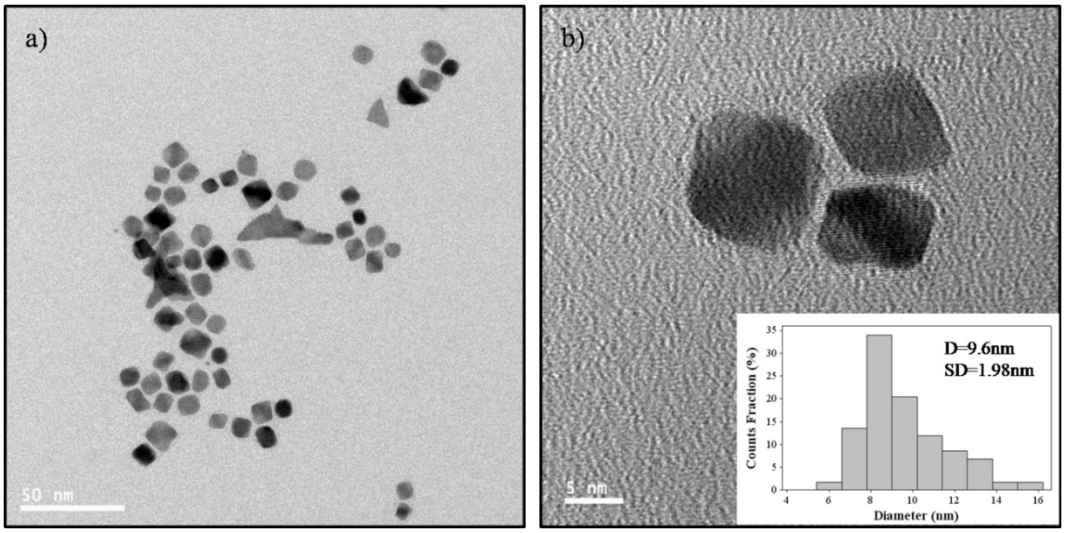

Figure 4.5. a) TEM micrograph of PVP-protected platinum colloids. b) High Resolution image showing the crystalline planes. The particle size distribution histogram is shown in the inset.

The TEM analysis performed on the colloidal solution deposited on a carbon coated copper grid reveals Pt NPs of spherical or faceted (cubic) shape, even if a small amount of anisotropic particles like tripods, tetrapods or octapods have been detected. These particular shapes have been observed also in the past [24], and are quite common for Pt nanocrystals produced by the polyol process: the fact that only a few particles with such shapes have been detected, confirms that the synthesis selected for obtaining isotropic particles works properly. The average size evaluated analyzing about 150 particles is

9.6±1.98 nm, so in perfect agreement with crystals size evaluated from XRD patterns, suggesting that the Pt NPs are nearly monocrystalline.

4.2.3 Au@Pt nanoparticles

4.2.3.1 Synthesis

The idea behind the synthesis of NPs with an Au core and a Pt shell lays in the distinctive optical properties of Au NPs and in the catalytic properties of Platinum NPs. In fact a combination of the two metals embedded inside an active matrix like TiO_2 can provide an increase in the performances of the sensing devices compared to the Au-TiO_2 or Pt-TiO_2 nanocomposites, because Pt can act as a catalyst in the gas detection kinetics, making the adsorption and the reaction of the gas faster, for example permitting to lower the operative temperature, while Au NPs are responsible for the optical modification of the nanocomposites, making possible the optical detection. So the idea is to synthesize Au cores of about 10nm in diameter and then cover this NPs with a shell of Pt: the main problem is the fact that a shell of metals like Pt or Pd is known to damp the Au SPR peak, as already reported [29,30]; in fact the optical properties of core-shell metallic NPs are dominated by the shell properties rather than the core [31], so a very thin shell of Pt is needed in order not to reduce too much the intensity of Au SPR peak, but to provide as well a catalytic effect. Moreover it has been also found that Pt alloying into Au nanocrystals can worsen Au optical properties damping the SPR peak [32], so the target of this work is the synthesis of Au@Pt core shell NPs with a thin Pt shell and without the formation of an alloy between the two metals.

The selected method for the preparation of these structures is the well established seeded growth method [33], and it is based on the synthesis presented by Lu *et al*. [34]: Au seeds of about 13 nm were again produced with the Turkevich method as described before. After cooling down to room temperature and adding water according to the evaporation loss to bring back the initial Au concentration (0.5 mM), a separately prepared solution containing Pt precursor in water (0.01 M) was added according to the desired Pt/Au molar ratio. Eventually the reducing solution (0.1 M ascorbic acid in water) was added under stirring, keeping the ratio ascorbic acid/Pt equal to 15. The ascorbic acid is a weak reducing agent, unable to reduce completely Pt ions at room temperature; but in this case Pt is completely reduced over Au NPs surface, because the presence of seeds promotes the heterogeneous nucleation.

The solutions show a progressive change in color for about 2 hours, more pronounced for samples with higher Pt amount, after which the color is stabilized. After 24 hours from ascorbic acid addition, PVP was added as capping agent keeping the ratio gPVP/mol(Au+Pt) = 1000 and then the solutions were concentrated in a rotary evaporator, precipitated with excess acetone and redispersed in ethanol to a final concentration of 30 mM based on Au atoms: in this way, the NPs concentration in the different batches is the same, and so a more accurate comparison between the nanocomposite films prepared starting from the different Au@Pt colloidal solutions can be made, even if the molar concentration of the metals (Au+Pt) is higher with increasing shell thickness. The concentrated solutions were stable at least for 2 months. Samples were named Au@PtX, being X the Pt/Au molar ratio.

4.2.3.2 Characterization

The Pt shell growth can be easily monitored with UV-Vis optical spectroscopy, since Au SPR peak is very sensitive to shell thickness, as discussed previously. Figure 4.6a shows optical absorption spectra for colloidal solution of Au NPs with different shell thickness, as synthesized in water after 24 hours from the reducing agent introduction, without the PVP capping. The shell thickness has been varied simply changing the amount of Pt precursor: for this reason, samples are labeled according to Pt/Au molar ratio, ranging from 0 (pure Au) to 2, as described before. Making simple calculations, without considering the lattice structure of the two metals (as a matter of fact, both cubic), but using bulk density values, the expected shell thickness should steadily increase from 0 to about 3 nm according to the Pt amount introduced.

From the optical absorption spectra a clear modification of Au SPR peak can be detected, being blue shifted and damped with increasing Pt amount. This behavior has been observed also in the past, and has been supported by simulations based on Mie theory of Au or Ag cores surrounded by a Pt or Pd shell of increasing thickness [29]. In Figure 4.6b a plot of Au SPR peak position as a function of the Pt/Au ratio is reported, together with a picture of the six colloidal solutions: again, the blue shift can be appreciated, together with a progressive change in color from pink red to dark brown. As can be seen, the evaluated shell thickness is in good agreement with the amount of Pt introduced, as expected.

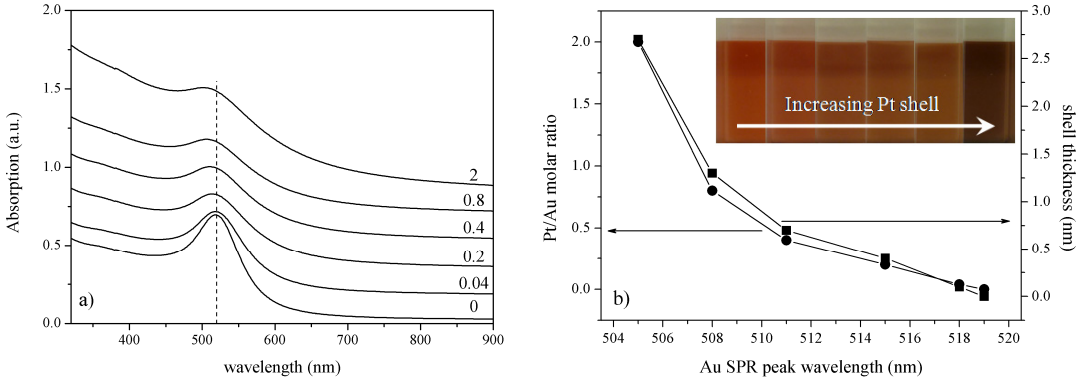

Figure 4.6. a) Optical absorption spectra of Au@Pt core@shell NPs in water with increasing Pt/Au molar ratio from 0 (Au cores) to 2; the dotted vertical line marks the Au cores SPR peak registered at 519 nm. b) Evolution of Au SPR peak wavelength with Pt/Au molar ratio; the inset shows a picture of the colloidal solutions inside standard cuvettes (1 cm path length).

To get a better insight on the shell formation, TEM analyses have been performed, and the results are reported in Figure 4.7. For very low Pt amount, *i.e.* for Au@Pt0.04 and Au@Pt0.2 samples (Figure 4.7a), no shell has been detected, because the Pt amount is not high enough to provide a detectable signal with this TEM resolution; moreover the NPs don't appear changed in size or shape compared to Au cores (see Figure 4.3), as expected. If the Pt amount is increased, a small modification in the nanoparticles can be detected, especially in the Fast Fourier Transform (FFT) analysis of high resolution images, where Pt lattice planes can be recognized (Figure 4.7b). Eventually if Pt amount is much higher (sample Au@Pt2), the NPs size is definitely increased, and also some faceting and irregular surface features start to appear, as shown in Figure 4.7c. The FFT analysis clearly shows both Pt and Au lattice planes, confirming a high amount of shell formation. This distinctive nanostructurated shell has been observed recently by Yamauchi and colleagues [35] in Au@Pt core@shell NPs synthesized by a sonochemical method, and the catalytic activity for methanol oxidation has been proved, confirming the premises that brought to these core-shell structures synthesis.

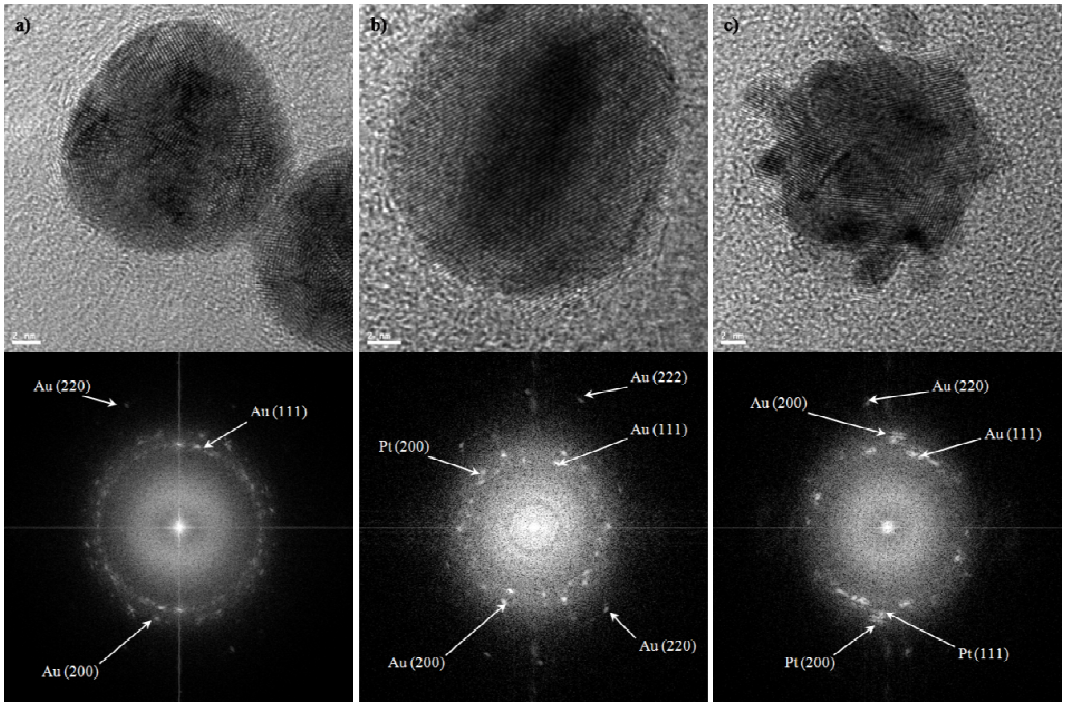

Figure 4.7. High resolution TEM images and respective FFT plots of Au@Pt0.2 (a), Au@Pt0.4 (b) and Au@Pt2 (c) nanoparticles.

After this preliminary study, it was decided to investigate the sensing properties of TiO_2 films containing two different Au-Pt core-shell structures: NPs with a thin shell so that Au SPR band wasn't modified too much (molar ratio Pt/Au=0.4, so with an expected shell thickness of about 1 nm) and NPs with a thicker shell, in order to have the certainty of Pt presence and to exploit its catalytic properties, sacrificing the Au SPR band shape (molar ratio Pt/Au=1.6, so with an expected shell thickness of about 2.5 nm). Figure 4.8 shows absorption spectra, XRD patterns and TEM images of these particles, after the PVP capping, precipitation with acetone and redispersion in ethanol as explained before.

As described before, a different optical spectrum related to Pt shell thickness can be recognized, with Au SPR more damped and blue shifted for the higher Pt/Au ratio. XRD analysis clearly shows the presence of Pt in the Au@Pt1.6 sample, because diffraction peaks become asymmetric at higher diffraction angles (*i.e.* smaller planes distances), as a consequence of the overlapping of Au and Pt diffraction peaks; since the particles size is small, the peaks are relatively broad, and so a clear distinction between the two is hardly possible, but Pt diffraction peaks can be definitely seen as shoulders at the right side of Au peaks. Eventually, TEM images confirm the spherical shape of Au@Pt0.4 NPs and the irregular nanostructured Pt shell of Au@Pt1.6 NPs. Analyzing the NPs average size, Au cores, Au@Pt0.4 and Au@Pt1.6 are 13.5±1 nm, 14.4±0.9 nm and 16.2±1.6 nm in

diameter, respectively: the increase in diameter due to the thicker shell is hereby confirmed.

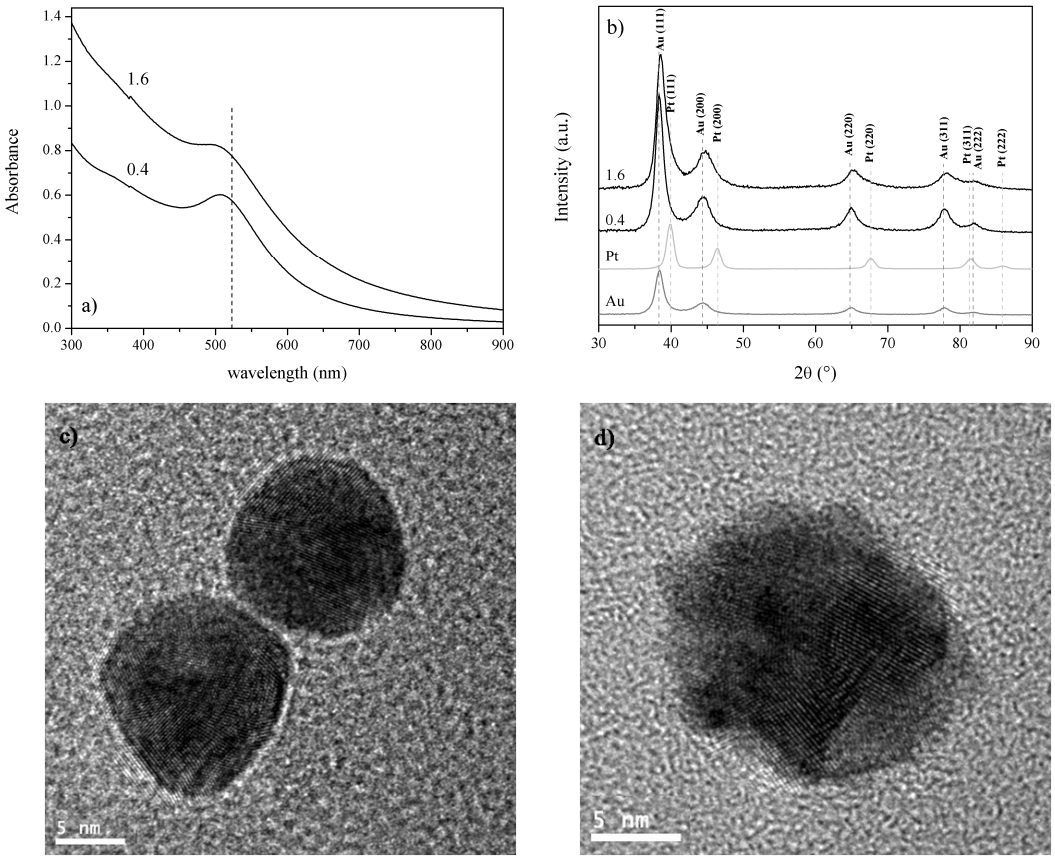

Figure 4.8. a) Optical absorption spectra of Au@Pt0.4 and Au@Pt1.6 NPs in ethanol capped with PVP; the dotted vertical line marks the Au cores SPR peak registered at 523 nm in ethanol. b) XRD patterns of Au (dark grey lines), Pt (light grey lines) and Au@Pt (black lines) NPs: theoretical diffraction lines for Au and Pt are reported as dashed lines. c) TEM image of two Au@Pt0.4 NPs. d) TEM image of one Au@Pt1.6 NP.

4.2.4 TiO_2 nanoparticles

4.2.4.1 Synthesis

TiO_2 is one of the most studied oxides in materials science research, due to its interesting physical and chemical properties, that can find applications in many scientific fields, like solar cells, gas sensing, photocatalysis, electrochromic devices, LEDs, hard coatings, biocompatible implants, pigments and so on. A detailed description of properties and applications of TiO_2 is not the purpose of this work, also because due to the enormous amount of published materials, it will be likely incomplete: an exhaustive review has been

presented recently by Chen and Mao [36], in which the authors describe different synthetic approaches to the synthesis of TiO_2-based nanomaterials, the physical and chemical properties of these nanomaterials, and their applications in photocatalysis, photovoltaic devices, electrochromic devices, hydrogen storage, sensing.

Wet chemical synthesis is one of the many possible ways to prepare TiO_2 NPs, but it has a lot of advantages for the preparation of optical devices: in fact it is possible to obtain small and extremely dispersed NPs in a proper solvent, that can be easily mixed with other colloidal solutions and deposited with standard methods (dip-coating, spin-coating, casting etc.), obtaining high quality thin films with the absence of scattering phenomena due to large particles or aggregation occurring between the particles. The synthesis adopted here is based on the work presented by Antonello *et al.* [37], because it has some advantages compared to similar syntheses: with this method it is possible to obtain extremely concentrated anatase nanocrystals of about 4 nm diameter, in alcoholic solvent without the need for an organic stabilizer or capping agent, compatible with colloidal suspensions of PVP-capped noble metal ethanolic solutions; moreover, it is possible to selectively precipitate the crystalline fraction by using the minimum amount of non-solvent, thus separating the amorphous NPs. In a typical synthesis, titanium isopropoxide (3 g) was added dropwise (0.5 mL/min) to a previously prepared solution consisting in 1.78 g of hydrochloric acid, 7.18 mL of methanol and 1.24 g of water under vigorous stirring. The solution was stirred at ambient temperature for one hour and subsequentely heated to 70 °C for four hours. Particles were then precipitated with acetone (about 3:1) and centrifuged at 4000 rpm for two minutes. The obtained precipitate was dispersed in methanol obtaining a clear colloidal sol of anatase TiO_2 NPs, of about 100 g/l concentration based on nominal TiO_2 weight. The concentrated solution was stable for days, allowing the deposition of several thin films without the need to prepare again the solution.

4.2.4.2 Characterization

The TiO_2 NPs synthesized with the described method resulted to be in the anatase phase, as confirmed by XRD and UV-Vis analyses shown in Figure 4.9. The diffraction pattern of tetragonal anatase structure (JCPDS No. 86-1157) can be easily recognized in Figure 4.9a: crystals size evaluated with the Debye-Scherrer relationship is 4.6±1.2 nm, in agreement with the particle size evaluated from TEM analyses (4.0±1.5 nm) previously reported [37].

Absorption spectrum (Figure 4.9b) show the typical TiO_2 absorption edge in the near UV range and transparency in the visible: no scattering features are detected, implying good colloidal stability and absence of aggregation phenomena, which is fundamental for composite materials to be used in optical applications.

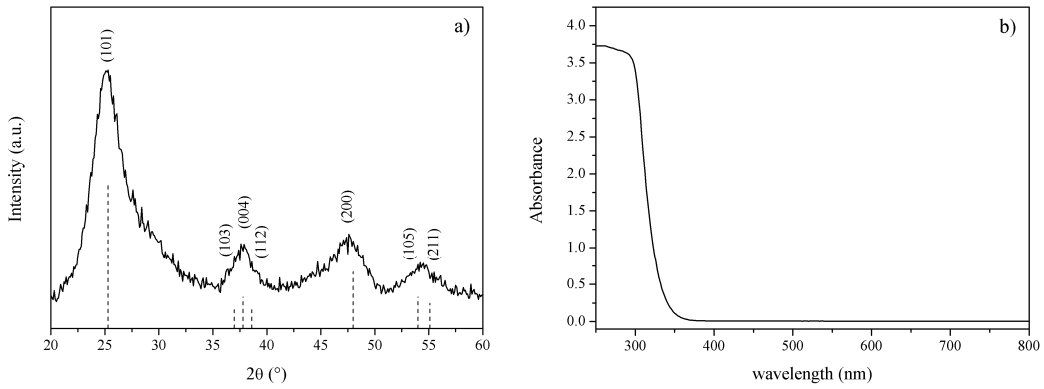

Figure 4.9. a) XRD patterns of the synthesized TiO_2 NPs. Main diffraction peaks and relative intensities for anatase crystalline structure are also reported. b) UV-Vis optical absorption spectrum of the TiO_2 colloidal solution.

4.2.5 ZnO-based nanoparticles

4.2.5.1 Synthesis

Zinc Oxide is another widely investigated material: the first reported studies about ZnO properties and characterization date back to the 1930s [38]. Its wide direct band gap (3.36 eV at 25 °C [39]) make ZnO an interesting materials for a wide range of applications, especially in optoelectronic devices; moreover many publications have been recently presented showing the the possibility to grow ZnO epitaxial layers, quantum wells, nanorods and related objects or quantum dots, on the hope to obtain a material for applications as: blue/UV optoelectronics like light-emitting or even laser diodes (in addition to the GaN-based structures), semiconductor spintronic, transparent, highly conducting oxide (TCO), when doped with Al, Ga, In or similar elements, as a cheaper alternative to indium tin oxide (ITO). Detailed and exhaustive reviews on properties and applications of ZnO have been published recently by Oxgur *et al.* [40], Djurisic and Leung [41], and Klingshirn [42], focused mainly on the physics of optical and electronic properties, the doping mechanisms and the influence of defects in ZnO properties.

As far as production methods are concerned, like for TiO_2 there is a lot of published material describing different syntheses for the production of ZnO structures: in the review published by Wang [43], different synthetic approaches to the preparation of ZnO

nanostructures like rods, belts, spirals, rings are described together with potential applications, while Liu and coworkers [44] presented a seeded-growth route to the synthesis of complex and oriented ZnO structures. Wet chemical synthesis of ZnO NPs has been chosen for the same reasons explained in the previous section for TiO_2 synthesis; a few years ago Spahnel presented a review on colloidal syntheses of ZnO [45], while recently a review on different approaches to the synthesis of ZnO 1-dimensional nanomaterials via solution process has been published by Deng and coworkers [46].

The synthetic procedure employed here is adapted from the work presented by Gamelin and coworkers [47]: briefly, 500 mg of Zinc acetate dihydrate (ZnAc) are dissolved in 22.5 mL dimethyl sulfoxide (DMSO); separately, 750 mg tetramethylammonium hydroxide (TMAH) are dissolved in 7.5 mL ethanol (EtOH). The TMAH solution is added dropwise (about 2 mL/min) to the Zinc solution under vigorous stirring at room temperature; after 10 minutes the solution is heated at temperatures ranging between 40 °C and 60 °C for 1 hour to promote Ostwald ripening of the particles. To prepare ZnO NPs doped with metal ions, it is sufficient to substitute the desired amount of Zn precursor with the dopant precursor, keeping the Zn+dopant molarity constant (see Appendix section for the synthesis details). The ZnO doping was performed with several transition metal ions: manganese (from manganese acetate tetrahydrate), nickel (from nickel acetate tetrahydrate) and cobalt (from cobalt acetate tetrahydrate).

After 1 hour at 40-60 °C, the solution was let cool down to room temperature, precipitated with the minimum amount (about 3:1 in volume) of methyl ethyl ketone (MEK) centrifuged at 1500 rpm for 5 minutes and redispersed in ethanol to a final nominal concentration of 0.8 M in molar zinc. The precipitating agent was chosen based on the quality of the washed particles: if using acetone for example, a higher amount of amorphous and less crystalline particles precipitate, and the redispersion in ethanol is sometimes incomplete, with the presence of big aggregates. The concentrated solutions were stable for few hours, while the as-synthesized NPs were stable several days.

4.2.5.2 Characterization

Zinc Oxide NPs synthesized with this method are found to be in the wurtzite crystalline structure, with a mean diameter ranging from about 3 to about 10 nm depending on the synthetic parameters. A first study on the kinetics of growth of the particles has been performed, letting the ZnO (pure and doped) colloids grow at room temperature up to 2 days after the TMAH addition: Figure 4.10 shows typical XRD patterns for wurtzite ZnO

nanocrystals (JCPDS No. 36-1451) at different reaction times: a clear progressive sharpening and narrowing of diffraction peaks with increasing reaction time can be noticed, indicating nanocrystals growth, as also highlighted in the table showing the average crystals size evaluated with the Scherrer relationship fitting the five diffraction peaks with Lorentzian functions.

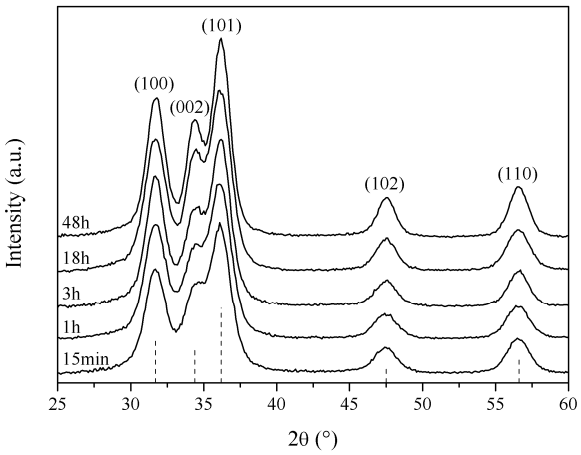

Reaction time (hours)	Crystallites size (nm)
0.25	6.7±0.3
1	7.0±0.5
3	7.5±0.5
18	7.4±0.4
48	8.9±0.6

Figure 4.10. XRD patterns of ZnO NPs synthesized with different reaction times; the theoretical diffraction lines of wurtzite crystalline phase are reported at the bottom. The table shows the crystallite size evaluated with the Scherrer relationship.

The same kinetics growth study has been performed on ZnO NPs doped with different metal ions (Co, Ni, Mn, 5% molar ratio with Zn), and interestingly the average size is smaller compared with undoped ZnO NPs, and also the effect of reaction time in growing the particles is less pronounced: in fact for pure ZnO the average crystallite size after 48 hours is about 9 nm, while for all the doped NPs it is about 5 nm; moreover the undoped particles grow about 30% in diameter from 1 to 48 hours of reaction, while all the doped crystals grow between 15 and 20%. All these results are summarized in Table 4.1.
These effects can be ascribed to the difference in size between Zn^{2+} ions and the other metal ions: since the dopants are substitutional to Zinc in the ZnO lattice structure, as described in the literature [47], the ZnO crystalline cell undergoes mechanical stresses due to the difference in size between the different cations, and so the excessive growth of the crystals is energetically unfavorable, because the increase in lattice energy due to the mechanical stress is not balanced by the reduction in the surface/volume ratio.

Table 4.1. Average crystallite size as a function of reaction time for ZnO NPs doped with different metal ions (doping level is 5%) evaluated with the Scherrer relationship and averaged on 5 diffraction peaks.

Reaction	Crystallites size (nm)		
Time (h)	ZnO:Co	ZnO:Ni	ZnO:Mn
1	4.3 ±0.5	4.6 ±0.3	4.4 ±0.4
8	4.5±0.4	5.5 ±0.5	4.6±0.5
24	4.8±0.5	5.5 ±0.5	5.2±0.7
48	4.9±0.6	5.4 ±0.5	5.2±0.6

A subsequent step in the optimization of the reaction parameters consisted in heating the colloidal solution at temperature between 40 °C and 60 °C just after TMAH addition: the effect on the particles is the same as increasing reaction time, since a growth of crystals has been observed: in this case though, the time scale is much smaller, as can be noticed in Figure 4.11. In fact after just 2 hours of heating the crystallites size is about 9 nm; nevertheless, the colloidal solutions after 2-3 hours started becoming cloudy, as a consequence of the destabilization of the repulsive forces between the particles, promoting their aggregation. So it was decided to perform the syntheses as described in the previous section, adding TMAH at room temperature and then heating the colloidal solutions for 1 hour, promoting NPs controlled growth through Ostwald ripening processes.

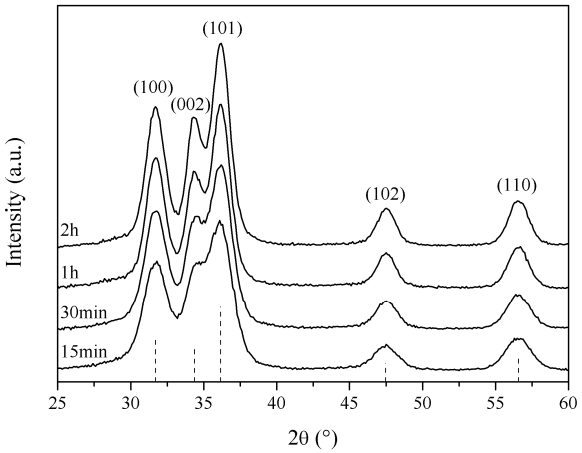

Reaction time (hours)	Crystallites size (nm)
0.25	6.2±0.4
0.5	7.0±0.3
1	8.6±0.6
2	8.7±0.6

Figure 4.11. XRD patterns of ZnO NPs annealed at 50 °C for different times; the theoretical diffraction lines of wurtzite crystalline phase are reported at the bottom. The table shows the crystallite size evaluated with the Scherrer relationship.

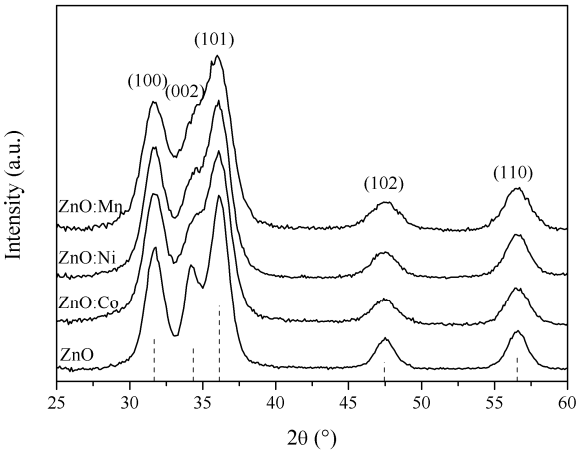

Sample	Crystallites size (nm)
ZnO	8.4±0.5
ZnO:Co	6.4±0.7
ZnO:Ni	6.3±0.5
ZnO:Mn	5.5±0.5

Figure 4.12. XRD patterns of ZnO and doped-ZnO NPs (doping level is 2.5%) annealed at 50 °C for 1 hour; the theoretical diffraction lines of wurtzite crystalline phase are reported at the bottom. The table shows the crystallite size evaluated with the Scherrer relationship.

The same experimental procedure has been repeated for the synthesis of doped ZnO NPs, to analyze the effect of the mild heating on the growth of the ZnO nanocrystals containing different metal ions. The results are reported in Figure 4.12: as can be seen, doped NPs are smaller compared to undoped ones, as a consequence of the stresses that generate inside the particles due to the difference in size between the ions. Moreover ZnO:Mn nanocrystals have the lower crystallite size, and this is maintained also in the thin films deposited from these solutions and heated at 500 °C (see section 4.3.2.2).

As it will be explained in detail later, due to better sensing results, Cobalt was chosen as ion to dope ZnO with, so a more accurate study on ZnO:Co NPs was performed, changing the doping concentration, and analyzing the effect on structural and optical properties. As anticipated before, the introduction of a different metal ion inside the ZnO lattice structure causes tensile or compressive stresses according to the size of the dopant ion (ions bigger than Zn^{2+} cause compressive stresses, ions smaller than Zn^{2+} cause tensile stresses): it is easy to understand that the higher the dopant amount, the more intense the stresses, and consequently the smaller the ZnO particles, keeping synthetic parameters constant. This fact can be easily seen comparing XRD patterns for ZnO and ZnO:Co NPs with Co amount equal to 1%, 2.5% and 5% heated at 40 °C for 1h (Figure 4.13) and at 60 °C for 1h (Figure 4.14), and evaluating the crystallite sizes through the Scherrer relationship.

A clear decrease in particles size is experienced increasing the Cobalt concentration, and also a slight shift towards smaller angles (*i.e.* bigger lattice distances) in XRD peaks can be detected (inset of Figure 4.14). This shift is consistent with a distortion of the crystalline cell of ZnO due to the introduction of substitutional Co^{2+} ion: being Zn^{2+} ion sligltly smaller than Co^{2+} (ionic radii inside crystals are 60 and 65 pm for Zn^{2+} and Co^{2+}, respectively [48]) the introduction of Cobalt causes an increase of the lattice parameters of wurtzite due to the compressive strength generated from the size difference between the two ions, resulting in a shift of diffraction peaks. Moreover comparing the diffraction patterns for the same cobalt doping at the two different heating temperatures, a clear effect of temperature in increasing the NPs size can be seen, as experienced also for pure ZnO NPs, even if this effect is less pronounced for high cobalt content NPs, due again to the mechanical stresses that arise in the crystals that slow down or even prevent further growth.

A confirmation of this effect comes from TEM analyses on ZnO and ZnO:Co colloids, as shown in Figure 4.15: even if the quality of the TEM images is not high, due to the poor contrast between the ZnO NPs and the background, a slight trend in size of NPs going from pure ZnO (Figure 4.15a) to 5% Co doping (Figure 4.15 d) can be detected, together with a progressive loss of the spherical shape of the colloids, that become more branched and irregular, as a further confirmation of the stresses induced by high doping level.

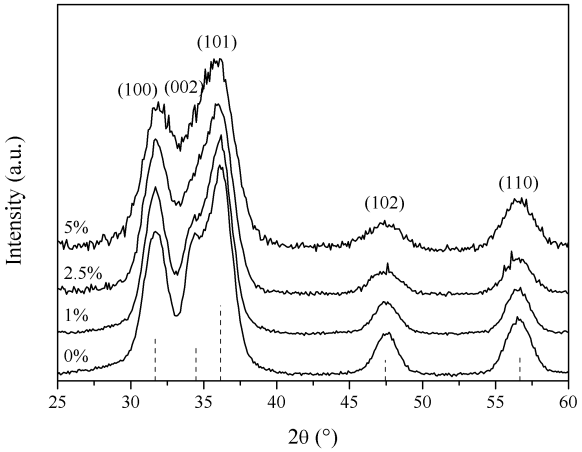

Co amount (%)	Crystallites size (nm)
0	6.7±0.3
1	6.4±0.5
2.5	5.3±0.5
5	4.7±0.5

Figure 4.13. XRD patterns of ZnO NPs doped with different concentrations of Co and annealed at 40 °C for 1 hour; the theoretical diffraction lines of wurtzite crystalline phase are reported at the bottom. The table shows the crystallite size evaluated with the Scherrer relationship.

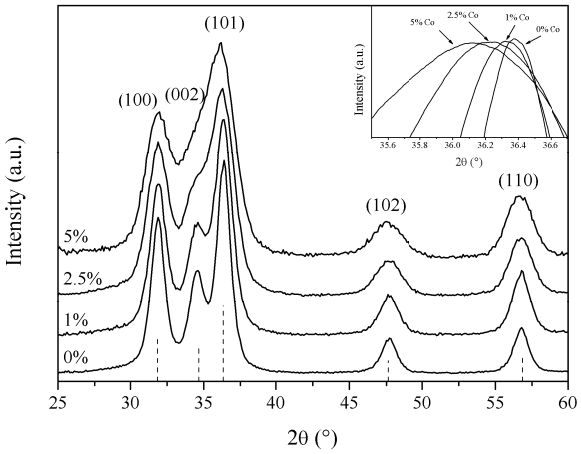

Co amount (%)	Crystallites size (nm)
0	10.9±0.6
1	8.7±0.7
2.5	6.5±0.6
5	5.6±0.6

Figure 4.14. XRD patterns of ZnO NPs doped with different concentrations of Co and annealed at 60 °C for 1 hour; the theoretical diffraction lines of wurtzite crystalline phase are reported at the bottom. The inset shows the effect of Cobalt doping in shifting and broadening the (101) ZnO peak. The table shows the crystallite size evaluated with the Scherrer relationship.

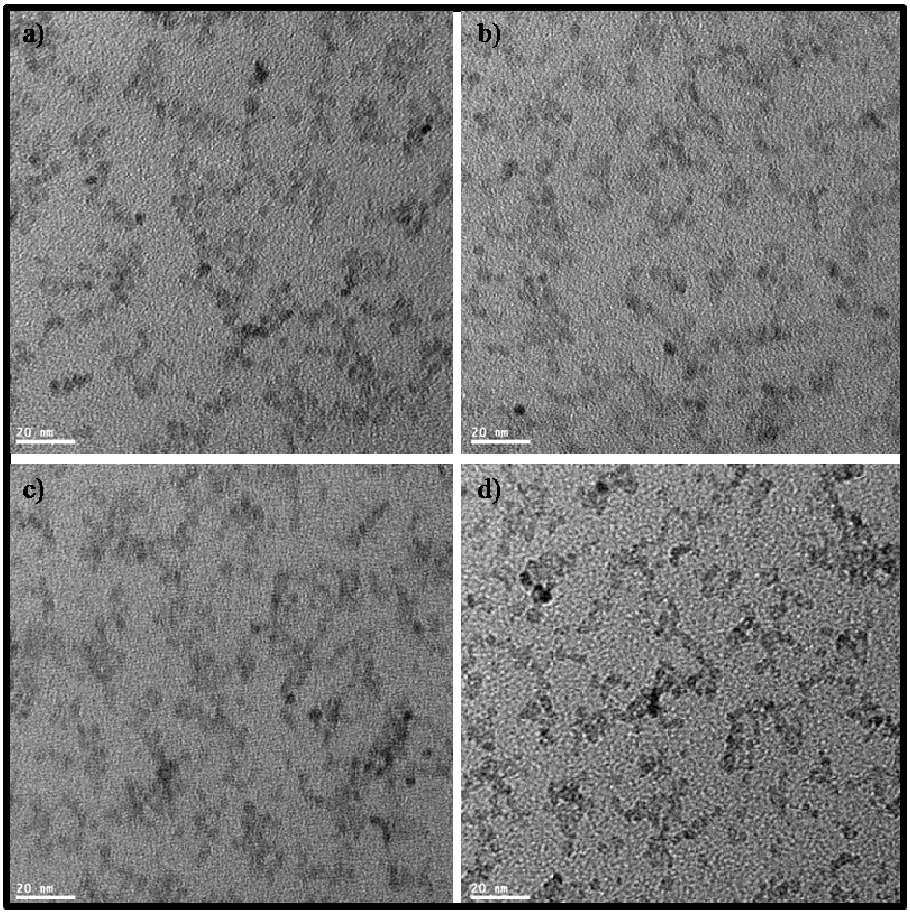

Figure 4.15. TEM image of ZnO and ZnO:Co colloids with different Co amount: a) 0%; b) 1%; c) 2.5%, d) 5% The scale bar in all images is 20 nm.

Optical characterization of the colloidal solutions in ethanol (nominal concentration in molar zinc 2.5 mM) show a clear absorption onset in the near UV due to ZnO band gap, and good transparency in the visible-NIR range, as shown in Figure 4.16.
The onset of absorption for bulk ZnO is in the range 3.2-3.4 eV (389-370 nm), as reported by several authors throughout the literature [49-51]: the colloidal solutions of ZnO NPs synthesized here absorb at slightly higher energies, as a consequence of band gap increase due to quantum size effect of small semiconducting particles.

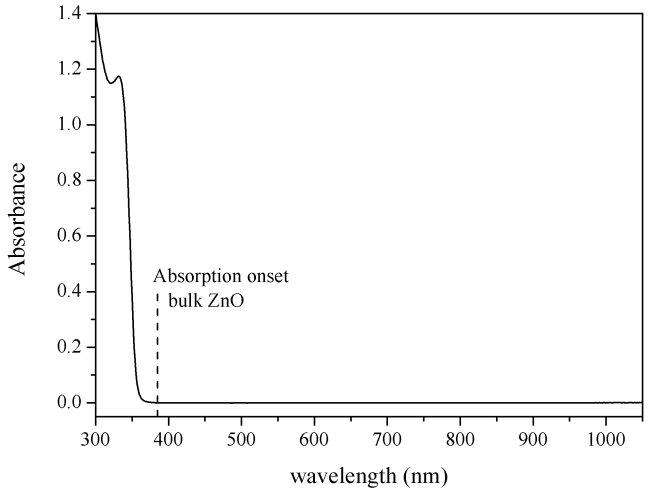

Figure 4.16. UV-Vis optical absorption spectrum of ZnO NPs in ethanol showing the UV absorption edge and good transparency in the Vis-NIR region.

When comparing the optical absorption spectra of ZnO NPs with different cobalt concentrations, two main effects can be detected: a blue shift and a damping of ZnO exciton peak (Figure 4.17 a), and the presence of three absorption bands in the 550-700 nm range (Figure 4.17 b). The effect on the ZnO exciton peak has been experienced with all the other metal ion dopants, with similar behavior between the different ions, so their comparison will be skipped for the sake of brevity; on the contrary, the absorption band in the visible range are distinctive of Cobalt.

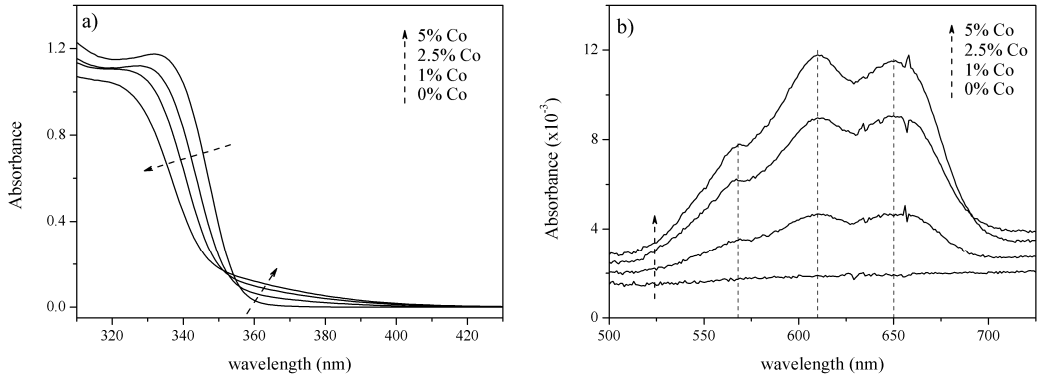

Figure 4.17. UV-Vis optical absorption spectra of ZnO and ZnO:Co colloidal solutions showing the change in UV absorption onset (a) and the typical absorption bands for Co^{2+} ions in tetrahedral coordination, highlighted as dashed lines (b).

The blue shift of the first exciton peak of ZnO can be explained considering what presented before about Co effect on crystallites size: since the band gap of nanocrystalline semiconductors can be tuned controlling the size of the crystals (when this size is in the quantum confinement range), the smaller the crystals, the wider the band gap; since the higher the cobalt amount, the smaller the ZnO crystallites, it is easy to understand the experienced shift in the UV absorption onset. This behavior has been observed also for the other metal ions doping. The absorption bands in the green-red range are due to Co^{2+} ions in tetrahedral coordination, more specifically in the tetraoxo cation coordination environment of wurtzite [52,53] , confirming the fact that Co^{2+} ion is substitutional to Zn^{2+} in the wurtzite crystalline structure.

4.3 Thin films deposition from colloidal solutions

4.3.1 TiO_2-based thin films

4.3.1.1 Synthesis

The final solutions for films deposition were prepared by mixing the methanolic suspension of TiO_2 NPs with PVP-capped Au, Pt or Au@Pt NPs in ethanol leading to a final TiO_2 concentration of 33 g/l and a noble metal:Ti molar ratio between 1 and 5%, according to the amount of metal NPs solution used. To adjust the final concentration to the desired value, ethanol was added; eventually, if a higher porosity was needed, PEG200 as templating agent was added keeping the PEG:Ti ratio equal to 0.67.

All the film samples were deposited by spin coating at 2000 rpm for 30 seconds on either SiO_2 and Si substrates and annealed in a muffle furnace directly at the desired temperature (ranging from 100 °C, to 500 °C) for 1 hour in air.

4.3.1.2 Characterization of TiO_2 films containing Au13 nanoparticles

All the samples prepared in this study are listed in Table 4.2.

Table 4.2. List of samples prepared indicating Au/Ti and PEG/Ti molar ratios, and the annealing temperature.

Name	Au/Ti (molar)	PEG/Ti (molar)	Annealing T (°C)
T3	0	0	300
T4	0	0	400
T5	0	0	500
TG3	0.05	0	300
TG4	0.05	0	400
TG5	0.05	0	500
TP3	0	0.67	300
TP4	0	0.67	400
TP5	0	0.67	500
TGP3	0.05	0.67	300
TGP4	0.05	0.67	400
TGP5	0.05	0.67	500

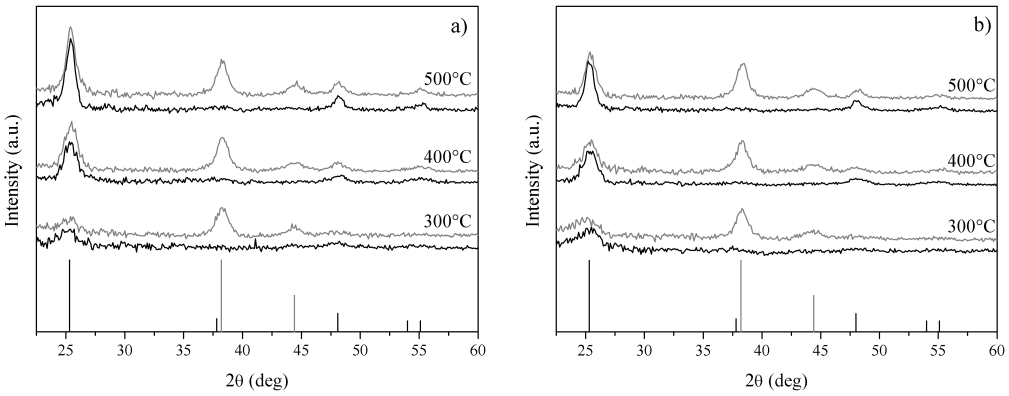

Figure 4.18. XRD spectra of: a) TiO_2 (black line) and TiO_2-Au (grey line) films without PEG. b) TiO_2 (black line) and TiO_2-Au films (grey line) with PEG. Theoretical diffraction lines of TiO_2-anatase (black line) and Au (grey line) are reported at the bottom.

XRD measurements performed on thin films (Figure 4.18) confirm the crystalline anatase phase of TiO_2 (JCPDS No. 84-1285) and show also Au peaks (JCPDS No. 04-0714) for the TG and TGP series. Thermal treatment affects the XRD peak width, which is related to crystallite size. Mean dimensions evaluated by applying the Scherrer equation are reported in Table 4.3 for both the crystalline phases. TiO_2 NPs grow in size at higher temperatures, due to coarsening of the particles, while estimated dimension at 300 °C annealing is comparable with the as-synthesized colloids. In PEG containing samples, the TiO_2 particle diameter has been estimated to be slightly smaller as compared with PEG-free samples at the same annealing temperature. It is likely that the porosity introduced by thermal decomposition of PEG, as will be discussed later, slows down the growth processes of titania particles. From these data, it is also shown that gold peaks do not undergo any relevant change in shape and intensity, indicating good Au NPs stability up to 500 °C annealing.

SEM micrographs of PEG-free samples annealed at different temperatures are reported in Figure 4.19. Au NPs of spherical shape are homogeneously dispersed on a micron scale, and only very few small aggregates are evident: so almost no migration or major aggregation phenomena occur during the deposition and annealing processes. It is noteworthy that samples annealed at higher temperatures show higher surface roughness, as a result of the higher crystallinity and the larger crystal size. Moreover, PEG containing samples show a slight smoother surface, especially the 500 °C annealed sample.

Table 4.3. Crystal size values of TiO_2 and Au particles evaluated from the Scherrer equation using the diffraction peaks at 25.3° for anatase and at 38.2° for gold.

Temperature (°C)	Diameter (nm)							
	T series		TG series		TP series		TGP series	
	TiO_2	Au	TiO_2	Au	TiO_2	Au	TiO_2	Au
300	5.1	/	4.6	5.6	4.2	/	4	5.3
400	7.4	/	7.3	5.9	6.3	/	7.1	5.8
500	10.1	/	10.2	6.1	8.6	/	9.1	6.1

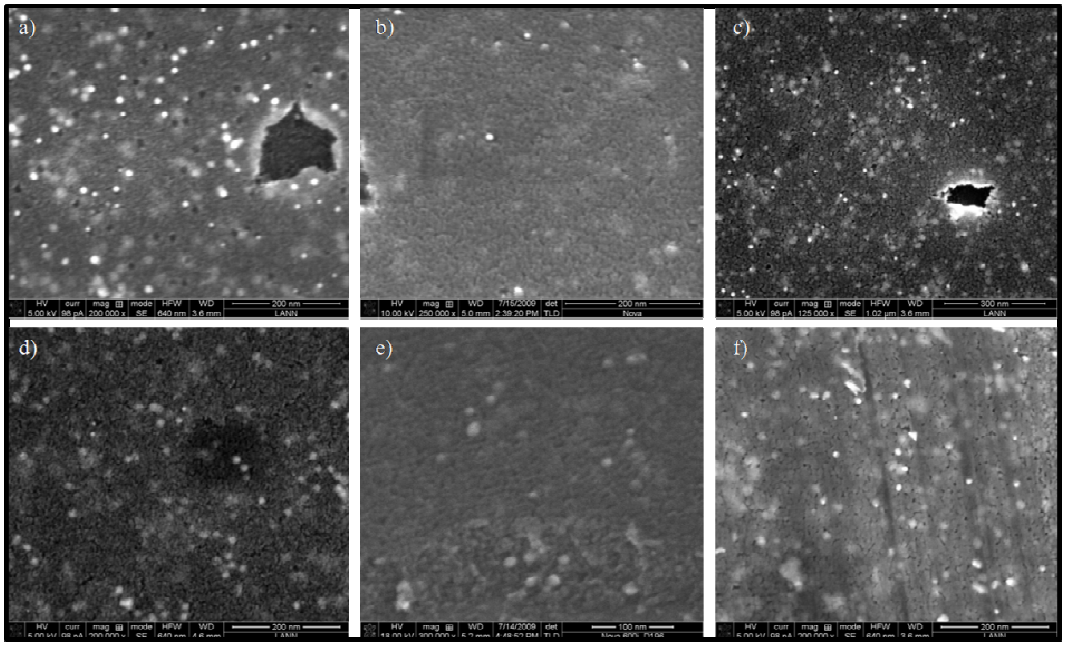

Figure 4.19. SEM images of TG3 (a), TG4 (b), TG5 (c), TGP3 (d), TGP4 (e), TGP5 (f) samples. Bright spots correspond to gold nanocrystals.

The presence of Au NPs is also evident in the cross-section TEM image (figure 4.20a) of the TG5 sample, where gold NPs appear as dark features, due to their higher mass-thickness contrast and scattering (diffraction) contrast, with respect to TiO_2. A good dispersion of metal particles inside the oxide matrix can be recognized, even if the presence of some small aggregates is also evident from this analysis. Au NPs are dispersed in the matrix with size in the range 8÷15 nm, consistent with the TEM analysis, and spherical shape, even if some slightly elliptical particles can be noticed in Figure 4.20a; in some cases it is possible to observe faceting (Figure 4.20c). The matrix is composed of TiO_2 crystalline NPs with dimension ranging between 5 and 12 nm, in agreement with XRD crystals size estimation. The thickness of the film is about 52 nm, in good accord with ellipsometric measurements (see below) and near the Si substrate surface the native SiO_2 layer of about 2-3 nm can be appreciated.

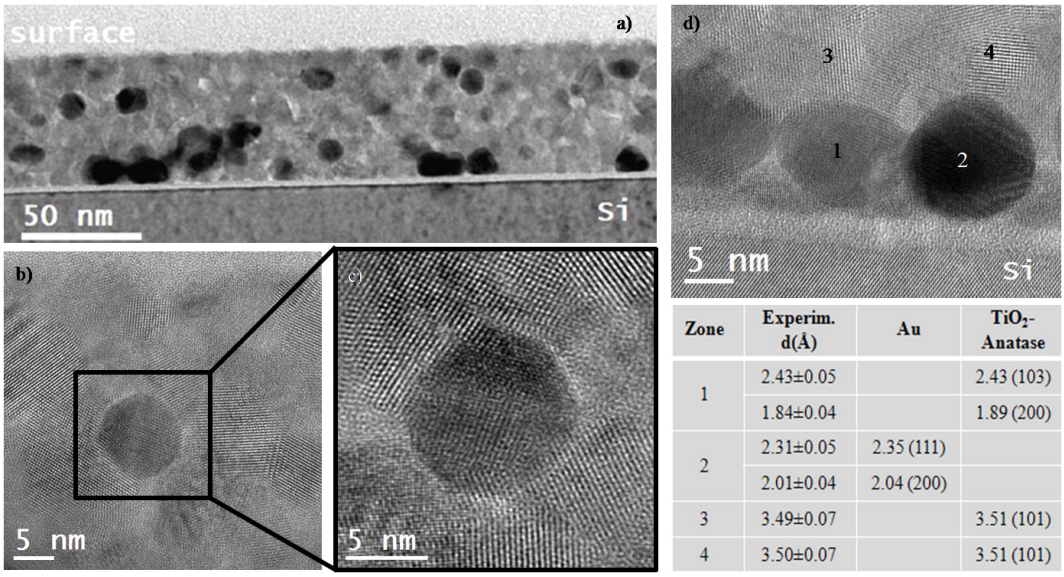

Zone	Experim. d(Å)	Au	TiO_2-Anatase
1	2.43±0.05		2.43 (103)
	1.84±0.04		1.89 (200)
2	2.31±0.05	2.35 (111)	
	2.01±0.04	2.04 (200)	
3	3.49±0.07		3.51 (101)
4	3.50±0.07		3.51 (101)

Figure 4.20. Cross section bright field TEM image of the TG5 sample (a), HRTEM image of one Au particle surrounded by TiO_2 particles (b), magnification the Au particle zone of figure 4b (c), and HRTEM image of Au and TiO_2 crystals (d): experimental lattice planes evaluated through FFT analysis, and theoretical lattice parameters for TiO_2 and Au for the 4 zones analyzed are shown in the table. Au NPs appear as darker spots compared to the lighter oxide matrix.

The HR-TEM picture in Figures 4.20b, 4.20c and 4.20d show the crystallinity of both TiO_2 and Au particles and lattice fringes of both phases are evident. The lattice distances retrieved by Fast Fourier Transform (FFT) of TEM data are found to be in agreement with the anatase and gold crystal structures, as confirmed by XRD data. EDX compositional analysis performed during TEM measurement also confirms the two phases detected, and gives a O/Ti ratio of 1.97, almost identical to the theoretical value for TiO_2 phase, and an Au/Ti atomic ratio of 0.06, very close to the nominal value. In Figures 4.20b and 4.20c a close facing of TiO_2 NPs on Au NPs is also observed, testifying a well developed Au/TiO_2 interface in this sample.

Figure 4.21 reports the absorption spectra of gold doped films with (Figure 4.21b) and without (Figure 4.21a) PEG. SPR peak of gold particles is clearly visible, and a progressive red-shift with increasing annealing temperature can be observed, for both the PEG-free and PEG-containing series.

It is well known that the SPR frequency is strongly related to NPs morphology (size and shape), to the dielectric properties of the material surrounding them and to the relative proximity of the particles [54]. From structural analyses no substantial morphology

changes of Au particles can be observed, while a very adherent coating of TiO_2 nanocrystals on Au particles is evident from TEM data. Thus we mainly attribute the change in plasmon peak position to the refractive index variation of the surrounding matrix. In each sample series, SPR wavelength is progressively red-shifted with increasing temperature, and this result is associated with the increase in refractive index of the material surrounding the gold particles.

This situation is confirmed from the results of the ellipsometry measurement. The refractive index curves of gold-loaded composite films are also shown in Figure 4.21 (c and d); Au NPs influence is evident, causing a typical anomalous dispersion curve in the SPR absorption region, because of the Kramers-Kronig relationship involving refractive index and absorption coefficient.

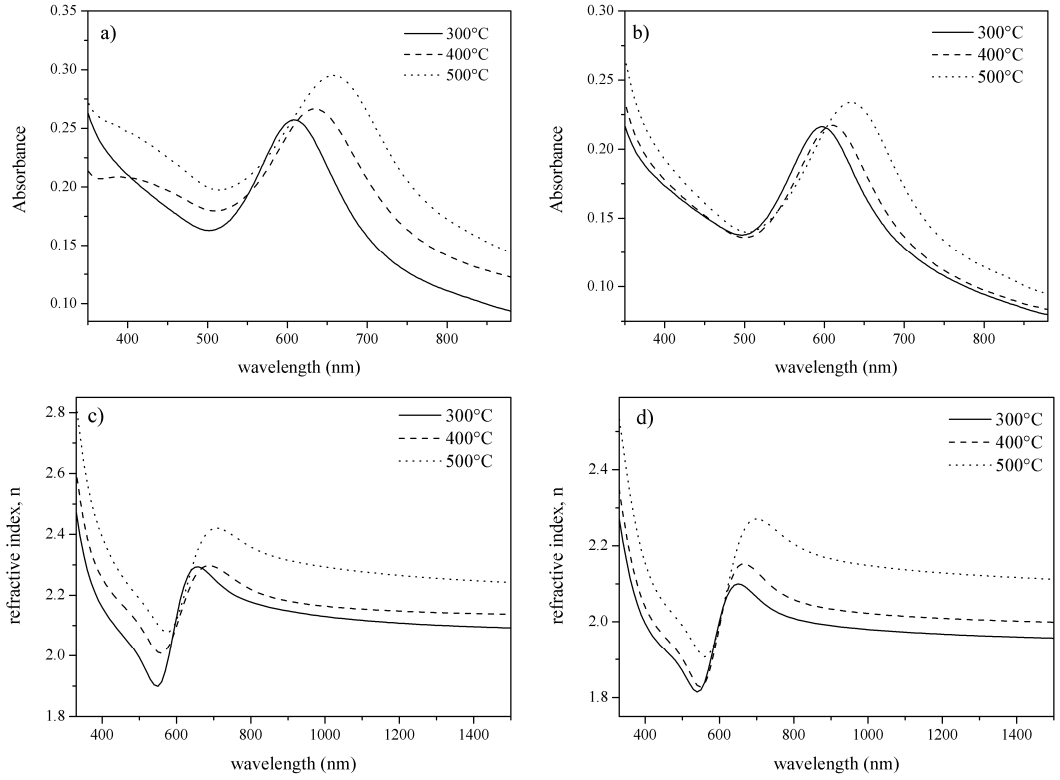

Figure 4.21. Effect of annealing temperature on UV-Vis absorption spectra of TG (a) and TGP (b) films, and on refractive index curves of TG (c) and TGP (d) films.

Refractive index values at 1100 nm are listed in Table 4.4. Values at that wavelength are here chosen as reference because they are sufficiently separated from the SPR absorption band to be modeled with a simple Cauchy dispersion model.

Refractive index is observed to increase for both PEG-free and PEG-doped samples with increasing annealing temperature. These data can be used to extract information about average film densification and porosity, but they do not take into account local structural variation. Differences in refractive index can be interpreted as differences in the amount of porosity by means of the effective medium optical models, where the most densified material has the highest refractive index. For this study the Bruggemann relationship was adopted [55], and the estimated porosity evaluated with this model can be written as follows:

$$Porosity = \frac{\left(\frac{n_{TiO_2}^2 - n^2}{n_{TiO_2}^2 + 2n^2}\right)}{\left(\frac{n_{TiO_2}^2 - n^2}{n_{TiO_2}^2 + 2n^2}\right) - \left(\frac{1 - n^2}{1 + 2n^2}\right)} 100\% \quad (4.1)$$

where n is the experimental refractive index and n_{TiO2} is the refractive index for fully dense anatase. Table 4.4 reports also porosity values obtained with this formula, where a value of 2.44 for refractive index at 1100 nm for bulk anatase was used [56,57]. The refractive index difference between 400 °C and 300 °C annealed samples is around 0.04, while the average difference in refractive index between 500 °C and 400 °C is around 0.12; a large increment of n occurs between 400 °C and 500 °C, as can be clearly seen from Figure 4.21, indicating that the densification process of TiO_2 colloids is activated at higher temperatures, affecting global porosity of the matrix [37].

Table 4.4. Refractive index values measured at 1100 nm, and estimated porosity through Bruggemann model for all Au-loaded samples.

Sample	Refractive index @ 1100 nm	Average Porosity (%)
TG3	2.117	22
TGP3	1.973	31
TG4	2.154	20
TGP4	2.015	29
TG5	2.277	11
TGP5	2.137	21

Moreover, the refractive index of PEG doped samples is lower as compared with PEG-free samples with a constant difference of about 0.14 for the three couples of samples, indicating, as expected, that PEG causes an increase in porosity after its thermal

decomposition (300 °C is sufficient for almost all PEG200 decomposition [58]). Similar evolution of porosity and refractive index with temperature is detected in Au-free samples (not reported).

Interestingly, optical data can be used also for a deeper appreciation of the local structure of composite film. SPR frequencies are in fact related to local dielectric properties of the matrix around the Au particles and the theoretical refractive index calculated from the SPR peak using the Mie relationship [59] is higher than the experimental refractive index of both the PEG doped and undoped TiO_2 matrices. The TiO_2-Au materials synthesized from colloidal solutions behave differently in comparison with previous results on TiO_2 sol-gel thin films doped with Au NPs [60], where the experimental refractive index is slightly higher than the theoretical value, maybe because of a higher amount of amorphous matrix or porosity adjacent to the Au crystals, compared to the average value of the sample, that can affect the position of the Au NPs SPR peak.

In this work, the optical results suggest that the material close to the gold surface has a higher refractive index as compared to the average value of the films, and thus a higher degree of densification of titania on gold particles can be inferred by these data.

These observations are summarized in Figure 4.22, where SPR peak position of Au-doped samples associated with refractive index of undoped matrix measured at the corresponding SPR wavelength is reported together with the theoretical refractive index calculated from SPR peaks by means of Mie relationship.

Moreover, increasing annealing temperature leads to further coverage of Au NPs, because the difference between theoretical and experimental refractive index becomes higher: thus, it is likely that in the TG3 sample, TiO_2 NPs are in poor contact with gold, while in TG4 and TG5 the coverage of Au becomes higher, while the global matrix densification is not complete, so leaving residual porosity.

This conclusion is also partially supported by HRTEM analysis of the TG5 sample presented in Figure 4.20, where a close facing of TiO_2 on Au particles is seen, even if no indication about the densification away from the Au particles can be retrieved from those images.

Such a mechanism of structural evolution is also suggested from the fact that the observed plasmon peaks broaden with increasing temperature (see Figure 4.21). Plasmon peak broadening could be partially associated to Au particles aggregation, even if the observed behavior can be better explained by the interaction between Au NPs and anatase surfaces [61,62]. This effect would agree with the increasing peak broadening with annealing

temperature in TG samples, since the interface area gets larger. In the TGP series samples, the structural evolution is delayed with respect to thermal treatment. Comparing TGP3 and TGP4 samples, the SPR wavelength only slightly increases while no broadening is observed, suggesting that at 400 °C the contact between Au and TiO_2 is not well developed. At 500 °C instead, a more pronounced red shift of the plasmon frequency, together with broadening of the peak is observed.

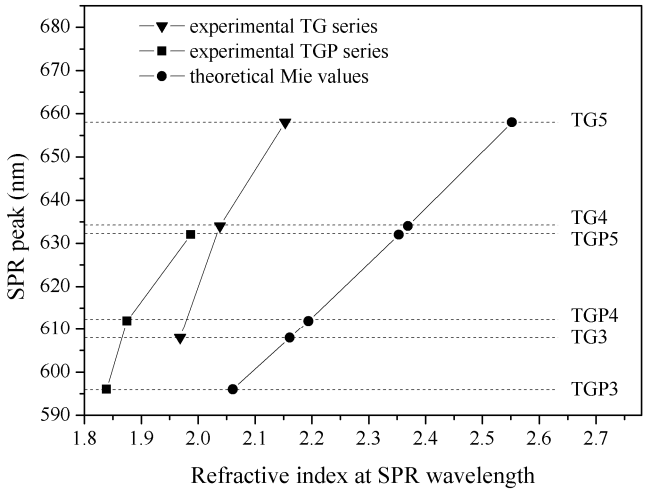

Figure 4.22. SPR peak position wavelength versus refractive index of undoped matrix measured at the same wavelength for TGP (squares), and TG (triangles) series. Theoretical refractive index values associated to the plasmon peak position according to the Mie relationship are also reported (circles).

To further understand the role of PEG, TG3 and TGP4 samples or alternatively TG4 and TGP5 samples can be compared: these couples of samples show similar SPR wavelengths, but refractive index and annealing temperature are different. In PEG-containing films, a higher thermal treatment is necessary in order to have the same SPR frequencies than PEG-free samples. Thus, following the arguments previously explained, a similar Au coverage by TiO_2 NPs is suggested for the two couples of samples mentioned before, while if the annealing temperature is kept constant, the extent of TiO_2/Au interface is limited in PEG containing samples. So, the presence of PEG not only introduces porosity but also affects the evolution of the colloids in the mixture interphase region.

In summary, the extent by which gold contacts titania is not strictly dependent on the overall degree of densification of the matrix, since samples with analogue average refractive index show very different SPR positions, and films with similar plasmon

resonance frequencies have different average refractive index values. Furthermore, all the samples show an experimental refractive index much lower than the theoretical value predicted by Mie theory. So, efficient coverage of TiO_2 on gold is here addressed as the key theme for experimental data interpretation: a combination of annealing temperature and template presence is thus responsible for the amount of titania facing the gold surface.

4.3.1.3 Gas sensing properties of TiO_2 films containing Au13 nanoparticles

The nanocomposite films have been subjected to gas sensing tests at temperatures between 250 °C and 350 °C and they were exposed to H_2 and CO with different concentrations ranging from 10 ppm to 1% v/v). Samples annealed at 300 °C were tested only at 250 °C operating temperature (OT) to avoid structural changes in the film during gas sensing measurements, but they show unstable baseline. This may arise from residual carbonaceous compounds still present inside the film or from incomplete stabilization after the 300 °C annealing treatment. In fact thermogravimetric analyses performed on TiO_2 colloids [37] and on PEG200 [58] show that the weight loss is not totally completed at 300 °C. So all the results presented here refers to samples annealed at 400 °C or 500 °C.

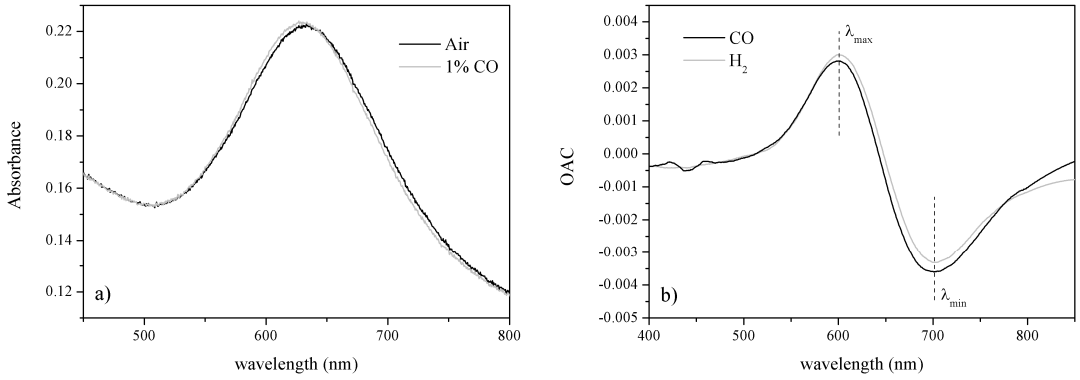

Figure 4.23. a) Absorption spectra of TG4 film measured in air (black line) and during exposure to 1% v/v CO (light grey line) at the operative temperature OT=300 °C. b) OAC plot of the same film after exposure to 1% v/v CO (black line) and H_2 (grey line) at the operative temperature OT=300 °C.

All Au-doped samples give a response to both gases, with a typical behavior of gold-doped semiconductor thin films [63], that has a wavelength dependence of optical sensitivity, allowing the operator to tune the sensor response. Samples without Au did not

give any appreciable optical response, so from now on every result refers to samples containing Au NPs. Figure 4.23 shows the optical spectra collecting in air and during 1% CO flowing for the TG4 sample performed at 300 °C, and also the Optical Absorbance Change (OAC), for the same film for 1% H_2 and 1% CO exposure. As can be seen from Figure 4.23b, the effect of CO and H_2 are very similar, and for this reason only the spectrum under 1% CO is reported in Figure 4.23a. Since the OAC curves are very similar in all samples (a small red shift is observed in PEG-free samples compared to PEG-containing samples annealed at the same temperature, and a red-shift is also observed comparing 500 °C and 400 °C annealed samples), the plots for the other samples are omitted. The shift of OAC curves is directly related to the SPR frequency of each film: since the modification of the plasmon band during gas exposure is very similar in all the samples, different SPR frequencies (see Figure 4.21) will result in a shift of OAC curves.

The Au plasmon peak during gas exposure undergoes a blue-shift: as a consequence, in the OAC plot, an absolute maximum and minimum can be determined, with wavelengths λ_{max} and λ_{min} corresponding to absolute maximum and minimum, respectively. 400 °C and 500 °C annealed samples were tested dynamically at both λ_{max} and λ_{min}, for each of the three temperatures. Table 4.5 lists these two wavelengths for all the tested samples.

Table 4.5. List of the wavelengths corresponding to absolute maximum and minimum of OAC curves.

Sample	λ_{max} (nm)	λ_{min} (nm)
TG4	600	700
TG5	620	720
TGP4	585	670
TGP5	600	690

The blue shift of Au SPR peak can be related to the interaction of reducing gases with the n-type semiconductor TiO_2 matrix, promoting a catalytic oxidation of the gas and an increase in the amount of conducting electrons, which in turn leads to a shift of the plasmon band to higher frequencies. However, a shift of Au SPR band can be also due to the adsorption of target gases in the matrix reactive sites, leading to a local change in the refractive index: since this adsorption would lead to an increase of average refractive index and so to a red shift of the Au SPR peak and since previous studies on electrical

conductivity change of similar samples [64] showed a decrease in resistivity during reducing gases exposure, the observed SPR blue shift can be related to the oxidation of CO and H_2, resulting in an injection of electrons inside the TiO_2-Au nanocomposite thin films.

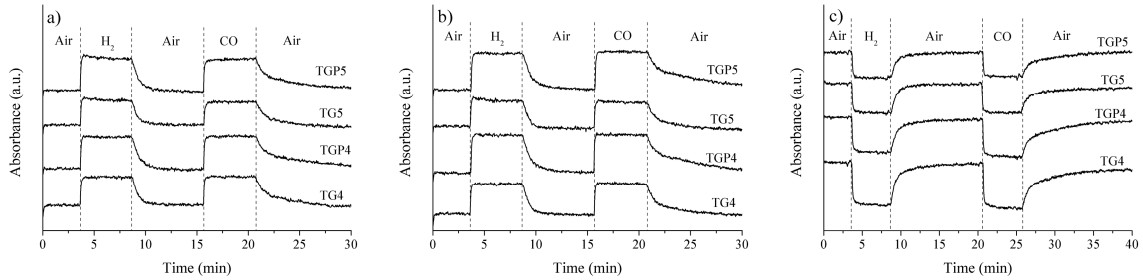

Figure 4.24. Dynamic response of the four Au doped films under exposure to Air-1%H_2-Air-1%CO-Air cycle: a) Test performed at λ_{min} and at 250 °C OT. b) Test performed at λ_{min} and at 300 °C OT. c) Test performed at λ_{max} and at 350 °C OT.

Figure 4.24 shows the temporal response of the four tested samples for a air-1%H_2-air-1%CO-air cycle. The dynamic performance of the sensors is quite good, with an almost square output signal, especially for PEG-free samples. This behavior represents an improvement in respect to previous results [64] where the optical sensing tests of sol-gel TiO_2 matrix loaded with Au NPs show a reversible but sometimes incomplete response, and also a drift in the baseline. Interestingly, sensors kynetics during hydrogen exposure is more efficient, showing better response and recovery if compared to carbon monoxide: this different behaviour can be due to the difference in size between the two gases, being H_2 smaller than CO, resulting in a diverse diffusivity inside the matrix; moreover the variation in the observed detection times can be related also to a difference in the reaction mechanisms, leading to different reaction products [65]: in fact there is a lot of literature dealing with the catalytic oxidation of CO over the Au-TiO_2 interface, resulting in the formation of CO_2, and operating at quite low temperatures (below 400 K) the preferential oxidation of CO over H_2 is usually observed [66-70]. As far as H_2 oxidation is concerned, there are some publications discussing adsorption and reaction of hydrogen over TiO_2-Au composites, leading to H_2O_2 and eventually H_2O formation [66,71,72]. It is noteworth saying that many authors reported the rapid decay of the preferential oxidation of CO in H_2-rich atmosphere over a TiO_2-Au catalyst when operative temperature is increased [73-75].

In our tests the operative temperature is much higher than the one needed for CO selective oxidation, and a very similar behaviour between the two gases has been observed, with the only difference of response and recovery times. So it can be stated that the observed difference in the dynamic behaviour is due to the difference in diffusivity and absorption of the target gas, in the oxidation kinetics over the films surface, and also in the desorption processes of the reaction products.

From the data reported in Figure 4.24 also the wavelength influence is evident: in fact operating near λ_{min} causes an increase in absorption during gas exposure, while operating near λ_{max} results in a decrease of absorbance during gas exposure.

Although these TiO_2-Au nanocomposite films are very thin, they reveal the capability to detect very low amount of the target gas with high sensitivity, as highlighted in figure 4.25: tests with CO concentration ranging from 10 ppm to 10000 ppm and with H_2 concentration ranging from 100 to 10000 ppm were performed on the TGP4 sample at 300 °C OT. The sample gives response also to 10 ppm CO, with response intensity decreasing linearly with the order of magnitude of target gas concentration, thus showing higher sensitivity at very low concentrations. Similar sensitivity and dynamic behavior have been observed in all the other samples.

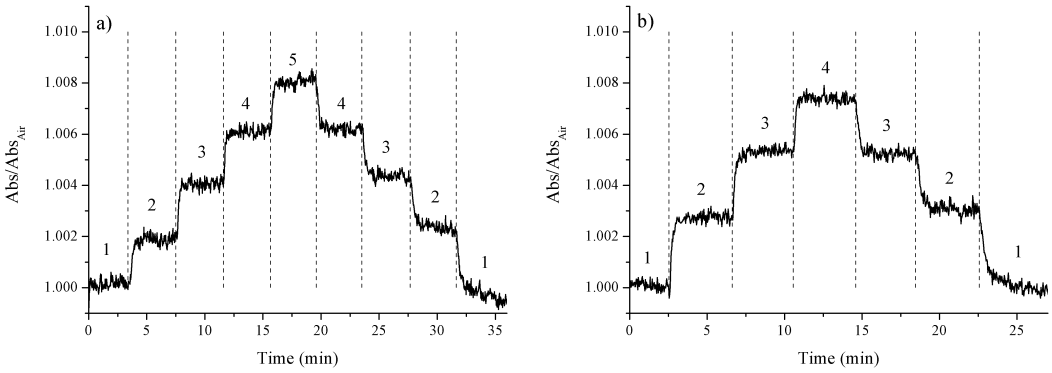

Figure 4.25. Dynamic response of the TGP4 sample at 585 nm and 300 °C OT, during exposure to: a) different CO concentrations (1 air, 2 = 10, 3 = 100, 4 = 1000, 5 = 10000 ppm); b) different H_2 concentrations (1 air, 2 = 100, 3 = 1000, 4 = 10000 ppm).

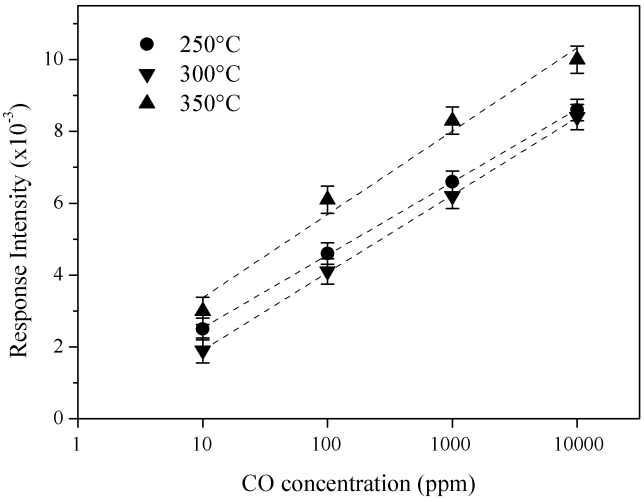

Figure 4.26. Sensitivity plots for CO detection for TGP4 sample tested at 585 nm at three different operating temperatures. Linear fits for the three experimental sets of data are also reported.

Figure 4.26 shows the Response Intensity plot (see Appendix section for details) for TGP4 sample as a function of the CO concentration, at the three different operating temperatures plotted in a linear-logarithmic scale: as can be seen the trend is linear, with a slight increase in intensity at 350 °C, while at 250 °C and 300 °C the difference between the data is inside the error bars, so no certain assertions can be made. Anyway, from these plots, it is easy to set calibration curves to correlate intensity of the response and CO concentration in the testing environment. Moreover the linear fit permits also to estimate the sensitivity threshold, being it around 2-3 ppm, considering the noise in optical absorption evaluated from the dynamic test reported in Figure 4.25a as lower limit of detection.

The relationship between the nanocomposite structure (porosity and interface between Au and TiO_2 crystals) and its optical gas sensing is addressed by analyzing the dynamic behavior in terms of response and recovery times, mainly focusing on recovery performance. These times have been evaluated from the three dynamic tests reported in Figure 4.24, as explained in the Appendix section. Each result has been averaged on three different measures to prevent anomalous or singular data; the error has been calculated as signal to noise ratio. Response time is short for every sample at every temperature, slightly higher for CO (ranging from 20 to 35 seconds), compared to H_2 (ranging from 12 to 15 seconds). The comparison of such data between the different samples is quite difficult, being the values very similar.

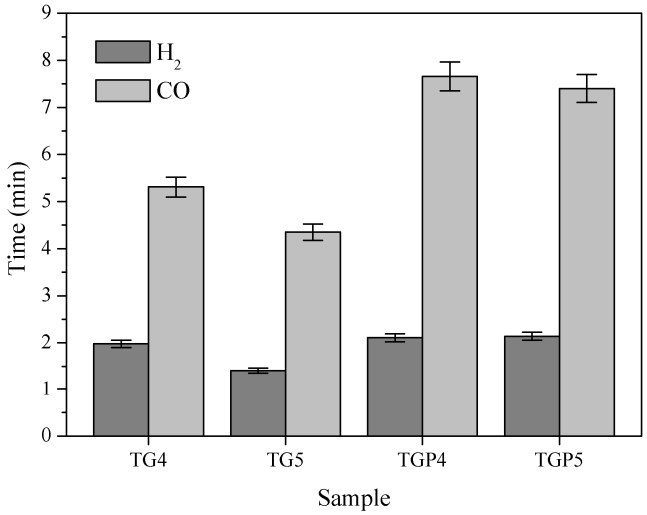

Figure 4.27. 90% average recovery times after 1% v/v CO (light grey bars) and 1% v/v H_2 (dark grey bars) exposure for the four samples.

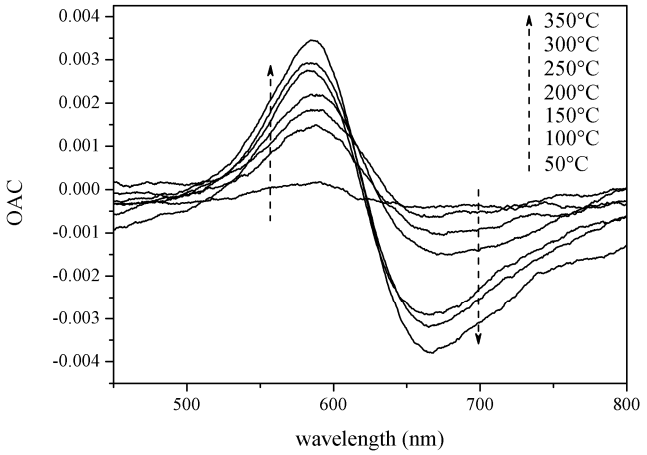

Figure 4.28. Optical Absorbance Change (OAC = A_{gas} - A_{air}) of TGP4 sample after exposure to 1% v/v H_2 at the operative temperatures ranging from 50 °C to 350 °C.

However, more useful information can be gained comparing the average recovery times, since values are higher and the error in the measure becomes less significant. Figure 4.27 shows the average recovery times for the 4 samples when exposed to 1% CO and 1% H_2: TG5 is the best sample while the two PEG-containing samples show the longest recovery times. Thus, it is evident that for optical gas sensing purposes, it is better to have a completely crystalline TiO_2 matrix with an extensive gold-anatase contact surface (TG5), rather than a more porous sample with a lower amount of Au-TiO_2 interface (PEG series). This behavior can be due to the effect of PEG in slowing the growth of TiO_2 crystals and limiting the Au-TiO_2 interface, as previously discussed when comparing XRD data and optical characterization. In addition, baseline recovery for PEG doped samples is

sometimes incomplete, suggesting the presence of residual carbon due to incomplete removal of the organic compound, that can react with the target gas affecting negatively the measurement.

Eventually, low temperature tests were also performed to check the operating temperature dependence of the sensing response: below 250 °C OT the intensity of the response rapidly decreased, particularly for CO detection. Moreover the transient times became quite long, especially the recovery of the baseline level was found to take several minutes. Nevertheless, a small but still measurable response was detected at 100 °C OT, as shown in Figure 4.28, suggesting that these materials are suitable for gas recognition at low temperature, even if a catalyst may be needed in order to improve the kinetics of the reaction with the target gas, since transient times of several minutes are not acceptable for a sensing device.

4.3.1.4 Characterization of TiO_2 films containing Au3 and Au13 nanoparticles

Considering the same system, *i.e.* TiO_2-Au, the effects of Au concentration and size have been evaluated: samples with Au13 concentration ranging from 1 to 4% molar, samples with Au3 (4%) and both Au13 and Au3 (2% each) have been prepared and characterized. The key idea behind this approach was to assess the effect of Au concentration on the sensing performances of the nanocomposites, and to evaluate a possible catalytic effect of small Au NPs, as also reported in the literature [76,77]. These films have been stabilized at 100 °C or annealed at 500 °C, depending on the gas sensing tests: samples annealed at 500 °C were tested as CO and H_2 sensors, as in the previous section, while samples only stabilized at 100 °C were tested with ethanol vapors at room temperature.

Structural and morphological characterizations confirm the successful embedding of the desired Au NPs amount inside the TiO_2 matrix, as shown in Figure 4.29: a clear increase in the intensity of the XRD peak corresponding to (111) lattice plane reflection of Au NPs (JCPDS No. 04-0714) together with the nominal Au concentration can be noticed, and also a clear difference in the broadening of this peak when comparing the Au3 and Au13 containing samples. These XRD peaks are very close to the patterns reported in Figure 4.2, as a proof of the successful embedding of the particles and the absence of structural modification inside the TiO_2 film.

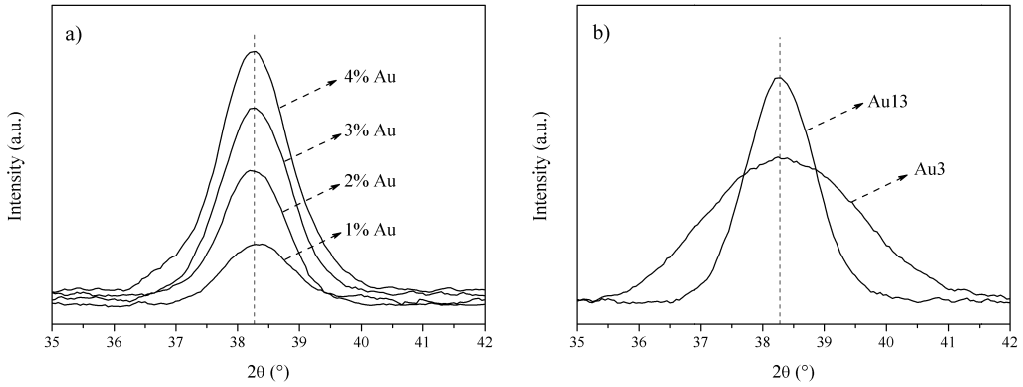

Figure 4.29. XRD patterns of a) TiO_2 films containing different concentrations of Au13 NPs. b) TiO_2 films containing Au13 or Au3 NPs. The theoretical (111) plane diffraction is highlighted with a dashed line.

Moreover, the Scherrer analysis on the lorentzian fit of these peaks gives a mean crystallite size in good agreement with previous data evaluated from the XRD peaks of the colloids: the estimated sizes for Au13 crystallites are 8.1 nm, 8.9 nm, 8.1 nm and 8 nm for 1%, 2%, 3% and 4% Au amount, respectively, while the crystals size for Au3 NPs is about 3.2 nm.

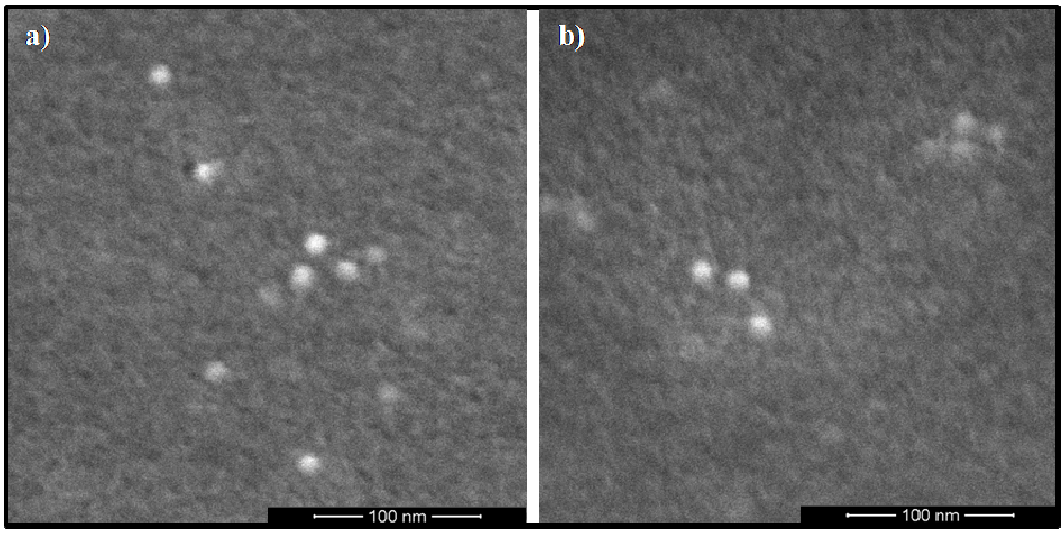

Figure 4.30. SEM images of: a) TiO_2 film containing 4% Au13 NPs annealed at 100 °C; b) TiO_2 film containing 2% Au13 NPs and 2% Au3 NPs annealed at 100 °C. Bright spots correspond to gold nanocrystals.

Morphological analyses on these samples have been performed with SEM, and the results are reported in Figure 4.30: the surface of the films is quite smooth, nevertheless the small surface roughness can be appreciated from the high resolution images; compared to

samples annealed at higher temperatures (see Figure 4.19), the surface roughness here is lower: the reason for this difference is that these samples have been thermally stabilized only at 100 °C, avoiding the TiO_2 NPs growth, thus keeping a quite flat and smooth surface. Au NPs are again clearly identified as brighter spots, but only Au13 particles can be seen, because the resolution of the SEM does not allow to recognize such small colloids, even if they show a high contrast in respect with the oxide matrix.

Optical spectroscopy gives another confirmation of the amount of Au embedded inside the films and also highlights the difference in shape and frequency of the SPR peak of Au13 and Au3 NPs. Figure 4.31a shows optical absorption spectra for the Au13 containing samples: as for XRD data, the effect of Au concentration on the intensity of the SPR peak is evident, while no shift with Au loading has been experienced, indicating that the particles are homogeneously dispersed inside the matrix and no plasmon coupling due to excessive Au concentration or aggregation phenomena is found to occur. The apparent broad absorption band of pure TiO_2 film is due to optical interference effect caused by the combination of thickness and refractive index of the oxide layer. When comparing samples with Au NPs of different sizes (Figure 4.31b), the effect on the optical absorption of the films is evident: in fact the SPR peak of Au3 colloids is less intense and blue shifted compared to Au13 (see Figure 4.1), and this effect is noticeable also in the TiO_2 films; the spectrum of the sample containing both Au3 and Au13 NPs appear to be effectively the sum of the two different contributions, with less intense SPR peak compared to only Au13 NPs, as a consequence of the different amount of Au13 loading, and a high frequency shoulder due to the presence of small Au NPs.

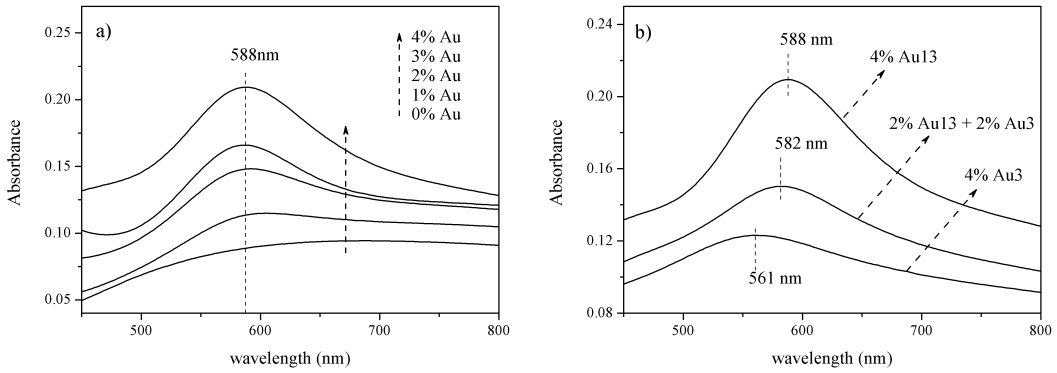

Figure 4.31. Optical absorption spectra of: a) TiO_2 film with different concentrations of Au13 NPs. b) TiO_2 films containing Au13 and Au3 NPs. The SPR wavelength of the different samples are highlighted with dashed lines.

Spectroscopic ellipsometry measurements on the thin films show again that the refractive index is substantially lower compared to dense TiO_2, as a consequence of high amount of porosity. All the refractive index values are between 1.83 and 1.94 at 1100 nm, and outside Au SPR range (when the refractive index can be modeled with a Cauchy dispersion curve) the wavelength dependence of the refractive index is the same for all the samples. However, samples with Au13 or Au3 are found to have respectively higher or lower refractive index values compared to the Au-free sample (Figure 4.32). A possible explanation of this behavior is that Au NPs increase slightly the refractive index of the TiO_2 film, as also observed in the past for SiO_2-Au nanocomposite thin films [78], but Au3 NPs colloidal solutions contained a high amount of PVP, necessary in order to obtain small particles as explained in section 4.2.1.1: the high content of organic compounds is responsible for the decrease in refractive index values. This effect was minimized washing more than one time the particles through precipitation-redispersion process, though avoiding excessive purification and the consequent NPs aggregation, but nevertheless the same behavior has been observed in all the samples prepared, suggesting that Au3 colloidal solutions contain a higher amount of complexing agent in respect of Au13 ones.

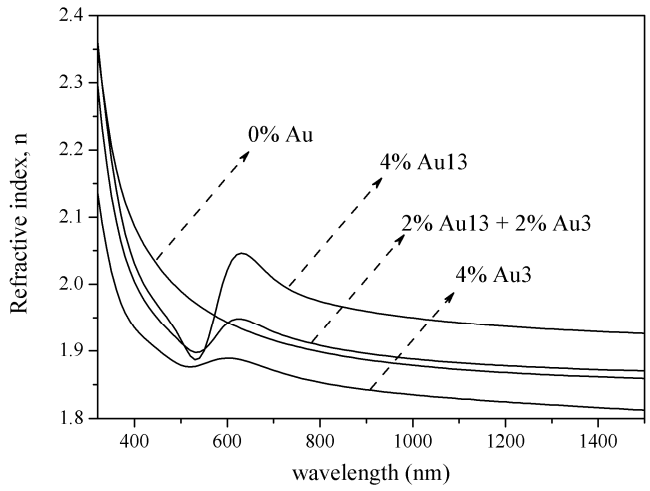

Figure 4.32. Refractive index dispersion curves of pure TiO_2 and Au-loaded TiO_2 thin films stabilized at 100 °C.

Using the measured refractive index values at 1100 nm, and supposing a refractive index for fully dense anatase at the same wavelength of 2.44, the porosity of the samples has been evaluated with the Bruggeman relationship (see section 4.3.1.2): all values are

between 33% and 40%, slightly higher for the sample containing Au3 NPs, and slightly lower for the sample containing Au 13 NP, as described before.

Thickness of these films evaluated with ellipsometry is found to be fairly independent from Au amount, being all the prepared thin films in the 80-115 nm range: the observed variation in thickness are likely to be due to small variations in the concentrations of TiO_2 colloidal suspensions or in the intrinsic variability of the spinning deposition procedure, since no trends with Au amount or type of Au NPs used have been detected.

4.3.1.5 Gas sensing properties of TiO_2 films containing Au3 and Au13 nanoparticles

Samples annealed at 500 °C have been tested as CO and hydrogen sensor to evaluate the effect of size and concentration of Au NPs in the sensing performances.

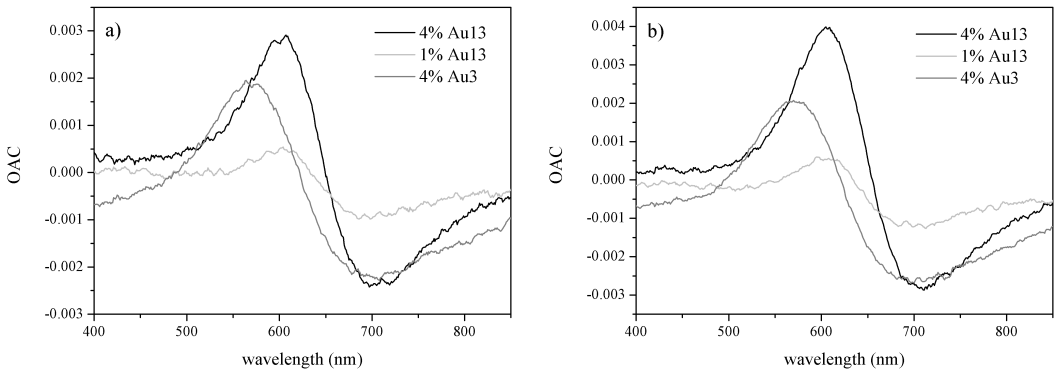

Figure 4.33. OAC curves of TiO_2 films containing different Au NPs after exposure to 1% v/v CO (a) and 1% v/v H_2 (b) at 300 °C OT.

As can be seen from Figure 4.33 there is a different effect in the intensity and wavelength dependence of the response according to type and concentration of Au NPs: comparing high (4%, black lines) and low (1%, light grey lines) Au13 amount, it can be seen that the behavior is substantially the same: the wavelength positions of OAC absolute maximum and minimum are almost the same, and only the intensity of the response is rather different, being higher in the sample containing 4% Au. These results confirm the role of Au NPs as optical probes, since Au free sample did not give any detectable results, while gold containing samples showed a response intensity proportional to Au amount. This fact may suggest a role of Au NPs themselves in the sensing performances, without any contribution of the matrix: even if this fact cannot be totally excluded (in the past an extremely weak but still detectable response of Au NPs inside inert SiO_2 matrix has been observed after the exposure to both CO and H_2 [79]), the fact that different matrixes

doped with Au NPs show different sensing responses to H_2 and CO (see for example chapter 3, Figure 3.24) supports the hypothesis that the oxide matrix is responsible for the detection mechanism, while Au NPs provide a tool to transform the interaction between the target gas and the oxide into an optically detectable signal. Of course, this might be not true for the detection of analytes with great affinity for Au surfaces, like thiols: in this particular case, also Au NPs themselves are able to change their optical properties, so providing a sensing material; anyway, it's not the case for reducing gases like CO and H_2.

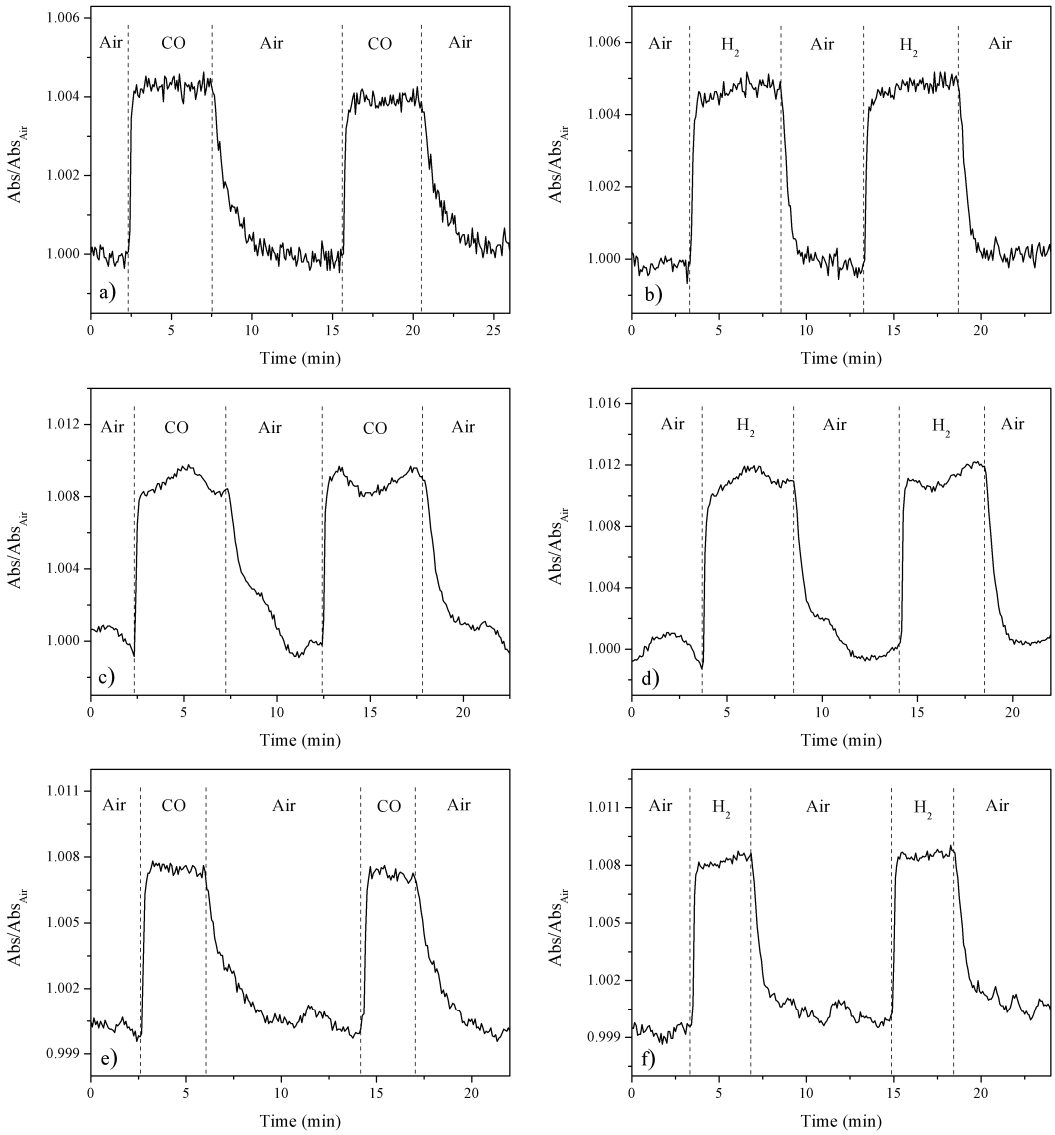

Figure 4.34. Dynamic response of the four TiO_2 films containing 4% Au13 NPs (a, b), 4% Au13 NPs (c, d) and 4% Au3 NPs (e, f) under exposure to 1%CO (a, c, e) and 1%H_2 (b, d, f) cycles at 300 °C OT. Tests have been performed at 605 nm in plots a-d and at 570 nm in plots e-f.

If now the OAC plots for Au3 (dark grey lines) and Au13 (black lines) loaded samples are compared, a difference in response intensity arising from the different Au SPR intensities of Au NPs of different sizes (see Figure 4.31b) can be appreciated; moreover, the OAC curves of Au3 containing sample are broadened and shifted towards lower wavelengths: such behavior is related to the Au SPR peak, since small gold colloids exhibit a more blue shifted and broadened plasmon band and this affects the shape of OAC curves.

Time resolved measurements have been performed at the same operative temperature (300 °C) at the wavelengths corresponding to absolute maximum and minimum of the OAC curves, but for the sake of brevity only the dynamic tests performed at the former wavelength are shown in Figure 4.34: the wavelength used in these tests are 605 nm for the samples containing Au13 NPs and 570 nm for the sample loaded with Au3 NPs. A clear and reversible response has been recognized in all the tested samples, for both H_2 and CO detection, and the baseline level is fully recovered in all the tests. Only the sample containing 4% Au13 NPs showed a quite strange behavior, with a sinusoidal modulation that appears to be summed to the usual step-like trend of dynamic tests; this effect has been presented randomly during the gas sensing tests, also with other samples, and has to be ascribed to a problem in the thermocouple reading the temperature of the sample heater: in fact during some tests the thermocouple lost the contact with the sample heater and so the heat was transferred in convection mode instead of conduction mode, causing a lost in precision of the thermocouple reading, and so a fluctuation in the heating rate. Nevertheless, the time resolved data can be easily analyzed also in the presence of this additional modulation, and so conclusions can be drawn as well.

From Figure 4.34 it can be seen that the intensity of the response can be easily related to the Au amount, as for the OAC data, and that the transient times are slightly better for hydrogen detection, being both response and recovery times shorter in the first case. Excluding the already discussed temperature control problem, the behavior is substantially the same for the three samples, and there is not an improvement when TiO_2 films are loaded with Au3 NPs, so a catalytic effect of small Au NPs is not likely to be present here for the detection of reducing gases.

In fact, comparing the recovery times between the three samples, for films doped with Au13 NPs the recovery times are around 50-60 seconds for hydrogen detection and about 2 minutes for CO detection, while the average recovery times for sample containing Au3

NPs are slightly longer, being around 80 seconds and 2.5 minutes for H_2 and CO, respectively.

So, not only an improvement on the sensing dynamic behavior has not been detected when embedding Au3 NPs inside the TiO_2 film, but also a slight worsening of the performance has been experienced: therefore a catalytic effect of small Au NPs has to be excluded, at least for the operative parameters used in the described tests.

Instead, samples annealed at 100 °C have been tested as VOCs sensors at room temperature in reflection mode as described in the Appendix section. The VOC selected for these tests is ethanol, with nitrogen as carrier gas: a nitrogen stream was flown inside a bubbler filled with ethanol, and the resulted stream (the ethanol concentration was 180 ppm) was let into the test cell. Also in this case a clear and reversible signal has been detected after exposure to ethanol vapors, and considering that the measurements have been performed in an inconvenient setup, with a low-resolution spectrophotometer analyzing the change in intensity of the reflected light coming from samples deposited on standard SiO_2 glass slides, the preliminary results reported here are promising for the employment of these materials as VOCs sensors. Moreover the response is wavelength dependent, as already experienced for reducing gases detection (Figure 4.35a), allowing the tuning of the sensor performances. The vertical scale of this graph is set as Optical Reflection Change (ORC), defined as the difference in the Reflection intensity (counts) between the spectrum collected under ethanol vapors and the spectrum collected in nitrogen atmosphere.

Again, a trend involving sensor response and Au amount can be drawn, as reported in Figure 4.35b, where the maximum of the ORC evaluated for the samples containing from 1% to 4% Au13 is reported: the error bars are calculated evaluating the noise of each measurement. A clear increase in the intensity of the response with increasing the Au amount can be seen, even if the trend is not linear, but appear to be more pronounced when increasing Au amount from 1% to 2%: but while making all these assertions, it has to be taken into account also the quite high signal to noise ratio, so a definitive and certain trend is difficult to draw; anyway, the increase of sensor sensitivity with Au amount can be claimed without doubts.

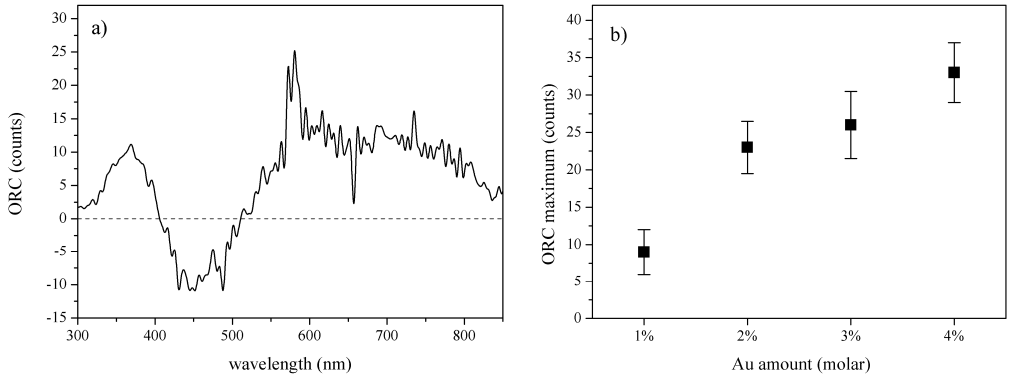

Figure 4.35. a) Optical Reflection Change (ORC) of TiO_2 films containing 2% Au NPs after exposure to 180 ppm ethanol vapors at room temperature. b) Response intensity of TiO_2 films loaded with different amounts of Au NPs, calculated at the wavelength corresponding to the maximum of ORC curves (~590 nm).

The wavelength dependence of the films sensitivity for ethanol detection can be easily appreciated looking at Figure 4.36, where the dynamic tests for a TiO_2 film loaded with 2% Au13 NPs performed at 3 different wavelengths are reported: the analysis wavelengths are 368 nm, 450 nm and 583 nm for Figure 4.36 a, b and c, respectively. These wavelengths have been chosen analyzing the ORC spectrum (see Figure 4.35a) and identifying the local maxima and mimima: during ethanol flow, the reflection of the sample is found to increase between 300 and 400 nm, and between 520 and 850 nm, while between 400 and 520 nm ethanol causes a decrease in the reflection intensity, so the three wavelengths selected for the dynamic tests correspond to relative maximum (or minimum according to the sign of ORC curve) of each of these three parts the ORC curve can be divided in.

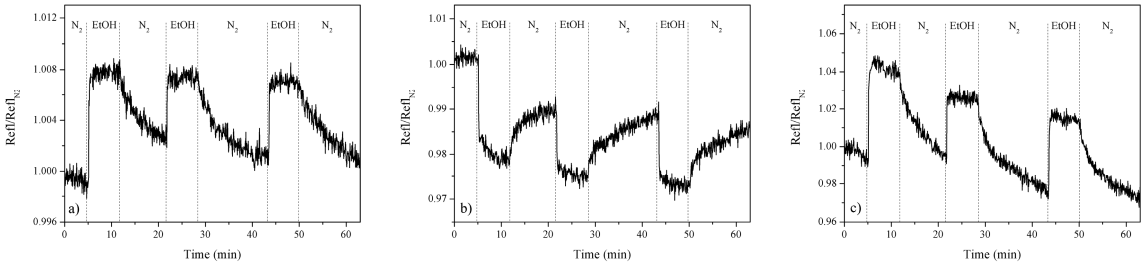

Figure 4.36. Dynamic performance of a TiO_2 films containing 2% Au13 NPs under exposure to multiple nitrogen-ethanol (180 ppm) cycles at room temperature at a) 368 nm; b) 450 nm; c) 583 nm.

These positive or negative variations in reflection intensity according to the analysis wavelength are obviously transferred also in the dynamic tests: in fact operating at 368 nm and 583 nm the reflection intensity increases, while operating at 450 nm a decrease in reflection is experienced.

Analyzing the transient times, the recognition of the VOC occurs immediately, with response times between 15 and 20 seconds for all the performed tests, while the recovery takes several minutes and sometimes a drift in the baseline is experienced. Even if this behavior is not ideal for a sensing device, if it is taken into account the fact that the sensor operates at room temperature, that the detection setup is in reflection mode and that the films are only 100 nm thick, the reported performances are quite interesting and promising; the response times are particularly attractive, because one of the most important parameter for a gas sensor is the quickness of the detection of the target analyte, and sometimes it can be put before the recovery time. So, such short response times for thin films tested at room temperature are noteworthy.

4.3.1.6 Characterization of TiO_2 films containing Au, Pt and Au@Pt nanoparticles

All the samples series prepared in this study are listed in Table 4.6. For every series, 5 samples were prepared and they were annealed at different temperatures (100 °C, 200 °C, 300 °C, 400 °C, 500 °C). The annealing temperature is indicated with 1, 2, 3, 4, 5 respectively, at the end of the sample name. The main scope of this study was to embed different types of nanoparticles inside TiO_2 nanocrystalline thin films and evaluate their stability with annealing temperature and their effect on the gas sensing performances.

Table 4.6. List of TiO_2-based samples series prepared indicating type and amount of noble metals embedded in the films.

Series name	Noble metal
TA	4% Au13 NPs
TP	4% Pt NPs
TAP	2% Au13 NPs + 2% Pt NPs
TS0.4	4% Au@Pt0.4 NPs
TS1.6	4% Au@Pt1.6 NPs

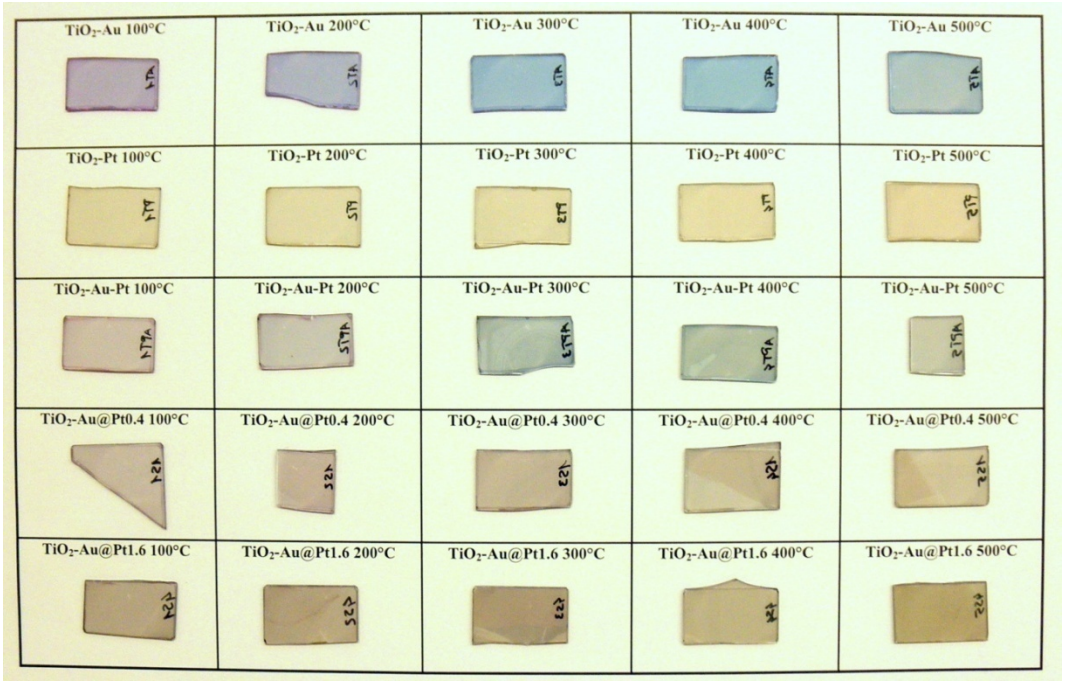

Figure 4.37. Picture of all the TiO_2-based samples prepared in this study. Each rectangular box is approximately 5.5 x 3.5 cm.

The samples prepared are shown in Figure 4.37: the chromatic differences due to the different type of the metal NPs and the annealing temperature are evident, and these differences will be discussed thoroughly in the following.

The thermal evolution of both matrix and metal NPs was studied with XRD: as observed before, a clear grain growth with annealing temperature can be seen for TiO_2 crystals, as a consequence of the decrease in energy due to the lowering of the surface/volume ratio promoted by the thermal treatment.

As far as Au and Pt NPs are concerned, no appreciable modification with annealing temperature can be seen, as shown in Figure 4.38b, c and d for films containing Au, Pt and both Au and Pt NPs, respectively; in fact the diffraction peaks for Au (JCPDS No.04-0784) and Pt (JCPDS No. 04-0802) do not undergo any relevant change in shape or any shift, indicating good stability of these particles up to 500 °C. Moreover in the nanocomposites containing both Au and Pt, the two metal NPs don't seem to interact (for example forming an alloy), because the diffraction peaks for both the cubic phases remain unchanged as highlighted by the dotted lines showing the theoretical position of the main diffraction peaks for the two metal structures. On the contrary, the Au@Pt core shell NPs are not stable up to 500 °C, but around 300 °C a shift of Au diffraction peaks towards higher angles (*i.e.* smaller lattice planes distances) starts to appear for both Au@Pt0.4 and

Au@Pt1.6 NPs. The reason of this behavior has to be ascribed to the formation of an alloy between the two noble metals, as already observed in the past [29,80].

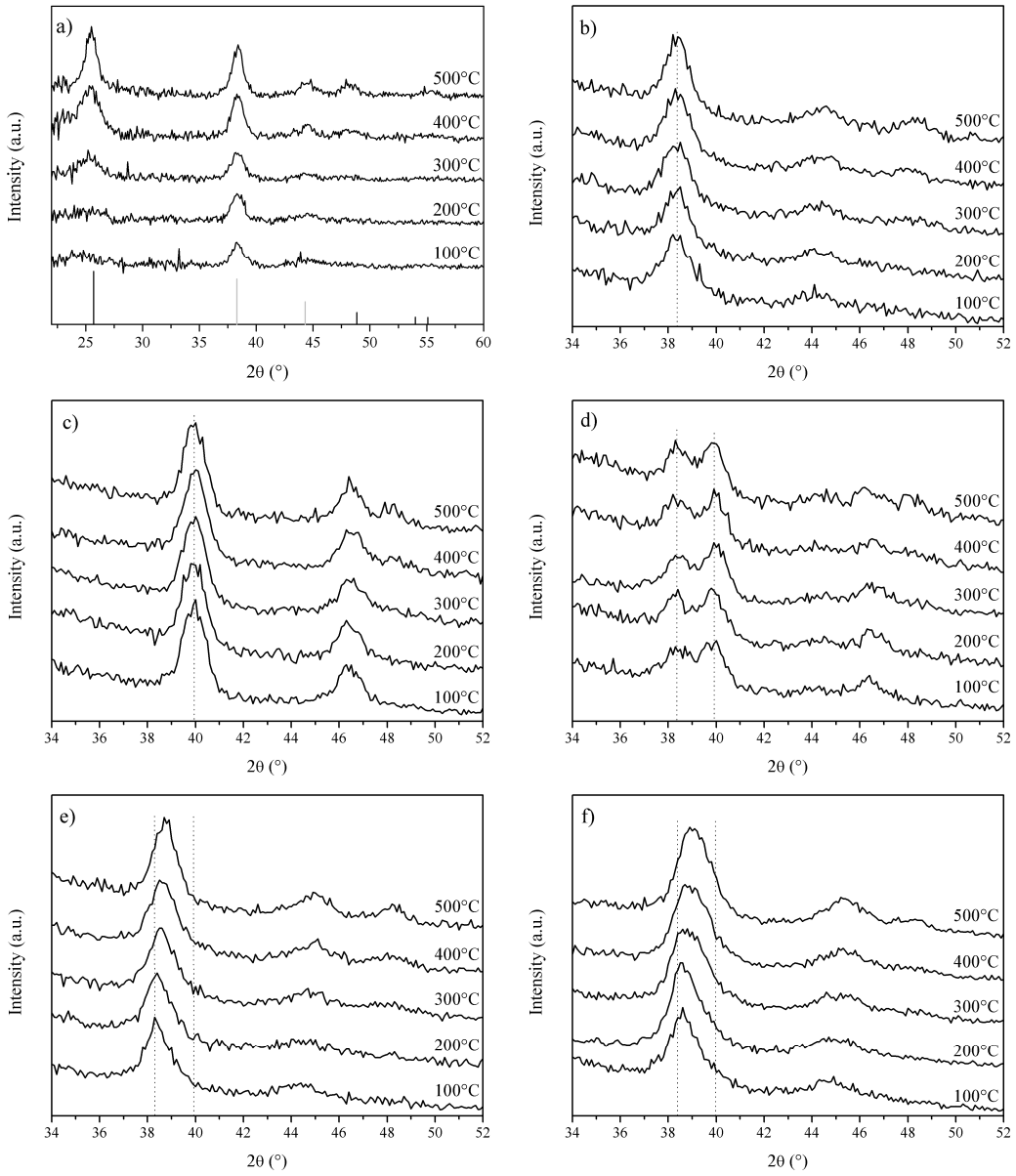

Figure 4.38. XRD patterns of TA sample series, with theoretical diffraction lines for anatase (black lines) and Au (grey lines) shown at the bottom (a); evolution with temperature of Au and Pt diffraction peaks for TA (b), TP (c), TAP (d), TS0.4 (e) and TS1.6 (f) sample series; theoretical diffraction lines for the most intense peak of Au and Pt are shown as dotted lines.

Unfortunately, since Au and Pt NPs are quite small in size, the XRD peaks especially at low angles are overlapping and appear as one broad peak, as observed in section 4.2.3.2 analyzing the XRD patterns of the colloids: so the estimation of the amount of Pt alloyed

through the Vegard's law is quite difficult, because the diffraction peak is actually the sum of two broad peaks, and so the peak position is hard to determine. Nevertheless, a clear shift of the peaks starting from 300 °C annealing can be detected, suggesting the already explained alloying of the two noble metals.

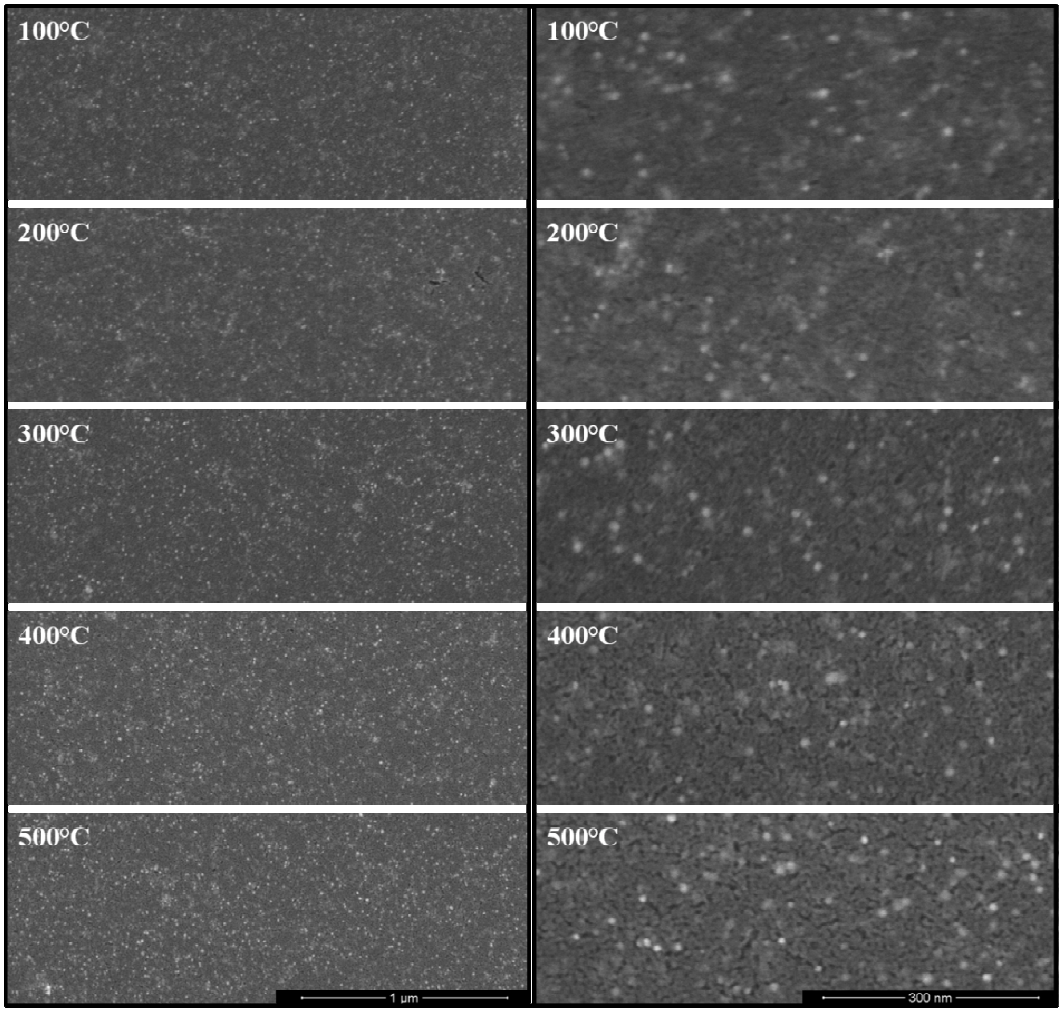

Figure 4.39. SEM images of TAP samples annealed at different temperatures at low (left side) and high (right side) magnifications. Bright spots correspond to Au and Pt nanocrystals.

From the SEM images shown in Figure 4.39 a homogeneous dispersion of Au and Pt NPs inside the TiO_2 films can be easily seen, since both metal NPs have higher contrast in respect to the oxide matrix; unfortunately since the size of the two types of NPs is similar, it is difficult to distinguish between Au and Pt. Anyway, no aggregation phenomena seem to occur, and the metal particles are randomly dispersed in the films. From the high resolution images reported in the right column, it is also possible to appreciate the

increase in crystallinity and surface roughness of the films with annealing temperature, as a consequence of the TiO_2 crystals growth as already observed from XRD data.

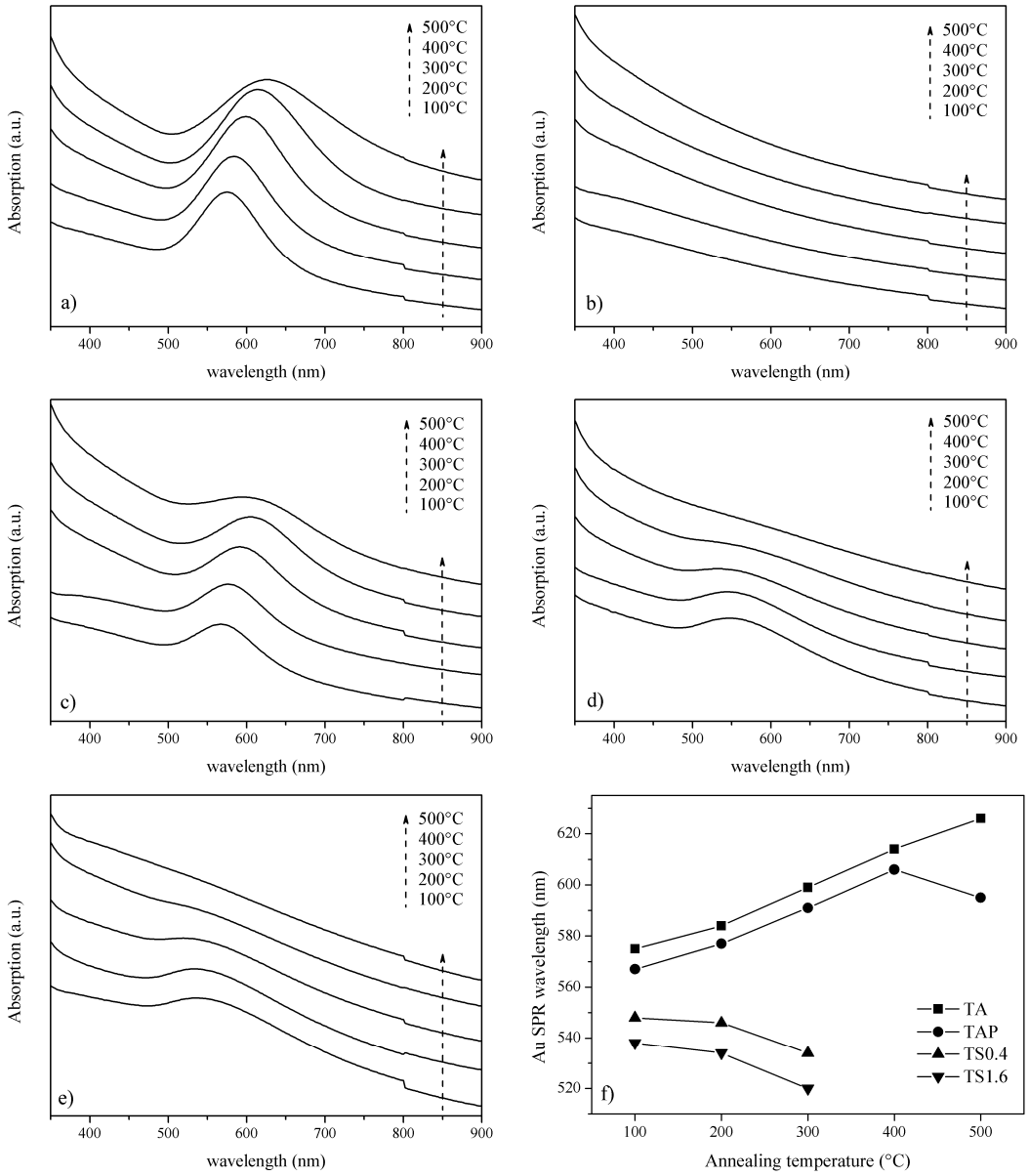

Figure 4.40. Optical absorption spectra of TA (a), TP (b), TAP (c), TS0.4 (d), TS1.6 (e) sample series. Plot of Au SPR wavelength as a function of annealing temperature for the sample series containing Au (f); TS0.4 and TS1.6 samples annealed at 400 °C and 500 °C, and the whole TP series are not shown in this graph because they do not present a definite Au SPR peak.

The whole set of samples has been analyzed with optical spectroscopy to evaluate the effect of the type of the metal NPs and of the annealing temperature on the optical properties of the nancomposite thin films.

From the optical absorption spectra, several information can be obtained: for all the samples, a slight increase in UV absorption onset with temperature can be detected, as a consequence of the increase in crystallinity and of the crystals growth promoted by the thermal treatment.

Analyzing the TA series, as observed section 4.3.1.2, the Au SPR peak is found to red shift increasing the annealing temperature, and also a broadening can be appreciated, especially for 400 °C and 500 °C thermal treatment. The reasons for this behavior have been presented previously. On the contrary, with the exception of the slight increase in UV absorption onset, no modification in the optical spectrum of Pt containing samples can be seen, since Pt NPs don't present a plasmon band in the visible range, only a tail of absorption that doesn't undergo any changes with the increase of refractive index of the matrix. This effect can be easily visualized looking at the samples picture reported in Figure 4.36: TA samples change color from pink-violet after the annealing at 100 °C to deep blue after the annealing at 500 °C, while the color of samples containing Pt NPs does not change significantly with thermal treatment, remaining always grey-yellowish.

The behavior of the samples containing both Au and Pt resembles the behavior of TA series up to 400 °C, as can be easily seen in the plot reported in Figure 4.40f: the only difference is that the Au SPR peak in the TAP samples series is always few nanometers blue-shifted compared to the TA samples. This behavior is ascribed to a difference in refractive index of the surrounding matrix, maybe due to a difference in PVP amount between Au and Pt, higher in the latter compared to the former. This fact has been confirmed by ellipsometric measurements reported in the following.

At 500 °C annealing the Au SPR peak in the TAP5 sample is found to blue shift and decrease in intensity, in contrast with the behavior detected for the TA5 sample. This unusual spectrum can be due to a partial alloying between the two metals, as described previously: however, no clear shift in Au XRD peaks is detected, and so a great amount of alloying is not likely to happen, even if being the XRD patterns quite noisy, a small amount of alloying cannot be totally excluded. So the observed modification of Au SPR peak can be due to a formation of a partial contact interface between the two metals, that is known to affect Au SPR properties [29], since Au is no longer completely faced to a dielectric medium, but it is partially in contact with another metal, and this fact influences both the Au plasmon resonance frequency and intensity.

Analyzing now the behavior of samples containing the Au@Pt core shell NPs, the trend is opposite compared to TA series: in fact a blue shift of Au SPR peak with increasing

temperature is experienced, more pronounced after 300 °C compared to 200 °C annealing, together with a progressive decrease in intensity of the peak, again especially after the 300 °C thermal treatment. So up to 200 °C the core-shell NPs are substantially stable, while from 300 °C the alloying between the two metals started to occur, affecting negatively the Au plasmon band. Eventually, after 400 °C and 500 °C annealing, the SPR peak degenerates as a consequence of the massive alloying, resulting in a broad shoulder below 520 nm; for this reason, in Figure 4.40f the SPR position of Au@Pt NPs only up to 300 °C is reported. So the effect of the Pt shell around the Au core is to damp and shift towards higher frequencies the plasmon band, as explained in section 4.2.3.2, but if the shell and the core start to alloy as an effect of the thermal annealing, this behavior becomes more pronounced, degrading the Au SPR peak. Again, this effect is rather evident analyzing the colors of the samples: TS0.4 samples are violet after low temperatures annealing, but they become progressively grayish as a consequence of the degradation of Au SPR peak; TS1.6 samples are much more darker also after the thermal treatment at 100 °C, because the Pt shell around Au NPs is thicker, causing the damping of the Au SPR peak: anyway, the observed trend in changing color towards the grey-yellow increasing the annealing temperature can be seen also in this sample series.

From ellispometric measurements, the optical constants *n* and *k* of all the films have been evaluated: the refractive index dispersion curves are reported in Figure 4.41, while the absorption coefficients curves as a function of wavelength are not reported since they don't add any further information to the previously presented absorption spectra. For all samples, the increase in annealing temperature causes an increase in refractive index, as expected from the thermally induced densification of the matrix, as reported in section 4.3.1.2. The refractive index curves are affected by the absorption properties of the samples, as described by the Kramers-Kronig relationship, because the real and imaginary part of every mathematical function (in this case, the complex refractive index) are not completely independent, but they have to observe this particular relationship. For this reason, all the samples containing Au NPs show the effect of Au SPR peak in the refractive index dispersion curve in the 500-800 nm range, much more evident in the TA samples, because they have the higher Au amount, and also the higher SPR intensity (as shown before, the Pt shell around Au cores causes a damping of the plasmon peak intensity). The TP samples don't show any evident absorption peak, so it can be thought that their refractive index follows a simple Cauchy dispersion: this is not correct, because the Pt NPs are absorbing in the whole visible and near infrared range, so a Cauchy

dispersion is not able to fit correctly the experimental data for the TP series. Some oscillators are needed to simulate the Pt NPs absorption, even if the resulting refractive index value is monotonously decreasing with wavelength, as in the Cauchy dispersion. Comparing the refractive index values for TA, TP and TAP series in the NIR region, where the absorption value is rather low and the refractive index dispersion is similar in all the samples, there is the confirmation of the constant difference in refractive index between Au containing and Pt containing samples: TA samples show a higher refractive index (between 0.06 and 0.1, depending on the annealing temperature) compared to Pt containing samples, and the TAP samples have always a refractive index value in between the TP and the TA samples, as expected. This difference can be ascribed to a different PVP amount inserted in the film together with the metal NPs: in fact being Pt NPs slightly smaller compared to Au, they have a higher surface to volume ratio, and so it is likely that they have high PVP amount compared to Au, keeping the metal molar concentration constant. As far as the sample containing the core-shell NPs are concerned, the TS0.4 samples have refractive index values very close to TA samples, as expected from the fact that their surface to volume ratio is almost the same of pure Au cores (since the shell is very thin) and so if the difference in refractive index is ascribed to a different PVP quantity, it is reasonable to suppose that samples loaded with Au NPs or Au@Pt0.4 NPs have a similar PVP amount. Eventually, samples containing Au@Pt1.6 NPs show the highest refractive index values among the whole set of samples: again, considering that their size is much higher compared to the other colloids, the high refractive index can be due to a smaller amount of PVP present inside the samples; nevertheless, since the samples were highly absorbing also in the NIR region, the high refractive index values can also be partially ascribed to the high absorption coefficient values, again as a consequence of the Kramers-Kroning relationship.

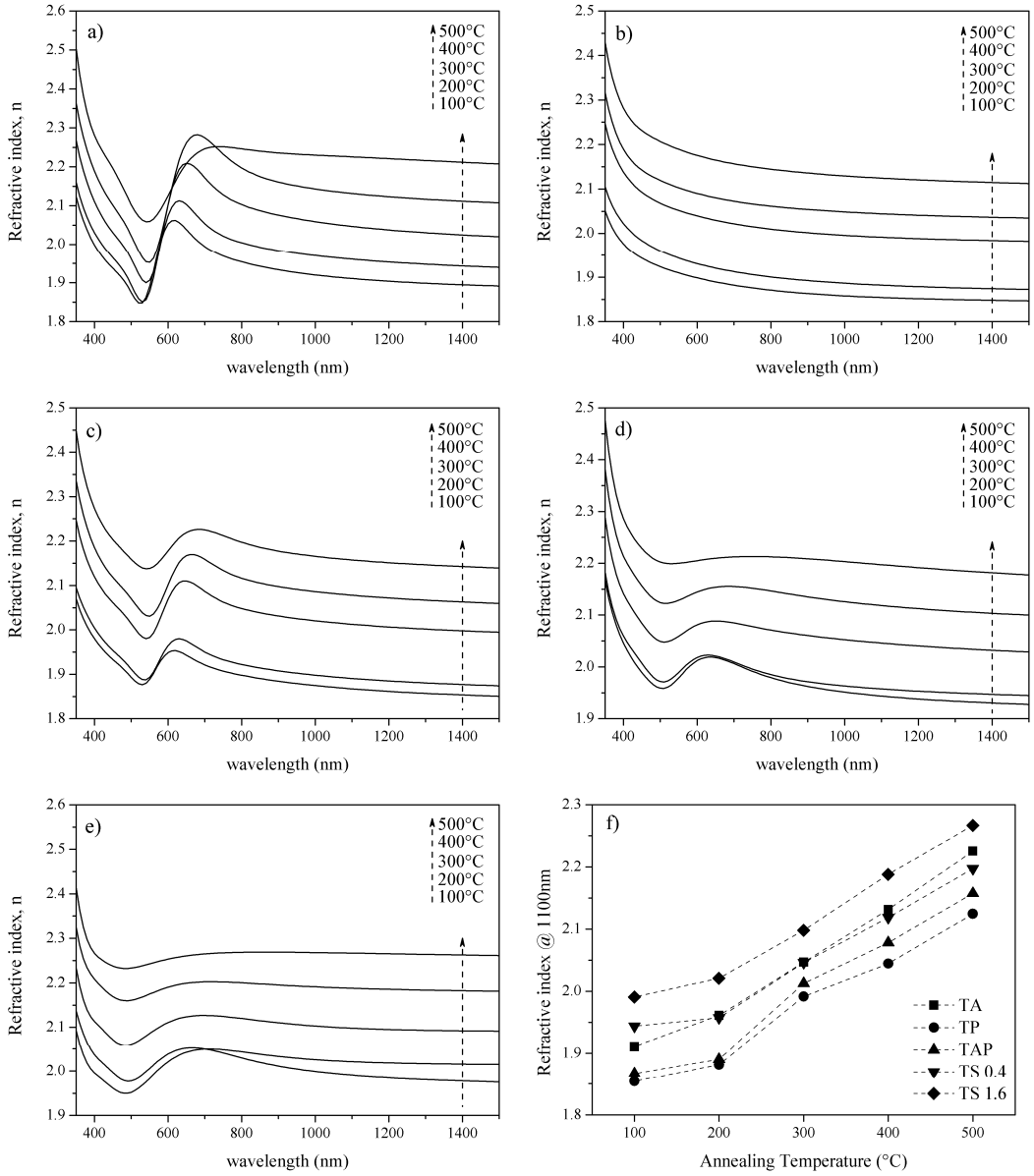

Figure 4.41. Refractive index dispersion curves of TA (a), TP (b), TAP (c), TS0.4 (d), TS1.6 (e) sample series. Plot of refractive index value at 1100 nm as a function of annealing temperature for the five sample series (f).

From the refractive index values also the porosity can be evaluated, using effective medium approximation models: again using the Bruggeman relationship (see equation 4.1) with a refractive index value for fully dense TiO_2-anatase of 2.44 (see section 4.3.1.2), and supposing that at 1100 nm the samples are not absorbing (even if considering what explained before, this might be not completely true), the porosity values have been estimated and the results are reported in Table 4.7. As expected the porosity decreases with increasing the annealing temperature, and porosity values between 30 and 40% after the 100 °C annealing, reduce to 12-19% after the 500 °C firing. It is useful to

remind that these values are an estimation, since they don't take into account that the refractive index of dense anatase might not be completely reliable for nanocrystalline materials, the organic compounds present especially in the films annealed at low temperatures are not considered in the porosity evaluation, and because the Bruggeman relationship used here is a simplification of the original EMA model that involves the complex dielectric function of the different media, so taking into account also absorption. Nevertheless, this approach has been universally adopted and widely used throughout the literature [81-83] , since porosity determination of thin films is a challenging task, because common techniques like gas absorption isotherms [84,85] , usually modeled with BET, Kelvin or BJH equations, cannot be applied because they require a huge amount of powder of the sample material (at least 50-100 mg) to obtain significant results: obviously, such an amount is difficult to obtain from thin films.

Table 4.7. Refractive index values at 1100 nm and estimated porosity with Bruggeman EMA model for the whole set of samples.

T (°C)	Refractive index at 1100 nm					Porosity (%)				
	TA	TP	TAP	TS0.4	TS1.6	TA	TP	TAP	TS0.4	TS1.6
100	1.911	1.854	1.867	1.944	1.991	35	39	38	33	30
200	1.961	1.882	1.891	1.957	2.021	32	37	36	32	28
300	2.047	1.992	2.013	2.046	2.098	27	30	29	27	23
400	2.131	2.044	2.078	2.118	2.188	21	27	25	22	17
500	2.226	2.124	2.158	2.197	2.267	15	21	19	16	12

Eventually, spectroscopic ellipsometry is also useful to evaluate sample thickness: since the nominal concentration of TiO_2 and metal NPs, as well as the deposition parameters (spinning rate and time) were kept constant throughout the whole set of experiments, the final thickness of the samples annealed at the same temperature is supposed to be similar. In fact, thin films annealed at 100 °C are in the 55-63 nm thickness range; the thickness decreases monotonously with increasing annealing temperature down to 37-40 nm as a consequence of the thermally activated shrinkage and densification of the matrix. The slight differences from one sample to another are due to the intrinsic variability of the spin coating process and also to some differences in the solutions, according to type of metal NPs, PVP amount, that can affect the overall viscosity and so the final thickness.

4.3.1.7 Gas sensing properties of TiO_2 films containing Au13, Pt and Au@Pt nanoparticles

In the previous section the high optical sensitivity of TiO_2 films containing Au NPs was demonstrated for CO and H_2 detection at operative temperatures between 250 °C and 350 °C. When trying to lower the operative temperature, the sensitivity of the material becomes lower and also the dynamic behavior is worsened, because the sensing processes like gases adsorption on the film surface, their reaction and the products desorption from the active materials are usually kinetically favored at high temperatures. For this reason samples containing Pt, a known catalyst for reducing gases detection, have been prepared. All the samples annealed at 200 °C have been tested at room temperature (20 °C) for hydrogen detection: since the starting material is crystalline, there is no need to anneal the samples at high temperatures to promote crystallization; only this heat treatment at mild conditions was performed in order to remove solvents, adsorbed water and stabilize the films. Moreover, an annealing at higher temperature was found to promote the alloying between Au and Pt, as described earlier, so it was decided to stabilize the samples without modifying the metal NPs morphology and composition.

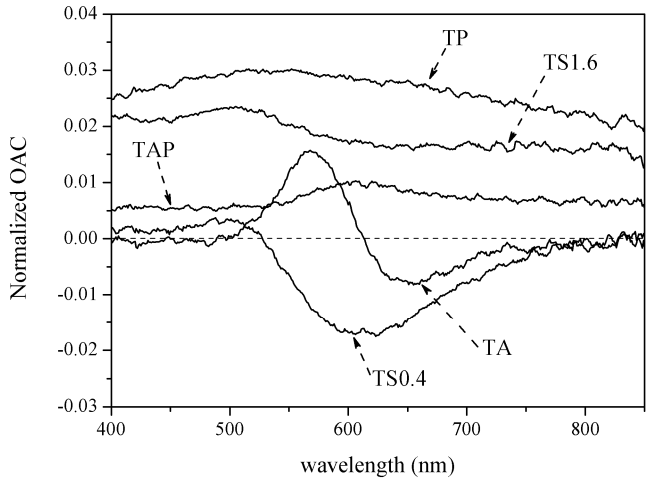

Figure 4.42. Normalized OAC plots of the five samples annealed at 200 °C after exposure to 1% H_2 at room temperature.

Figure 4.42 shows the OAC plots after exposure to 1% hydrogen at room temperature for the five samples tested, normalized to the respective thickness, in order to make comparable the different results. As can be seen, all samples give response to hydrogen, but few differences can be noticed according to the type of metal NPs embedded inside the nanocrystalline anatase films. TiO_2-Pt sample shows a uniform response in the whole

visible range, only slightly decreasing at higher wavelengths, but it can be described as almost constant. On the contrary, TiO_2-Au film shows the typical behavior of Au-doped oxide thin films, *i.e*. a wavelength dependence of the response, as already observed previously (see Figure 4.23 for example).

The OAC curve of the films containing separate Au and Pt NPs is somehow the sum of the two contributions, because over a constant response ascribable to Pt NPs, a small modulation due to Au SPR peak modification can be seen, even if this wavelength dependence is only just detectable. The behavior of TiO_2 films containing Au@Pt NPs is dominated by the shell thickness: when the Pt shell around Au cores is thick, the response resembles the OAC plot of Pt containing films, with a response intensity only weakly dependent on the wavelength; on the contrary, when the Pt shell is very thin, the response is rather similar to Au-doped sample, with a very small or null response far from the Au SPR frequencies, and a signal strongly dependent from the analysis wavelength inside the Au SPR range.

The relative response intensity between the five samples is different: TP sample is the most sensitive, directly followed by TS1.6 sample. This fact is not surprising, since these two have the highest Pt amount among the five films, but their response is not wavelength dependent. On the contrary, the other samples show a smaller response, but a more pronounced wavelength dependence, allowing to tune the sensor performances using wavelength modulation, especially when simultaneous multiple gases recognition is needed.

So with these tests the idea behind the synthetic approach used has been confirmed, because samples containing both metals show a behavior in between the Pt-doped or Au-doped sample, according to their nanostructure (separate Au and Pt NPs, or core shell NPs).

Each sample has been then dynamically tested at the wavelength corresponding to the maximum response evaluated from the OAC curves reported in Figure 4.42. These wavelengths are 570 nm, 540 nm, 605 nm, 595 nm and 500 nm, for TA, TP, TAP, TS0.4 and TS1.6 sample, respectively. The tests are reported in Figure 4.43.

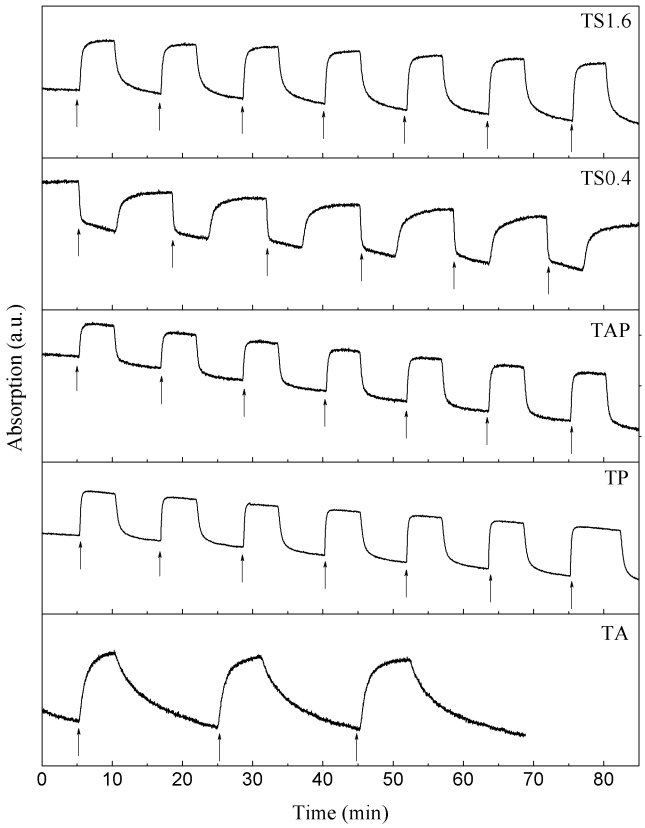

Figure 4.43. Time-resolved response for the five samples annealed at 200 °C after repeated cycles air-1%H_2-air at room temperature. The arrows indicate the hydrogen stream introduction inside the test cell. The wavelength used for the tests are 570 nm (TA), 540 nm (TP), 605 nm (TAP), 595 nm (TS0.4) and 500 nm (TS1.6).

As expected, the TiO_2-Au sample shows the worse dynamic behavior, with very long response and recovery times, respectively about 3 and 10 minutes, while all the samples containing Pt present a better time resolved performance. In details, all response times are in the 20-40 seconds range, quite interesting for sensors operating at room temperature. As far as the recovery times are concerned, they are in the 130-150 seconds range, so quite close to the recovery times detected for TiO_2-Au samples operating at high temperature presented in section 4.3.1.3. Slightly higher recovery times (170 seconds) are detected for the TS0.4 sample, the film containing Au@Pt NPs with a thin Pt shell, consistent with the very low amount of Pt present. It is interesting to notice that an improvement compared to TiO_2-Au sample is experienced either with core-shell Au@Pt NPs and with separate Au and Pt NPs, confirming that the two metals are able to interact with each other even if not in close contact. Moreover, the influence of the analysis wavelength can be seen: TS0.4 sample is tested at wavelength in which the hydrogen presence causes a decrease in absorbance, while all other samples are tested at a

wavelength corresponding to an increase in absorbance. This behavior can be exploited to improve the selectivity between interfering gases.

A slight baseline drift is experienced in some tests, possibly due to incomplete stabilization of the samples after the 200 °C annealing: a prolonged treatment at that temperature might solve this problem, without promoting the alloying of Au and Pt. Nevertheless, the overall results are extremely promising, considering that the tests have been performed at room temperature, and that the films are only 50-60 nm thick: in particular, the fast response and recovery times, and the step-like dynamic performances after repeated air-hydrogen cycles are noteworthy.

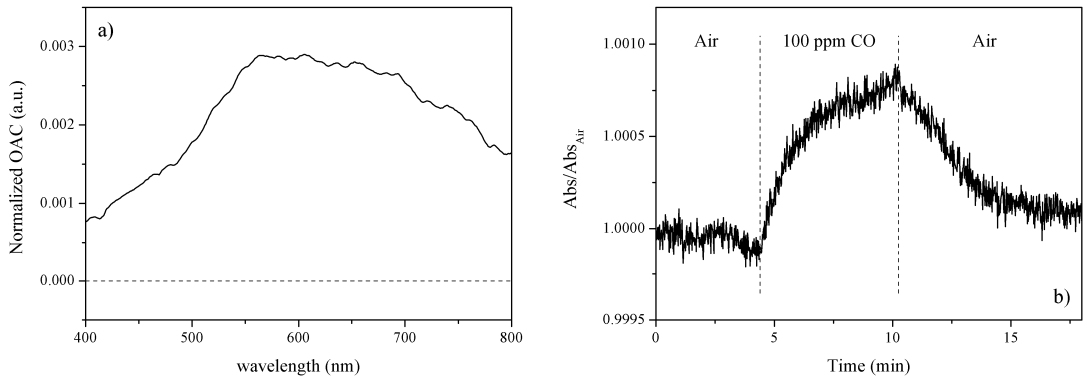

Figure 4.44. a) Normalized OAC plot of TS1.6 sample annealed at 200 °C after exposure to 0.01% CO at room temperature. b) Time-resolved response TS1.6 sample annealed at 200 °C after a cycle air-0.01%CO-air at room temperature.

Preliminary tests have been performed also with CO exposure at room temperature: TS1.6 sample annealed at 200 °C was chosen for this test, and the results are reported in Figure 4.44. A weak but still detectable response is detected after 100 ppm CO exposure, and the response is reversible, and slightly wavelength dependent, as observed previously for hydrogen exposure. Response and recovery times are not ideal, and also the intensity of the response is quite low, but considering that the test is performed at room temperature, with a 60 nm thick film and with a relatively low CO concentration, these preliminary results are promising.

Further tests for hydrogen detection have been performed at 150 °C OT on the samples annealed at 500 °C: since the films containing Au@Pt NPs showed the alloy formation between the two metals, they are not considered for these measurements. Interestingly, TiO_2-Pt sample does not show any appreciable optical response, as can be seen from Figure 4.45, while the other two samples present the usual response of Au-containing thin

films. The response is higher in TA sample compared to TAP, because the Au amount is higher, as described before. The fact that TP sample does not respond can be ascribed to two main reason: the sensitivity of Pt-doped samples is much higher at lower temperatures, and the porosity as well as the surface area is reduced in these samples, as a consequence of the higher annealing temperature. So it is likely that bigger anatase crystals provide less specific surface for the gas adsorption, and that Pt NPs are much less efficient at 150 °C. The drop in sensitivity of Pt-doped semiconducting oxides when increasing too much the operative temperature has been widely discussed in the literature: for example, Wlodarski and coworkers [86] showed that the maximum optical response for a nanostructured WO_3-Pt film for hydrogen detection is achieved at about 70 °C, while over 140 °C the response is almost null.

Nevertheless, from the time resolved tests performed on the two Au containing samples, an effect of Pt NPs can be found: in fact the behavior of TAP sample is almost ideal, with extremely fast response and recovery times (about 10 and 30 seconds, respectively), and a step-like dynamic performance, while TA sample, although showing a quite good performance as well, presents a slight baseline drift, and longer response and recovery times (about 30 and 120 seconds, respectively).

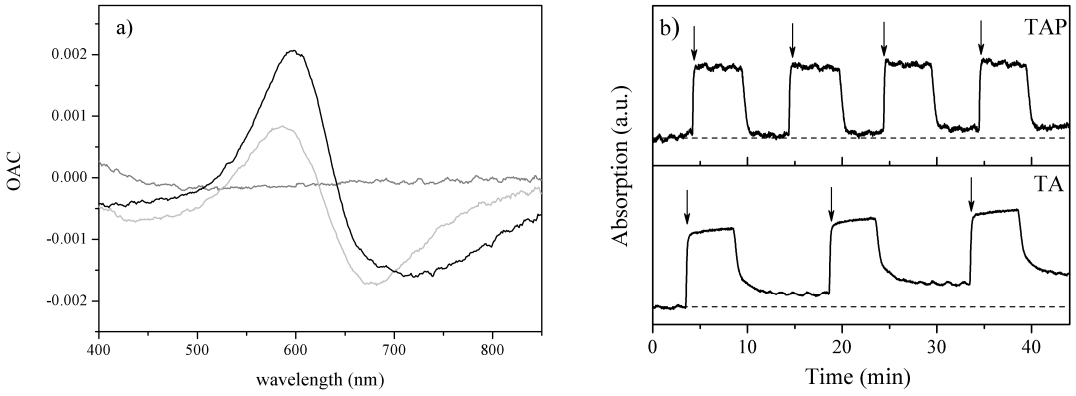

Figure 4.45. a) OAC plots for TA (black line), TP (dark grey line) and TAP (light grey line) samples annealed at 500 °C after exposure to 1% H_2 at 150 °C OT. b) dynamic tests for TA and TAP samples annealed at 500 °C performed at 598 nm and 585 nm respectively, after repeated cycles air-1%H_2-air at 150 °C OT. The arrows indicate the hydrogen stream introduction inside the test cell, and the response value in air is highlighted with a dashed line.

So it is likely that Pt NPs are not able to provide a good optical signal when embedded inside a TiO_2 film tested at 150 °C OT, but if Au NPs are present, a synergetic effect

between Au optical properties and Pt catalytic properties occur, providing an enhancement in the sensing properties.

These results are extremely promising for the use of TiO_2-based nanocomposites at low temperatures, for a variety of different applications, like SPR devices, optical fibers based devices, gratings-based devices, and room temperature measurements of biological samples.

4.3.2 ZnO-based thin films

4.3.2.1 Synthesis

The final solutions for films deposition were prepared by mixing the ethanolic suspension of ZnO (or doped-ZnO) NPs with PVP-capped Au NPs in ethanol leading to a final ZnO nominal concentration of 0.4 M and a Au:Zn molar ratio between 0.3 and 5%, according to the amount of metal NPs solution used. Au free samples were prepared substituting Au NPs solution with ethanol.

All the film samples were deposited by spin coating at 2000 rpm for 30 seconds on either SiO_2 and Si substrates and annealed in a muffle furnace directly at the desired temperature (ranging from 100 °C to 500 °C) for 1 hour in air. On occasion, multilayered samples were prepared: the film was spun coated, stabilized at 250 °C for 10 minutes, then the procedure was repeated 4 times, and the final annealing was done at 500 °C for 1 hour.

Impedance spectroscopy measurements were performed on thin films deposited on patterned ITO-on-SiO_2 electrodes, prepared via standard photolithography techniques using AZ Electronics 1518 photoresist: the polymer was spun on the entire substrate, then it was patterned with UV light: the exposed polymer became stabilized, while the unexposed polymer was etched with 0.4% wt NaOH aqueous solution, exposing the ITO. Then the unprotected ITO was etched in 6% wt HCl aqueous solution, and eventually the remaining polymer was washed away with acetone. After spinning and annealing the ZnO-based films, the gold electrodes were evaporated.

4.3.2.2 Characterization of ZnO and doped-ZnO films containing Au13 nanoparticles

For a preliminary study, ZnO colloids doped with 2.5% molar of Cobalt, Manganese and Nickel ions were synthesized, and used for thin films deposition. Both Au-free and 5% Au-loaded samples were prepared, with a 5-layer structure.

These systems were only briefly characterized because the main target was to identify the best dopant ion in order to improve the gas sensing behavior of the ZnO-based thin films, and then to focus on that particular material.

The XRD patterns of the synthesized films containing Au NPs after the 500 °C annealing are shown in Figure 4.46: both Au (JCPDS No.04-0784) and ZnO (JCPDS No. 36-1451) diffraction peaks are clearly evident, and a big difference in the FWHM of ZnO peaks compared to the as synthesized NPs can be seen (compare with Figure 4.12). This is due to crystals growth promoted by high temperature annealing. In fact performing the Scherrer analysis on these diffraction patterns, the average size of the ZnO crystals is between 12 and 22 nm according to type of dopant, as shown in the table.

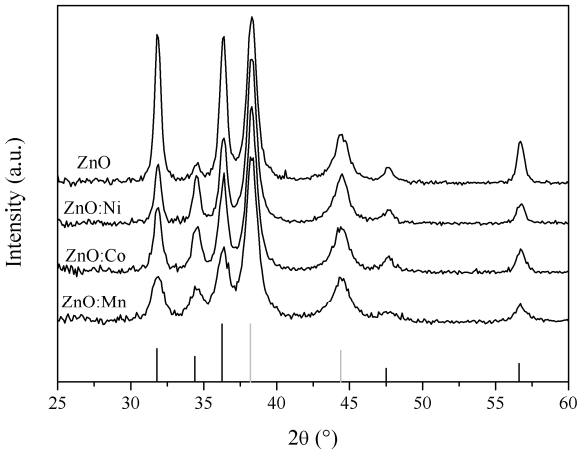

Sample	ZnO crystallites size (nm)
ZnO	21.7±0.7
ZnO:Ni	21.1±0.6
ZnO:Co	17.5±0.6
ZnO:Mn	11.9±0.4

Figure 4.46. XRD patterns for ZnO and doped-ZnO thin films containing Au NPs annealed at 500 °C for 1 hour; the theoretical diffraction lines for wurtzite (black lines) and Au (grey lines) crystalline phases are reported at the bottom. The table shows the ZnO crystallite size evaluated with the Scherrer relationship.

Again, the influence of the dopant is to reduce the ZnO crystallite growth, even if this effect is much more evident for Mn compared to the other ions. An explanation of this behavior can be related to multiple oxidation states of Mn: in fact while Zn and Ni ions exist mainly in the +2 oxidation state, and Co ions are usually +2 and +3, Mn ions can be found with several oxidation states, being the most common +2, +3, +4, +6, +7. The presence of a ion with high oxidation state will lead to a substantial amount of negatively charged Zn vacancies, inducing a high extent of mechanical stresses in the lattice, preventing the crystals from growing. This effect has to be summed to the difference in size between the two ions, another cause of mechanical stresses as described in section

4.2.5.2. A similar but less pronounced effect can be seen in Cobalt doped ZnO film, while the effect of Nickel in reducing the crystallites size is not so pronounced after 500 °C annealing: this fact might be related again to the difference in oxidation state between the doping ions.

As expected, Au diffraction peaks are not evidently affected by the type of ZnO NPs, and they don't undergo any relevant change in shape due to the high temperature annealing, as observed also for TiO_2-based nancomposites.

Atomic Force Microscopy measurements were conducted to analyze samples morphology and evaluate their thickness: the results are reported in Figure 4.47 and Table 4.8. As can be seen, the surface of the samples is quite structured, due to ZnO crystalline grains; nevertheless the surface roughness is not high, being below 4 nm for all the samples, providing good optical quality and absence of scattering phenomena. The thickness evaluated scratching the samples and letting the AFM tip scanning the edge of the line, is in the range 70-90 nm for all the sample, but a trend in the thickness can be seen, being pure ZnO sample the thickest, and Co-doped and Mn-doped samples the thinnest.

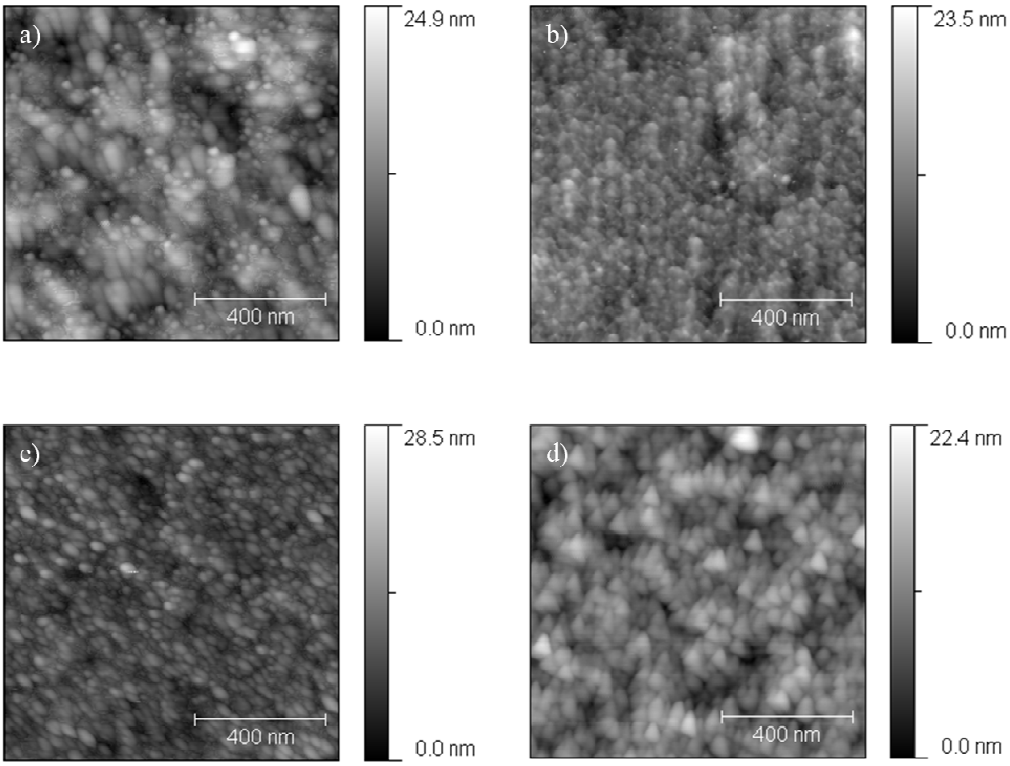

Figure 4.47. AFM images of a) ZnO; b) ZnO:Co; c) ZnO:Ni; d) ZnO:Mn films containing Au NPs annealed at 500 °C.

Table 4.8. Thickness and surface roughness for the four samples containing Au annealed at 500 °C evaluated from AFM images.

Sample	Thickness (nm)	Surface roughness (nm)
ZnO	92.3±2.8	3.4
ZnO:Co	67.9±2.5	2.3
ZnO:Ni	78.1±5.9	2.4
ZnO:Mn	67.6±3.3	2.7

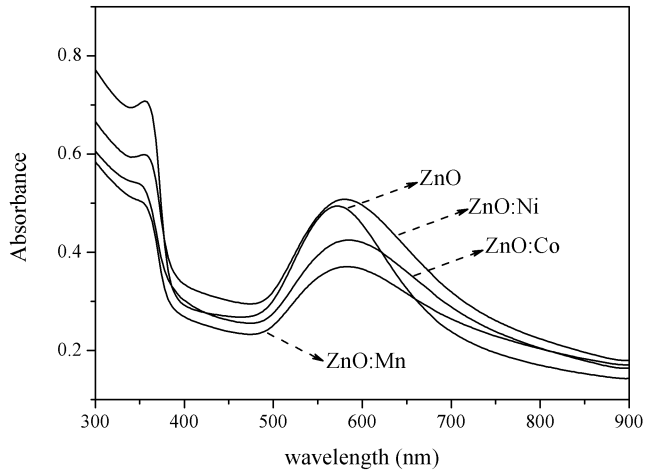

Figure 4.48. Optical absorption spectra for ZnO and doped-ZnO thin films containing Au NPs annealed at 500 °C.

Optical absorption spectra of the Au-containing sample are shown in Figure 4.48: a clear broadening of Au SPR peak, and also a small red shift is detected when Au NPs are embedded inside a doped-ZnO matrix with respect to the pure ZnO. This effect might be related to a difference in the electronic properties of the doped-ZnO, that can interact with the surface free electrons of Au NPs, affecting the SPR frequencies.

From the intensity of the ZnO exciton peak it is possible to have an idea of the thickness of the films, as reported in the literature [87]: undoped ZnO film is the thickest, followed in order by Ni-doped, Co-doped and Mn-doped. These data are in well agreement with the thickness estimated from AFM measurements. Since the precipitation-redispersion protocol was the same for the different ZnO colloidal solutions, and so were the deposition parameters, this difference in thickness can be ascribed to different precipitation threshold of ZnO colloids undoped or doped with different ions, or to different solubility of these particles in the solvent/nonsolvent mixture (being also the size of the particles slightly different), leading to a different amount of precipitate particles, and so to a difference in the molar concentration of the final solution used for depositions;

eventually, also experimental errors in the spinning solution preparations can be the cause of such thickness difference. The actual thickness of the sample has thus to be taken into consideration when comparing the gas sensing results.

4.3.2.3 Gas sensing properties of ZnO and doped-ZnO films containing Au13 nanoparticles

These materials were tested as optical sensors for CO detection; different operating temperatures were used, in order to identify the best operative conditions: all the samples gave null or very low response between 25 °C and 200 °C OT, while in the 250 °C - 350 °C range the response was easily detected. Since at 250 °C OT the transient times were slightly long, and sometimes an incomplete retrieval of the baseline was experienced, all the test reported in the following, if not specified, have been carried out at 300 °C OT. The aim of these tests was to select the best dopant ion between Ni, Co and Mn: as shown also in the previous chapter for ZnO films prepared with the sol-gel method, Au-free samples did not give any appreciable response, while Au-containing samples showed the typical wavelength dependent behavior of Au-doped transition metal oxides: Figure 4.49a shows the OAC curves for the 4 prepared samples exposed to 1% CO at 300 °C OT.

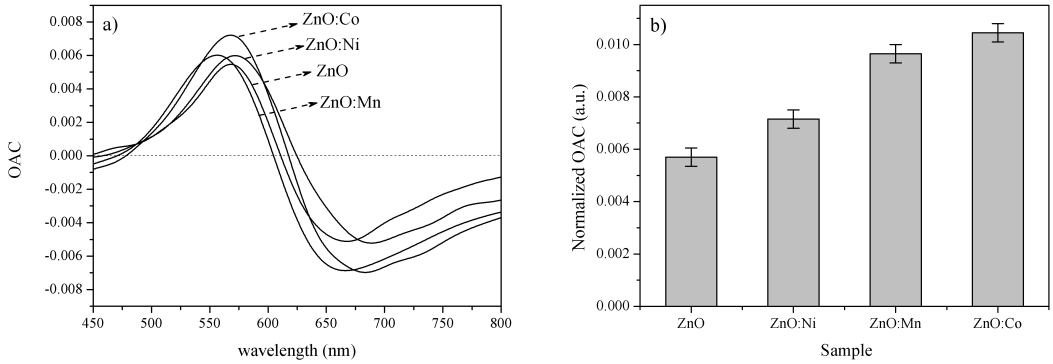

Figure 4.49. a) OAC curves for ZnO and doped-ZnO thin films containing Au NPs annealed at 500 °C for 1 hour. b) Normalized OAC maximum for the four tested samples.

A difference in the intensity of the response can be seen comparing the four samples: in fact undoped ZnO shows the less intense OAC maximum and minimum, despite the highest thickness, while Co-doped sample is the most sensitive to CO, even if the thickness is much lower compared to pure ZnO sample.

This difference in sensitivity becomes clearer when normalizing these values to the sample thickness, as shown in Figure 4.49b. The normalization has been performed calculating the average response of each sample summing the absolute OAC value both at positive and negative maximum wavelength, and then dividing by the sample thickness as measured with AFM. Cobalt and Manganese doped samples show evidently the best sensing response, while undoped ZnO has the lower response, confirming the positive effect of doping ZnO crystals with transition metal ions. The enhancing effect of Co and Mn ions might be related to their multiple oxidation states, that allows a variation of charge carriers concentration, improving the material performances, as shown in the literature for ZnO films doped with trivalent ions like Al^{3+} or Ga^{3+} [88-90]; as a matter of fact Ni-doped ZnO does not show a great improvement, and according to what presented before, this fact can be ascribed to the main oxidation state of Ni, being the same as Zn.

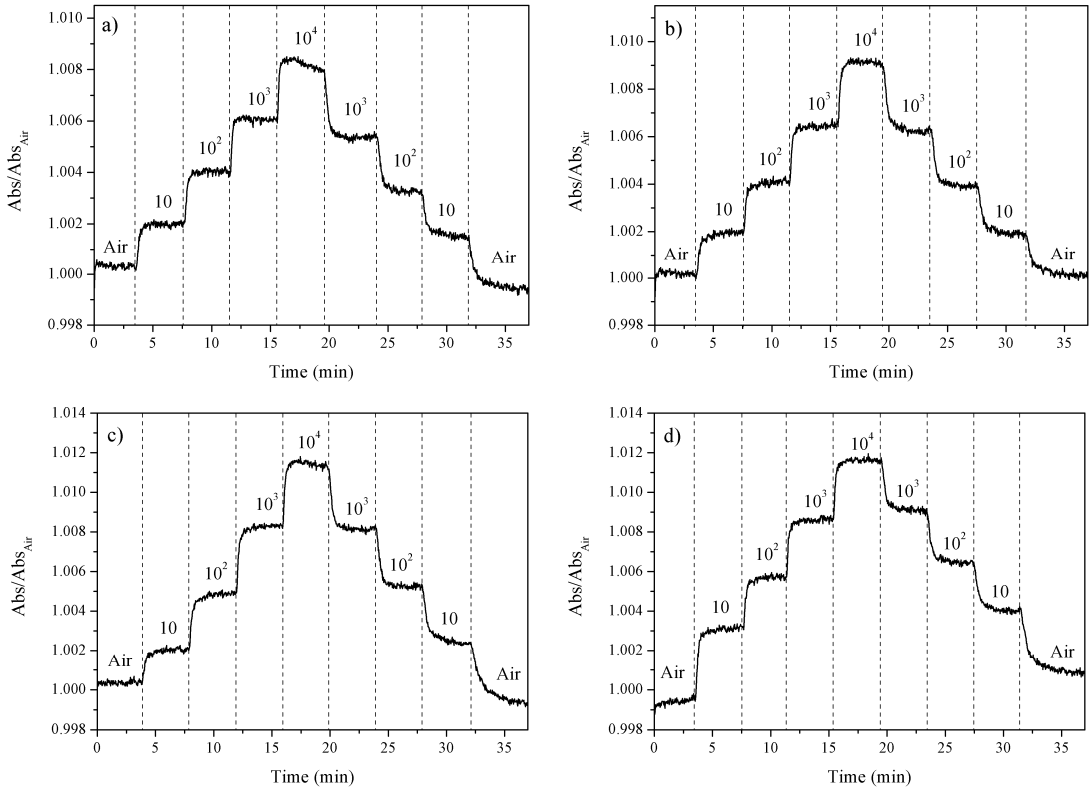

Figure 4.50. Dynamic response of a) ZnO-Au; b) ZnO:Ni; c) ZnO:Co; d) ZnO:Mn samples at the wavelength corresponding to the maximum of OAC curve and at 300 °C OT, during exposure to different CO concentrations expressed in ppm.

Nevertheless, all ZnO samples show acceptable dynamic behavior after repeated exposures to different CO concentrations in air, as reported in Figure 4.50: the response

times are relatively fast, while the recovery times are a little longer but still satisfactory. As can be seen, even if these samples are relatively thin, they are able to detect down to 10 ppm CO, with a linear-logarithmic relationship between intensity of the optical variation and target gas concentration, already observed for the TiO_2-Au samples presented in section 4.3.1.3 and the ZnO-NiO films discussed in Chapter 3.

Comparing the Abs/Abs_{Air} values, it can be seen that the Co and Mn doped samples show the best performance, while the undoped ZnO has the lower intensity: this is a confirmation of the normalized response shown in Figure 4.49b, since the dynamic tests are normalized to the absorbance value in air, so somehow they take into account the thickness of the samples. From these dynamic tests the sensitivity and the detection limits can be evaluated, plotting the Response Intensity value (see Appendix section for details) versus the CO concentration, as reported in Figure 4.51. These values have been averaged measuring the intensity of the response for two different tests for each sample. The linear fits of the experimental data shown as dashed lines confirm the linear relationship between the response and the analyte concentration, and also extrapolating the data at lower concentrations the detection limit can be estimated in the 1-3 ppm range. Again, being the sensitivity defined as the slope of the response curve versus concentration, the Co-doped sample showed the highest sensitivity (highest slope of the fitting line) and also the highest response intensity, together with Mn-doped sample.

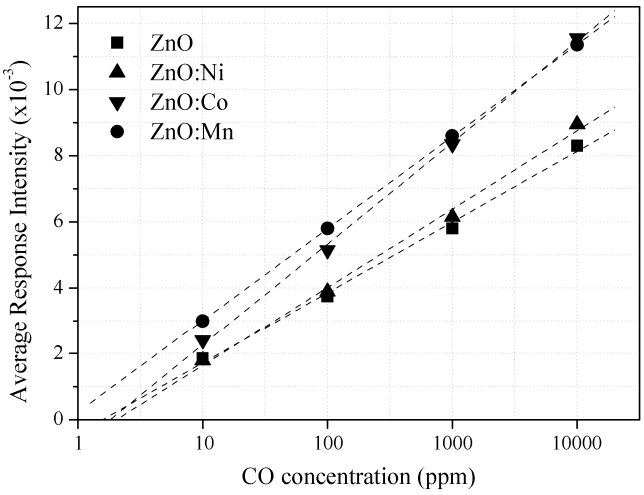

Figure 4.51. Sensitivity plots for CO detection for the four samples tested at the wavelength corresponding to maximum of OAC curves and at 300 °C OT. Linear fits for the four experimental sets of data are also reported.

According to all the presented data, even if also ZnO:Mn nanocomposites show good response, Cobalt was chosen as transition metal ion to dope ZnO NPs with, because of the higher stability of the colloidal solutions, a wider range of size of the ZnO crystals obtainable upon thermal treatment, and the easiness of the precipitation/redispersion procedure.

4.3.2.4 Characterization of ZnO and ZnO:Co films containing Au13 nanoparticles

A more thorough characterization of Co-doped ZnO films has been carried out, as also discussed in Section 4.2.5.2 analyzing the colloidal solutions of ZnO nanocrystals. Like for TiO_2 based samples, the effect of embedding different concentrations of Au NPs has been studied. Two different types of thermal treatments were chosen: an annealing at 100 °C is performed on samples to be used for ethanol sensing at room temperature, while samples annealed at 500 °C are for CO sensing in transmission mode at 300 °C OT.

Structural characterization has been performed with XRD on thin films annealed at 100 °C, but being the crystals quite small and the films very porous and thin, the signal detected was very low, so only one XRD pattern is shown, since the signal to noise ratio is relatively low: anyway, as can be seen in Figure 4.52, the diffraction peaks for both ZnO and Au are detectable. Again, a focused XRD analysis in the 34-42 degrees range has been performed, showing the increase in Au (111) diffraction peak intensity with increasing Au amount in the spinning solution, confirming the successful embedding of different concentrations of Au NPs inside nanocrystalline ZnO films. For the sake of brevity these data are not shown since they are similar to the graphs shown in Figure 4.29.

It is though interesting analyzing the morphology of the ZnO films evaluated with SEM: samples stabilized at 100 °C show a quite high surface roughness and bigger pores (Figure 4.53) if compared with the TiO_2 samples annealed at the same temperature presented in Figure 4.30. This is due to the different crystalline structure and morphology of the two oxides, since TiO_2 crystalline films tend to organize in a more compact and dense coating, while ZnO films have a more open structure, even if the initial particles size is roughly the same for the two materials. Moreover since the contrast of ZnO is much different compared with TiO_2, in these SEM images it is quite hard to identify Au NPs, even if some brighter spots corresponding to the noble metal are still detectable.

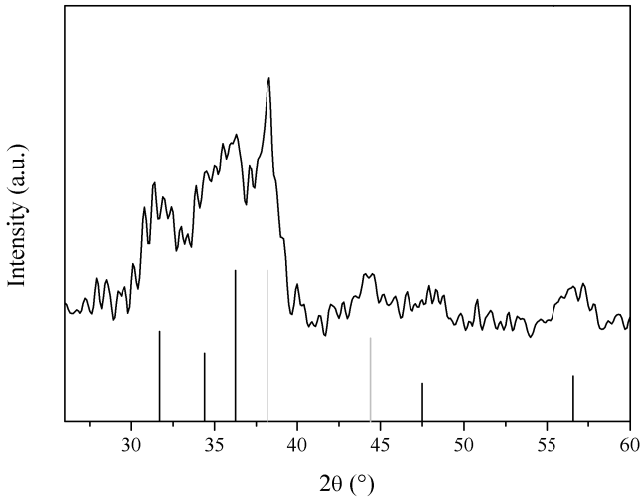

Figure 4.52. XRD patterns of a ZnO film containing 4% Au13 NPs annealed at 100 °C. The theoretical diffraction lines of wurtzite ZnO (black lines) and Au (grey lines) are reported at the bottom.

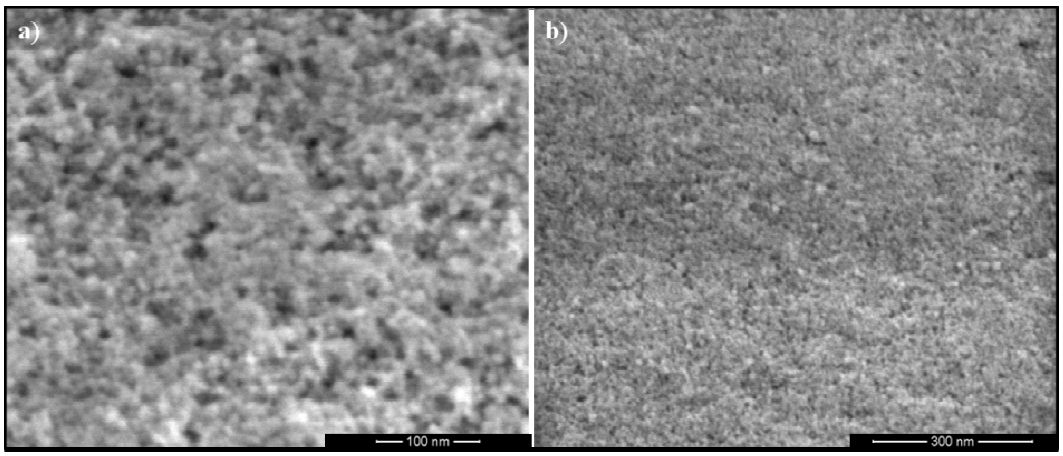

Figure 4.53. SEM images of: a) ZnO film; b) Co-doped (5%) ZnO film, both containing 3% Au NPs annealed at 100 °C.

The higher surface roughness of ZnO thin films becomes much more evident analyzing samples annealed at higher temperatures, when the crystals grow and the potential amorphous phase becomes crystalline, as can be seen comparing the SEM images presented in Figure 4.54 for the 500 °C annealed samples with the previously presented SEM for TiO_2-Au samples treated at the same temperature.

In addition, comparing the morphology of the ZnO films with different Cobalt doping, a slight increase in densification and a consequent decrease in surface roughness and porosity increasing the Cobalt amount can be detected; the cause of this experimental evidence can be ascribed to the different size of ZnO particles according to Co doping:

the bigger the particles, the rougher the surface of the sample, and on the opposite way, the smaller the particles, the more compact and smooth the sample. In any case, with the exception of these differences, all the ZnO samples are porous and with a great amount of surface area, both fundamental conditions for thin films to be used as gas sensors.

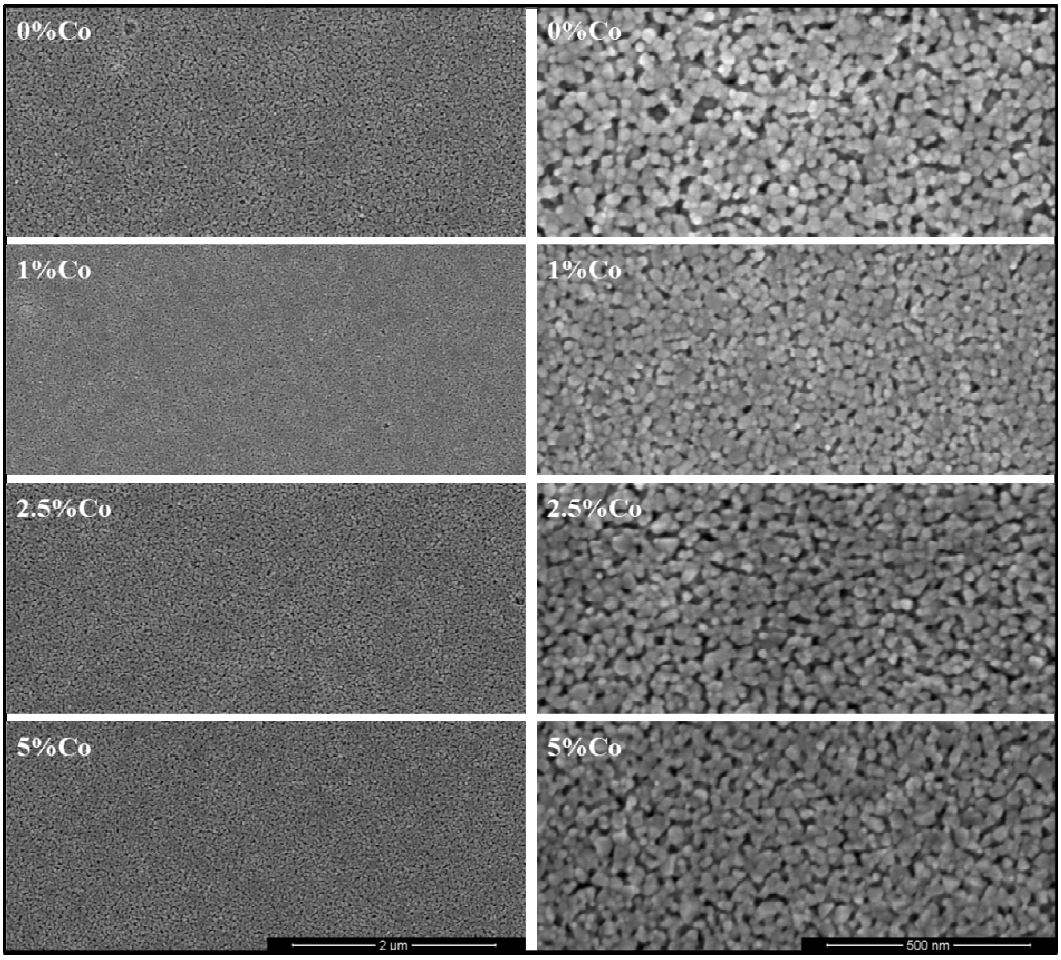

Figure 4.54. SEM images of ZnO films with different Co concentrations, all containing 1% molar Au NPs and annealed at 500 °C, at low (left side) and high (right side) magnifications.

As shown before, XRD characterization is useful to evaluate the crystalline phases present inside the films, their crystallites size, and also to have an estimation of the amount of Au embedded; all these results are presented in Figure 4.55.

ZnO wurtzite peaks (JCPDS No. 36-1451) are evident in all samples, and performing the Scherrer analyses on all the five ZnO peaks shown the average crystallite size has been estimated to be 29.3±2.2 nm for pure ZnO samples, 28.1±2.5 nm for 1%Co doped ZnO, 25.0±2.8 nm for 2.5%Co doped ZnO, and 23.5±2.4 nm for 5%Co doped ZnO, confirming

the trend seen for the colloidal NPs (higher Cobalt doping causes smaller crystals formation). Au diffraction peaks intensity is directly related to the metal concentration, since thickness of the films and size of the samples probed with the XRD were similar in all samples.

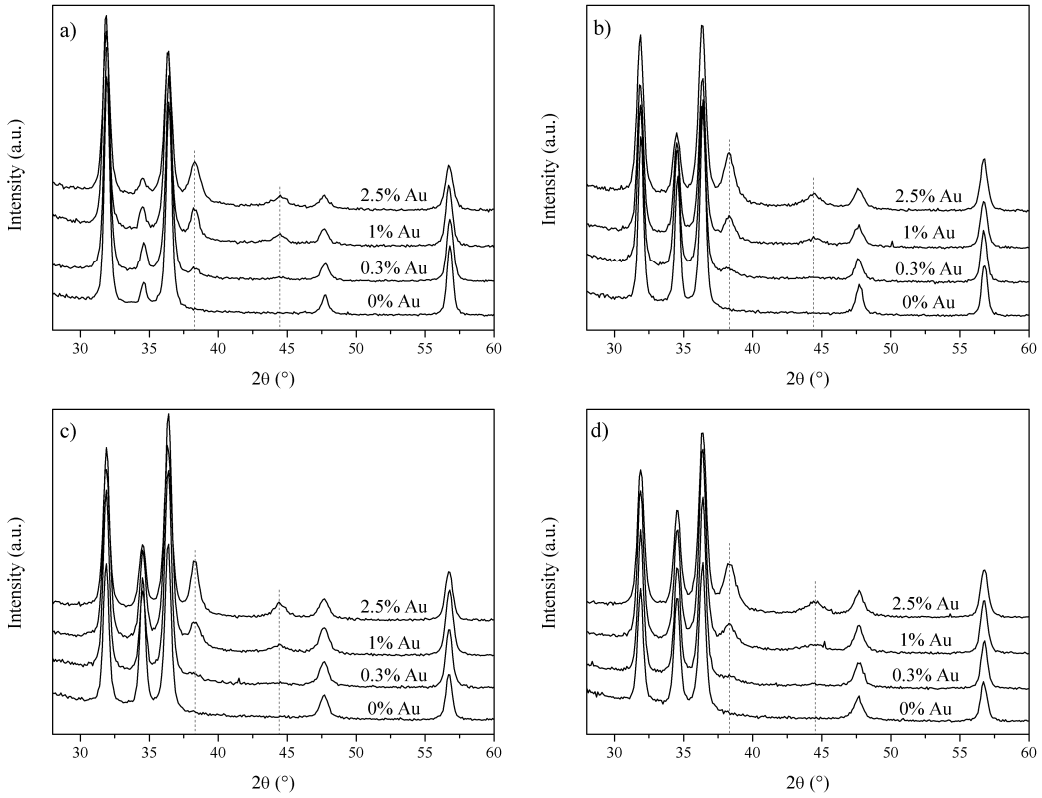

Figure 4.55. XRD patterns of ZnO films with a) 0% Co; b) 1% Co; C) 2.5% Co; d) 5% Co, containing different Au NPs amount and annealed at 500 °C. Vertical dotted lines highlight the theoretical diffraction peaks for cubic Au

Optical characterization is also useful to evaluate the effect of cobalt ions doping and Au NPs embedding on the optical properties of Zinc oxide films: the main results of the optical characterization are shown in Figure 4.56 for samples composed of 4 layers annealed at 500 °C as described in section 4.3.2.1.

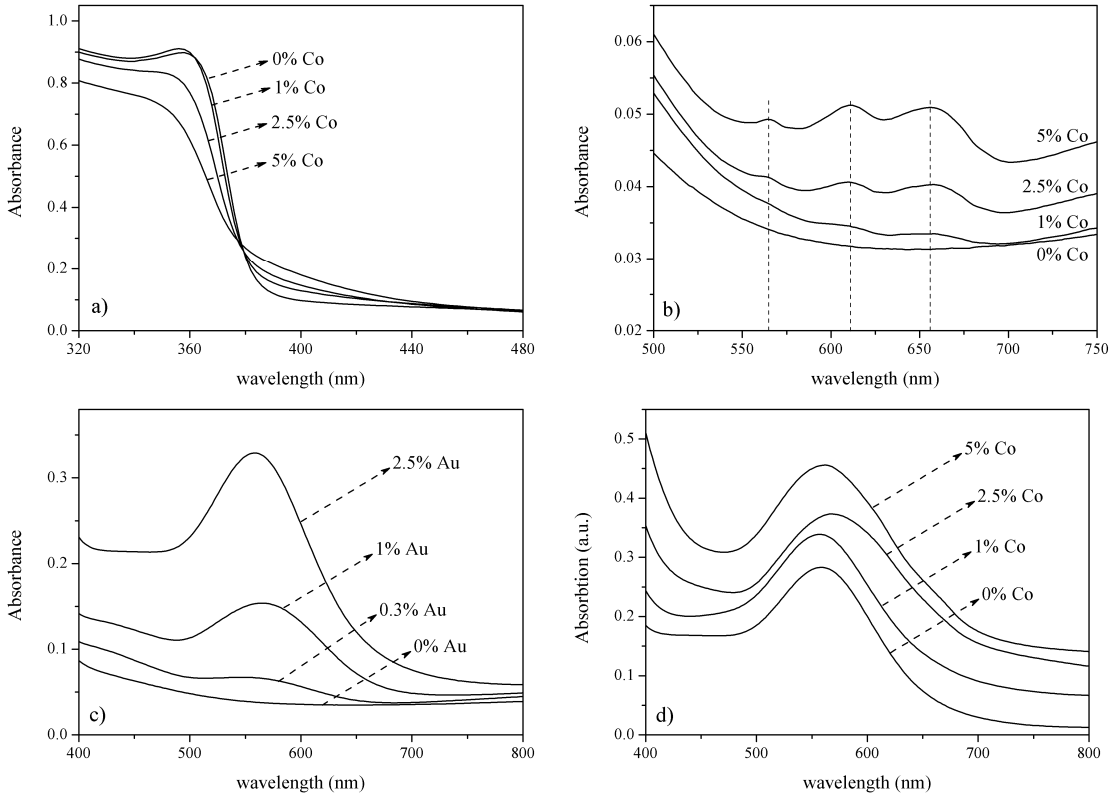

Figure 4.56. Absorption spectra of ZnO-based films annealed at 500 °C: a) Au-free ZnO films with different Co concentrations showing the UV absorption onset region; b) Au-free ZnO films with different Co concentrations showing the Co absorption bands; c) undoped ZnO films with different Au amount showing the increase in Au SPR peak intensity; d) ZnO films with different Co concentrations and 2.5% Au showing the Co effect on Au SPR peak.

In Figure 4.56a e 4.56b the effect of Co^{2+} is presented: as already seen for the colloidal suspensions, cobalt ions incorporation inside the wurtzite crystalline structure of ZnO causes a blue shift of ZnO first exciton peak and also a tail of absorption in the high energy region of the visible range (380-450 nm); moreover at higher wavelengths the three typical absorption bands of cobalt ions in tetrahedral coordination: since this behavior is the same observed for the colloidal suspension, it can be said that no segregation phenomena of Co ions induced by the high annealing temperature appear to occur, because the effect on the UV absorption onset and on the 560-680 nm region are the same observed for the as-synthesized NPs in solution. Figure 4.56c shows the effect of Au NPs concentration on undoped ZnO films: a clear increase in Au SPR peak intensity is detected when increasing the Au NPs concentration from 0.3% to 2.5%, while no evident shift of the peak wavelength is seen, as expected from the relatively low

concentration of the metal NPs, that otherwise, if the concentration is high enough and so the particles come in close proximity, can interact with each other, causing a coupling of the plasmon resonances, resulting in a red shift of the SPR frequency [91]. Eventually, Figure 4.56d shows the effect of cobalt doping on the Au SPR band: the Au plasmon peak broadens with increasing Co amount, and it is also found to red shift accordingly, even if the shift experienced for the ZnO sample containing 2.5% Co is higher compared to the sample containing 5% Co; this experimental evidence can be ascribed to some minor aggregation of Au NPs inside the film during the deposition procedure, that as just said, can product a coupling of the plasmon resonances and so a red shift of the SPR peak.

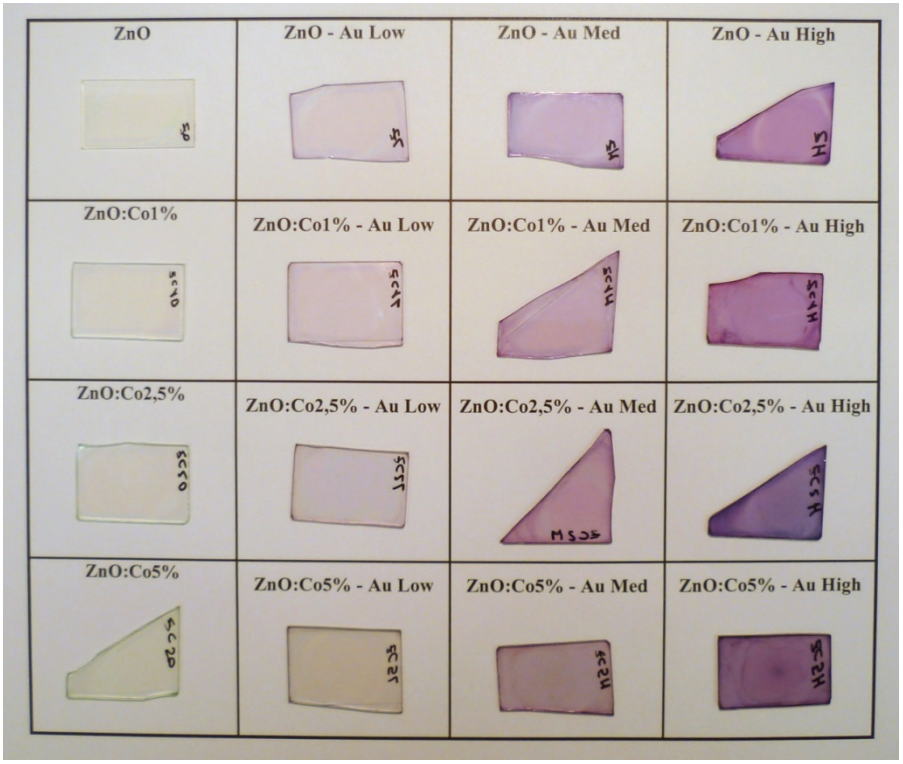

Figure 4.57. Picture of ZnO films with different Co and Au amount (Au Low = 0.3%; Au Med = 1%; Au High = 2.5%). Each rectangular box is approximately 4.5 x 3.9 cm.

All the considerations about the differences in optical absorption spectra can be easily visualized in Figure 4.57, that shows a picture of a set of samples with various Co^{2+} doping level and different Au NPs amount, all annealed at 500 °C. Comparing the Au-free samples, they are all almost transparent, even if a pale blue-green color is detectable in the high Cobalt amount samples, as a consequence of Co^{2+} absorption band in the visible range discussed before. All Au doped samples show a pink-violet color, due to the

Au SPR peak, and the color intensity is in direct relationship with the noble metal amount. Moreover, a slight change in color from pink-violet towards blue can be seen increasing the Cobalt amount, keeping the Au NPs concentration constant, as a consequence of the already mentioned red shift of the plasmon peak. In the end, also the singular sample with 2.5% Cobalt and the highest Au concentration can be appreciated, being its color slightly outside the trend of the other samples, as discussed analyzing Figure 4.56d.

Impedance spectroscopy measurements were performed in order to evaluate the electrical properties of these ZnO-based films, and analyze the effect of cobalt ion doping and Au NPs embedding.

Impedance spectra were collected between 10 and 10^6 Hz at applied voltages between -1 and 2 V. Two semicircular features were observed in the Nyquist plots for all samples measured. The low frequency impedance component can be ascribed to conduction along the particle surface (or grain boundaries) while the high frequency component is attributed to conduction through the particle core, with the latter usually more pronounced than the former. Nevertheless, also the porosity can contribute to the low frequency component [92]. These plots are not reported here for the sake of brevity, because every sample was tested at least in 4 different contacts and so the number of graph to report would have been too high. Moreover these plots are useful to gain information about mobility, resistivity and doping density, all information that will be presented in a more condensed view in the following. Considering the system as a sum of resistors and capacitors as described in the literature [93], and focusing on the core conduction, so ignoring the surface contribution, the equivalent circuit of the ITO-ZnO-Au sandwich structure can be schematized as the following:

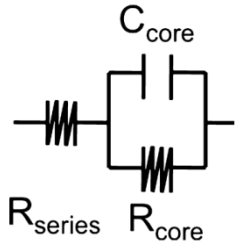

where both the resistance and the capacitance of the ZnO film are considered.

The film resistivity can be easily calculated from the real part of the impedance (directly related to the resistance *R*), with the equation:

$$\rho = R\frac{A}{d} \tag{4.2}$$

knowing the area of interest of each contact (A) and the device thickness d; the mobility μ can be obtained from the following relationship [94]:

$$\mu = \frac{d^2 f}{2E} \tag{4.3}$$

where d is again the film thickness, f is the frequency at which the imaginary component of the impedance reaches the relative maximum (or alternatively, the frequency at which the real component of the impedance plateaus at low frequencies), and E is the applied voltage.

Unfortunately, despite the high number of data collected, the results were inconclusive and sometimes contrasting, as can be seen in Figure 4.58, where the core resistivity and the mobility for the 16 samples tested (the same samples shown in Figure 11) are plotted as a function of Au and Co concentration.

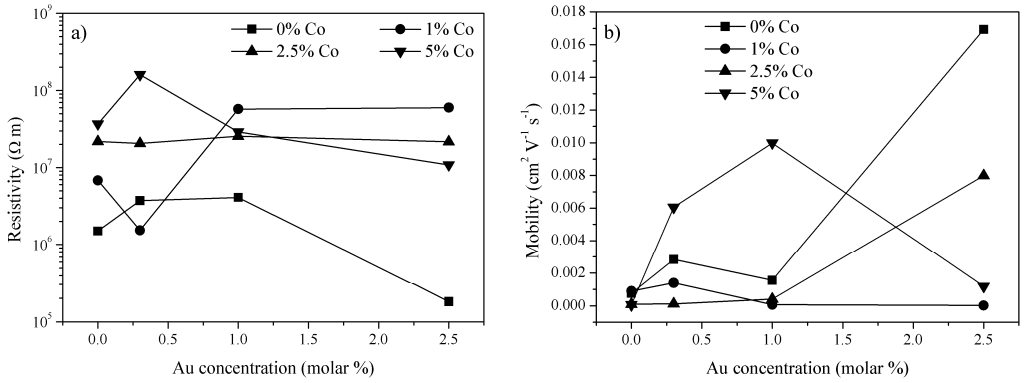

Figure 4.58. Resistivity (a) and mobility (b) values for pure and Co-doped ZnO as a function of Au NPs concentration.

As can be seen, no definite trends can be drawn from these data: the possible explanations are related to the intrinsic porosity of these samples. In fact, to obtain resistivity and mobility values, the thickness of the sample is required: but this thickness is the effective thickness between the ITO and the Au contacts, and not the average thickness of the sample measured with ellipsometry or profilometry. When evaporating gold contacts, the Au vapors penetrates through the film pores and so the actual thickness might be

substantially lower than the measured one, and more important, can significantly vary from one contact and another, and from one sample and another. As a matter of fact, many contacts were found to be shortened, as a consequence of the formation of a contact area between the ITO and the evaporated gold. Such an indetermination is the main source of the unreliability of these electrical data: it was tried to minimize this effect by increasing the sample thickness, but the effort was useless. The only trend that seems effectively proved, even if in countertendency with the expectations, is reported in Figure 4.59: the resistivity of the Au-free films is found to increase with increasing Cobalt concentrations, while the mobility is found to decrease. These results are in strong countertendency with the literature, where substitutional ions with higher oxidation number compared to Zn^{2+} inside the ZnO lattice are proved to increase the electrical conductivity of the films, compared to undoped ZnO [88-90].

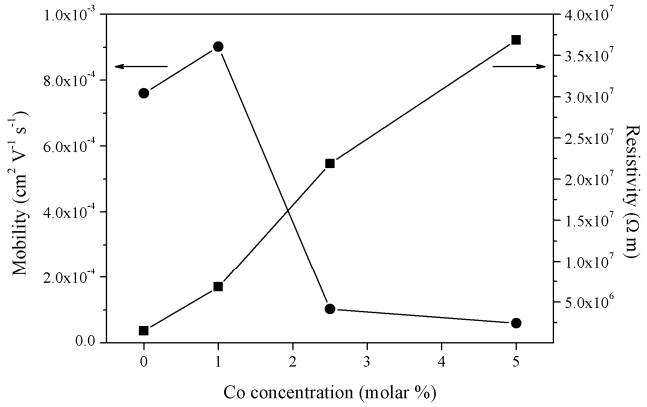

Figure 4.59. Comparison of resistivity and mobility values as a function of Cobalt concentrations for Au-free samples.

From impedance spectroscopy measurements the doping density *N* can be also inferred using the following relationship [95]:

$$\frac{1}{C^2} = \frac{2}{e\varepsilon\varepsilon_0 N}\left(E - E_{fb} - \frac{kT}{e}\right) \tag{4.4}$$

where *C* is the capacitance evaluated from the imaginary part of the impedance, ε is the dielectric constant of ZnO, ε_0 is the permittivity of free space, *E* is the applied potential and E_{fb} is the flatband potential. So by plotting C^{-2} as a function of the applied voltage (the so-called Mott-Shottky plot), from the linear region of this graph it is possible to

estimate the donor density (holes or electrons according to the type of the semiconducting material; in the case of n-type ZnO, electrons), because the flatband potential can be obtained extrapolating the linear fit for $C = 0$. Moreover, also the depletion width w can be calculated, using the following relationship:

$$w = \sqrt{-\frac{e\varepsilon\varepsilon_0 E_{fb}}{eN}} \tag{4.5}$$

These results are reported in Figure 4.60: all the data have been obtained measuring all samples at least on 4 contacts and for 4 different frequencies (1 MHz, 100 kHz, 10 kHz, 1 kHz): the data presented here refers only to the 10 kHz measurements, since similar trends for the other frequencies have been observed.

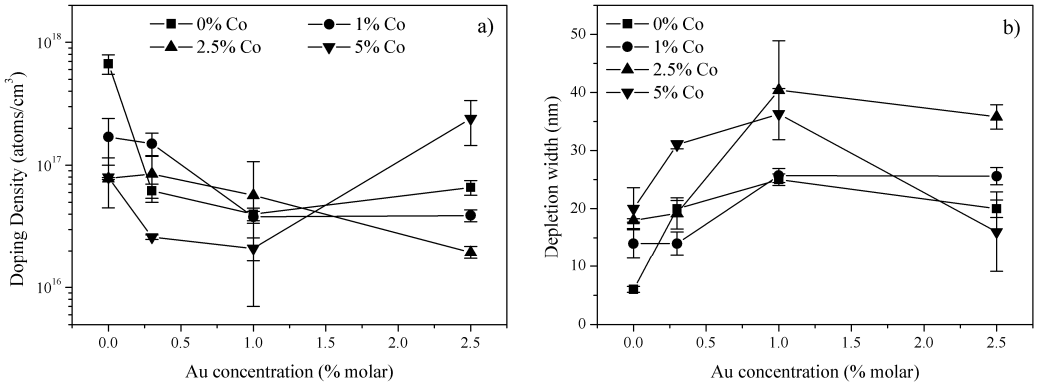

Figure 4.60. Doping density (a) and depletion width (b) values at 10 kHz for pure and Co-doped ZnO as a function of Au NPs concentration.

As before, the results are inconclusive, since no definite trend can be seen: it is difficult to isolate the contribution of Au NPs and Cobalt ions in the electric properties of ZnO films: if considering the samples without Au NPs (Figure 4.61), again a trend in countertendency with the expectations is experienced, since an increase in Cobalt doping causes a decrease in the donor density and an increase in the depletion width.

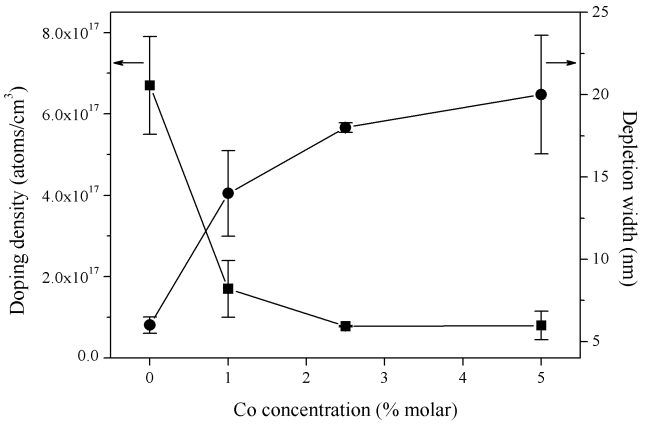

Figure 4.61. Comparison of doping density and depletion width values at 10 kHz as a function of Cobalt concentrations for Au-free samples.

As a consequence, these experiments are going to be re-scheduled trying to optimize the experimental setup, reducing the issues related to effective thickness evaluation, and possibly coupling the impedance spectroscopy analyses with field-effect transistor measurements in order to have two independent measurements of mobility and charge carriers concentration.

4.4 Conclusions

In this chapter, different combinations of noble metals / metal oxides nanocomposite films have been synthesized starting from colloidal solutions of both matrix and dopant materials. In this way, some limitations of the sol-gel based approach can be overcome, like the poor control on the size, shape and dispersity of the crystals, the presence of amorphous phase, the need for high temperature annealing. High quality nanocomposite materials are achievable in this way, with the desired physical and chemical properties that have been tailored and optimized in the colloidal syntheses.

The first part of the chapter has been dedicated to the characterization of the different metal and oxide NPs: monodisperse spherical Au colloids of about 13 nm have been synthesized with the Turkevich method, by reducing the metal precursor with sodium citrate in boiling water. After a concentration and a purification process, concentrated ethanolic solutions of PVP-capped Au NPs were obtained. Smaller spherical Au colloids (about 3 nm in diameter) have been synthesized with a stronger reducing agent in methanol in the presence of PVP, and again purified, concentrated and stocked in ethanol. Platinum NPs of spherical or faceted shape and of about 10 nm size were produced with

the polyol method reducing a metal salt in ethylene glycol at high temperature in the presence of PVP: also in this case the particles were washed, transferred into ethanol and concentrated. Eventually, Au@Pt core@shell NPs were synthesized with the seeded growth method, promoting the heterogeneous nucleation of Pt over Au seeds in the presence of a weak reducing agent. The influence of the thickness of the platinum shell around Au NPs on the optical and morphological properties of the particles has been discussed, and an interesting nanostructured shell for high Pt content NPs has been observed. Again, concentrated ethanolic solution of purified, PVP-capped NPs were obtained.

TiO_2 nanocrystals in the anatase phase have been synthesized in a mixture of methanol and water with an acid catalyzed sol-gel procedure without any capping agent; after the reaction, the particles were purified, concentrated and redispersed in methanol. Wurtzite ZnO NPs undoped and doped with transition metal ions (Co, Ni, Mn) were prepared in DMSO with a base catalyzed sol-gel process, and after the purification process they were stocked in concentrated ethanolic solutions. The effect of the synthetic parameters and of the metal ions doping has been fully discussed, showing a relationship between the size of ZnO crystals and the time/temperature combination of the synthesis and the type and concentration of dopant.

The second part of the chapter has been focused on the synthesis of thin films starting from the colloidal solutions. TiO_2-based nanocomposites containing Au NPs were annealed at different temperatures and the optical and morphological properties according to temperature, organic porogen presence, type and concentration of Au NPs were discussed: porous thin films with homogeneous dispersion of Au NPs with a well developed Au-TiO_2 interface were produced, and a relationship between refractive index, porosity and contact interface between Au and TiO_2 crystals has been presented. Optical sensing tests for reducing gases detection show reversible response in the 250 °C – 350 °C for CO detection, while for hydrogen a response was detected down to 100 °C, but with much lower sensitivity and higher transient times. Nevertheless, in the 250°C – 350 °C range, the TiO_2-Au films are extremely sensitive to reducing gases, with a linear relationship between absorbance variation and order of magnitude of target gas concentration, and a lower detection limit of about 2 ppm, quite good for 40-50 nm thick films. Moreover, the effect of Au concentration has been evaluated: the higher the Au amount, the more intense the response, as a confirmation of the fact that Au NPs are

necessary in order to produce the optical signal for the gases detection. A comparison between bigger and smaller Au NPs has been also carried out, trying to evaluate a possible catalytic effect of small Au NPs, but the sensing performances were not improved using smaller particles, also because the optical variations induced by CO and H_2 are evident in the Au SPR region, and being the plasmon peak of small Au NPs quite weak compared to bigger Au NPs, the use of small particles was found to worsen the optical sensing response. Moreover, an effect on lowering the response and recovery times wasn't found either, so a catalytic effect of small Au NPs helping the CO and H_2 reaction on the TiO_2 surface is not likely to be present. Eventually, samples annealed at 100 °C were tested at room temperature for VOCs detection in reflection mode: a reversible response to the exposure of 180 ppm of ethanol in nitrogen was experienced, with an interesting fast response time.

Then TiO_2-based films containing Au, Pt and Au@Pt NPs were prepared and the stability of the different types of metal NPs with annealing temperature was analyzed: the core-shell NPs were found to be stable up to 200 °C annealing, while starting from 300 °C the two metals began to alloy, with a consequent worsening of the optical properties of the films. So the nanocomposites annealed at 200 °C were tested for room temperature sensing of hydrogen, and a reversible and fast response was experienced for all Pt-containing samples, while the film containing only Au NPs showed very slow response and recovery times. Moreover, the samples with embedded Au@Pt core-shell NPs showed a fast but also wavelength dependent response, as a consequence of the synergetic effect of the catalytic properties of Pt NPs with the optical properties of Au NPs. Preliminary tests for CO sensing at room temperature showed also reversible and relatively fast response when Pt and Au are both present in the film. These results are extremely promising because the films were annealed at low temperatures, so they can be deposited on a variety of different substrates, like polymers, optical fibers, SPR devices and so on.

ZnO-based films were prepared mixing undoped and doped ZnO colloids with Au NPs ethanolic suspensions: the effect of transition metal ions inside the wurtzite crystalline structure of ZnO has been discussed and exploited to enhance the sensitivity to CO: porous thin films of about 70-90 nm after a 500 °C annealing showed reversible response to CO with a linear-logarithmic relationship between intensity of the response and target gas concentration. A trend according to the type of dopant has been discovered, with the

maximum sensitivity been obtained with Cobalt doping. Nevertheless, all the ZnO-based films were able to easily detect 10 ppm CO, and the lower detection limit has been estimated to be in the 1-3 ppm range. A more thorough study has then been carried out on the Co-doped samples, due to the best sensing results: the properties observed for the colloidal NPs solutions (effect of doping amount on the crystallite size and on the optical properties) have been also detected on thin films annealed at 500 °C: a decrease in crystallite size with increasing Co amount was clearly seen, and this fact reflects on the progressive blue shift of the first ZnO exciton peak; moreover Co^{2+} ions in tetrahedral coordination produce three distinctive absorption bands in the visible, that were clearly detected also in the annealed films, confirming that no segregation of Cobalt oxide phases is happening.

The increase in the sensing performances has been ascribed to Co multiple oxidation states that can enhance the electron transfer between the reducing gas and the oxide matrix: to prove this effect, a set of electrical measurements has been performed on films with different Co^{2+} and Au NPs amount. Unfortunately, the results were inconclusive, possibly as a consequence of the great porosity of the films; for this reason, the electrical tests have been rescheduled for the next months.

Bibliography

[1] Y. Sun, Y. Xia, *Science*, **2002**, *298*, 2176-2179.

[2] Y. Sun, B. Gates, B. Mayers, Y. Xia, Y. *Nano Lett.*, **2002**, *2*, 165.

[3] L.M. Liz-Marzàn, *Langmuir*, **2006**, *22*, 32.

[4] C.B. Murray, D.J. Norris, M.G. Bawendi, *J. Am. Chem. Soc.*, **1993**, *115*, 8706.

[5] J. Van Embden, J. Jasieniak, P. Mulvaney, *J. Am. Chem. Soc.*, **2009**, *131*, 14299.

[6] M. Niederberger, M.H. Bartl, G.D. Stucky, *J. Am. Chem. Soc.*, **2002**, *124*, 13642.

[7] N.R. Jana, Y. Chen, X. Peng, *Chem. Mater.*, **2004**, *16*, 3931.

[8] M. Niederberger, N. Pinna, *Angew. Chem. Int. Ed.*, **2008**, *47*, 5292.

[9] B.V. Enustun, J. Turkevich, *J. Am. Chem. Soc*., **1963**, *85*, 3317.

[10] G. Frens, *Nature (London): Phys. Sci.*, **1973**, *241*, 20.

[11] B.K. Pong, H.I. Elim, J.X. Chong, W. Ji, B.L. Trout, J.Y. Lee, *J. Phys. Chem. C*, **2007**, *111*, 6281-6287.

[12] R.G. Freeman, K.C. Grabar, K.J. Allison, R.M. Bright, J.A. Davis, A.P. Guthrie, M.B. Hommer, M.A. Jackson, P.C. Smith, D.G. Walter, M.J. Natan, *Science*, **1995**, *267*, 1629.

[13] J. Kimling, M. Maier, B. Okevne, V. Kotaidis, H. Ballot, A. Plech, *J. Phys. Chem. B*, **2006**, *110*, 15700-15707

[14] M. Brust, M. Walker, D. Bethell, D.J. Schiffrin, R. Whyman, *Chem. Commun.*, **1994**, *7*, 801-802.

[15] N.R. Jana, X. Peng, *J. Am. Chem. Soc.*, **2003**, *125*, 14280-14281.

[16] Y.C. Shiang, C.C. Huang, H.T. Chang, *Chem. Commun.*, **2009**, 3437–3439.

[17] C.C. Huang, H.Y. Liao, Y.C. Shiang, Z.H. Lin, Z. Yang, H.T. Chang, *J. Mater. Chem.*, **2009**, *19*, 755-759.

[18] C. Zhou, C. Sun, M. Yu, Y. Qin, J. Wang, M. Kim, J. Zheng, *J. Phys. Chem. C*, **2010**, *114*, 7727–7732.

[19] E. Hao, T. Lian, *Chem. Mater.*, **2000**, *12*, 3392-3396.

[20] M.M. Alvarez, J.T. Khoury, T.G. Schaaff, M.N. Shafigullin, I. Vezmar, R.L. Whetten, *J. Phys. Chem. B*, **1997**, *101*, 3706.

[21] V.K. LaMer, *J. Am. Chem. Soc.*, **1950**, *72*, 4847.

[22] H. Tsunoyama, H. Sakurai, N. Ichikuni, Y. Negishi, T. Tsukuda, *Langmuir*, **2004**, *20*, 11293-11296.

[23] G. Cao, *Nanostructures and Nanomaterials*, Imperial College Press, London, **2004**, 64.

[24] T. Herricks, J. Chen, Y. Xia, *Nano Lett.*, **2004**, *4*, 2367-2371.

[25] J. Chen, T. Herricks, Y. Xia, *Angew. Chem. Int. Ed.*, **2005**, *44*, 2589 –2592.

[26] F. Fievet, J.P. Lagier, M. Figlarz, *MRS Bull.*, **1989**, *14*, 29.

[27] B. Wiley, Y. Sun, B. Mayers, Y. Xia, *Chem. Eur. J.*, **2005**, *11*, 454-463.

[28] S. Alayloglu, A.U. Nilekar, M. Mavrikakis, B. Eichhorn, *Nature Materials*, **2008**, *7*, 333-338.

[29] L.M. Liz-Marzan, A.P. Philipse, *J. Phys. Chem.*, **1995**, *99*, 15120.

[30] J.W. Hu, Y. Zhang, J.F. Li, Z. Liu, B. Ren, S.G. Sun, Z.Q. Tian, T. Lian, *Chem. Phys. Lett.*, **2005**, *408*, 354–359.

[31] L. Lu, H. Wang, Y. Zhou, S. Xi, H. Zhang, J. Hu, B. Zhao, *Chem. Commun.*, **2002**, 144-145.

[32] G. De and C.N.R. Rao, *J. Mater. Chem.*, **2005**, *15*, 891.

[33] N.R. Jana, L. Gearheart, C.J. Murphy, *Chem. Mater.*, **2001**, *13*, 2313-2322.

[34] L. Lu, G. Sun, H. Zhang, H. Wang, S. Xi, J. Hu, Z. Tian, R. Chen, *J. Mater. Chem.*, **2004**, *14*, 1005-1009.

[35] H. Ataee-Esfahani, L. Wang, Y. Nemoto, Y. Yamauchi, *Chem. Mater.*, in press. DOI: DOI:10.1021/cm102074w.

[36] X. Chen, S.S. Mao, *Chem. Rev.*, **2007**, *107*, 2891-2959.

[37] A. Antonello, G. Brusatin, M. Guglielmi, V. Bello, G. Mattei, G. Zacco, A. Martucci,. *J. Nanopart. Res.*, **2010**, DOI: 10.1007/s11051-010-9923-4.

[38] C. W. Bunn, *Proc. Phys.* Soc. London , **1935**, *47*, 835.

[39] Y. Chen, D.M. Bagnall, Z. Zhu, T. Sekiuchi, K. Park, K. Hiraga, T. Tao, S. Koyama, M.Y. Shen, T. Goto, *J. Cryst. Growth*, **1997**, *181*, 165.

[40] Ü. Özgür, Ya.I. Alivov, C. Liu, A. Teke, M.A. Reshchikov, S. Doğan, V. Avrutin, S.J. Cho, H. Morkoç, *J. Appl. Phys.*, **2005**, *98*, 041301.

[41] A.B. Djurisic, Y.H. Leung, *Small*, **2006**, *2*, 944-961.

[42] C. Klingshirn, *ChemPhysChem.*, **2007**, *8*, 782-803.

[43] Z.L. Wang, *J. Phys. Condens. Matter*, **2004**, *16*, R829–R858.

[44] Z.R. Tian, J.A. Voigt, J.Liu, B. Mckenzie, M.J. Mcdermott, M.A. Rodriguez, H. Konishi, H. Xu, *Nature Materials*, **2003**, *2*, 821-826.

[45] L. Spahnel, *J. Sol-Gel Sci. Technol.*, **2006**, *39*, 7–24.

[46] B. Weintraub, Z. Zhou, Y. Li, Y. Deng, *Nanoscale*, **2010**, *2*, 1573-1587.

[47] D.A. Schwartz, N.S. Norberg, Q.P. Nguyen, J.M. Parker, D.R. Gamelin, *J. Am. Chem. Soc.*, **2003**, *125*, 13205-13218.

[48] R.D. Shannon, *Acta Crystallogr.*, **1974**, *A32*, 751.

[49] D.R. Lide, *Handbook of Chemistry and Physics*, CRC press, 72nd Edition, 12-75, **1991**.

[50] L. Znaidi, G.J.A.A. Soler Illia, S. Benyahia, C. Sanchez, A.V. Kanaev, *Thin Solid Films*, **2003**, *428*, 257-262.

[51] S.J. Pearton, D.P. Norton, K.Ip, Y.W. Heo, T. Steiner, *Progr. Mater. Sci.*, **2005**, *50*, 293-340.

[52] H.A. Weakliem, *J. Chem. Phys.*, **1962**, *36*, 2117-2140.

[53] P.V. Radovanovic, N.S. Norberg, K.E. McNally, D.R. Gamelin, *J. Am. Chem. Soc.*, **2002**, *124*, 15192-15193.

[54] K.L. Kelly, E. Coronado, L.L. Zhao, G.C. Schatz, J. *Phys. Chem. B*, **2003**, *107*, 668.

[55] D.A.G. Bruggeman, *Ann. Phys.* (Leipzig), **1935**, *24*, 636.

[56] G.E. Jellison Jr., L.A. Boatner, J.D. Budai, B.S. Jeong, D.P. Norton, *J. Appl. Phys.*, **2003**, *93*, 9537.

[57] S. Tanemura, L. Miao, P. Jin, K. Kaneko, A. Terai, N. Nabatova-Gabain, *Appl. Surf. Sci.*, **2003**, *212–213*, 654.

[58] S. Grandi, A. Magistris, P. Mustarelli, E. Quartarone, C. Tomasi, L. Meda, *J. Non-Cryst. Solids*, **2006**, *352*, 273.

[59] C.F. Bohren, D.R. Huffman, *Absorption and Scattering of Light by Small Particles*, Wiley (New York), **1998**.

[60] D. Buso, J. Pacifico, A. Martucci, P. Mulvaney, *Adv. Funct. Mater.*, **2007**, *17*, 347.

[61] P. Alemany, R.S. Borse, J.M. Burlitch, R. Hoffmann, *J. Phys. Chem.*, **1993**, *97*, 8464.

[62] M. Lee, L. Chae, K.C. Lee, *Nanostructured Materials*, **1999**, *11*, 195.

[63] T. Kobayashi, M. Haruta, M. Ando, *Sens.Actuators B*, **1993**, *13-14*, 545.

[64] D. Buso, M.L. Post, C. Cantalini, P. Mulvaney, A. Martucci, *Adv. Funct. Mater.*, **2008**, *18*, 3843.

[65] I. Lundstrom, *Sens. Actuators B*, **1996**, *35-36*, 11-19.

[66] J. Steyn, G. Pattrick, M.S. Scurrell, D. Hildebrandtd, M.C. Raphulub, E. Van Der Lingenb, *Catal. Today*, **2007**, *122*, 254.

[67] M.M. Schubert, V. Plzak, J. Garche, R.J. Behm, *Catal. Lett.*, **2001**, *76*, 143.

[68] W.Y. Yu, C.P. Yang, J.N. Lin, C.N. Kuo, B.Z. Wan, *Chem. Commun.*, **2005**, *3*, 354.

[69] H. Dyrbeck, N. Hammer, M. Rønning, E.A. Blekkan, *Topics in Catalysis*, **2007**, *45*, 21-24.

[70] B.K. Chang, B.W. Jang , S. Dai, S.H. Overbury, *J. Catal.*, **2005**, *236*, 392-400.

[71] C. Sivadinarayana, T.V. Choudhary, L.L. Daemen, J. Eckert, D.W. Goodman, *J. Am. Chem. Soc.*, **2004**, *126*, 38-39.

[72] M. Okumura, Y. Kitagawa, K. Yamagcuhi, T. Akita, S. Tsubota, M. Haruta, *Chem. Lett.*, **2003**, *32*, 822-823.

[73] Y. Denkwitz, B. Schumacher, G. Kucerová, R.J. Behm, *J. Catal.*, **2009**, 267, 78.

[74] J. Rasko, J. Kiss, *Catal. Lett.*, **2006**, *111*, 87-95.

[75] Y.F. Yang, P. Sangeetha, Y.W. Chen, *Int. J. Hydrogen Energy*, **2009**, *34*, 8912-8920.

[76] H.Tsunoyama, H. Sakurai, N. Ichikuni, Y. Negishi, T. Tsukuda, *Langmuir*, **2004**, *20*, 11293-11296.

[77] H. Tsunoyama, T. Tsukuda, H. Sakurai, *Chem. Lett.*, **2007**, *36(2)*, 212-213.

[78] S. Cho, H. Lim, K.S. Lee, T.S. Lee, B. Cheong, W.M. Kim, S. Lee, *Thin Solid Films*, **2005**, *475*, 133-138.

[79] E. Della Gaspera, *Ottimizzazione strutturale di film sottili nanocompositi per sensori ottici di gas*, Master Thesis, University of Padova, **2007**, 158.

[80] G. De, C.N.R. Rao, *J. Mater. Chem.*, **2005**, *15*, 891-894.

[81] A.M. Seco, M.C. Goncalves, Rui M. Almeida, *Mater. Sci. Eng. B*, **2000**, *76*, 193–199.

[82] M.T. Othman, J.A. Lubguban, A.A. Lubguban, S. Gangopadhyay, R.D. Miller, W. Volksen, H.C. Kim, *J. Appl. Phys.*, **2006**, *99*, 083503.

[83] D. Grosso, A.R. Balkenende, P.A. Albouy, M. Lavergne, L. Mazerolles, F. Babonneau, *J. Mater. Chem.*, **2000**, *10*, 2085-2089.

[84] H.Y. Zhu, N. Maes, A. Molinard, E.F. Vansant, *Microporous Mater.*, **1994**, *3*, 235-243.

[85] M. Kruk, M. Jaroniec, A. Sayari, *Langmuir*, **1997**, *13*, 6267-6273.

[86] M.H. Yaacob, M. Breedon, K. Kalantar-Zadeh, W. Wlodarski, *Sens. Actuators B*, **2009**, *137*, 115-120.

[87] X.L. Cheng, H. Zhao, L.H. Huo, S. Gao, J.G. Zhao, *Sens. Actuators B*, **2004**, *102*, 248-252.

[88] Z. Ben Ayadi, L. El Mir, K. Djessas, S. Alaya, *Nanotechnology*, **2007**, *18*, 445702.

[89] Q.B. Ma, Z.Z. Ye, H.P. He, Y. Luo, L.P. Zhu, J.Y. Huang, Y.Z. Zhang, B.H. Zhao, *ChemPhysChem*, **2008**, *9*, 529-532.

[90] H. Wang, M. Xu, J. Xu, M. Ren, L. Yang, *J. Mater. Sci.*, **2010**, *21*, 589-594.

[105] R.G. Freeman, K.C. Grabar, K.J. Allison, R.M. Bright, J.A. Davis, A.P. Guthrie, M.B. Hommer, M.A. Jackson, P.C. Smith, D.G. Walter, M.J. Natan, *Science*, **1995**, *267*, 1629.

[92] C.W. Nan, A. Tschope, S. Holten, H. Kliem, R. Birringer, *J. Appl. Phys.*, **1999**, *85*, 7735–7740.

[93] M. Andres-Verges, A.R. West, *J. Electroceram.* **1997**, *1*, 125–132.

[94] R. Kassing, *Phys. Status Solidi A*, **1975**, *28*, 107–117.

[95] A.W. Bott, *Current Separations*, **1998**, *17*, 87-91.

Chapter 5

Au nanoparticles layers within oxide sol-gel thin films

Contents

5.1 Introduction and background

The idea behind the synthesis of metal NPs layers covered with oxide active films lies in the fact that this approach permits to obtain high quality nanocomposite materials with extremely interesting properties, without all the issues related to the compatibilization of the different constituents, as described in Chapter 2. The control over the surface chemistry of the particles and a proper functionalization of the substrate are the main parameters to be controlled for such a procedure, in order to avoid particles aggregation, and to strongly bind the metal NPs to the substrate. Moreover an accurate tailoring of all the operative steps of the deposition process allows to finely tune the surface coverage and the self organization of the particles, obtaining the desired properties of the

assembled layers. For example, the plasmon coupling of close packed Au and Ag NPs has been described in the past [1], and in the recent years it has been used to improve SERS and sensing materials performances. Layers of metal NPs, possibly ordered in superlattice structures have been reported in the past years but only few reports of metal oxide / noble metal nanocomposites syntheses exploiting the distinctive properties of these 2-dimensional arrays have been reported so far. Their applications in several fields like sensing, catalysis, solar cells are evident, as well as their advantages compared to the previously presented approaches: in fact they combine an accurate control of key parameters like size, shape and organization of the particles with a relatively easy experimental procedure, without the need to mix together the different colloidal solutions, so avoiding all the issues related to the compatibilization of the different components.

In this chapter various nanocomposites based on Au NPs layers will be presented: first, Au NPs deposited on glass substrates with different particles densities are covered with TiO_2 and NiO sol-gel films and their morphological and optical properties are characterized; these materials have been tested for reducing gases detection at high temperature (300 °C) and VOCs detection at low temperature (150 °C).

Then similar Au NPs layers are covered with ZnO, TiO_2 and NiO sol-gel films containing Pt NPs, in order to evaluate a possible catalytic effect of Pt NPs in enhancing the sensing performances. Unfortunately, since these materials have been prepared in the last period of this doctoral project, the gas sensing tests are still in progress.

Eventually, structures with a more complex architecture are prepared and characterized: Au NPs layers are deposited over an active sol-gel film (NiO, TiO_2) and then covered with a different sol-gel film (TiO_2, NiO, ZnO). Within these structures, the Au NPs layer faces one material on one side and a different material on the other side, with potentially interesting electrical and optical properties. Detailed characterization and preliminary sensing results of these samples are also reported and discussed in the last part of this chapter.

5.2 Synthetic procedure

5.2.1 Au nanoparticles

Spherical Au NPs of about 13 nm in diameter were synthesized with the Turkevich method [2] by reducing Au ions in water at 100 °C with sodium citrate as described in

Chapter 4. A different concentration protocol has been adopted, in order to provide a complexing agent able to anchor Au NPs to a properly functionalized substrate. 11-mercaptoundecanoic acid (MUA) was chosen as capping agent thanks to its ability to strongly bind to the surface of Au NPs with the sulfur atom, providing at the other end of the organic chain a carboxyl group, that can be exploited for the anchoring on the substrate. After the NPs formation, the solution was let cool down to room temperature and a proper amount of an aqueous basic MUA solution was added and the solution was kept under stirring for 2 hours: in a typical synthesis, 5 mL of a 2 mM MUA solution in a mixture of NH_3 (2.5% v/v) and water were added dropwise under constant stirring to 200 mL of 0.5 mM Au NPs solution. After two hours, a 1 M HCl aqueous solution was added dropwise under constant stirring to reduce the pH and induce Au NPs flocculation, as described by Buso [3]. As soon as the color of the solution changed from ruby red to violet, no more acid was added, and the solution was let sediment overnight; the supernatant was discarded and the sediment was redispersed in slightly basic water leading to 60 mM final stock solutions.

5.2.2 Substrate functionalization

Since Au NPs were protected with a carboxy-terminated molecule, it was decided to functionalize the substrates with amino moieities, with the idea of promoting an amidic bond formation, so covalently anchoring the Au NPs to the substrate. After the substrates were thoroughly cleaned and activated as described in Appendix section, they underwent the functionalization process according to the following procedure: first, substrates were dried with dry air or nitrogen streams, then they were placed on a hot plate at 100 °C in order to remove adsorbed water, but without removing the hydroxyl groups, necessary for the functionalization. (3-aminopropyl)trimethoxysilane (APS) was chosen as functional molecule due to its ability to react with –OH groups through a condensation reaction, so exposing the amino groups. Since a condensation can also occur between two hydrolyzed siloxanic termination of two APS molecules, the APS concentration in the functionalization solution must be optimized, and the water has to be removed from this solution in order to promote the reaction only between APS siloxanic termination and the hydroxyl group on the surface of the substrate. After the substrates were dried, they were immersed into a 1% v/v solution of APS in toluene at 60 °C for 5 minutes in a controlled environment (R.H. < 20 %): toluene was chosen as solvent because it is not soluble with water, so limiting the side reaction described before. Substrates were then extracted and

immediately washed thoroughly with fresh toluene, dried in a nitrogen stream and then placed on a hot plate at 70 °C for 5 minutes to remove adsorbed toluene molecules. These substrates were used within the day, in order to prevent amines oxidation.
A part of this chapter is dedicated to the description of Au NPs layers embedded in between two different oxide films: as a consequence the APS functionalization process and Au NPs deposition has to be carried out on the surface of a sol-gel film. The synthetic approach used for this particular set of samples will be described later on (section 5.5.1).

5.2.3 Au nanoparticles layers deposition

Au NPs aqueous suspensions of different concentrations according to the desired surface coverage were mixed with ethanol in a 1:1 volume ratio, to improve the wettability of the substrate, since after the functionalization with amino-terminated silane molecules, the surface became hydrophobic. In fact, first experiments performed depositing only water-based solutions lead to inhomogeneous particles layers, with lots of aggregates and big portions of the substrates remaining uncovered. The final Au NPs concentration in the solution for the deposition process was varied between 10 mM and 50 mM in molar gold.
All depositions were made by spin coating at 2500 rpm for 30 seconds on either Si or SiO_2 functionalized substrates; samples were then stabilized on a hot plate at 100 °C for 15 minutes, and subsequently used as substrates themselves for sol-gel films coating.

5.2.4 Sol-gel layers deposition

Transition metal oxide films used to coat Au NPs layers were TiO_2, NiO and ZnO: in the following the recipes adopted are presented. To deposit a TiO_2 layer, a solution of Ethanol (0.413 mL), Titanium Butoxide (TiBu, 0.447 mL) and AcetylAcetone (AcAc, 0.216 mL) is prepared under vigorous stirring at room temperature. After 10 minutes, 0.1 mL Milli-Q water are added and let stir for additional 20 minutes. Just before deposition, 1.83 mL ethanol or an equivalent volume of Pt NPs in ethanol (synthesized with the same procedure described in Chapter 4) are added, the total solution is let stir for 5 more minutes, and then it is used for films deposition.
To deposit the NiO layer, 300 mg of Nickel Acetate tetrahydrate (NiAc) were dissolved in 2 mL methanol and subsequently 0.18 mL diethanolamine (DEA) were added under stirring. After 40 minutes, 1.4 mL ethanol (or ethanolic suspension of Pt NPs) were added and after additional 5 minutes the solution was spun.

To deposit the ZnO layer, 200 mg of Zinc acetate dihydrate (ZnAc) was dissolved in 0.9 cc ethanol, and subsequently 0.066 mL monoethanolamine (MEA) were added under stirring. After 30 minutes, 0.35 mL ethanol (or ethanolic suspension of Pt NPs) were added and the solution was used for film depositions after 5 more minutes of stirring.
All depositions were made by spin coating at rotating speeds ranging from 2000 to 4000 rpm according to the desired final thickness. Samples were then stabilized on a hot plate at 200 °C for 10 minutes and then put inside a muffle furnace at 500 °C for 1 hour. A slightly different thermal treatment has been adopted for the Au NPs layers embedded inside two oxide films, and it will be described in section 5.5.1.

5.3 Au nanoparticles layers covered with NiO and TiO_2 sol-gel films

5.3.1 Characterization

Au NPs layers starting from colloidal solutions of different concentrations (10 mM, 30 mM, 50 mM in molar gold) are prepared, characterized and eventually covered with TiO_2 or NiO sol-gel layers. According to the Au NPs concentrations, the samples have been labeled low (L) medium (M) and high (H) surface coverage. Table 5.1 lists the samples prepared in this study. TiO_2 and NiO films deposited on bare Si and SiO_2 substrates are prepared as well as reference.

Table 5.1. List of samples prepared indicating the Au amount and the top layer.

Sample name	Au NPs amount	Top layer
AuL	Low	/
AuM	Medium	/
AuH	High	/
AuLN	Low	NiO
AuMN	Medium	NiO
AuHN	High	NiO
AuLT	Low	TiO_2
AuMT	Medium	TiO_2
AuHT	High	TiO_2

The surface functionalization and the Au NPs deposition processes described in the previous section are effectively a simple and reproducible way to deposit the metal NPs with different surface coverage: Figure 5.1 shows SEM and AFM images of the samples

synthesized in this study. Au NPs can be easily recognized, and also a clear difference in surface coverage of the silicon substrate can be detected in both characterization. The size of the particles on the AFM images appears higher than the actual value as a consequence of the convolution of the measurement with the finite angle of the tip [4].

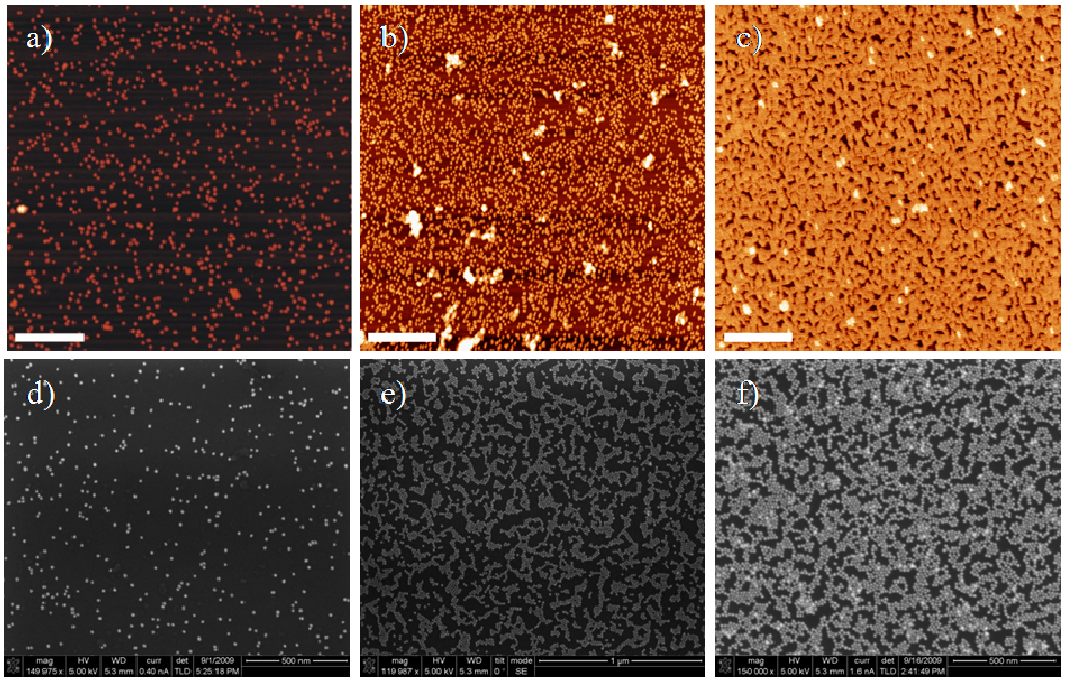

Figure 5.1. AFM (a, b, c) and SEM (d, e, f) images of Au NPs layers with different surface coverage: Low (a,d,), Medium (b,e), High (c,f). The scale bar on all AFM images is 1 μm.

Au NPs are homogeneously dispersed on a micron scale and only few particles are overlapping each other in the highest surface coverage sample, indicating that almost all particles are on one single layer. The surface coverage has been evaluated from the SEM images as ratio between the projected surface of the Au NPs and the total surface of the analyzed area, and the values resulted to be about 62%, 34% and 6% for the high, medium and low coverage sample, respectively. Surface coverage values evaluated from AFM images resulted to be higher, as a consequence of the already cited aberration due to the microscope tip, and so not reliable: for this reason, they are not reported.

The possible anchoring mechanism between MUA-capped Au NPs and APS-functionalized substrates has been briefly investigated. The two possible reaction mechanisms are a simple electrostatic interaction between the surface of Au NPs and the amino functions of the substrate or a covalent bond between amino and carboxyl groups,

coming from APS and MUA respectively, leading to amidic groups formation. It is known from the literature that such a reaction is strongly favored in the presence of activating agents, such as a mixture of Pentafluorophenol and 1-(3-dimethylaminopropyl)-3-ethylcarbodiimide hydrochloride (EDC) [5], but the formation of the amidic bond in the absence of these compounds is not clear. For this reason, ATR (attenuated total reflectance) FT-IR measurements have been performed on a bare APS-functionalized substrate, and on a functionalized substrate covered with a layer of Au NPs: the results are shown in Figure 5.2.

As can be seen, the bare substrate shows only a broad absorption peak at about 1650 cm^{-1}, and two very weak peaks at 1465 cm^{-1} and 1379 cm^{-1}, while Au NPs layer shows a series of peaks in the 1300-1900 cm^{-1} range. The band at 1650 cm^{-1} can be ascribed to a weak bending vibration of water molecules [6], and also to residual ethanol [7]: this is consistent in the sample containing the Au NPs layer, because water and ethanol were the solvents used for the spinning deposition, while it is unexpected on the APS layer; nevertheless, this peak may arise from adsorbed moisture. The vibrational peak at 1379 cm^{-1} can be attributed to asymmetric rocking of H-C-H bonds, coming from the APS organic chain [8]: its presence cannot be excluded in the Au NPs layer sample, because it is overlaid with an intense peak at about 1410 cm^{-1}: it is reasonable to assume its presence, as a consequence of the H-C-H groups coming from both APS and MUA molecules. Also the peak at 1465 cm^{-1} is distinctive of the asymmetric C–H bending coming from the organic carbon chain of both APS and MUA molecules, and it is recognizable in both spectra as well. The peak at 1712 cm^{-1} is assigned to C=O stretching band coming from the carboxyl group of the MUA molecule [9], as a further confirmation of Au NPs presence. Interestingly, the peak at 1560 cm^{-1} appears only in the sample containing Au NPs, and it has been ascribed to N-H bending modes of the amidic bond [5], confirming that a certain amount of covalent bonds between amino and carboxyl groups is taking place, leading to amides formation.

The C=O stretching of the amidic group has been found at 1660 cm^{-1} by Whitesides and coworkers [5], but since here it is overlapped with water and ethanol vibrations, every assumption about its presence would be merely speculative. The last peak at 1411 cm^{-1} is difficult to assign: in the past it has been ascribed to C–H vibrations, but the data available are controversial; nonetheless, Bertilsson and Liedberg [10] observed two peaks at 1418 cm^{-1} and 1470 cm^{-1} related to C–H vibrations of the organic chain of thiols self assembled on a gold surface: as a matter of fact, these peaks are quite close to the peaks

observed in this study. In conclusion, a first, qualitative confirmation of the amidic bond formation between some of the carboxyl groups of the MUA-capped Au NPs and some of the amino groups of the APS-functionalized substrate has been presented.

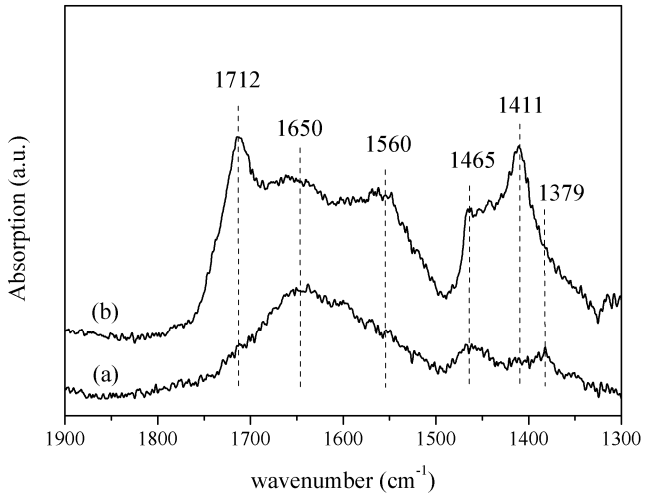

Figure 5.2. FT-IR spectra of a bare APS-functionalized silicon substrate (a) and a functionalized substrate covered with Au NPs layer (b).

The stability with temperature of the uncovered Au NPs layers has been also investigated: samples with about 34% surface coverage have been annealed at 100 °C, 200 °C, 300 °C and 400 °C for one hour and then imaged with the SEM. Figure 5.3 shows the evolution of Au NPs layers with the temperature: a clear change in the morphology of the layer can be seen just after the 200 °C, while minor modifications in the average particles size can be seen after the 300 °C and the 400 °C annealing. Analyzing the average particles size, it can be noticed that there is an abrupt increase in Au NPs diameter (from monodisperse particles of 13±1 nm to bigger polydisperse particles of 32±13 nm) after the annealing at 200 °C; only a small increase in the mean diameter can be seen after the 300 °C (37±15 nm) and 400 °C (43±18 nm) annealing. This behavior has been observed also in the past [11], and has to be ascribed to the very close-packing of the as-synthesized Au NPs layer, which provides a certain amount of surface contact between neighboring particles (Figure 5.3a), that is the main cause of the temperature-driven sintering. As soon as the particles coalesce with each other, the interparticle distance becomes higher (Figure 5.3b) and therefore further growing is made more difficult, or even prevented.

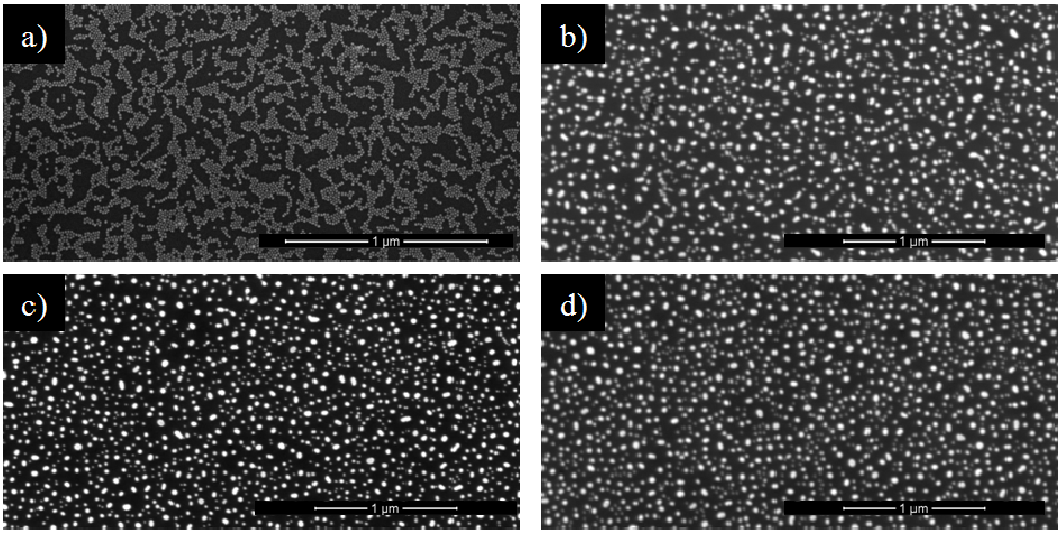

Figure 5.3. SEM images of Au NPs layers annealed at different temperatures: a) 100 °C; b) 200 °C; c) 300 °C; d) 400 °C.

Optical absorption spectra of the same sample (34% surface coverage) deposited on glass and annealed between 100 °C and 400 °C are reported in Figure 5.4. As can be seen, Au SPR peak undergoes some changes with annealing temperature: after the 200 °C annealing, it appears slightly reduced in intensity, red shifted and broadened at higher wavelength, as a consequence of the initial coalescence phenomena. With increasing the annealing temperature, a progressive blue shift and a higher reduction in intensity is experienced: this is due to the subsequent growth of the particles, that in turn leads to an increase of the average interparticle distance, causing a lower extent of SPR coupling. Moreover, the number of particles decreases as a consequence of the sintering, and so their optical cross section is lower, causing a reduction in the absorbance of the sample. The chromatic effect of the thermal annealing can be seen in the picture shown in the inset of Figure 5.4: Au NPs layer annealed at 100 °C is blue-colored, as a consequence of the plasmon coupling (the wavelength corresponding to the SPR peak registered in aqueous solutions is around 520 nm, corresponding to a red-colored solution), while Au NPs layer annealed at 400 °C is pink-reddish, as a consequence of the plasmon decoupling after the particles growth and the consequent increase in the mutual distance.

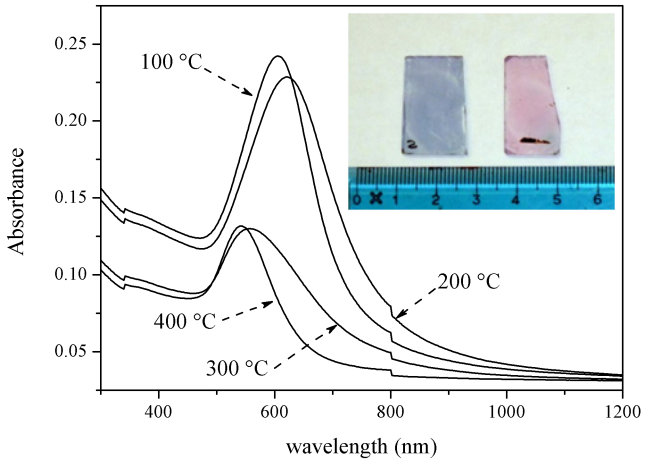

Figure 5.4. Optical absorption spectra of Au NPs layers annealed between 100 °C and 400 °C. The inset shows a picture of the samples annealed at 100 °C (left) and at 400 °C (right); the scale bar is in cm.

These tests demonstrated that 200 °C are sufficient to promote the sintering and the coarsening of close-packed Au NPs, with a consequent modification of their optical properties: in fact Au NPs become bigger and more separated from each other, and so a blue shift of the Au SPR peak is experienced (not reported). Nonetheless, it will be shown later on that when the Au NPs layer is covered with sol-gel films, the particles thermal stability is improved by the presence of the oxide layer, maybe as a consequence of the percolation of the sol-gel solution in between the particles, providing a physical barrier to the sintering and coarsening of the metal NPs.

From the UV-Vis-NIR absorption spectra shown in Figure 5.5, the effect of both surface coverage and sol-gel layer can be appreciated: increasing the Au NPs surface coverage leads both to an increase and a red shift of the SPR peak of Au NPs, as reported in previous publications [12,13]. The increase in absorbance with surface coverage is related to the fact that, being Au NPs in one layer, the higher the surface coverage, the higher the concentration of NPs interacting with the incoming beam, leading to an increase in absorption as described by the well-known Lambert-Beer equation [14,15]. The red shift of the plasmon peak with increasing the surface coverage can be ascribed to the decrease in the mutual distance between Au NPs, leading to a coupling of the plasmon resonances [1]. Unlike the Au NPs layers covered with sol-gel films, the uncovered Au NPs layer have not been annealed at 500 °C due to the sintering of metal NPs previously shown. The effect of the sol-gel layer deposited on top of the Au NPs monolayer is to broaden and red-shift the SPR peak: this effect is much more pronounced for TiO_2 compared to

NiO, due to the higher refractive index of the former compared to the latter (2.51at 590 nm for TiO_2 [16], 2.33 at 620 nm for NiO [17], and also to the interaction between anatase crystals and the surface of Au NPs, causing spreading and scattering of conduction electrons as described previously [18,19].

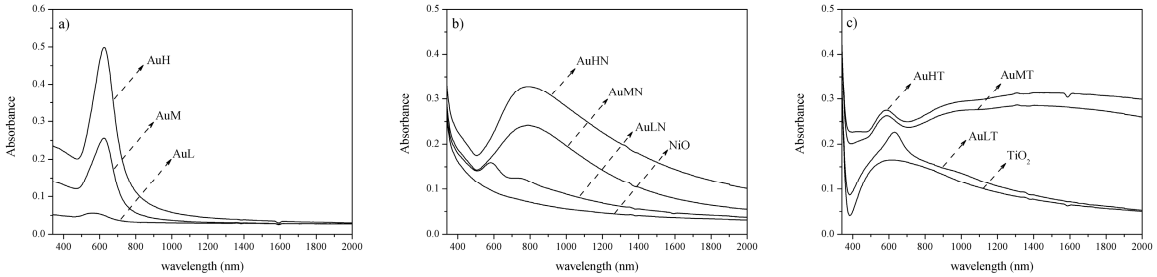

Figure 5.5. Optical absorption spectra of a) Au NPs layers annealed at 100 °C; b) Au NPs layers covered with NiO and annealed at 500 °C; c) Au NPs layers covered with TiO_2 and annealed at 500 °C.

Moreover, looking particularly at the Low surface coverage samples coated with the oxide layers, there are two distinct SPR peaks: the one at high frequencies is centered at about 590 nm and 630 nm for NiO and TiO_2 respectively, and it is compatible with randomly dispersed Au NPs inside those matrixes that are not interacting with each other. A low frequencies peak appears in the low surface coverage samples around 750 nm and 1000 nm for NiO and TiO_2 respectively, and it is found to progressively red shift and become prevalent with increasing the Au NPs surface coverage: this peak can be ascribed to the coupling of Au NPs plasmons, as already observed by Astilean and colleagues [11]. The fact that this peak becomes more intense with increasing the surface coverage, supports this hypothesis. So the coupling of Au NPs plasmons due to their proximity and the interaction of the metal NPs with the matrix are responsible for the intense red shift and the broadening of the Au SPR peak.

Morphological characterization is useful to understand the structure of the nanocomposite and evaluate the effect of the Au NPs layer in the sol-gel matrix formation.

XRD measurements have been performed to analyze the crystallinity of the samples and the results are reported in Figure 5.6: as can be clearly seen, the intensity of Au peaks (JCPDS No. 040714) is in good agreement with the different surface coverage, and so with the amount of Au NPs present inside the films. On the contrary NiO (JCPDS No. 471049) and anatase TiO_2 (JCPDS No. 841285) peaks have similar intensities, suggesting that the Au monolayers used as substrates do not influence too much the process of

matrix formation; however, a slight difference in broadening of NiO peaks is detected, as will be explained in the following.

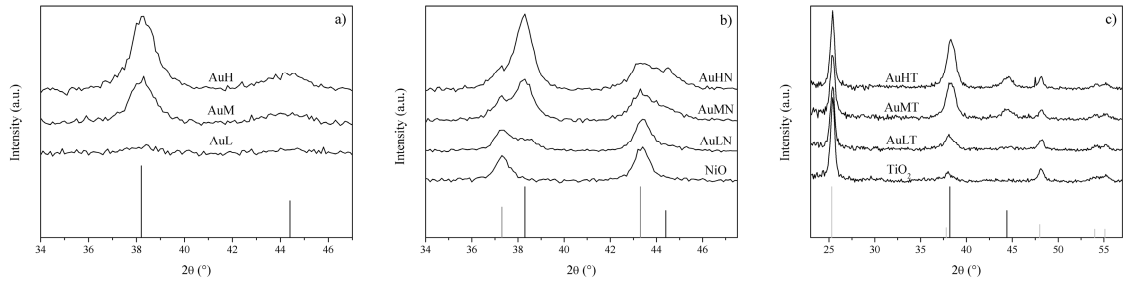

Figure 5.6. XRD patterns of a) Au NPs layers; b) Au NPs layers covered with NiO; c) Au NPs layers covered with TiO_2. Theoretical diffraction lines for Au (black lines) NiO (grey lines in figure b) and TiO_2 (grey lines in figure c) are reported at the bottom.

Table 5.2. Mean crystallite diameters calculated according to the Scherrer Equation for the 3 crystalline phases detected.

Sample	Diameter (nm)		
	Au	TiO_2	NiO
AuL	7.4 ± 0.4	/	/
AuM	7.9 ± 2.6	/	/
AuH	7.5 ± 2.8	/	/
NiO	/	/	16.7 ± 0.4
AuLN	9.3 ± 2.1	/	15.2 ± 1.3
AuMN	11.1 ± 3.8	/	14.2 ± 0.2
AuHN	11.6 ± 3.2	/	13.7 ± 0.4
TiO_2	/	20.1 ± 0.2	/
AuLT	7.5 ± 0.4	19.2 ± 1.5	/
AuMT	10.8 ± 0.2	21.3 ± 7	/
AuHT	11.3 ± 0.4	22.6 ± 4.2	/

Crystallite sizes have been evaluated with the Scherrer formula fitting the experimental profiles and the results are reported in Table 5.2. As can be noticed, the crystallite size of Au NPs is slightly higher when the monolayer is covered with the sol-gel coating: this effect is related to the annealing process, that might induce some coarsening or sintering of the particles. Nevertheless, the size evaluated from the XRD is in the range 8-11 nm, so the particles can be described as nearly monocrystalline.

NiO and TiO_2 crystallites sizes are in the range 14-17 nm and 19-23 nm, respectively; for NiO a trend can be detected, being the crystals slightly smaller when the sol-gel solution is deposited on the high surface coverage Au monolayer, and slightly higher when deposited on the low surface coverage one, or on bare glass substrates. This behavior has not been observed for TiO_2 crystals, where the data are randomly distributed and their difference is inside the error bars. The trend observed in NiO crystals size can be ascribed to the mutual affinity between NiO and Au crystals observed in the past [20], due to their small lattice mismatch: so Au NPs can act as nucleating spots for NiO crystals and being the number of nuclei related to the number of Au NPs, *i.e.* to the surface coverage, the higher the nuclei number, the smaller the crystals size.

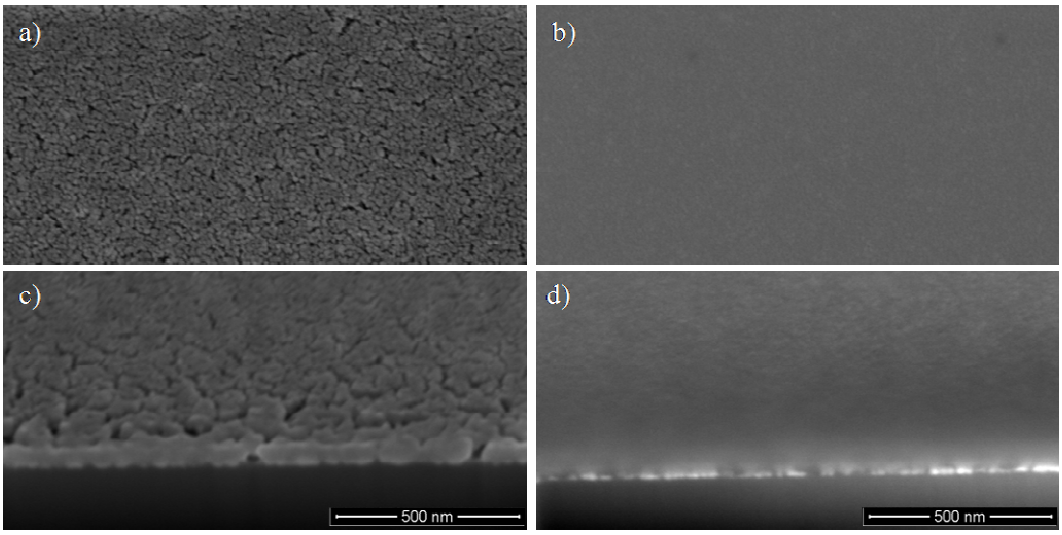

Figure 5.7. SEM images of Au NPs monolayer with high surface coverage, coated with NiO in plan view (a) and in cross section (c); covered with TiO_2 in plan view (b) and in cross section (d). The scale bar in all images is 500 nm.

SEM analyses of the coated monolayers both in plan view and in cross section have been carried out to evaluate the morphology of the nanocomposite: as can be seen from Figure 5.7, NiO films are rougher and with a more irregular and slightly cracked surface, while TiO_2 films are smoother. From the cross sectional images the thickness of the films can be measured, being around 50 nm, and also Au NPs at the interface between the substrate and the film can be detected as brighter spots, confirming that the monolayer is not damaged by the spinning process of the sol-gel solutions. Au NPs are easier to see when coated with TiO_2, while when coated with NiO, the contrast between the two materials is similar and for this reason Au NPs appear only slightly brighter. Moreover, since imaging

the samples with a SEM in cross section is quite difficult, the cross section of TiO_2 coated sample is slightly out of focus because a continuous drift of the electron beam signal was experienced.

5.3.2 Gas sensing tests

These Au NPs layers covered with NiO and TiO_2 sol-gel films have been tested as ethanol vapors sensors at 150 °C operative temperature in reflection mode as described in the Appendix section. In all tests the ethanol amount was set constant at 180 ppm, using nitrogen as carrier gas.

The effect of ethanol vapors on the reflection intensity of the different films tested is shown in Figure 5.8, where the ORC parameter as a function of wavelength is reported for uncovered Au NPs layer, Au NPs layers covered with NiO and TiO_2, and pure NiO and TiO_2 films. All tests have been performed on the Au NPs layers with high surface coverage.

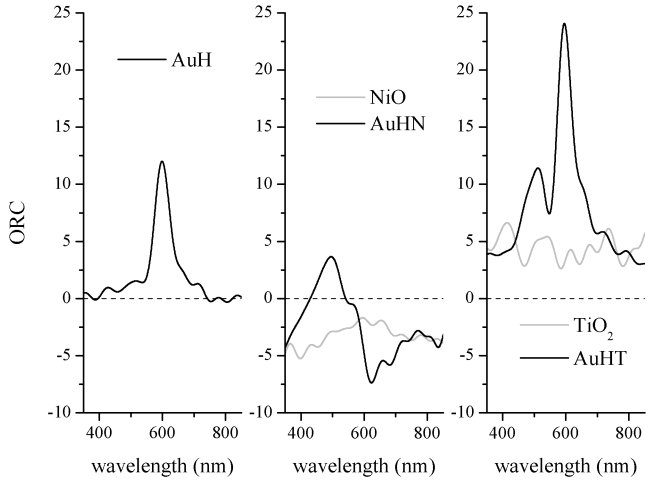

Figure 5.8. ORC plots for the high surface coverage Au NPs layers bare and covered with NiO and TiO_2 films, and for pure NiO and TiO_2 films when exposed to 180 ppm ethanol at 150 °C OT. Zero value of response is highlighted with a dotted line.

As can be seen, outside Au SPR peak wavelength range, the response is similar to the response of the matrix that Au NPs are facing: in fact the ORC parameter is negative for NiO film, positive for TiO_2 films, and null for the uncovered layer. The SPR wavelength range shows a wavelength dependent response, also for the uncovered Au NPs layer, as a consequence of the role played by the noble metal particles as optical probes for the sensing dynamics. Moreover, compared to the pure oxide films, the covered Au NPs

layers show a higher response intensity, at least for a certain range of frequencies, providing a confirmation of the enhancement in the sensing behavior obtained combining the close-packed Au NPs layer and the oxide active films. In fact, the ORC maximum of the covered Au NPs layers is higher than the sum of the Au NPs layer and the oxide film alone, especially for TiO_2, so a synergetic effect between the two components is likely to occur. Moreover, the effect of the different metal oxide can be also seen: the ethanol effect on NiO is to reduce the reflection intensity, while its interaction with TiO_2 causes an increase in reflection. This fact can be explained considering the different electric nature of the two semiconductive oxides, being NiO a p-type and TiO_2 a n-type semiconductor.

As reported in the literature, volatile organic compounds can be oxidized on the surface of semiconducting materials; for example, in the case of ethanol (C_2H_5OH), the main reaction mechanisms can be described as the following [21,22]:

$$2C_2H_5OH + O_2 \rightarrow 2CH_3CHO + 2H_2O \quad (5.1)$$

$$C_2H_5OH \rightarrow C_2H_4 + H_2O \quad (5.2)$$

In the first reaction, ethanol is oxidized to acetaldehyde by dehydrogenation of the ethanol molecule and subsequent reaction with oxygen leading to water formation; this reaction can proceed further, with a subsequent oxidation of acetaldehyde to acetic acid. The second reaction is a direct dehydration of ethanol to ethylene with water formation. There are other possible ethanol oxidation reactions leading for example to the formation of diethylether or diethylacetal, but they are less common and require specific reaction conditions [22]. The preferred path is related to the type of the metal oxide (basic oxides promote the first reaction, acid oxides the second), to the presence of adsorbed oxygen species on the surface of the oxide, or to the presence of oxygen in the gas phase (as can be seen, oxygen is necessary for the first reaction). In any case, the oxidation of the ethanol molecules will produce an electron injection inside the oxide: but being anatase TiO_2 a n-type semiconductor and bunsenite NiO a p-type semiconductor, in the case of TiO_2 the ethanol oxidation will lead to an increase in conductivity, because electrons are injected in the conduction band of anatase while in the case of NiO will lead to a decrease in conductivity, due to electrons-holes recombination. As a consequence, it is reasonable to suppose that a difference in the electronic properties of the metal oxides produces a

difference in the reflection intensity, and that this difference is of opposite sign according to the type of the semiconducting material.

It has to be noticed that the experimental setup is not ideal, since it employs a low-resolution spectrophotometer and the light is collected in reflection mode, so the data collected are sometimes quite noisy. Nevertheless the trend is rather clear, and the effect of the coupling Au NPs layers and metal oxide films in enhancing the sensing properties has been proved.

Dynamic tests have been performed on the AuHT sample, the most sensitive among the tested ones, and the results are reported in Figure 5.9. A reversible signal during repeated cycles of nitrogen-ethanol exposure can be detected, even if the signal to noise ratio is quite low, as a consequence of the low resolution setup used, as described before. Moreover the sensing dynamics are not ideal, because both response and recovery times are occurring in a time scale of few minutes.

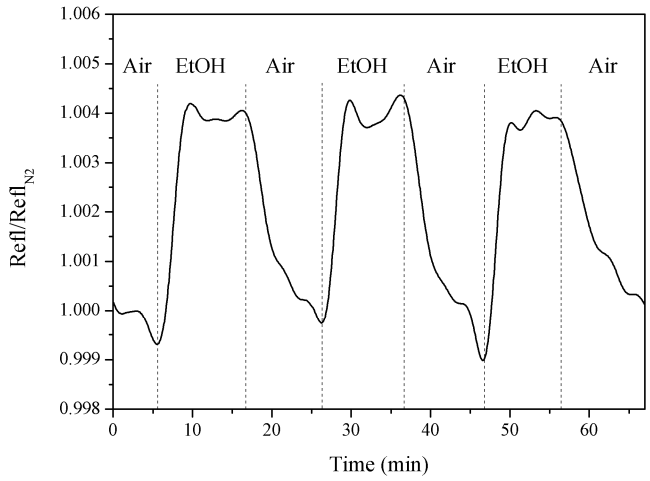

Figure 5.9. Dynamic tests for AuHT sample at 594 nm and 150 °C OT under repeated cycles nitrogen-180 ppm ethanol.

Nevertheless, the results are promising, especially for applications of these materials in transmission mode, or in devices where the reflection is enhanced, like SPR configurations or on the surface of unclad optical fibers.

These films have also been tested as optical sensors for reducing gases detection in transmission mode at 300 °C OT. It is known from the literature that NiO thin films are able to optically detect reducing gases [23], and that the effect of reducing gases is to lower the conductivity and the absorption of p-type semiconductors [24]; on the contrary, although TiO_2 films are electrically active in the recognition of gases like hydrogen and

CO, they don't present any detectable optical signal [25]. A possible explanation of this behavior is that TiO_2 films are completely transparent in the visible range, while NiO films are slightly absorbing, and so a change in the absorption properties is much more evident in absorbing films. This behavior is confirmed by the gas sensing tests of pure NiO and TiO_2 layers reported in Figure 5.10a and Figure5.10b, respectively.

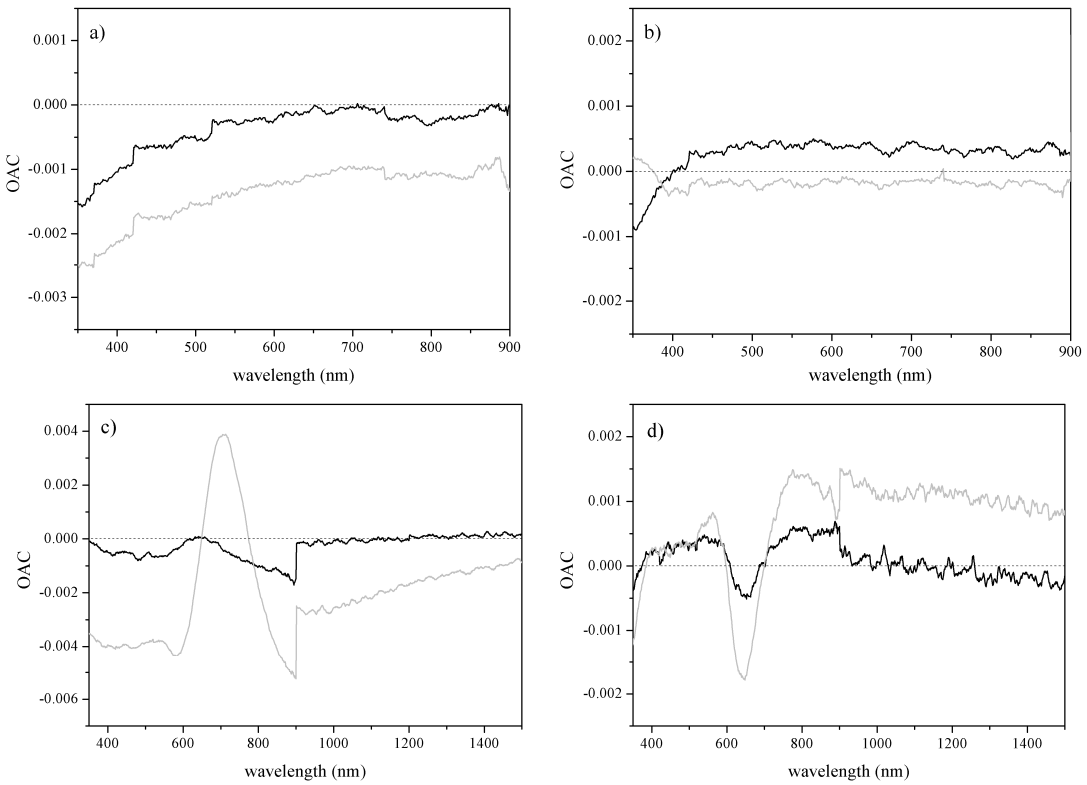

Figure 5.10. OAC curves for NiO (a) TiO_2 (b), AuMN (c) and AuMT (d) films when exposed to 1% CO (black lines) and 1% H_2 (grey lines) at 300 °C OT. The step in the signal detected at 900 nm is due to the change in grating of the spectrophotometer.

The effect of Au NPs presence is evident in the SPR range of frequencies, but being the SPR peak quite broad, especially for Au NPs layer covered with TiO_2, the Au effect can be experienced for a wide range of wavelengths: in fact a small but detectable signal during hydrogen exposure can be seen also at 1400-1500 nm. Moreover, as observed also in the past, the Au presence effect is summed to the optical response of the pure oxides. The response becomes also strongly wavelength dependent, allowing to select and tune the device response by choosing an appropriate wavelength of analysis, permitting selective recognition of different gases in the same environment.

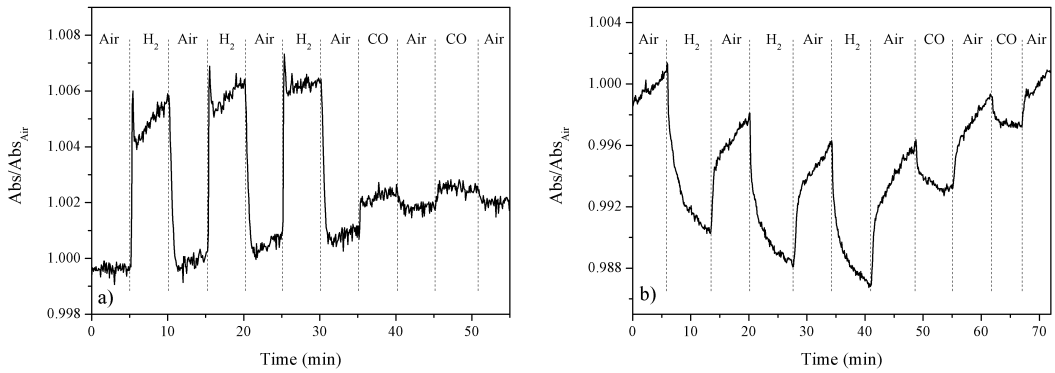

Figure 5.11. Dynamic response after exposure to 1% CO and 1% H_2 for a) AuMN sample at 685 nm and 300 °C OT; b) AuMT sample at 646 nm and 300 °C OT.

Some dynamic tests performed on the Au containing samples are shown in Figure 5.11: even if not ideal, especially for the Au NPs layer covered with TiO_2, the results show a reversible response with different intensities for hydrogen and CO exposure, allowing multiple gas detection. A better time-resolved behavior is experienced for NiO-Au double layer, with very fast response and recovery times, and an acceptable signal to noise ratio, especially for hydrogen detection, taking into account that these films are only 50 nm thick, as confirmed by SEM analyses. Nevertheless a drift of the baseline can be seen in both measurements, maybe as a consequence of a temperature change during the experiment, or more likely to a permanent change in the optical properties of the films. In fact if the nanocomposite is not completely stabilized, or if it presents dirt or organic compounds on its surface, a prolonged test at 300 °C might induce slight changes in the film structure and properties, as a consequence of the stabilization of the oxide matrix, the organic compounds removal, and so on. For this reason, the samples are going to be tested again in the next months, ensuring the minimization of all the previously presented causes of the instability of the baseline. Anyway, these preliminary results, together with the ethanol sensing tests outputs shown before, are promising for the use of Au NPs layers covered with different oxides as optical sensors. Eventually, it is noteworthy that the optical variation as a function of wavelength induced especially by hydrogen for NiO-covered and TiO_2-covered Au NPs layer is somehow opposite, so combining the two oxides it is possible – at least in theory – to enhance the selectivity of the overall device: this approach based on Au NPs layers sandwiched between two different oxide layers will be presented in section 5.5.

5.4 Au nanoparticles layers covered with sol-gel films containing Pt

5.4.1 Characterization

As explained in the previous chapter for TiO_2-based nanocomposites containing Au and Pt NPs, the idea behind the synthesis of active metal oxide thin films containing these two noble metals NPs, lays in the combination of the catalytic properties of Pt NPs with the optical properties of Au NPs; in this particular case, Au NPs layers are prepared as described in section 5.2 using 30 mM Au solutions and covered with sol-gel oxides containing different concentrations of Pt NPs. The different Pt concentrations have been set to 0% (pure oxide layer), 1%, 2% and 4% molar with respect to the sol-gel oxide concentration; the samples prepared in this study are summarized in Table 5.3.

Table 5.3. List of samples prepared indicating the Pt amount and the top layer.

Sample name	Top Layer	Pt NPs amount
MNP0	NiO	0%
MNP1	NiO	1%
MNP2	NiO	2%
MNP4	NiO	4%
MTP0	TiO_2	0%
MTP1	TiO_2	1%
MTP2	TiO_2	2%
MTP4	TiO_2	4%
MZP0	ZnO	0%
MZP1	ZnO	1%
MZP2	ZnO	2%
MZP4	ZnO	4%

Optical spectroscopy measurements in the visible and near infrared range have been performed to evaluate the Pt effect on the optical properties of the coated Au NPs layers: the results are presented in Figure 5.12. In all samples, an increase in Pt loading causes a degradation of Au NPs SPR peak, and also a higher diffuse absorption value at low frequencies. The first effect, *i.e.* the damping of Au plasmon peak, can be ascribed to the formation of a partial surface contact between Au and Pt NPs, as already observed in the previous chapter for the TiO_2-Au-Pt system, and also described in the literature [26]. Such a behavior can be also due to an alloying between Au and Pt, but XRD analyses presented in the following exclude a massive alloying, even if, as a consequence of the

relatively poor signal to noise ratio, a small extent of alloying might occur. So it is likely that when depositing the sol-gel solution containing Pt NPs over the Au NPs layer, the two metal NPs come into contact, and this event affects the Au NPs optical properties. The second effect, the higher absorption value outside Au SPR frequencies range, is due to the optical properties of Pt NPs, that present a tail of absorption in the visible and NIR range, as also observed in the previous chapter.

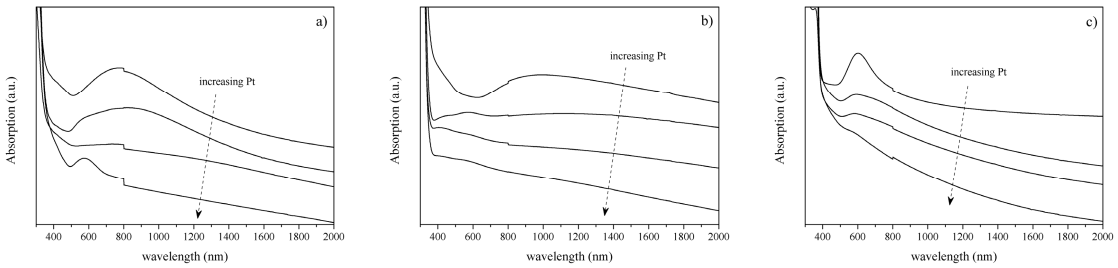

Figure 5.12. Optical absorption spectra of Au NPs layers covered with a) NiO and NiO-Pt films; b) TiO_2 and TiO_2-Pt films; c) ZnO and ZnO-Pt films.

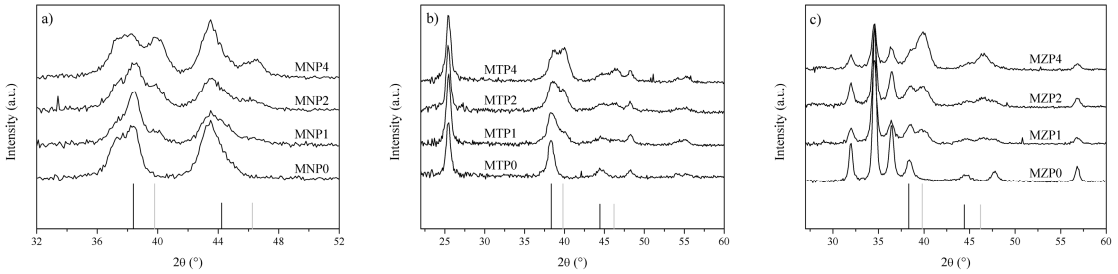

Figure 5.13. XRD patterns of Au NPs layers covered with a) NiO and NiO-Pt films; b) TiO_2 and TiO_2-Pt films; c) ZnO and ZnO-Pt films. Theoretical diffraction lines for Au (black lines) and Pt (grey lines) are reported at the bottom. The other diffraction peaks detected are assigned to cubic NiO (a), anatase TiO_2 (b) and wurtzite ZnO (c).

The spectra in Figure 5.12 have been vertically translated in order to help the visualization, but the actual values of absorbance outside the Au SPR range are increasing with increasing Pt NPs amount, as a consequence of the Pt NPs optical properties.

Structural and morphological characterization performed by XRD and SEM helps to get information about the Pt loading, the crystalline phases present inside the different samples, and the surface morphology of the films.

From the XRD patterns shown in Figure 5.13 the different crystalline phases according to samples composition can be detected: for all samples cubic Au peaks at about 38.2° and 44.4° (JCPDS No.04-0784, highlighted with black lines at the bottom) coming from the

Au NPs layers can be clearly seen, and their intensity does not vary significantly between the different films, as a further confirmation of the similar surface coverage of Au NPs in all the samples. Cubic Pt peaks (JCPDS No. 04-0802, highlighted with grey lines at the bottom) are not detected in Pt free samples, as expected, while they are clearly detected in all Pt containing samples, with increasing intensity according to Pt concentration, confirming the different amount of Pt NPs embedded inside the different oxide films. Au and Pt crystallite size evaluated with the Scherrer relationship is in the 8-12 nm and 7-10 nm, respectively, so in good agreement with previously reported TEM and XRD data. The other detected peaks are ascribed to the different oxides: in details, cubic NiO peaks (JCPDS No. 47-1049) at about 37.3° and 43.4° are present in Figure 5.13a, while anatase peaks (JCPDS No. 86-1157), especially the most intense at 25.3°, are clearly identified in Figure 5.13b; eventually, wurtzite ZnO peaks (JCPDS No. 36-1451) can be easily detected in Figure 5.13c. Therefore, all oxide films are crystalline after the 500 °C annealing, and the Pt loading has been confirmed from the diffraction analyses. Moreover, as anticipated before, no shift in Au or Pt diffraction peaks is detected, excluding the alloying between the two metals; however, considering that the diffraction peaks for both Au and Pt NPs are quite broad due to the relatively small size of the NPs and that the signal to noise ratio of the XRD patterns is not very high, a small extent of alloying cannot be totally excluded, provided the accuracy of these measurements.

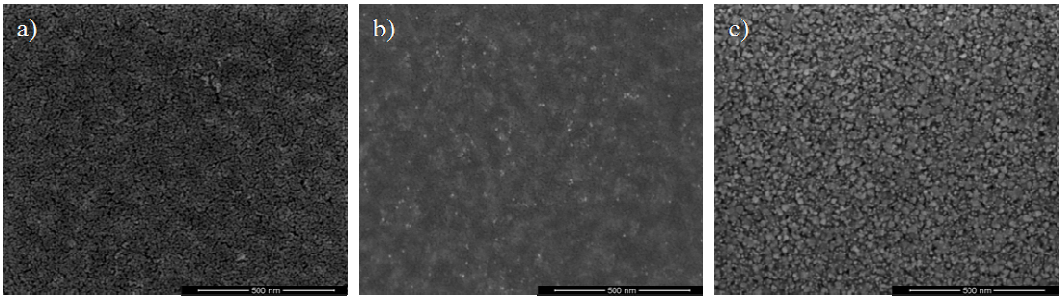

Figure 5.14. SEM images of Au NPs layers covered with a) NiO-Pt layer; b) TiO_2-Pt layer; c) ZnO-Pt layer. The Pt NPs amount in all samples is 4%.

From the SEM images reported in Figure 5.14 the surface morphology of the three metal oxides can be noticed: the TiO_2 film is rather smooth and compact, if compared to the other two, that on the contrary present a higher surface roughness and bigger pores. Pt NPs can be easily noticed as brighter spots inside the TiO_2 matrix, and they are also recognizable within the ZnO film, even if they present a lower contrast difference; they

are not detectable inside the NiO layer, due to the similar scattering contrast between the oxide and the metal particles, as also observed in the cross section image for the Au NPs monolayer covered with NiO reported in Figure 5.7c.

5.4.2 Gas sensing tests

These nanostructured films are about to be tested as optical sensors for CO and hydrogen recognition, analyzing if Pt NPs play a role in the sensing dynamics as a consequence of their catalytic properties, for example improving the detection times or lowering the operative temperature, as already observed for nanocrystalline TiO_2-based films presented in Chapter 4.

5.5 Au nanoparticles layers embedded between two different oxide films

5.5.1 Synthetic approach

As anticipated before, the synthetic route has been slightly modified in order to obtain Au NPs layers embedded in between two sol-gel oxide films. First, the bottom oxide coating (NiO, TiO_2, ZnO) is deposited according to the previously presented recipes, and then the sample is annealed at 500 °C for 10 minutes. Before depositing the Au NPs layer, the surface of the oxide film has to be reactivated, promoting the formation of –OH bonds able to react with APS molecules, so providing the amino-functionalization necessary for Au NPs anchoring. In fact, as a consequence of the thermal annealing, all the hydroxyl groups are removed. The optimized activating procedure for NiO and TiO_2 films consists in dipping the samples into a 4% H_2O_2 aqueous solution at room temperature for 1 minute, followed by a thorough rinsing with DI water: a droplet of water was deposited on the samples before and after the hydrogen peroxide treatment, and an evident decrease in contact angle has been observed, confirming the formation of polar groups on the surface. Starting from here, the usual procedures of substrate functionalization, Au NPs layer deposition and the subsequent sol-gel film spinning and heat treatment are performed. In this way, the bottom layer is annealed only 10 minutes more than the top layer, so it can be said that the morphology and the structure of the different oxides do not change too much if they are deposited as bottom or top layer. The spinning rate was calibrated and adjusted in order to obtain films of about 45-50 nm after the 500 °C annealing for all the three oxides used. As far as ZnO is concerned, several etching

solutions were tested, also extremely diluted, but due to the high surface area and the high reactivity of ZnO films, irreversible modification were experienced as will be described in the following. For this reason, ZnO films were used only as top layers.

5.5.2 Characterization

The different samples prepared consist on a bottom layer (TiO_2, NiO) an intermediate layer of Au NPs (with different surface coverages) and a top layer (TiO_2, NiO, ZnO): a detailed list is presented in Table 5.4.

Table 5.4. List of samples prepared indicating the Au NPs amount and the type of bottom and top layer.

Sample name	Bottom Layer	Au NPs amount	Top Layer
NT0	NiO	0	TiO_2
NTL	NiO	Low (10mM sol)	TiO_2
NTM	NiO	Med (20mM sol)	TiO_2
NTH	NiO	High (30mM sol)	TiO_2
NZ0	NiO	0	ZnO
NZL	NiO	Low (10mM sol)	ZnO
NZM	NiO	Med (20mM sol)	ZnO
NZH	NiO	High (30mM sol)	ZnO
TN0	TiO_2	0	NiO
TNL	TiO_2	Low (10mM sol)	NiO
TNM	TiO_2	Med (20mM sol)	NiO
TNH	TiO_2	High (30mM sol)	NiO
TZ0	TiO_2	0	ZnO
TZL	TiO_2	Low (10mM sol)	ZnO
TZM	TiO_2	Med (20mM sol)	ZnO
TZH	TiO_2	High (30mM sol)	ZnO

Again, optical spectroscopy is a powerful tool to investigate Au NPs amount and organization in between the two oxide layers. The results are reported in Figure 5.15. In all samples a progressive increase of the intensity of Au SPR peak is observed with increasing Au NPs surface coverage, as described in the previous sections, but few differences between the samples series can be seen. Looking at the UV absorption edge of the metal oxides, a sharper onset just below 400 nm is observed for samples containing a ZnO layer (Figure 5.15 b and d), while samples composed only of NiO and TiO_2 show a more gradual increase of absorption with decreasing the wavelength (Figure 5.15 a and

c). This is due to the different optical band gap absorption onsets for the three oxides used for the synthesis, being more intense and sharper for ZnO films compared to TiO_2 and NiO, as can be also seen in some optical spectra reported in Chapter 3 and Chapter 4.

ZnO and TiO_2 coatings are transparent in the visible and near infrared range, while NiO is slightly absorbing, especially at high frequencies; nonetheless this absorption is quite weak, so every absorption feature between 400 nm and 1500 nm can be ascribed to the optical properties of Au NPs layers facing the oxide films; the apparent absorption of TiO_2-containing samples is related to the high refractive index of the anatase coatings, causing optical interference, and can be easily taken into account considering as reference material the Au-free sandwich structure. Excluding the spectra reported in Figure 5.15a, in all dataset an increase in intensity of the SPR peak component at higher wavelengths with increasing Au NPs surface coverage can be seen, as already observed previously, as a consequence of the reduced mutual distance between close-packed Au NPs, that leads to a stronger coupling of the plasmon resonances. In details, Au NPs layers embedded between NiO (bottom) and ZnO (top) films, show the low frequency peak at about 700 nm (Figure 5.15b), quite close to the peak observed in Au NPs layers covered with NiO films (see Figure 5.5b), even if slightly blue shifted, as a consequence of the presence of the ZnO layer, that having a lower refractive index, contributes to a higher SPR frequency value. So in this particular sample, both the bottom and the top layers seem to have an effect on Au NPs optical properties.

On the contrary, Au NPs layers deposited on TiO_2 films and covered with NiO (Figure 5.14c) and ZnO (Figure 5.14d), are very similar to simple Au NPs layers deposited on glass substrates and covered with the respective oxide film (see Figure 5.5c or Figure 5.12). In the TN sample series, the low frequency plasmon peak is registered at 750-760 nm, in good agreement with the previously reported value for NiO-coated Au NPs layers, suggesting a very small role played by the TiO_2 substrate in interacting with the Au NPs and modifying their optical properties. In a similar way, the absorption peak of TZ sample series due to Au NPs plasmon coupling is detected at about 630-650 nm, only few nanometers red shifted compared to Au NPs layers deposited on glass and covered with ZnO, so again the TiO_2 bottom layer is not highly influencing the optical properties of the metal NPs layer. The spectrum of the TZM sample is not reported because the sample was damaged and it wasn't possible to get a reliable optical spectrum.

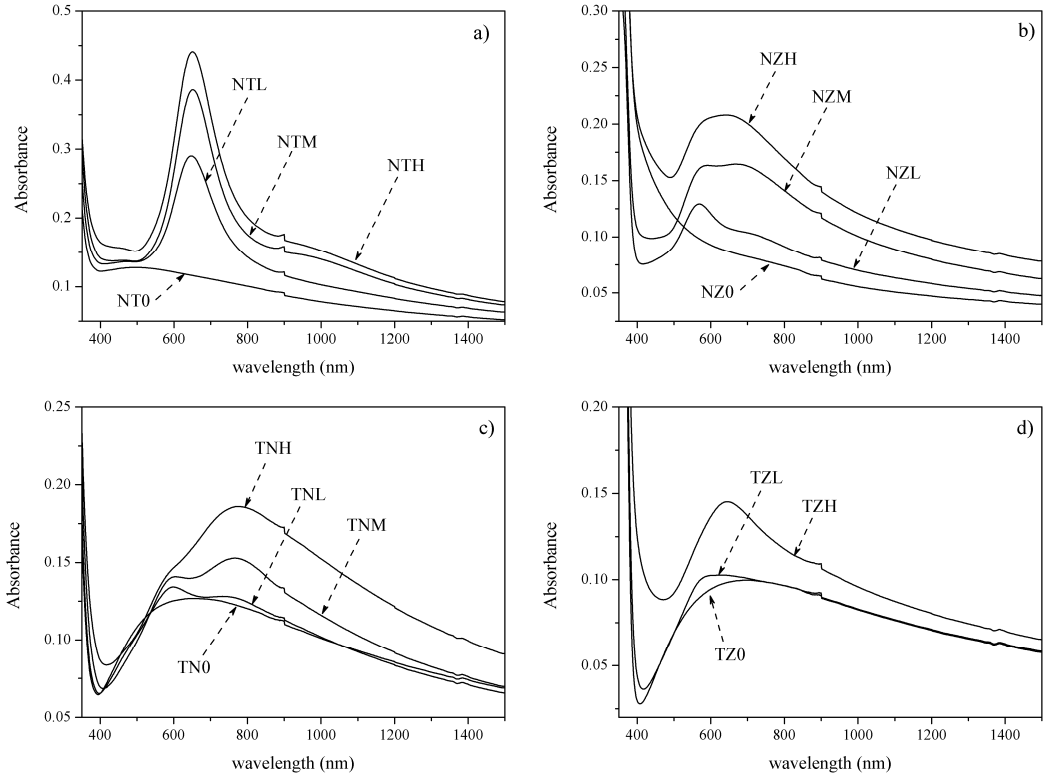

Figure 5.15. Optical absorption spectra of Au NPs embedded in between different oxides: a) NiO-Au-TiO_2 series; b) NiO-Au-ZnO series; c) TiO_2-Au-NiO series; d) TiO_2-Au-ZnO series.

This difference in optical properties of the Au NPs layers deposited on NiO and TiO_2 substrates can be ascribed to the different morphology of the two oxides: analyzing the SEM images of the surface of the two oxides reported in Figure 5.7, a clear difference in surface roughness can be seen, being TiO_2 film smoother and with smaller pores, while the NiO layer shows a more rough surface, with bigger pores and also small cracks. So when depositing the Au NPs layer over these two oxides, it is likely that metal NPs have a higher contact surface with the NiO layer compared to the TiO_2 layer, because they get stuck in between cracks and pores, while the TiO_2 surface resembles more the plain surface of the glass or silicon substrates, providing Au NPs with less contact surface. As a consequence, when coating the Au NPs layer with the sol-gel solution for the top layer, if the bottom oxide is TiO_2 the majority of the contact surface occurs between the Au NPs and the top layer, while if the bottom film is NiO, thanks to its surface roughness it provides a high amount of contact area, contributing heavily to the Au layer optical properties. All these assumptions are graphically described in Figure 5.16.

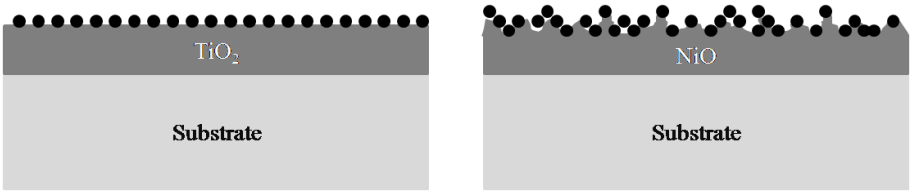

Figure 5.16. Schematic representation of Au NPs layers (black spots) deposited over a TiO_2 film (left) and over a NiO film (right).

Eventually, the spectra of the NT series are quite different compared to the other datasets, as can be seen in Figure 5.15a: a sharp and narrow Au SPR peak is registered at 650 nm, and only a weak shoulder can be seen at about 900-1000 nm: these optical spectra resemble a lot the spectra of Au NPs randomly dispersed inside TiO_2 films (where usually the Au SPR peak is detected around 620-650 nm): an explanation of this behavior can be found in a partial detachment of Au NPs from the bottom layer when depositing the TiO_2 top layer, resulting in a partial mixing of Au NPs inside the TiO_2 film, while some NPs remain anchored to the bottom layer, providing the weak SPR peak at higher wavelengths. This sample series has been synthesized three times, always obtaining similar results. A partial confirmation of the previous assumptions is provided from RBS analyses presented in the following.

X-ray diffraction analysis gives a confirmation of the different Au amount according to the concentration of the solutions used for the Au layer deposition, and also verifies the crystallinity of the three oxides: all these results are reported in Figure 5.17. Typical diffraction patterns for TiO_2 (JCPDS No. 86-1157, highlighted with ●), NiO (JCPDS No. 47-1049, highlighted with ■), ZnO (JCPDS No. 36-1451, highlighted with ▼) and Au (JCPDS No.04-0784, highlighted with ▲) can be easily identified in all the samples, according to the respective composition. Analyzing the oxide diffraction peaks, they don't undergo any relevant change from one sample to another, nor in intensity or broadening, validating the reproducibility of the different sol-gel recipes adopted. However, it has to be said that such a comparison, especially for diffraction peaks intensity, is merely qualitative, since although all the samples had approximately the same film thickness and the same substrate size, the difference in XRD peaks intensity is strongly related to the thickness of the samples, the x-ray beam spot size, the careful alignment of the sample stage, because the measurements have been performed at glancing angle (0.5°), and so a quantitative comparison would be rather speculative. As far as Au diffraction peaks are concerned, few differences can be observed among the

different samples: increasing the Au NPs amount (from Low, to Medium, to High) a clear progressive increase in Au peaks intensity is detected, as also described in the previous sections, confirming the different surface coverage. Nonetheless, analyzing the relative intensities of Au peaks with respect to the oxide peaks across the different sample series, there seems to be a higher amount of Au NPs when deposited over NiO films, compared to TiO_2. This experimental evidence is in agreement with the previous discussion about the different morphology between the two oxides: in fact it is reasonable to suppose that a flat surface, such as the TiO_2 film, can anchor less particles compared to a rough and structured one, such as the NiO film. These assumptions are well schematized in Figure 5.16.

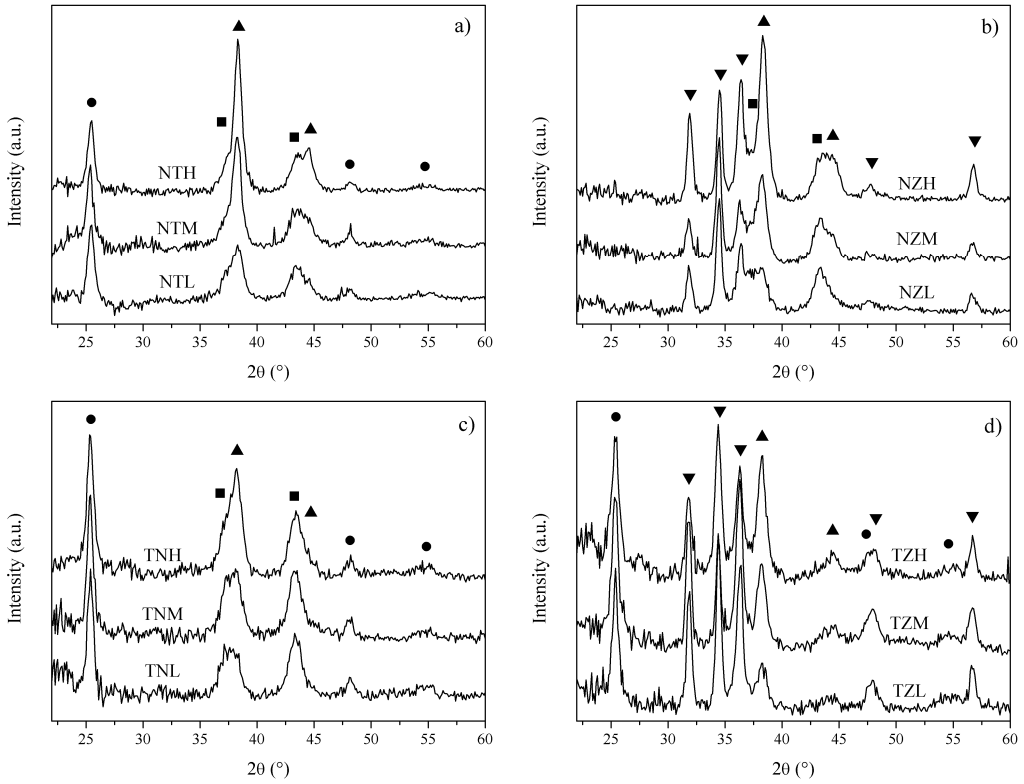

Figure 5.17. XRD patterns of: a) NiO-Au-TiO_2 series; b) NiO-Au-ZnO series; c) TiO_2-Au-NiO series; d) TiO_2-Au-ZnO series). Theoretical diffraction peaks positions for TiO_2 (●), NiO (■), ZnO (▼) and Au (▲) are also reported.

XRD has also been adopted to evaluate the effect of the activation of the bottom oxide layer before performing the APS functionalization process: as described in section 5.5.1, NiO and TiO_2 films were immersed in a hydrogen peroxide dilute solution in order to create –OH surface bonds. XRD measurements performed before and after the etching

treatment (not reported) do not show any modification of the oxide diffraction peaks, nor in intensity or FWHM, excluding any change in the morphology and chemical composition of the oxide layers. When trying to slightly etch ZnO films, irreversible modifications of the oxide are experienced, even using extremely diluted etching solutions. Both basic and acid solutions were used, and the results are reported in Figure 5.18.

When ZnO samples are immersed also only for few seconds in a H_2O_2(30%wt):H_2O=1:100 or a HCl(1N):H_2O=1:1000 solution (all ratios are by volume), ZnO diffraction peaks become weaker and broader, as a consequence of the corrosion of the crystals that causes a reduction in the crystalline fraction of ZnO, and consequently smaller crystals. Moreover, a diffraction peak is detected at about 38.2° after both the basic and the acid treatment: this peak can be ascribed to the formation some zinc hydroxide species, such as $Zn(OH)_2$ (JCPDS No. 24-1444), and to zinc chloride $ZnCl_2$ (JCPDS No. 16-0851) after the basic and the acid etching, respectively. For this reason it was decided to prepare the sandwich structures using NiO and TiO_2 as bottom layers, leaving ZnO as top layer only.

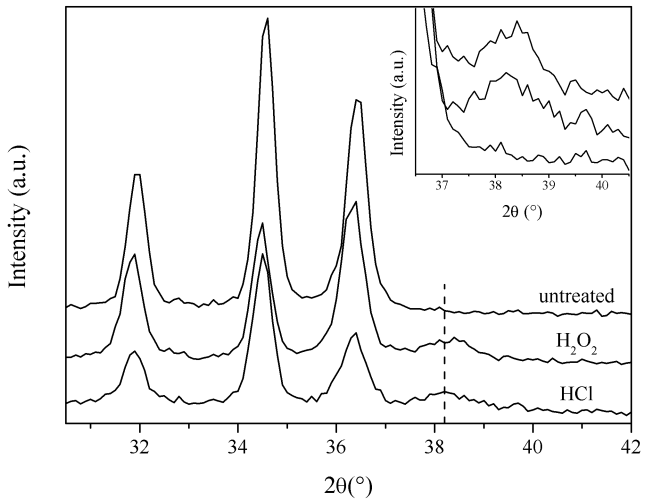

Figure 5.18. XRD patterns of a ZnO film before and after the etching treatments. The dotted line highlights the presence of a new diffraction peak, as also shown in the inset.

Some samples were also characterized with Rutherford Backscattering Spectrometry (RBS): this technique is quite useful to get information about thickness, composition and distribution over thickness of the different components. The analyzed samples are NT0, NTH and TNH: they were chosen in order to analyze if the order of the oxides in the

multilayer samples plays a role in the overall structure. The results are presented in Figure 5.19.

The spectrum of the Au-free sample shows two distinct peaks, centered at about 1.44 MeV and 1.5 MeV, and ascribable to Ti and Ni signals, respectively. The simulation has been performed considering a simple sandwich structure composed of a bottom layer of NiO and a top layer of TiO_2, letting the thickness vary: the best fit was obtained with a TiO_2 layer of 38 nm and a NiO film of 40 nm. The two values are extremely close to each other, as a confirmation of the correct choice of the deposition parameters in order to get similar thicknesses, even if the thickness values are lower compared to the results of ellipsometric analyses (not shown) and SEM analyses (see below): the reason for that is related to the fact that both SEM and ellipsometry take into account the porosity of the films, while the RBS technique is based on nominal density for the different materials, and measuring the atoms/cm^2 values, the apparent thickness evaluated with RBS is reliable only if measuring fully densified materials. Nonetheless, having obtained similar thicknesses for both oxides coatings, is a further proof of the accuracy of the experimental procedure. The same sample containing a layer of Au NPs in between the two oxides (Figure 5.19b) shows the same two peaks at 1.44 MeV and 1.5 MeV, and an additional peak at 1.82 MeV, due to metallic Au. These experimental data have been modeled using a bottom layer of fully dense NiO of 40 nm thickness, an intermediate layer of Au (3.4 nm) and a top layer of dense TiO_2 of 40 nm. Again, the two oxide films are of the same thickness, slightly lower than the expected one (45-50 nm) due to the porosity effect described before. Since the software used for the fitting procedure does not take into account the possibility of having a layer composed of NPs, the simulation has been carried out with a bulk gold layer, obtaining a thickness of 3.4 nm as best fit. Using the integral of the Au peak, the dose of Au atoms can be estimated, being it around $2 \cdot 10^{16}$ at/cm^2; knowing the actual size of the Au NPs (13 nm), and using simple mathematics involving the density, the molar mass and the Avogadro number, it is possible to estimate the Au NPs surface coverage, being it about $2.9 \cdot 10^{11}$ NPs/cm^2. Considering the area of a single Au NPs having a diameter of 13 nm, the estimated surface coverage is about 38%. This value, although being affected by a quite big error due to the simple calculations that for example don't take into account NPs size dispersity, is quite close to the surface coverage value evaluated from a bare Au NPs layer deposited from a 30 mM Au NPs solution (34%, see Figure 5.1). So the surface coverage of Au NPs is thereby confirmed. Analyzing the last RBS spectrum (Figure 5.19c), few differences with the previous one

can be seen: in fact, the Ti peak is registered at slightly lower energies (1.41 MeV compared to 1.44 MeV), while on the contrary the Ni peak is found at higher energies (1.53 MeV compared to 1.5 MeV). This difference is due to the fact that the two oxide layers have been inverted: in this sample, the NiO film is probed first by the ion beam, while the beam reaches the TiO_2 film after passing through the NiO, resulting in a peak position for Ti at lower energies. As a matter of fact, the theoretical energy positions for Ti and Ni signals (with the experimental setup used) are 1.44 MeV and 1.53 MeV, respectively. The fact that in some samples they are found at lower energies, is due to their distance from the surface. The simulation has been performed considering a bottom TiO_2 layer of 47 nm thickness, an intermediate Au layer of 2.3 nm, and a top NiO layer of 38 nm: in this sample the thickness of the anatase films is slightly higher than expected, but it has to be said that the fitting in this particular sample is not perfect. Anyway, an error in the spinning procedure is plausible. Analyzing the experimental Au peak, it is slightly shifted at lower energies (1.81 MeV compared to 1.82 MeV registered for the previous sample): such a behavior can be explained considering that in this particular sample Au NPs are slightly more distant from the surface, but since the top layer is of the same thickness in both samples, a more reasonable explanation is that in the previous sample (NTH) Au NPs where slightly nearer to the surface. This effect can be due to a partial detachment of the Au NPs from the NiO film, as already supposed analyzing the optical absorption spectra, that showed a narrow and definite Au SPR peak at high frequencies, instead of a broad peak at lower frequencies. So RBS analysis gives a confirmation of the partial mixing of Au NPs when depositing a TiO_2 film over a NiO-Au double layer structure. In fact, performing more complex simulations with no definite interfaces between the different layers, or considering each layer as composed of a mixture of the oxide and a certain amount of gold, the Au signal fitting is slightly improved.

Also for this sample the surface coverage has been evaluated, obtaining the Au dose from the integral of the Au signal, being it $1.34 \cdot 10^{16}$ at/cm^2. Again, doing the same calculations as before, the Au NPs surface coverage has been estimated to be $1.98 \cdot 10^{11}$ NPs/cm^2, corresponding to 26%. This value is lower than the one presented before, and this can be ascribed to a lower amount of Au NPs embedded in between the two films, but also to the quite noisy signal and the poor fitting of the experimental data. Nevertheless, the surface coverage is not extremely different compared to the supposed value.

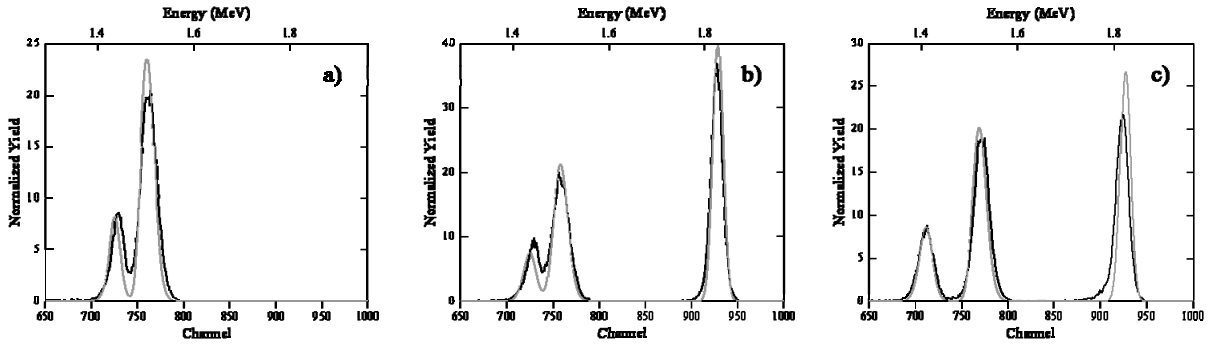

Figure 5.19. RBS spectra (black lines) and respective simulations (red lines) of a) TN0 sample; b) TNH sample; c) NTH sample.

A thorough SEM characterization has been carried out performing the measurements in cross section, in order to evaluate the presence of the two layers, their thickness and morphology, and to examine the Au NPs distribution across the samples. Figure 5.20 shows the Au NPs layer embedded between TiO_2 and NiO films: anatase film is the bottom layer in Figure 5.20a, and the top layer in Figure 5.20b. The morphology of the two oxides is clearly different, as already observed in the plan view SEM images reported in Figure 5.7 and Figure 5.14: TiO_2 films are more compact and smoother, while NiO layers have a more structured morphology, with the crystalline grains clearly identifiable. The thicknesses evaluated from the SEM images is in good agreement with the predicted values: in the TNH sample, TiO_2 and NiO films have been measured to be around 47 nm and 49 nm respectively, while in NTH samples the evaluated thickness is 43 nm and 47 nm, respectively. Anatase layer is always few nanometers thinner than NiO layers, but the target thickness of about 45-50 nm has been certainly fulfilled.

Au NPs can be seen as brighter spots, but since the difference in contrast with NiO crystals is quite low, it is sometimes difficult to distinguish them. Nevertheless, especially in Figure 5.20b, few bright particles in between the two oxide films can be easily recognized.

Similar samples with different Au NPs amount have been imaged in order to evaluate if a trend in the Au NPs could be observed, but since the cross sectional images were quite difficult to acquire, and due also to the previously described poor contrast difference between Au and NiO crystals, it was not possible to detect a difference in the Au NPs amount at the interface between the two oxides. Anyway, two more images of a sample composed of a bottom film of NiO and a top film of TiO_2, with embedded in between a layer of Au NPs with a different surface coverage are reported in Figure 5.21. From the

low magnification image, the high quality of the sandwich structure over few microns can be appreciated, and also Au NPs as brighter spots can be seen throughout the whole image, in between the two oxides. The high resolution image provides a confirmation of the sample thickness, and allows also a closer look on few Au NPs embedded inside the double layer structure.

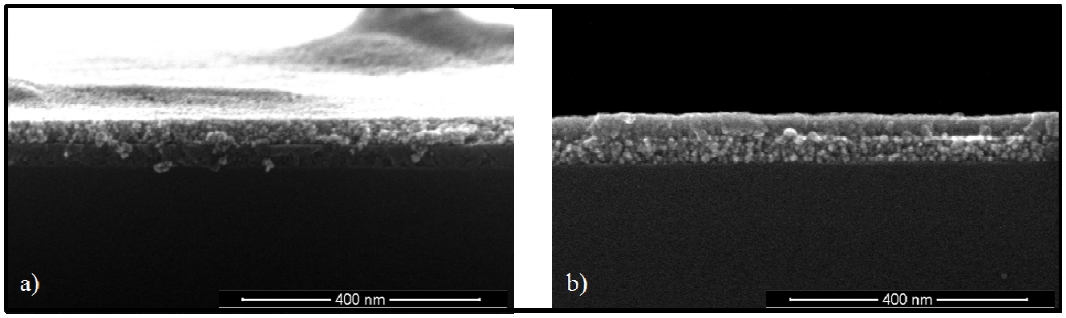

Figure 5.20. SEM images of a) TNH sample and b) NTH sample. Brighter spots correspond to Au NPs.

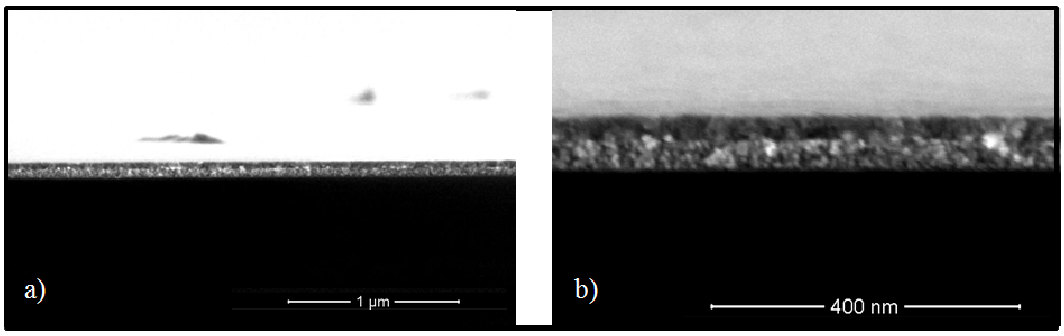

Figure 5.21. SEM images of NTM sample at different magnifications. Brighter spots correspond to Au NPs.

Figure 5.22 shows some images of a sample composed of Au NPs embedded between a bottom TiO_2 layer and a top ZnO layer. Again, the difference in morphology between the two oxides can be seen, being ZnO rougher and TiO_2 smoother, but also Au NPs can be clearly seen due to the higher contrast difference. Bright circular spots exactly at the ZnO-TiO_2 interface are seen in all four images, and due to the high resolution images, their size has been estimated in the 10-15 nm range, so extremely close to the value of the as-synthesized particles. So the observed coarsening of the particles when annealing a bare Au NPs layer seems not to happen here, as a consequence of the effect of the top oxide film in providing a physical barrier to the Au NPs diffusion. Figure 5.22d shows a picture of the double layer where a portion of the ZnO layer is missing (probably as a

consequence of the sample cutting and handling): few Au NPs deposited over the TiO_2 film can be easily seen, giving another proof of the metal NPs presence at the interface between the two oxides.

Moreover, the thickness of TiO_2 and ZnO layers has been evaluated as well, being 48 nm and 54 nm, respectively; again, the theoretical thickness is hereby confirmed, even if the ZnO film is slightly thicker than expected; though, it has to be said that being the surface of ZnO quite rough, the correct evaluation of the thickness is quite complicated, and the error in the measure might be relevant.

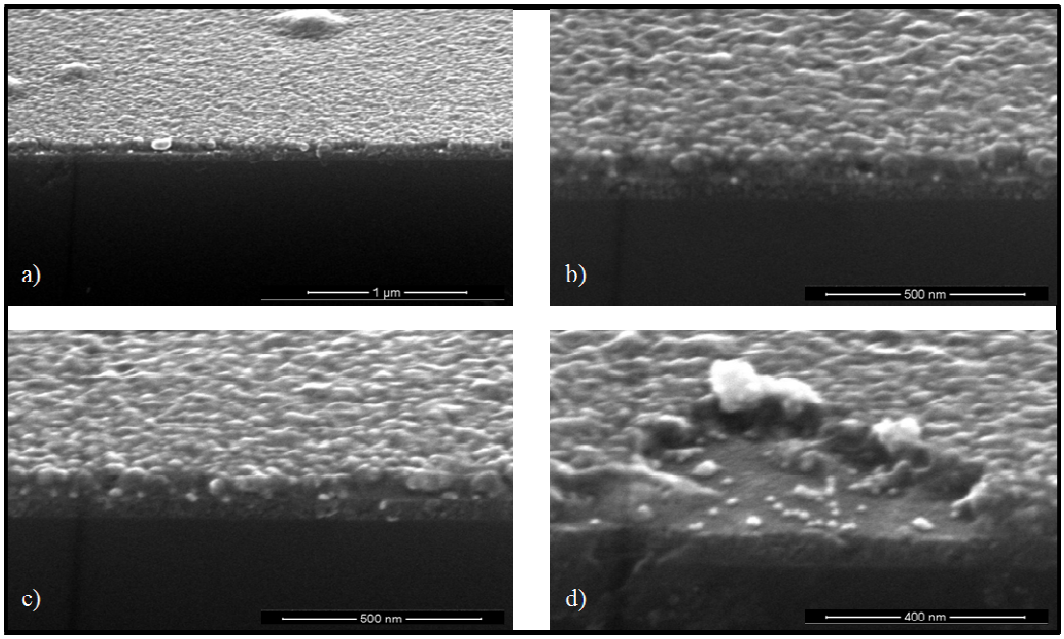

Figure 5.22. SEM images of TZM sample at different magnifications. Brighter spots correspond to Au NPs.

5.5.3 Gas sensing tests

Some of the synthesized double layers have been used for preliminary tests for optical recognition of reducing gases at high temperature (CO and H_2 at 300 °C OT) and of VOCs at low temperature (ethanol vapors at 150 °C).

Figure 5.23 presents OAC values as a function of the wavelength for NTH and TNH samples, when exposed to CO and H_2, both 1% v/v in dry air. The two samples respond rather differently: outside the 600-900 nm range, a decrease in absorption when exposed to both gases is seen for both samples, as a consequence of the already discussed optical sensing properties of the NiO film. Inside the 600-900 nm range, NTH sample show a

sharp and strongly wavelength dependent signal, more intense for hydrogen compared to CO, while in TNH sample only a weak modulation of the OAC curve is observed.

The explanation of this large difference is found in the optical absorption spectra of the two samples: NTH sample shows a narrow Au SPR peak, possibly due to a partial detachment of Au NPs when depositing the top TiO_2 layer, while TNH optical spectrum presents a much broader, weaker and red shifted plasmon peak. As a consequence, the difference from the spectra collected during gas exposure and the spectra collected in air, *i.e.* the OAC parameter, is strongly affected, being much higher when the optical spectrum has steep features, and much lower when the optical spectrum has plainer features. These results are not exactly the desired ones, but nonetheless a reversible response for both gases is experienced and some distinctive wavelengths corresponding to maximum and minimum (or null) response can be identified, theoretically permitting selective gas recognition through an appropriate choice of the analysis wavelength.

Figure 5.24 shows time-resolved tests for multiple exposure to the two tested gases. An easily detectable signal for both gases is observed, higher for hydrogen compared to CO, as predicted from OAC curves, with relatively fast response times (between 30 and 60 seconds) and acceptable recovery times, even if not ideal.

Unfortunately, if present, the wavelengths corresponding to null response were rather similar for both gases (see Figure 5.23a), so a selective recognition of the two gases is not likely to be possible for this systems. Nevertheless further samples are going to be prepared and tested to definitely prove this assumption.

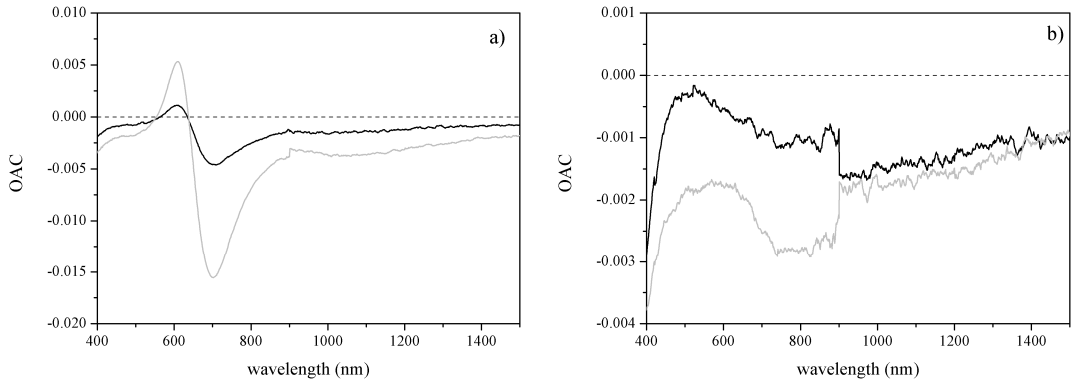

Figure 5.23. OAC curves for a) NTH sample and b) TNH sample after exposure to 1% CO (black lines) and 1% H_2 (grey lines) at 300 °C OT.

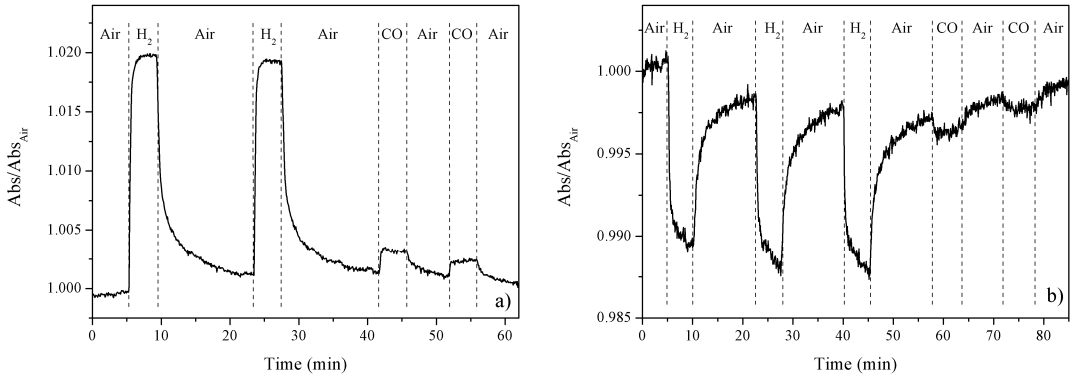

Figure 5.24. Dynamic tests after exposure to 1% CO and 1% H_2 for a) NTH sample at 609 nm and 300 °C OT; b) TNH sample at 580 nm and 300 °C OT.

The same couple of samples has been tested also for ethanol sensing at low temperatures, and the results are reported in Figure 5.25. As can be seen, the response to the exposure to ethanol vapors (180 ppm) is fairly different for the two samples, even if they present the same layers, only with the opposite order: ORC curve for TNH sample (grey line) resembles a lot the shape of the ORC curve obtained for a Au NPs layer covered with NiO, shown in Figure 5.8b, even if slightly vertically translated; the ORC curve for NTH samples seems effectively the sum of the response of Au NPs layer covered with NiO and covered with TiO_2 (see figure 5.8b and figure 5.8c, respectively). In fact, the NiO film is responsible for the decrease in absorption detected in both samples, while the effect of ethanol on the TiO_2 layer is to increase the reflection intensity.

Interestingly, in the TNH sample the strong reflection peak associated to Au-TiO_2 interface (see again Figure 5.8) is not present, while it is clearly detectable in NTH sample: there are two possible explanations for this behavior: the first one is related to the previously discussed difference in the optical absorption spectra, also responsible for the diversity in the shape and intensities of OAC curves reported in Figure 5.23. The second potential reason has to be ascribed to the diffusivity of the ethanol molecules inside the oxide films: it can be supposed that being the ethanol molecule bigger compared to CO and H_2, and being the sensing tests performed at low temperature, the diffusion of ethanol is mainly limited by the surface oxide layer. In this perspective, in the NTH sample the response is dominated by the TiO_2 film, while in the TNH one, the NiO film is the main responsible for the sensing performances.

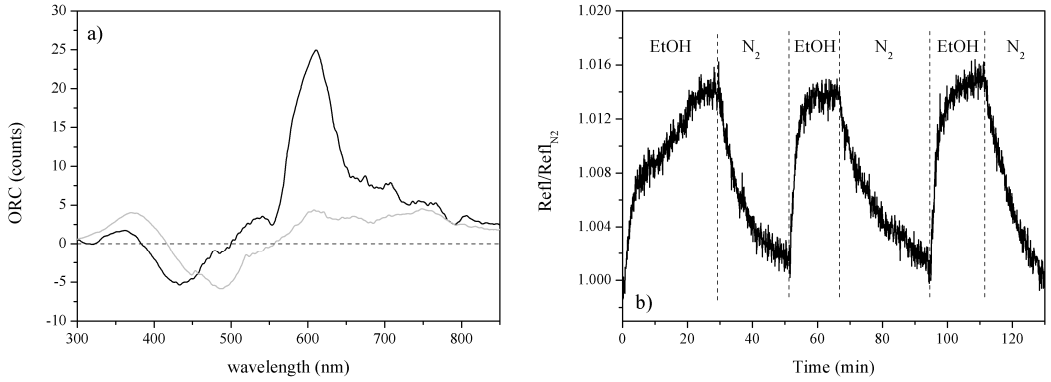

Figure 5.25. a) ORC curves for NTH sample (black line) and TNH sample (grey line) after exposure to 180 ppm ethanol at 150 °C OT. b) Dynamic tests for NTH sample after exposure to multiple ethanol-nitrogen cycles at 610 nm and 300 °C OT.

An example of the dynamic tests is reported in Figure 5.25b: reversible sensing dynamics for ethanol exposure can be observed, even if the response and recovery times are relatively high, about 5 minutes and 15 minutes, respectively. Of course the performance of these materials is far from being ideal, but considering the quite low temperature of analysis and the low resolution setup, these results are encouraging for persisting in the coupling different metal oxide films with in between a layer of Au NPs, trying to improve the sensitivity and the selectivity towards interfering species.

5.6 Conclusions

In this chapter, the preparation of nanocomposite materials based on Au NPs layers covered with oxide films or embedded in between two different oxide films has been discussed; this approach has been developed in order to avoid the compatibilization issues between the different solutions containing the precursors or the colloids necessary for the nanocomposite synthesis. In fact a multi step procedure based on separate layers deposition has been adopted and the resulting nanocomposite samples have been fully characterized and tested as optical sensors for reducing gases and VOCs detection.

In the first part, Au NPs layer with different surface coverage have been deposited on Si or SiO_2 substrates and eventually coated with NiO or TiO_2 sol-gel layers. SEM and AFM have been used to evaluate the metal NPs organization on the functionalized substrate surface, while IR analyses confirm a partial formation of covalent bonds between amino groups coming from the APS-functionalized substrate and carboxyl groups of the MUA

molecule used as capping agent for Au NPs. A modification of the Au SPR peak according to Au NPs surface coverage and type of the oxide used as coating has been observed and discussed. After the annealing treatment both the oxides used are found to be crystalline, and from XRD spectra also a confirmation of the surface coverage can be obtained. Gas sensing tests for CO and H_2 detection show a reversible and wavelength dependent response for all the samples tested, with different sensitivity according to the target gas and the type of the oxide layer. The multilayer nanocomposites have been also tested as ethanol sensors at low temperature, showing almost opposite response according to the oxide layer, and this fact has been related to the semiconductive type of the two oxide used (p-type NiO versus n-type TiO_2); time resolved tests reveal a non ideal behavior, with quite long transient times, but this preliminary results are promising.

Similar nanocomposites but containing a dispersion of Pt NPs inside the oxide (NiO, TiO_2 or ZnO) film have been also prepared, trying to evaluate a catalytic effect of Pt NPs in enhancing the sensing properties of the multilayered samples. The sensing tests on these materials are in progress at the moment.

The second part has been devoted to the synthesis and characterization of more complex structures, composed of a bottom oxide layer, an intermediate layer of Au NPs, and a top layer of a different oxide. The main idea behind this approach was to provide two different interfaces to Au NPs, in order to enhance the selectivity of the final nanocomposite towards interfering gases.

A detailed optical, structural and morphological characterization has been presented coupling optical spectroscopy in the visible and NIR range, XRD, RBS and SEM, providing the confirmation of the embodiment of Au NPs in between the two oxide layers, even if sometimes a partial detachment of the metal particles and a subsequent random mixing with the top coating can be inferred from the experimental data. Nevertheless these multilayered structures represent a higher level of materials engineering, providing accurate control on NPs morphology, organization and proper interface with the desired semiconductive material.

Preliminary sensing tests for reducing gases and VOCs detection, even if not ideal, show a reversible and wavelength dependent response, and these results are encouraging for further samples preparation and gas sensing measurements, aiming to improve the selectivity of the device, allowing multiple gases recognition using a single sample, simply choosing the appropriate analysis wavelength.

Bibliography

[1] R.G. Freeman, K.C. Grabar, K.J. Allison, R.M. Bright, J.A. Davis, A.P. Guthrie, M.B. Hommer, M.A. Jackson, P.C. Smith, D.G. Walter M.J. Natan, *Science*, **1995**, *267*, 1629.

[2] B.V. Enustun, J. Turkevich, *J. Am. Chem. Soc*., **1963**, *85*, 3317.

[3] D. Buso, *Sol-Gel films containing metal and semiconductor nanoparticles for gas sensing*, PhD Thesis, University of Padova, **2008**, 158.

[4] P. Mulvaney, M. Giersig, *J. Chem. Soc., Faraday Trans.*, **1996**, *92*, 3137.

[5] J. Lahiri, E. Ostuni, G.M. Whitesides, *Langmuir*, **1999**, *15*, 2055-2060.

[6] A. Brunet-Bruneau, J. Rivory, B. Rafin, J.Y. Robic, P. Chaton, J. Appl. Phys. 1997, 83, 1330.

[7] R. M. Almeida, C. G. Pantano, *J. Appl. Phys*., **1990**, *68*, 4225-4232.

[8] P. Innocenzi, P. Falcaro, D. Grosso, F. Babonneau, *J. Phys. Chem. B*, **2003**, *107*, 4711- 4717.

[9] C. Martinet, V. Paillard, A. Gagnaire, J. Joseph, *J. Non-Cryst. Solids*, **1997**, *216*, 77.

[10] L. Bertilsson, B. Liedberg, *Langmuir*, **1993**, *9*, 141-149.

[11] F. Toderas, M. Baia, L. Baia, S. Astilean, *Nanotechnology*, **2007**, *18*, 255702.

[12] S. Gao, N. Koshizaki, H. Tokuhisa, E. Koyama, T. Sasaki, J.K. Kim, J. Ryu, D.S. Kim, Y. Shimizu, *Adv. Funct. Mater.*, **2010**, *20*, 78-86.

[13] D. Buso, L. Palmer, V. Bello, G. Mattei, M. Post, P. Mulvaney, A. Martucci, *J. Mater. Chem.*, **2009**, *19*, 2051-2057.

[14] W.W. Yu, L. Qu, W. Guo, X. Peng, *Chem.Mater.*, **2003**, *15*, 2854–2860.

[15] K.C. Grabar, P.C. Smith, M.D. Musick, J.A. Davis, D.G. Walter, M.A. Jackson, A.P. Guthrie, M.J. Natan, *J. Am. Chem. Soc.*, **1996**, *118*,1148.

[16] P.D. Cozzoli, A. Kornowski, H. Weller, *J. Am. Chem. Soc.*, **2003**, *125*, 14539.

[17] R.J. Powell, W.E. Spicer, *Phys. Rev. B*, **1970**, *2*, 2182-2193.

[18] P. Alemany, R.S. Borse, J.M. Burlitch, R. Hoffmann, *J. Phys. Chem.*, **1993**, *97*, 8464.

[19] M. Lee, L. Chae, K.C. Lee, *Nanostructured Materials*, **1999**, *11*, 195.

[20] D. Buso, M. Guglielmi, A. Martucci, G. Mattei, P. Mazzoldi, C. Sada, M.L. Post, *Cryst. Growth Des.*, **2008**, *8*, 744-749.

[21] B. Bhooloka Rao, *Mat. Chem. Phys.*, **2000**, *64*, 62-65.

[22] Y. Gucbilmez, T, Dogu, S. Balci, *Ind. Eng. Chem. Res.*, **2006**, *45*, 3496-3502.

[23] T. Kobayashi, M. Haruta, M. Ando, *Sens. Actutators B*, **1993**, *13-14*, 545-546.

[24] M. Ando, T. Kobayashi, S. Iijima, M. Haruta, *J. Mater. Chem.*, **1997**, *7*, 1779.

[25] D. Buso, M. Post, C. Cantalini, P. Mulvaney, A. Martucci, *Adv. Funct. Mater.*, **2008**, *18*, 3843-3849.

[26] L.M. Liz-Marzan, A.P. Philipse, *J. Phys. Chem.*, **1995**, *99*, 15120.

Chapter 6

Conclusions and future perspectives

After all the data presented and discussed, after all the graphs and the tables shown, it is time to stop for a moment, look back and answer a simple question: what was this all about? These final pages try to give an answer to this, and put together all the results in a general and comprehensive view.

The main scope of this doctoral project was to synthesize nanocomposite materials based on noble metals and metal oxides nanocrystals through wet chemistry techniques to be used as reducing gases and VOCs optical sensors. Several aspects are of paramount importance when dealing with gas sensors: of course a proper choice of the active material is the first and most important task, but usually this is not enough. The porosity of the material has to be optimized in order to provide high specific surface, being the gas sensing a surface mechanism, and to allow an easy path for the gas to reach the surface of the active materials and for the reaction products to leave the sample. Also a proper contact interface between the different constituents of the nanocomposite has to be provided, since several reaction mechanisms are improved or catalyzed by a distinctive metal/oxide interface. Moreover, it is necessary to perform an in-depth control on size, shape and organization of the different components at the nanoscale, in order to obtain the desired properties. Eventually, all these characteristics have to be implemented inside a thin film of good optical quality, so aggregation phenomena or uncontrolled reactions that can lead to scattering features have to be prevented or, if not possible, minimized.

Clearly, the optimization of the nanocomposites structure, morphology and optical properties has to be balanced by the operative difficulty in synthesizing the materials: usually a higher control on the key parameters described before, requires a more complex and longer synthetic procedure. The optimal combination between the two aspects is related to the specific application.

Three main synthetic routes were followed to prepare the noble metal / metal oxide thin films which correspond to the three main chapters of this thesis.

The first approach is based on the preparation of a solution containing all the precursors needed for the film, its deposition on proper substrates, and a high temperature annealing to promote the crystallization of all the components. Occasionally, a subsequent impregnation procedure followed by another annealing was performed in order to embed other components inside the nanocomposite films. These syntheses are rather simple and quick, they allow to deposit high thickness samples, usually with high noble metal NPs amount, and several oxide-based materials can be prepared; on the opposite way, since the reduction of noble metal ions and the crystallization of the oxides is promoted by the thermal treatment, a poor control (if any) can be put on the morphology and properties of the different constituents.

With this approach several materials have been prepared: Au NPs embedded inside a matrix composed of Ti and Ni mixed oxides were found to be an extremely sensitive and selective material for hydrogen sulfide detection, with almost no interference with other reducing gases like hydrogen and CO, especially avoiding the formation of anatase phase, and selecting the correct operative wavelength [1]. Detection limit down to few ppm has been proved, and a great reproducibility of the sensing response has been observed; moreover quite fast transient times (few tens of seconds) are detected. The effect of the matrix composition and the Au NPs presence has been assessed for both the sensing performances and the reaction mechanism evaluation: Au NPs were found to act as optical probes, promoting a strong and wavelength dependent optical variation when exposed to the target gas, especially in the SPR wavelength range, while they does not seem to be directly involved in the reaction mechanism. Reaction product analysis shows the formation of sulfur oxides, like SO_2 and SO_3 after the interaction of H_2S with the active nanocomposite, and a higher amount of SO_x formation is detected when $NiTiO_3$ phase is present, while both anatase and rutile are less efficient in decomposing the hydrogen sulfide molecules [2]. No modification in film structure nor composition is

detected after the H_2S interaction, suggesting a direct catalytic oxidation of hydrogen sulfide to sulfur oxides.

With a similar procedure, ZnO-NiO nanocomposite films containing Au NPs have been also prepared and tested as optical CO sensors: in Au-free samples, or in Au-containing samples but outside the Au SPR range, the sensing response is governed by NiO, because ZnO itself is optically inactive. On the contrary, the ZnO-Au nanocomposite material is able to detect the target gas with a wavelength dependent response, and the presence of NiO helps to obtain the desired sensitivity according to the analysis wavelength, so in theory liming the problems of cross sensitivity with other gases. All tested samples show a linear-logarithmic relationship between the response intensity and the target gas concentration, allowing an easy calculation of calibration curves [3].

A slightly more complicated approach based on the initial synthesis of the oxide matrix and its subsequent impregnation with noble metal ions, to be then reduced by means of thermal annealing, has been used for the synthesis of SiO_2-NiO-Ag and WO_3-Au-Pt nanocomposites. In the first case, a mesoporous silica matrix containing NiO nanocrystals has been synthesized with the sol-gel method, and then impregnated with Ag ions. After the thermal annealing, metallic Ag NPs are formed, and the sensing properties of the Ag-NiO interface inside of a porous inert matrix have been presented: reversible dynamics for both CO and hydrogen detection are observed, with a sensitivity comparable with the previously reported results on SiO_2-NiO-Au nanocomposites [4], confirming the possibility to substitute Au with the cheaper Ag. In the second case, a sputtered W film underwent an acid treatment and thermal annealing to promote a microstructured WO_3 film formation; a subsequent impregnation with Au and Pt was performed, and different sensing performances according to type of the dopant and operative temperature are observed: at high temperatures the response is governed by Au optical properties, while at low temperatures the Pt catalytic properties are needed [5].

So this synthetic approach has been proved to be an effective way to prepare good quality nancomposites with high optical sensitivity towards reducing gases, and for some materials compositions, also a remarkable selectivity has been observed.

To increase the control over the morphology and structure of the nanocomposite films, a different approach was used: all metal (Au, Pt, Au@Pt) and oxide (TiO_2, ZnO) NPs were synthesized with colloidal techniques, with the desired size, shape and size distribution. Purification and concentration protocols have been developed, in order to obtain high quality solutions that can be directly mixed together and used for thin films deposition. In

this way, the materials are crystalline at room temperature, so a thermal annealing is not necessary for the crystallization of the components, but it can be used to promote sintering, densification, or organic template removal processes, according to the desired final properties. The price to pay for this higher control on the film properties, is a longer and more complex synthetic procedure, especially when dealing with the compatibilization of the different colloidal solutions.

TiO_2-Au samples were found to be extremely sensitive to CO and H_2, with detection limit of few ppm, despite the low thickness of the films (30-50 nm); moreover response and recovery times were quite fast, especially when a well developed anatase-gold interface is present [6]. These materials have been also tested as ethanol vapors sensors at room temperatures, providing quite good results, especially for the very fast response times.

When both Au and Pt NPs are embedded inside a nanocrystalline TiO_2 layer, an interesting synergistic effect between Au optical properties and Pt catalytic properties is experienced: room temperature hydrogen sensing tests show a reversible, wavelength-dependent response with fast transient times, while TiO_2-Pt response is not wavelength dependent, and TiO_2-Au response is extremely slow.

Nanocrystalline ZnO films (undoped and doped with transition metal ions) containing Au NPs are tested as CO optical sensors: detection limits down to 1 ppm and fast and reproducible response are detected in all samples. A positive effect in enhancing ZnO sensitivity is obtained when doping ZnO with ions having multiple oxidation states: a possible explanation is related to the promotion of electron transfer due to CO oxidation thanks to a reversible change in the dopant oxidation state.

With this approach, higher quality nanocomposite thin films have been prepared, generally with smaller particles (*i.e.* higher specific surface), and without the need for high temperature annealing, highlighting these materials as ideal candidates for deposition over delicate substrates that can't undergo high thermal treatments, like unclad optical fibers, polymers, SPR devices, gratings.

The last part of this thesis has been devoted to the synthesis of even more complex structures, where not only the particles size and shape is optimized, but also their organization inside the nanocomposite structure is controlled. Au NPs layers covered with or embedded in between sol-gel oxide films have been prepared through a multi-step procedure, avoiding all the compatibilization issues related to the mixing of the different colloidal solutions: in fact every layer is composed by one material, simplifying the operative procedure, even if the final nanocomposite has a rather complex structure. The

main idea behind this approach was to promote the Au NPs plasmons coupling due to relative proximity of the metal particles, and to exploit their distinctive optical properties for gas sensing applications. First, Au NPs have been deposited on glass substrates with different surface coverages, and coated with NiO and TiO_2 layers: reversible and wavelength dependent sensing response has been observed for both reducing gases and VOCs exposure, showing promising results for the use of these materials as gas sensors. Then, Au NPs have been successfully embedded in between two different oxide films, providing two different interfaces for Au NPs, with the aim to improve the device selectivity. Preliminary sensing tests are certainly not ideal, but encouraging in proceeding with this approach to the synthesis of high quality nancomposites.

So the work described in this thesis aims to present different ways to synthesize high quality noble metal / metal oxide nanocomposite thin films through wet chemistry techniques to be used as optical sensors for reducing gases and VOCs detection: the relationships occurring between materials composition, structure, and properties have been always addressed and exploited to understand the gas sensing performances. Different syntheses lead to different quality of the nanocomposites, with higher or lower control on the film properties, usually according to the experimental and operative difficulty.

This thesis represents only a small step in the big field of gas sensors, but several recipes have been presented leading to several different materials, that have been fully characterized and tested. Of course a lot has still to be done, but the work presented here can be a valuable starting point for the implementation of the described nanocomposites inside actual devices, like SPR-based sensors, or optical fibers setups, with a relatively simple and cheap experimental procedure, nonetheless providing high quality and high performances materials.

Bibliography

[1] E. Della Gaspera, M. Guglielmi, S. Agnoli, G. Granozzi, M. L. Post, V. Bello, G. Mattei, A. Martucci, "Au nanoparticles in nanocrystalline TiO_2-NiO films for SPR-based, selective H_2S gas sensing", *Chem. Mater.*, **2010**, *22*, 3407-3417

[2] E. Della Gaspera, M. Guglielmi, A. Martucci, G. Giallongo, S. Agnoli, G. Granozzi, F. Quaglio, "Role of Au nanoparticles and $NiTiO_3$ matrix in H_2S sensing and its catalytic oxidation to SO_x", *Sens. Lett.*, in press.

[3] E. Della Gaspera, A. Martucci, M.L. Post, "ZnO-NiO thin films containing Au nanoparticles for CO optical sensing", *Sens. Lett.*, in press.

[4] E. Della Gaspera, D. Buso, M. Guglielmi, A. Martucci, V. Bello, G. Mattei, M. Post, C. Cantalini, S. Agnoli, G. Granozzi, A. Sadek, K. Kalantar-zadeh, W. Wlodarski, "Comparison study of conductometric, optical and SAW gas sensors based on porous sol-gel silica films doped with NiO and Au nanocrystals", *Sens. Actuators B*, **2010**, *143*, 567-573.

[5] E. Della Gaspera, A. Martucci, M. Yaacob, J. Ou, K. Kalantar-Zadeh, W. Wlodarski, "WO_3-Au-Pt nanocrystalline thin films as optical gas sensors", *Sens. Lett.*, in press.

[6] E. Della Gaspera, A. Antonello, M. Guglielmi, M.L. Post, V. Bello, G. Mattei, F. Romanato, A. Martucci, "Colloidal approach to Au-loaded TiO_2 thin films with optimized optical sensing properties", *J. Mater. Chem.*, in press.

Appendix

Materials and Methods

Contents

A.1 Chemicals and synthesis setup

All chemicals were purchased from Aldrich and used without any further purifications. The chemicals used and the abbreviations adopted in the text are listed below.

Ethanol (EtOH); Milli-Q water; Titanium (IV) butoxide (TiBu); 2,4 Pentanedione or Acetylacetone (AcAc); Nickel chloride hexahydrate; Hydrogen tetrachloroaurate trihydrate; Tetraethoxy Silane (TEOS); Pluronic F127; Hydrochloric Acid 1N and 37%wt; N[3(trimethoxysilyl)propyl]-ethylenediammine (DAEPTMS); Aminopropyltrimethoxysilane (APS); Mercaptopropyltrimethoxysilane (MPS); Ammonium hydroxide solution 25%wt; Hydrogen peroxide solution 30%wt; Silver Nitrate; Zinc Acetate (ZnAc); Monoethanolamine (MEA); Tri-sodium citrate dihydrate (Na-citrate); 10000 g/mol poly(N-vinylpyrrolidone) (PVP-10K); Acetone; Sodium borohydride ($NaBH_4$); Hexachloroplatinic acid hydrate; Sodium Chloride; Sodium Nitrate; Ethylene glycol; Titanium isopropoxide (TiIp); Methanol (MeOH); Dimethyl

Sulfoxide (DMSO); Tetramethylammonium hydroxide (TMAH); Manganese acetate tetrahydrate; Nickel acetate tetrahydrate; Cobalt acetate tetrahydrate; Methyl ethyl ketone (MEK); 200g/mol polyethyleneglycol (PEG200); 11-mercaptoundecanoic acid (MUA); Nickel Acetate tetrahydrate (NiAc); Diethanolamine (DEA).

Sol-gel syntheses were conducted on capped glass vials of 10-20 mL volume under standard fume hoods at room temperature. Au NPs syntheses were conducted on Erlenmeyer flasks of 250-500 mL volume (if needed, using a hot-plate as the heating source). Pt NPs syntheses were conducted in a 100 mL three-necked flask connected with a standard Schlenk-line for inert gas / vacuum switching operations. The heating source was a heating mantle with thermocouple feed temperature control. The necks of the flask were sealed with rubber septa and used for injection operations. TiO_2 and ZnO NPs syntheses were conducted in one-neck flasks and heated on a oil bath with a reflux column to avoid solvent losses.
Standard SiO_2 (HSQ300 fused silica glass slides from Heraeus) or Si (<100> oriented, p-type boron-doped, from Silicon Materials) substrates were used for films depositions. All depositions were made with a Special Coating Systems G3P-8 spin coater, except the samples prepared in the NanoScience laboratory of the Melbourne University, that have been spun with a Headway Research spin coater. If not specified, all samples were stabilized at the desired temperature on a hot plate, and then annealed in muffle or tube furnaces preheated at the desired temperature.

A.2 Instrumentation

A.2.1 X-Ray Diffraction

The crystalline phases of the thin films were characterized by X-Ray diffraction (XRD) by using a Philips PW1710 diffractometer equipped with grazing incidence X-Ray optics. The analyses were performed at 0.5° incidence, using CuKα Ni filtered radiation at 30 kV and 40 mA. Due to limited amount of produced materials, also powder samples were most often analyzed with the grazing angle optics. This was performed by depositing on a glass substrate a thick layer of powder. The X-Ray incident angle was set equal to 3°.
In both cases, the average crystallite size *D* was calculated from the Scherrer equation:

$$D = K\frac{\lambda}{\cos\theta\,\Delta w} \quad (A.1)$$

after fitting the experimental profiles with Lorentzian functions: in this relationship, λ=1.54 Å is the Cu k_α wavelength, θ the diffraction angle, Δw the full width at half maximum (FWHM) of the diffraction peak, and K=1 is the shape factor.

A.2.2 Electron Microscopy

Scanning Electron Microscope (SEM) was used to evaluate the surface morphology of the nanocomposites using different microscopes: low resolution images were taken on a Philips SEM equipped with Energy Dispersive X-ray (EDX) spectroscopy for elemental analysis. High resolution images were taken on a xT Nova NanoLab SEM operating at 5kV and 0.4nA.

Transmission Electron Microscopy (TEM) analysis on scratched fragments of the film and of nanoparticles deposited from colloidal solutions both deposited on carbon-coated copper grids were performed with a Philips CM20 STEM system operating at 200 kV. High Resolution Transmission Electron Microscopy (HR-TEM) cross-section measurements of thin films were taken with a field emission FEI TECNAI F20 SuperTwin FEG-(S)TEM microscope operating at 200 kV and equipped with an energy-dispersive x-ray (EDX) spectrometer for compositional analysis and a Gatan 794 Multiple Scan Camera, allowing digital image recording on a 1024 × 1024 pixel CCD array.

The size distribution of the NPs has been evaluated with Fiji-Image JA 1.44b image analyzer software [1] measuring a minimum of 150 particles.

A.2.3 Optical Spectroscopy

UV-Vis-NIR absorption spectra were taken using a JASCO V-570 spectrometer. Absorption measurements of liquid samples was performed with quartz or polycarbonate cuvettes (1 cm optical path), while thin films on quartz substrates were analyzed placing the substrate perpendicularly to the light beam.

Fourier transform infrared spectroscopy (FTIR) measurements have been performed in the 400–4000 cm^{-1} range using a Jasco FTIR 6300 instrument using a resolution of 2cm^{-1} on thin films deposited on a silicon substrate.

A.2.4 Spectroscopic Ellipsometry

Transmittance at normal incidence and ellipsometry quantities Ψ and Δ have been measured using a J.A. Woollam V-VASE Spectroscopic Ellipsometer in vertical configuration, at various angles of incidence (usually three angles, 65°, 70°, 75°) in the wavelength range 300-1700 nm. Refractive index *n*, absorption coefficient *k*, and film thickness have been evaluated from Ψ, Δ and transmittance data using the WVASE32 ellipsometry data analysis software, fitting the experimental data with the 3-parameter Cauchy dispersion, Gaussian and Tauc-Lorentz oscillators for the non absorbing region, Au SPR peak and oxides UV absorption edge, respectively. A detailed description of ellipsometric measurements in reverse side mode is presented in section A.3.

A.2.5 X-ray photoelectron spectroscopy

The surface composition of thin films deposited on a Si wafer (with its native oxide layer) was analyzed by X-ray Photoelectron Spectroscopy (XPS) using a modified VG ESCALAB MK II (Vacuum generators, Hastings, England) where a twin (Mg/Al) anode x-ray source, a sputter gun, and a hemispherical electrostatic analyzer with a five channel detector are mounted. The XPS data reported were obtained using Al-K_α radiation (1486.6 eV) as an excitation source, while valence band (VB) ultraviolet photoemission spectra (UPS) have been obtained using a VUV high intensity source (Omicron HIS 13). The charging effect has been compensated by referencing all the binding energies (BEs) to the C 1s peak at 284.8 eV. Photoemission spectra have been obtained at room temperature using a normal emission geometry. Before taking XPS measurements, the samples were degassed overnight under UHV (pressure lower than 10^{-8} mbar). In order to derive the chemical composition of the films, the theoretical photoemission cross sections by Yeh and Lindau have been used [2], while the electron inelastic mean free path has been calculated with the TPP2 algorithm [3].

A.2.6 Atomic Force Microscopy

Atomic Force Microscopy (AFM) height profiles were recorded with a multimode atomic force microscope (with a Nanoscope III controller). All profiles were recorded in tapping mode at room temperature, in air. The recorded images were analyzed using either the WSxM software provided by Nanotec Electronica S.L., or the Gwyddion 2.18 image analysis software.

A.2.7 Impedance Spectroscopy

Gold contacts were evaporated on the surface of the samples to allow electrical measurements: the samples were masked using an appropriate shadow mask and placed in a Emitech K975 thermal evaporation chamber. The chamber pressure was lowered to below 10^{-3} mbar before evaporation of the metal. Gold films were deposited to a final thickness of about 100 nm.

Electrical measurements were carried out on a Keithley 2612 source-measure-unit. Impedance measurements were made on an Autolab potentiostat and modeled in the accompanying FRA software.

A.2.8 Rutherford backscattering spectrometry

Rutherford backscattering spectrometry (RBS) was performed with an electrostatic accelerator, Van de Graaff type, using single-charged alpha particles ($^4He^+$) at 2 MeV and 20 nA. The incident beam is perpendicular to the sample, while the backscattered beam is collected at 20 deg.

A.2.9 Gas sensing tests

Sensing tests for gases detection were studied with two different setups:

The first setup is located at the *Institute for Chemical Process and Environmental Technology* (ICPET) at the National Research Council of Canada (NRC) , Ottawa (ON), Canada. Samples were tested by making optical absorbance measurements using a custom-built gas flow cell coupled with a Varian Cary1E spectrophotometer. Details are reported elsewhere [4].

The second setup has been fabricated at the Department of Mechanical Engineering-Materials of the Padova University during this doctoral project: it is now fully operative and can hold up to 6 gas cylinders. Samples were tested by making optical absorbance measurements using a Harrick gas flow cell coupled with a Jasco V-570 spectrophotometer. The cell is provided with a heater in order to perform the gas sensing tests up to 400 °C.

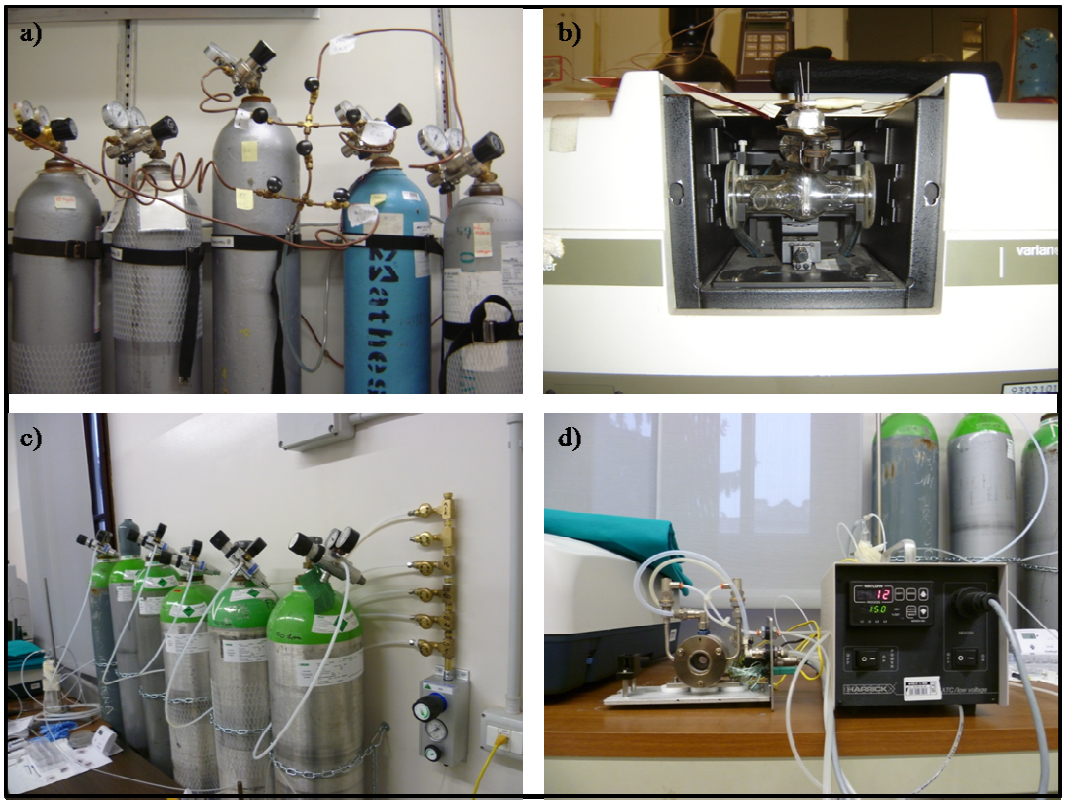

Figure A.1. Pictures of gas sensing setup at NRC laboratories (a, b). Pictures of gas sensing setup at University of Padova laboratories (c, d).

The tested films were exposed to:

Hydrogen (H_2): 100 ppm to 10000 ppm, *i.e.* 1%v/v,

Carbon Monoxide (CO): 1 ppm to 10000 ppm, *i.e.* 1%v/v,

Hydrogen Sulfide (H_2S): 1ppm to 100ppm,

Propane (C_3H_8): 3000 ppm, *i.e.* 0.3%v/v,

all balanced in dry air, at a flow rate of 0.4 L/min and at operative temperature (OT) ranging from 50 °C to 350 °C. The substrate size was approximately 1 cm × 2 cm and the incident beam was normal to the film surface and covering a 6 mm × 1.5 mm section area.

The tests were performed with the following procedure: first, subsequent absorption spectra over the whole desired wavelength range are collected under different atmospheres. Once the spectra are consistent, the response intensity is evaluated using the Optical Absorbance Change parameter, defined as the difference between the absorbance during gas exposure and the absorbance during air exposure, $OAC = A_{Gas} - A_{Air}$.

The OAC curve as a function of the wavelength allows to identify the wavelengths where the response is maximum, or where one gas is not interfering with another: once these

wavelengths have been chosen, time resolved tests are performed at a single wavelength varying the gas composition and concentration in the test cell over time.

A useful parameter to analyze the sensitivity of the samples is the Response Intensity (*RI*) that can be defined as follows:

$$RI = \left|1 - \frac{Abs_{CO}}{Abs_{Air}}\right| \quad \text{(A.2)}$$

To analyze the dynamic behavior of the samples, response and recovery times are calculated as the time needed to reach 90% of the total response, or to recover 90% of the baseline, respectively.

Being both H_2S and CO highly toxic and dangerous gases, they were handled very carefully: they were not supplied concentrated, but pressure cylinders with different concentrations of the target gas balanced in dry air were used. Concentrations lower than 10 ppm were achieved diluting the 10 ppm flow with pure air. All regulators were in stainless steel, as the pipe fittings, while the all the tubes were in copper or teflon, and before each use they were tested with a commercial leak detector fluid to ensure no gas leak occurs. After exiting the sample test cell, the exhaust gas was let flowing through a bubbler filled with an aqueous solution of lead acetate: excess H_2S reacts with lead ions producing an insoluble lead sulfide that precipitate as a black powder. The final gas flow was dispersed under a fume hood.

Sensing tests for volatile organic compounds (VOCs) detection were performed at the Materials Laboratory of the National Institute of Nuclear Physics (I.N.F.N.) in Legnaro (PD), Italy, in reflection mode using a custom built stainless steel cell provided with a heater that allows to perform the gas sensing tests up to 150 °C. The reflection spectra are collected at an incident angle of 90° thanks to a reflection probe composed of a tight bundle of seven optical fibers (six illumination fibers around one read fiber), connected to a OceanOptics USB2000 spectrophotometer. This setup was used for ethanol sensing tests: a nitrogen stream was let flow inside a bubbler filled with ethanol, and if needed the final stream was diluted with pure nitrogen, to lower the ethanol concentration. The final flowrate was set constant at 0.5 L/min. From the weight loss of the bubbler and knowing the nitrogen stream flowrate, it is possible to estimate the ethanol concentration: all testes reported have been performed with ethanol concentration of 180 ppm.

As for transmission measurements, the parameter used to evaluate the response as a function of wavelength is defined Optical Reflection Change, the difference between the

reflection intensity measured during gas exposure and the reflection intensity measured during air exposure, ORC = $R_{Gas} - R_{Air}$.

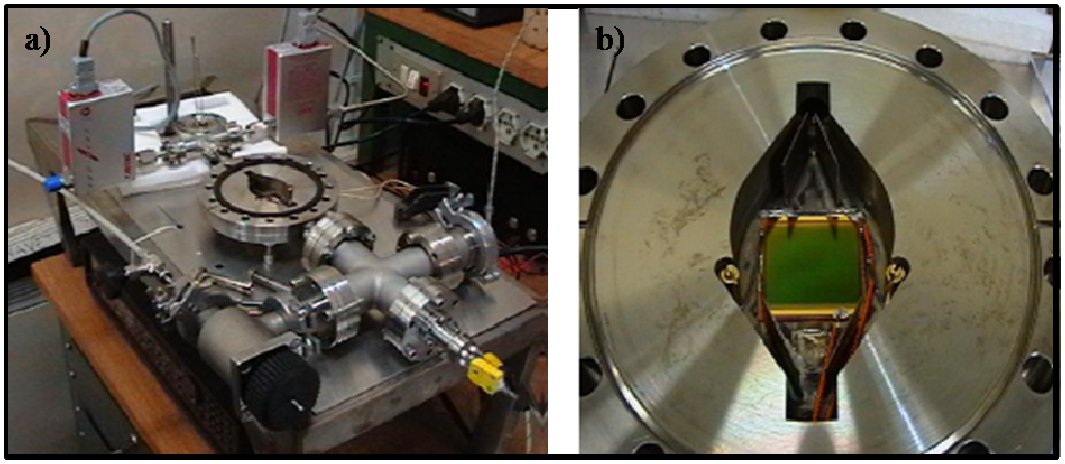

Figure A.2. Pictures of the VOCs sensing setup at INFN laboratories.

Gas phase reaction product analysis was performed using Radiello® diffusion samplers [5] positioned inside a sealed chamber provided with gas inlets and outlets, at the exit of the sensing cell containing the sample.

A.3 Spectroscopic ellipsometry measurements in different environments

Porosity measurements of thin films is a challenging task, because common techniques like gas absorption isotherms [6,7] , usually modeled with BET, Kelvin or BJH equations, cannot be applied because they require a huge amount of powder of the sample material (at least 50-100 mg) to obtain significant results: obviously, such an amount is difficult to obtain from thin films.

Spectroscopic ellipsometry can be used to measure the dielectric and optical properties of thin films and then porosity can be inferred from the refractive index values. There are mainly two different ways to measure porosity with ellipsometry: the first method involves the measurement of the refractive index of the sample and the comparison with the refractive index of the same material fully densified. From this difference it is possible to infer the porosity through Effective Medium Approximation (EMA) models, like Bruggeman [8,9]. There are though several limitations: first of all, the tabulated values for fully densified materials may not be reliable for nanostructured films; then amorphous phase - if present - may play an important role in lowering the experimental

refractive index of a supposed fully crystalline thin film; moreover, if the film is composed of different phases, it may be difficult to know exactly the volume fraction of each phase. So with this technique the evaluation of the porosity amount may be quite incorrect.

The second procedure involves the measurement of the refractive index of the sample first in air or nitrogen, and then in other environments, for example water [10], ethanol [11,12] or other organic solvents [13]. It has been proved that this technique can also provide information about pores size distribution [14-16]. From the difference in the refractive index of the film measured under the two environments it is possible to evaluate the open porosity, since the two environments have different refractive index values. Considering for example to perform the ellipsometric measurements under nitrogen and then under water, the experimental complex dielectric functions can be approximated with linear EMA models as follows:

$$\varepsilon_N = X\varepsilon_N^{matrix} + (1-X)\varepsilon_N^{pores} \quad \text{(A.3)}$$

$$\varepsilon_W = X\varepsilon_W^{matrix} + (1-X)\varepsilon_W^{pores} \quad \text{(A.4)}$$

where *N*, *W* and *X* stand for nitrogen, water and matrix volume fraction, respectively.

The epsilon value of the matrix is obviously the same in both measurements, while the epsilon value of the pores filled with nitrogen and water is essentially the value for pure nitrogen and pure water respectively, assuming than the two environments fill completely the pores; according to these observation, by subtracting the two equations it is possible to calculate the pore volume fraction *P*:

$$P = (1-X) = \frac{\varepsilon_W - \varepsilon_N}{\varepsilon_W^{pores} - \varepsilon_N^{pores}} \quad \text{(A.5)}$$

If considering non absorbing media and samples, so assuming $\varepsilon_2 = 0$, the previous equation can be simplified as the following:

$$P = (1-X) = \frac{n_W^2 - n_N^2}{n_W^{2\,pores} - n_N^{2\,pores}} \quad \text{(A.6)}$$

The porosity so evaluated is on the conservative side, since only the open pores are accessible by the water, and also the pores may be only partially filled with it (even if this effect can be minimized leaving the sample under water environment for a certain time before performing the measurement, or using other liquid or vapors to improve the wettability of the film).

Moreover, as described by Cohen and coworkers [10], with this approach it is also possible to estimate the refractive index of the matrix: this turns out very useful in the

case of nanocrystalline materials, when the tabulated values for fully dense materials may not be reliable, as explained before. In fact, combining equation (A.3) and (A.4) it is possible to obtain the ε value of the matrix as following:

$$\varepsilon^{matrix} = \frac{\varepsilon_W \varepsilon_N^{pores} - \varepsilon_N \varepsilon_W^{pores}}{\varepsilon_W + \varepsilon_N^{pores} - \varepsilon_N - \varepsilon_W^{pores}} \quad (A.7)$$

Currently, sample holders to perform these measurements are already available: they consist in closed cells with two windows, one perpendicular to the incident beam and another one perpendicular to the reflected beam. This is a huge limitation because it is possible to measure the sample only at one precise angle (usually 70 or 75 deg). Since to obtain the refractive index dispersion curve with ellipsometry the experimental data (psi and delta) have to be fitted with a model, it would be better to perform the ellipsometry measurements at different angles, in order to lower the fitting error and the correlation between parameters.

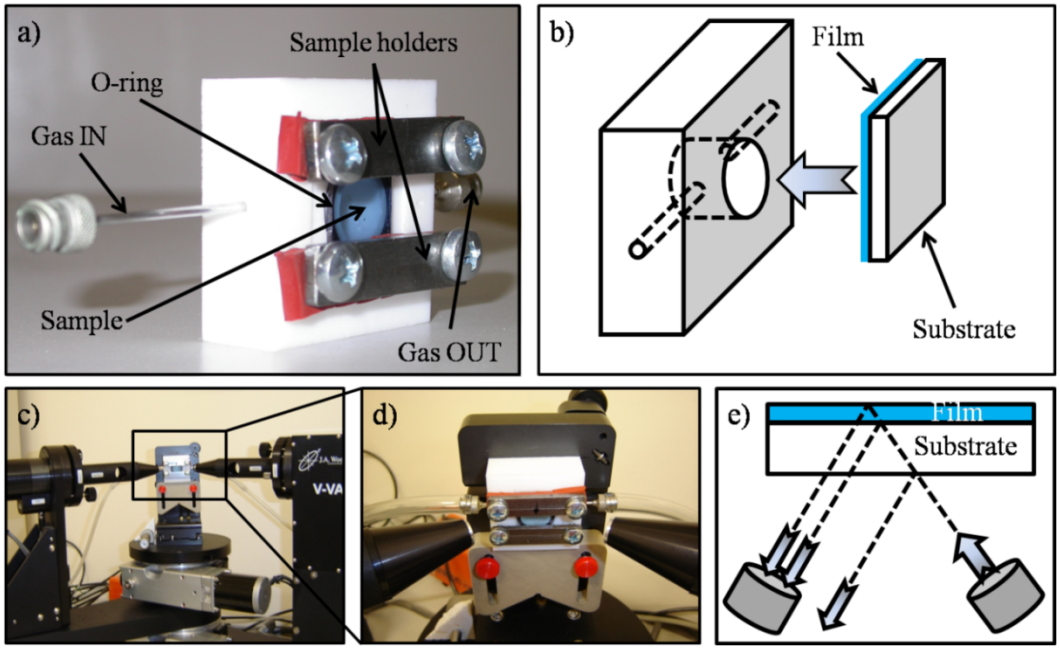

Figure A.3. a) Picture of the cell showing the different parts; b) Scheme of the cell showing how to place the sample; c) Picture of the ellipsometer equipped with focussing probes and the test cell; d) zoom on the cell; e) Scheme showing the multiple reflections coming from the sample and how to align the detector, excluding the first reflection that does not carry any information about the thin film.

A new and innovative ellipsometer sample holder has been designed and fabricated during this doctoral project, in which the sample is mounted in "reverse side": so the

sample is probed on the back side, but aligned in order to collect the reflected beams coming from the film-substrate and film-environment interfaces and not from the substrate-air interface. To allow these measurements, the film has to be deposited on transparent substrates. In this way the analysis can be carried out at different angles, improving the fit quality. Moreover, there is no need for windows.

Pictures and schemes of the cell with a sample mounted are reported in Figure A.3. The cell is provided with inlet and outlet for gas/liquid stream and the sample itself is pressed over the o-ring and used as a sealing. The total volume of the cell is approximately 1 mL, considerably small compared to most of commercial cells, allowing low solvent consumption during the analyses.

The key point of this approach is the sample alignment: the sample has to be aligned in order to collect the reflections resulting from the interaction of the upcoming beam with the thin film, and not the reflection coming from the back of the sample: the reflections coming from the air-substrate, substrate-film and film-environment interfaces will be called from now on first, second and third reflection, respectively. Ideally, the first reflected beam should be physically separated from the second and the third, as shown in Figure A.3e: so either the beam spot has to be very small, or the substrate has to be very thick. Since usually thin films are deposited on glass slides of 1 mm thickness, there is the need of focussing probes in order to reduce the spot size down to 200-400 μm in diameter, at least to prevent excessive overlapping of the reflected beams. Moreover, the amount of backside multiple reflections collected and the extent of overlapping between the reflected beams are angle dependent: the smaller the angle of incidence, the higher the number of backside reflections that reach the detector and also the extent of overlapping is higher; when performing the fitting of the experimental data, all these assumption has to be taken into account.

The first experiment was designed as a proof of concept: the same sample was measured in standard mode and then in “reverse side” mode in order to evaluate if the refractive index dispersion was the same in the two different analyses. For this purpose a crystalline TiO_2 (anatase) thin film of 25 nm thickness was used (the synthetic procedure for the TiO_2 film has been described in section 5.2.4). The measurement was performed at 4 different angles of incidence (40, 50, 60 and 70°), and the experimental psi and delta data were fitted with a standard 3-parameter Cauchy dispersion, since the sample is transparent in the visible range; as can be seen from Figure A.4, the same refractive index dispersion was obtained, with a very small difference (less than 0.15%) between the two

measurements, that can be considered of the same order of magnitude of the experimental error of the ellipsometer. Moreover, the thickness evaluated in the two configurations is also the same, 24.9 nm in standard mode analysis and 25.5 nm in “reverse side” mode analysis: the error is around 2.5%, reasonably acceptable, considering that the two measurements may not have been performed in the same exact spot, due to the fact that the sample had to be flipped over.

Furthermore, the quality of the fitting is almost the same, since the mean squared error (MSE) is comparable in both measurements (MSE=1.32 in standard mode and MSE=1.08 in “reverse side” mode): this is a confirmation that performing the measurement in “reverse side” does not affect too much the experimental data quality, even if the beam that reaches the detector is reduced in intensity after passing through the sample substrate.

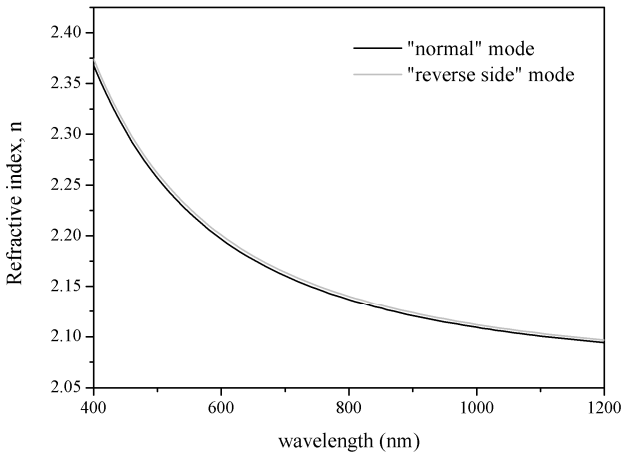

Figure A.4. Refractive index dispersion curves of the same TiO_2 thin film measured in the “normal” mode, and in the “reverse side” mode.

Table A.1. Comparison of correlation values between 3 couples of fitting parameters in the single angle and multiangle analyses. The fitting parameters are: *A* (*A* factor in Cauchy dispersion formula); *B* (*B* factor in Cauchy dispersion formula); *C* (*C* factor in Cauchy dispersion formula).

Parameters	Correlation (single angle)	Correlation (multiangle)
A-B	0.809	0.708
A-C	0.747	0.639
B-C	0.974	0.963

Analyzing only the standard measurement data, it can be noticed that the multi angle approach improves the quality of the fit by reducing the correlation between parameters: in fact considering in the fitting procedure only the data collected at the angle of incidence of 70°, the correlation between the fitting parameter is slightly higher compared to the multiangle approach, as reported in Table A.1. Moreover the MSE is similar in both cases (1.51 for the single angle and 1.35 for the multiangle) so again the quality of the fit is not worsen by including in the fitting procedure multiple datasets.

Since similar behavior has been observed also in other samples, the reverse mode measurements have been proved to be consistent and reproducible, and so this approach can be used to improve the ellipsometry analyses under different environments. In the following we present few examples of measurements performed with the custom built cell under nitrogen and ethanol vapors in order to evaluate the open porosity of the samples; eventually a test performed filling the cell with ethanol will be presented, confirming the feasibility also of measurements in liquid environment.

The first test has been carried out on a crystalline $NiTiO_3$-TiO_2 film of about 110 nm thickness annealed at 600 °C (see section 3.2.1 for synthetic details); the film is transparent in the visible range so it can be modeled with a simple Cauchy dispersion. The measurement has been performed in "reverse side" mode at 3 different angles of incidence (55, 60 and 65 deg) under nitrogen and ethanol vapors atmospheres. Ethanol vapors have been obtained bubbling a nitrogen stream into an ethanol solution before it enters the cell.

As can be noticed from the dispersion curves reported in Figure A.5, the refractive index of the sample measured under ethanol vapors atmosphere is higher compared to nitrogen atmosphere. This is due to the fact that ethanol has a higher refractive index compared to nitrogen (n=1.36 and n=1, respectively): since the thin film can be modeled as an effective medium composed of matrix and pores, when the pores are filled with ethanol the average refractive index measured with the ellipsometer is found to be higher. Using the formula (A.6), and considering the experimental refractive index at 800 nm (n=1.992 under nitrogen and n=2.037 under ethanol), the estimated open porosity is at least 21%. It is noteworthy saying that the refractive index dispersion curve measured under ethanol vapors does not change in shape, but appears only vertically shifted compared to the curve measured under nitrogen: this is another confirmation that ethanol vapors filling the pores don't change the optical properties of the thin film. Moreover the film thickness is almost the same in both cases, 107.3 nm under nitrogen and 108.1 under ethanol vapors,

with the difference being less than 1%: so as expected, the different environments affect only the fitting of the optical constant of the film, and not its thickness.

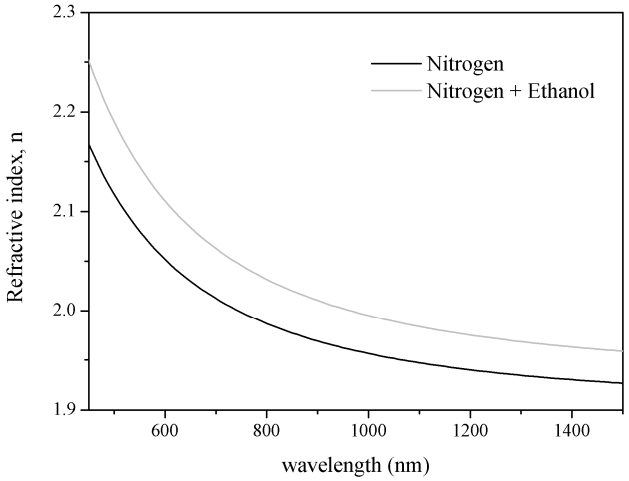

Figure A.5. Refractive index dispersion curves for a $NiTiO_3$-TiO_2 film measured in reverse side mode under nitrogen (black line) and ethanol vapors (grey line) atmospheres.

The second test has been performed on an amorphous TiO_2 film of about 105 nm thickness containing Au nanoparticles annealed at 200 °C (see section 5.2.4 for synthetic details), measured in "reverse side" at 4 different angles (40, 50, 60 and 70 deg) under nitrogen and ethanol vapors atmospheres. In this case the sample is not transparent in the visible range, so the experimental data have to be fitted not only with a Cauchy dispersion, but also with a Gaussian oscillator to fit Au NPs SPR peak: since refractive index and extinction coefficient are related by the Kramers-Kronig relationship, the dispersion curve for n is also affected by the absorption band of Au NPs. Again the refractive index of the film measured under ethanol vapors is higher compared to the value under nitrogen, and the dispersion curves don't change in shape but they appear only translated. Using the equation (A.6), and considering the experimental refractive index at 1000 nm (1.849 under nitrogen and 1.914 under ethanol), the estimated open porosity is at least 29%. As expected, also in this case the thickness evaluated in the two different environments is the same (105.7 nm under nitrogen and 106.2 nm under ethanol vapors).

Comparing the single angle (70°) and the multiangle approach, the latter helps also to reduce the correlation between the fitting parameters, as observed before: in fact being the evaluation of the optical constant an iterative process, if the number of parameters to be

fitted is high, there might be strong correlation between some of them, since sometimes more than one combination of two parameters can give as a result the same (or very similar) effect in fitting the experimental data, so reaching one of the local minima in the MSE function. In this particular example a quite strong correlation has been experienced for some parameters, as reported in Table A.2: as can be noticed, only for one couple of parameters the correlation is not improved by the multiangle analysis fitting procedure, while for all other couples the correlation is substantially reduced.

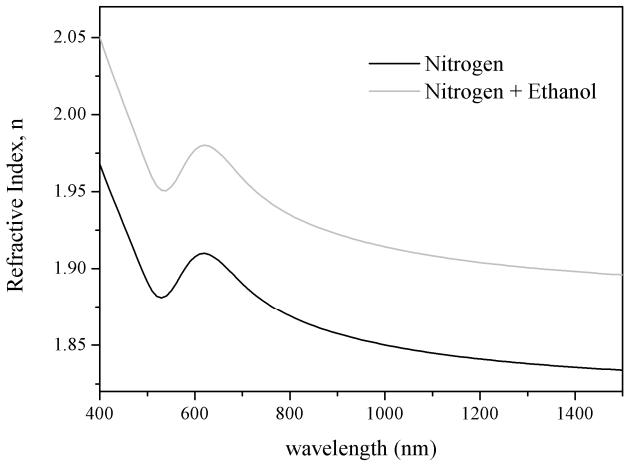

Figure A.6. Refractive index dispersion curves for a TiO_2-Au film measured in reverse side mode under nitrogen (black line) and ethanol vapors (grey line) atmospheres.

Table A.2. Comparison of correlation values between 4 couples of fitting parameters in the single angle and multiangle analyses. The fitting parameters are: *A* (*A* factor in Cauchy dispersion formula); *B* (*B* factor in Cauchy dispersion formula); *C* (*C* factor in Cauchy dispersion formula); *t* (thickness of the film); *Br* (broadening of the Gaussian oscillator); *En* (energy center of the Gaussian oscillator).

Parameters	Correlation (single angle)	Correlation (multiangle)
A-t	0.785	0.417
B-C	0.953	0.951
A-Br	0.821	0.327
En-Br	0.661	0.585

A different test has been performed on a highly porous TiO_2 crystalline film of about 100 nm thickness annealed at 500 °C (again the synthetic procedure is similar to the one

reported in section 5.2.4), measured in "reverse side" at 3 different angles (50, 60 and 70°) under air and ethanol environment: in this case the cell has been filled with liquid ethanol to demonstrate the feasibility of the measurements also in liquid environments. The high porosity of this particular sample has been obtained using an organic templating agent (Pluronic F127) that is removed during the thermal treatment. Compared to the picture shown in Figure A.3a, a slightly different cell has been adopted: the only difference was that inlet and outlet were placed at the top of the sample holder, in order to allow complete filling of the cell with the liquid; moreover the measurements have been performed in steady state, so without a continuous liquid stream. The experimental refractive index dispersion curves measured in the two different environments and modeled with a Cauchy dispersion are reported in Figure A.7: as in the previous examples, a clear increase in the refractive index value when performing the measurement in ethanol can be appreciated, and also the dispersion curve is not modified in shape, confirming again that the filling of the pores with ethanol does not affect the optical properties of the film.

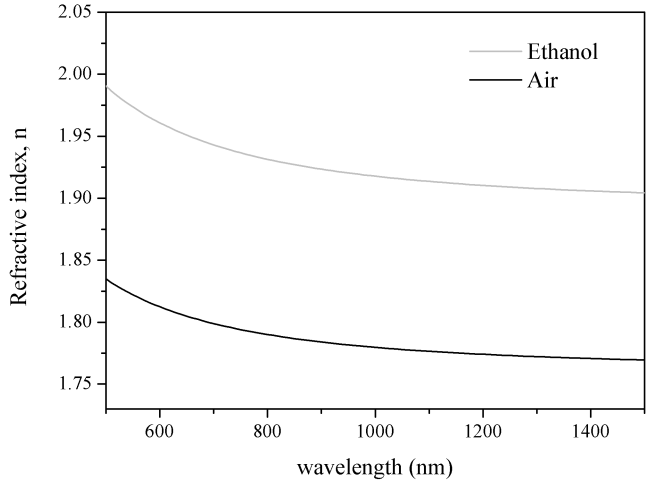

Figure A.7. Refractive index dispersion curves for a TiO_2 film measured in reverse side mode under air (black line) and liquid ethanol (grey line) environments.

Using again the formula (A.6), and considering the experimental refractive index at 1000 nm (1.779 in air and 1.919 in ethanol), the estimated open porosity is 61%. The thickness is again very similar in the two different environments (101.3 nm in air and 103.5 nm in ethanol).

To definitely prove that these measures are effective and reliable in evaluating the porosity amount, the same sample has been annealed again at 800 °C and eventually at

1000 °C performing the ellipsometric measurements in air and in ethanol after each treatment, with the idea of promoting the densification of the film with the thermal treatment, so reducing the porosity: together with a decrease in thickness (the thickness is about 85 nm and 71 nm after 800 °C and 1000 °C annealing, respectively) due to film shrinkage, the refractive index measured in air is found to increase as a consequence of the densification of the film and the increase in the crystalline fraction. The refractive index measured in ethanol is found to increase as well, but not as much: the explanation of this behavior is that the amount of porosity is reduced by the thermal treatment, and so is the amount of ethanol that fills the pores. Table A.3 shows the refractive index values measured in air and in ethanol at 1000 nm for the sample annealed at the three temperatures, and also the evaluated open porosity, confirming the trend discussed so far.

Table A.3. Refractive index values measured in air and in ethanol and estimated open porosity for a porous TiO_2 sample annealed at different temperatures.

Annealing temperature (°C)	Refractive index at 1000 nm in air	Refractive index at 1000 nm in ethanol	Open Porosity (%)
500	1.779	1.919	61%
800	1.93	2.035	49%
1000	2.131	2.202	35%

In conclusion, a new method to measure porosity of thin films with ellipsometric analyses has been presented: the sample is mounted on a custom-built cell in “reverse side” mode, so it is probed on the back side but aligned in order to collect the reflected beams coming from the substrate-film and film-environment interfaces. In this way it is possible to perform ellipsometric analyses under different environments (both liquid and gas phases) at various angles of incidence, and so estimate the open porosity amount by means of effective medium approximation models. Compared to the single angle measurements, this multiangle approach allows an improvement of the fitting results by reducing the correlation between fitting parameters. Several examples have been presented, confirming the feasibility of the “reverse side” measurements both in vapors and liquid environments.

A.4 Materials Recipes

A.4.1 Substrates cleaning

A cleaning and hydroxylation protocol was developed: first substrates were sonicated for 15 minutes in acetone to remove excess organic compounds, then they were washed thoroughly with deionized (DI) water and then immersed in hot (70 °C) basic piranha solution, a mixture of DI water, H_2O_2 (30% wt solution) and NH_3 (25% wt solution) according to 5:3:1 volume ratios, for 20 minutes in order to remove residual organic compounds and slightly etch the surface of the substrate creating –OH dangling bonds useful to improve their wettability and to allow sol-gel film anchorage. After a careful rinsing with DI water, substrates were stored under water, and dried in a air or nitrogen stream just before the deposition process.

A.4.2 Optimized recipe for TiO_2-NiO-Au precursors solutions

In a typical synthesis for a 50% molar TiO_2 – 50% molar NiO sample, 0.55 mL of Titanium Butoxide are added to 0.47mL of EtOH under stirring; 0.266 mL Acac are subsequently added and the solution is stirred for 20 minutes; then 0.117 mL of water are slowly added under vigorous stirring. In two separate vessels, 0.384g of $NiCl_2 \cdot 6H_2O$ are dissolved in 2.95 mL EtOH and 51mg $HAuCl_4 \cdot 3H_2O$ are dissolved in 0.647 mL EtOH. The TiO_2 and NiO solutions are mixed under stirring, and the Au solution, or 0.647 mL EtOH are eventually added, leading to Au-containing, or Au-free solutions, respectively.
The spin coating deposition has to be carried out under nitrogen atmosphere, and the as deposited film has to be annealed immediately at the desired temperature in a preheated oven.

A.4.3 Optimized recipe for SiO_2-NiO-Ag solutions and films

In a typical synthesis for 70%SiO_2-30%NiO sample, 1.57 mL EtOH, 1.5 mL TEOS, 0.485 mL H_2O, 0.02mL HCl 1N are mixed in this order under stirring. Separately, 847 mg Pluronic F127 are dissolved in 3.13 mL EtOH, 0.12 mL H_2O and 0.02 mL HCl 1N, and added dropwise to the previously prepared solution. The Nickel solution was prepared dissolving 1.19 g $NiCl_2 \cdot 6H_2O$ in 6.52 mL EtOH, and subsequently adding 1.09 mL DAEPTMS under stirring. The two solutions were then mixed and the resulting solution was used to deposit the films. After an annealing at 800°C for 1 hour, the

mesoporous film were dipped for few seconds in a hot (60°C) basic piranha solution (H_2O_2:NH_3:H_2O = 3:1:10), rinsed with water, dried and subsequently dipped in a solution of toluene (15 mL) and APS (0.75 mL) at 60 °C for 5 minutes. The samples were then washed with fresh toluene and dried in a nitrogen stream. Ag impregnation was performed dipping the samples in a solution composed of 340 mg $AgNO_3$ and 20 mL water, and let in dark for 4 hours. Eventually, samples were washed with acetone, dried and annealed at 700 °C for 1 hour.

A.4.4 Optimized recipe for the synthesis of 13 nm Au NPs

280 mg trisodium citrate in 24 ml Milli-Q water preheated at 70 °C was quickly added to a 400 mL boiling aqueous solution containing 80 mg $HAuCl_4$. After the solution turned red-wine colored, it was stirred at boiling point for an additional 15 minutes and then was cooled down to room temperature.

If the particles were to be redispersed in ethanol, PVP-10K was dissolved in water (200 mg in 4 mL) and this solution was mixed with aqueous gold colloids under constant stirring. After 2 hours the solution was concentrated in a rotary evaporator to about 100-150 mL and Au NPs were precipitated with excess acetone, centrifuged at 4000 rpm for 5 minutes and re-dispersed in ethanol leading to a 30 mM concentrated sol.

If the particles were to be stocked in water, after the as-prepared colloidal solution was brought to room temperature, a solution composed of 4.5 mg MUA, 10 mL H_2O and 0.3 mL NH_3 solution (25% in water) is slowly added under constant stirring; the total solution is let stir for 2 hours then a 1M HCl solution is added dropwise under stirring, until the Au NPs solution color turns from ruby red to violet. Then no more acid was added, and the solution was let sediment overnight; the supernatant was discarded and the sediment was redispersed in slightly basic water leading to 60 mM final stock solution.

A.4.5 Optimized recipe for the synthesis of 3 nm Au NPs

Smaller Au NPs are synthesized dissolving 18 mg $HAuCl_4$ into 3 mL methanol, and adding this solution to a previously prepared methanolic solution of PVP-10K (75 mg in 38 mL) under stirring. After 30 minutes, a separately prepared solution composed of 8 mg $NaBH_4$ dissolved in 3 mL methanol are quickly injected under strong stirring, and the resulting brownish solution is let stir for additional 30 minutes. The methanol is then removed by mean of rotary evaporation, and the sediment is easily redispersed in water;

the particles are then precipitated with excess acetone, centrifuged at 4000 rpm for 5 minutes, and redispersed in ethanol leading to 30 mM concentrated solutions.

A.4.6 Optimized recipe for the synthesis of 10 nm Pt NPs

In a typical synthesis, 67 mg of H_2PtCl_6 and 18.7 mg of NaCl were dissolved in 3 mL ethylene glycol, degassed and kept under intert atmosphere (nitrogen). Separately, 150 mg $NaNO_3$ and 55 mg PVP were dissolved into 13 mL ethylene glycol, degassed, and brought at 160 °C under intert atmosphere. After 20 minutes, the former solution was quickly injected into the latter: a change in color from pale orange to black was observed within few minutes. The Pt colloidal solution was kept at 160 °C under nitrogen for 30 minutes, then cooled down to room temperature, precipitated with excess acetone, centrifuged at 4000 rpm for 5 minutes and redispersed in ethanol leading to a 30 mM nominal concentration.

A.4.7 Optimized recipe for the synthesis of Au@Pt core@shell NPs

Au cores are synthesized as described in section A.4.4, and after the solution is cooled down to room temperature, the water losses due to evaporation during the synthesis are compensated. Separately, 82 mg H_2PtCl_6 are dissolved in 20 mL water (from now on called Pt solution), and 350 mg ascorbic acid are dissolved in 20 mL water (from now on called reducing solution). If considering 100 mL of 0.5 mM Au cores solution, before adding the Pt and the reducing solutions, it is further diluted with 20 mL water, leading to a 0.42 mM concentration in atomic Au. According to the desired size of the shell, various amounts of Pt solutions can be added (0.2 mL, 1 mL, 2 mL, 4 mL, 10 mL); after 15 minutes of stirring, the reducing solution is added keeping the volume ratio reducing solution / Pt solution equal to 1.5: the respective amounts of reducing solution are 0.3 mL, 1.5 mL, 3 mL, 6 mL, 15 mL. A change in color is experienced for several hours, more pronounced for higher Pt amount samples. After letting the prepared solution stir for 24 hours, PVP-10K was dissolved in water (5 mg in 1 mL) and this solution was mixed with aqueous Au@Pt colloids under constant stirring. After 2 hours the solution was concentrated in a rotary evaporator to about 30-40 mL and the NPs were precipitated with excess acetone, centrifuged at 4000 rpm for 5 minutes and re-dispersed in ethanol leading to a 30 mM concentrated sol.

A.4.8 Optimized recipe for the synthesis of 4 nm TiO_2 NPs

In a typical synthesis, 3 g of titanium isopropoxide was added drop wise to a previously prepared solution consisting in 1.78 g of hydrochloric acid, 7.18 mL of methanol and 1.24 g of water. The solution was stirred at ambient temperature for one hour and subsequently heated to 70 °C for four hours. Particles were then precipitated with excess acetone and centrifuged at 4000 rpm for two minutes. The obtained precipitate was dispersed in minimum amount of methanol obtaining a clear colloidal sol of anatase TiO_2 NPs. The concentrated solution is stable for few days. The best is to use the solution for films deposition within the following day.

A.4.9 Optimized recipes for the synthesis of ZnO and doped-ZnO NPs

500 mg of Zinc acetate dihydrate (ZnAc) are dissolved in 22.5 mL dimethyl sulfoxide (DMSO); separately, 750 mg tetramethylammonium hydroxide (TMAH) are dissolved in 7.5 mL ethanol (EtOH). The TMAH solution is added dropwise (about 2 mL/min) to the Zinc solution under vigorous stirring at room temperature; after 10 minutes the solution is heated at 40 °C for 1 hour to promote Ostwald ripening of the particles, obtaining 6-7 nm NPs. To obtain 8 nm the solution has to be heated at 50 °C. For bigger (10-11 nm) particles, the solution must be heated at 60 °C. To prepare ZnO NPs doped with metal ions, it is sufficient to substitute the desired amount of Zn precursor with the dopant precursor, keeping the Zn+dopant molarity constant: for example, to obtain ZnO crystals with 1% Co, 495 mg ZnAc are mixed with 5.7 mg Cobalt Acetate tetrahydrate (CoAc); to get a 2.5% doping, 487.5 mg ZnAc are mixed with 14.2 mg CoAc; eventually, to have a 5% cobalt doping, 475 mg ZnAc and 28.3 mg CoAc are mixed together. Then the previously reported recipe is followed. After the solution has been heated for 1 hour, it was let cool down to room temperature, precipitated with the minimum amount (about 3:1 in volume) of methyl ethyl ketone (MEK), centrifuged at 1500 rpm for 5 minutes and redispersed in ethanol to a final nominal concentration of 0.8 M in molar zinc. The concentrated solutions are stable only for few hours, so they have to be used immediately for films deposition.

A.4.10 Optimized recipe for the synthesis of Au NPs layers

After the substrates were cleaned as reported in section A.4.1, they were dried and then placed on a hot plate at 100 °C in order to remove adsorbed water. Afterwards they were immersed into a solution composed of 0.3 mL APS in 30 mL toluene at 60 °C for 5

minutes in a controlled environment (R.H. < 20 %). Substrates were then extracted and immediately washed thoroughly with fresh toluene, dried in a nitrogen stream and then placed on a hot plate at 70 °C for 5 minutes to remove adsorbed toluene molecules. These substrates were used within the day, in order to prevent amines oxidation. Aqueous MUA-capped Au NPs solution were diluted with ethanol to a 1:1 volume and then directly spun over the APS functionalized substrates; samples were then stabilized on a hot plate at 100 °C for 15 minutes, and subsequently used as substrates themselves for sol-gel films coating.

A.4.11 Optimized recipe for the synthesis of TiO_2-based sol-gel solution

A solution of Ethanol (0.413 mL), Titanium Butoxide (TiBu, 0.447 mL) and AcetylAcetone (AcAc, 0.216 mL) is prepared under vigorous stirring at room temperature. After 10 minutes, 0.1 mL Milli-Q water are added and let stir for additional 20 minutes. Just before deposition, 1.83 mL ethanol or an equivalent volume of metal (Au, Pt) NPs in ethanol are added; the total solution is let stir for 5 more minutes, and then it is used for films deposition. The spin coating procedure has to be carried out under nitrogen atmosphere.

A.4.12 Optimized recipe for the synthesis of NiO-based sol-gel solution

300 mg of Nickel Acetate tetrahydrate (NiAc) were dissolved in 2 mL methanol and subsequently 0.18 mL diethanolamine (DEA) were added under stirring. After 40 minutes, 1.4 mL ethanol (or ethanolic suspension of metal NPs) were added, and after additional 5 minutes the solution was spun under nitrogen atmosphere.

A.4.13 Optimized recipe for the synthesis of ZnO-based sol-gel solution

To deposit a ZnO layer, 200 mg of Zinc acetate dihydrate (ZnAc) was dissolved in 0.9 cc ethanol, and subsequently 0.066 mL monoethanolamine (MEA) were added under stirring. After 30 minutes, 0.35 mL ethanol (or ethanolic suspension of metal NPs) were added and the solution was used for film depositions after 5 more minutes of stirring. Again, the spinning procedure is performed under nitrogen atmosphere.

Bibliography

[1] See the website http://rsb.info.nih.gov/ij.

[2] J.J. Yeh, I. Lindau, *Atomic Data and Nuclear Data Tables*, **1985**, *32*, 1.

[3] S. Tanuma, C.J. Powell, D.R. Penn, *Surf. Interface Anal.*, **1993**, *21***,** 165.

[4] A. Martucci, M. Pasquale, M. Guglielmi, M.L. Post, J.C. Pivin, *J. Am. Ceram. Soc.*, **2003**, *86*, 1638.

[5] See the website and the references reported in www.radiello.com/italiano/inter_it.htm.

[6] H.Y. Zhu, N. Maes, A. Molinard, E.F. Vansant, *Microporous Mater.*, **1994**, *3*, 235-243.

[7] M. Kruk, M. Jaroniec, A. Sayari, *Langmuir*, **1997**, *13*, 6267-6273.

[8] D.A.G. Bruggeman, *Ann. Phys.* (Leipzig), **1935**, *24*, 636.

[9] M.T. Othman, J.A. Lubguban, A.A. Lubguban, S. Gangopadhyay, R.D. Miller, W. Volksen, H.C. Kim, *J. Appl. Phys.*, **2006**, *99*, 083503.

[10] D. Lee, M.F. Rubner, R.E. Cohen, *Nano Lett.*, **2006**, *6*, 2305-2312.

[11] V. Rouessac, A. Van Der Lee, F. Bosc, J. Durand, A. Ayral, *Microporous Mesoporous Mater.*, **2008**, *11*, 417-428.

[12] A. Bourgeois, A. Brunet Bruneau, V. Jousseaume, N. Rochat, S. Fisson, B. Demarets, J. Rivory, *Thin Solid Films*, **2004**, *455-456*, 366-369.

[13] M.A. Fardad, E.M. Yeatmana, E.J.C. Dawnay, M. Green, F. Horowitz, *J. Non-Cryst. Solids*, **1995**, *183*, 260-267.

[14] M.R. Baklanov, K.P. Mogilnikov, V.G. Polovinkin, F.N. Dultsev, *J. Vac. Sci. Technol. B*, **2000**, *18*, 1385-1391.

[15] Y. Sakatani, D. Grosso, L. Nicole, C. Boissière, G.J. de A.A. Soler-Illia, C. Sanchez, *J. Mater. Chem.*, **2006**, *16*, 77–82.

[16] A. Bourgeois, A. Brunet Bruneau, S. Fisson, B. Demarets, D. Grosso, F. Cagnol, C. Sanchez, J. Rivory, *Thin Solid Films*, **2004**, *447-448*, 46–50.